

Periodic Lateral Polar Structure-based Waveguides in III-Nitrides for Quasi-Phase Matched Second Harmonic Generation

vorgelegt von
Diplom-Physiker
Dorian Eduardo Alden Angeles
geb. in Mexiko Stadt, Mexiko

Von der Fakultät II – Mathematik und Naturwissenschaften der Technischen
Universität Berlin zur Erlangung des akademischen Grades

Doktor der Naturwissenschaften
Dr. rer. nat.

genehmigte Dissertation

Promotionsausschuss:

Vorsitzender: Prof. Dr. Michael Lehmann

Gutachter: Prof. Dr. Axel Hoffmann

Gutachter: Prof. Dr. Zlatko Sitar

Gutachter: Prof. Dr. André Strittmatter

Tag der wissenschaftlichen Aussprache: 24. April 2017

Berlin 2017

ABSTRACT

Lasers emitting in the ultraviolet spectrum below 300 nm are desired for a variety of applications. Currently available deep UV laser systems are expensive, inefficient, stationary, require frequent maintenance and have a high operation cost. Alternatively, UV laser light can be obtained through frequency doubling as second harmonic generation using nonlinear crystals. The III-Nitrides are attractive for nonlinear optical applications due to their large nonlinear optical coefficients, wide transparency window and high thermal conductivity. The birefringence in III-Nitrides is weak, thus an alternative phase matching approach is necessary.

In this work, quasi-phase matched second harmonic generation in the UV using AlN lateral polar structure based waveguides is demonstrated for the first time. A process scheme for controlling the polarity of epitaxial AlN and GaN layers deposited on sapphire substrates via metalorganic chemical vapor deposition (MOCVD) is presented. The process is extended to achieve periodic lateral polar structures with domain sizes in the nanometer scale by introducing laser interference lithography. Subsequently, the surface roughness RMS value of the lateral polar structures is reduced to 10 nm and below, over a $90 \mu\text{m}^2$ area through promoting step flow growth at the nitrogen polar surface through control of the vapor supersaturation. Next, thickness differences between the alternating polar domains at reduced vapor supersaturation values is demonstrated to arise from mass transport between the adjacent opposite-polar domains, and the growth conditions leading to equal deposition rate for both polarities are established. Waveguides are then etched into the AlN lateral polar structures and tested for quasi-phase matched second harmonic generation. Employing 550 nm and 250 nm thick AlN lateral polar structures-based waveguides, 5th and 7th order quasi phase matched second harmonic generation is demonstrated at 344 nm and 386 nm respectively, in agreement with theoretical calculations. In parallel, single polar AlN waveguides are fabricated for modal dispersion phase matched second harmonic generation, where wavelengths as low as 305 nm are achieved.

Lastly, the transparency in AlN bulk single crystals are investigated where point defects leading to below bandgap energy absorption centers in the UV-C spectral range are identified and attributed to carbon impurities. For this, a novel approach for determining the impurities type and concentrations in the crystal is presented, where photoluminescence spectroscopy, photoluminescence excitation spectroscopy, transmission spectroscopy and secondary ion mass spectroscopy data is used in combination with a density functional theory based theoretical model which accounts for charge balance conservation in the crystal and the formation energy of defects.

ZUSAMMENFASSUNG

Laser mit Emission im UV-C Spektralbereich haben viele potentielle Anwendungen. Die zurzeit verfügbaren Laser mit Emissionswellenlängen zwischen 150 nm und 300 nm sind Excimer Laser, welche ineffizient, teuer, und groß sind. Alternativ, kann UV-C Laser Licht durch Frequenzverdopplung erzeugt werden. Die Gruppe III-Nitride sind durch ihre besonderen Materialeigenschaften (hohe elektrische Suszeptibilität, Transparenz und thermische Leitfähigkeit) besonders attraktiv für nichtlineare optische Anwendungen. Da Doppelbrechung in V-III Kristallen nicht ausreicht um Winkel-Phasenanpassung zu erreichen werden alternative Phasenanpassungsmethoden für die Erzeugung von UV Licht benötigt.

In dieser Arbeit wird gezeigt, dass UV Laser Licht durch Frequenzverdopplung mittels quasi-Phasenanpassung in Wellenleitern basierend auf periodisch gepolten AlN erzeugt werden kann. Dazu wurde ein Verfahren zur makroskopischen Polaritätskontrolle von MOCVD gewachsenen AlN und GaN Schichten entwickelt, welches hier vorgestellt wird. Des Weiteren wurden Strukturen im Nanometerbereich mittels Laser Interferenz Lithographie erzeugt, und die mittlere Oberflächenrauigkeit der periodische Strukturen auf 10 nm über eine $90 \mu\text{m}^2$ Fläche verringert. Dieses wurde durch Kontrolle der Übersättigung der Gasphase erreicht welche Stufenwachstum in der N-polaren AlN Domäne kontrolliert. Höhenunterschiede zwischen nebeneinanderliegenden Domänen gegensätzlicher Polarität werden durch Massentransport in der Gasphase erklärt. Durch eine Anpassung der Wachstumsbedingung konnten gleich dicke Al- und N-polare Domänen erreicht werden, was notwendig ist um Wellenleiter basierend auf periodisch gepolten AlN Strukturen herzustellen. Frequenzverdopplungsversuche wurden durchgeführt an 550 nm und 250 nm dicken Wellenleiter mit 10 μm Periodizität. Dabei konnte UV Laser Licht mit 344 nm und 386 nm Wellenlänge erzeugt werden. Die experimentellen Ergebnisse zeigten eine exzellente Übereinstimmung mit theoretischen Berechnungen für die 5te beziehungsweise 7te Ordnung der quasi-Phasenanpassung. Des Weiteren wurden Al-polare AlN Wellenleiter hergestellt und untersucht, wobei Frequenzverdopplung mittels Moden Dispersion (MDPM) wurde erreicht. Die niedrigste Wellenlänge für die Frequenzverdopplung die erreicht wurde war 305 nm.

Abschließend wurden die optischen Eigenschaften von AlN Einkristalle mittels Photolumineszenz-Anregungsspektroskopie, Transmissionspektroskopie und SIMS untersucht, und die Ergebnisse mit Berechnungen basierend auf Dichtefunktionaltheorie verglichen. Dabei wurde festgestellt, dass Kohlenstoff auf einem Stickstoff Gitterplatz verantwortlich für das Absorptionsband mit Maximum um 4.7 eV ist. Dieses Ergebnis basiert auf einer Korrelation der Photolumineszenzbänder um 3.9 eV und 2.7 eV und dem Absorptionsband bei 4.7 eV.

Contents

| | |
|--|-----------|
| List of Figures | i |
| List of Tables..... | ix |
| 1 Introduction | 1 |
| 1.1 Group III-Nitrides: History and Their Role in Current Technologies | 1 |
| 1.2 Material Properties and Potential Future Applications..... | 2 |
| 1.3 Objectives of this work | 6 |
| 2 Theoretical background..... | 9 |
| 2.1 Second Order Nonlinear Optical Processes | 9 |
| 2.1.1 Second Harmonic Generation (SHG)..... | 9 |
| 2.1.2 Waveguide Modes | 14 |
| 2.1.3 Modal Dispersion Phase Matching..... | 17 |
| 2.1.4 Quasi-Phase Matching in III-Nitride Waveguide Structures..... | 18 |
| 2.2 Surface Kinetics in III-Nitride Growth..... | 22 |
| 2.3 Point Defects..... | 27 |
| 2.3.1 Energy of Formation for Point Defects | 27 |
| 2.3.2 Franck-Condon Approximation..... | 31 |
| 3 Experimental Setup..... | 34 |
| 3.1 Optical Spectroscopy | 34 |
| 3.1.1 Photoluminescence and Photoluminescence Excitation Spectroscopy | 34 |
| 3.1.2 Second Harmonic Generation Spectroscopy | 36 |
| 3.1.3 Transmission Spectroscopy | 36 |
| 3.1.4 Micro-photoluminescence Spectroscopy Setup | 38 |
| 3.2 Growth Setup | 39 |
| 3.3 Laser Interference Lithography | 40 |
| 4 Polarity Control..... | 43 |
| 4.1 Historical Perspective | 43 |

| | | |
|----------|--|------------|
| 4.2 | III-Polar AlN and GaN | 45 |
| 4.3 | N-Polar AlN and GaN | 48 |
| 4.4 | Polarity Dependent Wet Etching in KOH | 50 |
| 5 | Lateral Polar Structures | 53 |
| 5.1 | AlN Lateral Polar Structures | 53 |
| 5.1.1 | Nanometer Scale AlN Lateral Polar Structures | 61 |
| 5.1.2 | Promoting Step Flow Growth through Control of Al Vapor Supersaturation | 73 |
| 5.1.3 | Mass Transport between Polar Domains | 77 |
| 5.1.4 | Influence of Crystallographic Orientation on the IDB | 88 |
| 5.2 | GaN Lateral Polar Structures | 90 |
| 5.2.1 | Nanometer Scale GaN Lateral Polar Structures..... | 92 |
| 5.2.2 | Promoting Step Flow Growth for Smooth GaN LPS..... | 94 |
| 6 | Point Defects in AlN | 99 |
| 6.1 | PVT Grown AlN Bulk Single Crystals | 99 |
| 6.1.1 | Historical Perspective | 99 |
| 6.1.2 | Absorption, PL and PLE Characterization..... | 101 |
| 6.1.3 | High Temperature Absorption Spectra | 109 |
| 7 | UV Laser Light as Second Harmonic Generation | 116 |
| 7.1 | Modal Phase Matched SHG | 116 |
| 7.2 | Quasi Phase Matched SHG in AlN LPS Waveguides..... | 118 |
| 7.2.1 | 10 μm Periodicity..... | 120 |
| 7.2.2 | 1.2 μm Periodicity..... | 124 |
| 8 | Conclusions and Future Work | 127 |
| 8.1 | Summary and Conclusions..... | 127 |
| 8.2 | Future Work | 129 |
| 9 | Publications and Conference Contributions | 130 |
| 9.1 | Publications | 130 |

| | | |
|-----------|------------------------------|------------|
| 9.2 | Conference Talks | 131 |
| 10 | References | 132 |
| 11 | Acknowledgements..... | 148 |

List of Figures

| | |
|--|----|
| Figure 1-1: Schematic of the III-Nitride wurtzite structure, where the basal plane (c-plane) and the primary (m-plane) and secondary (a-plane) prismatic planes are highlighted. | 3 |
| Figure 1-2: Calculated bandgap energy as a function of III-Metal composition x for the III-Nitrides ternary alloys using Vegard's law. Bowing parameters b are taken from Pelá et al. ²² | 5 |
| Figure 2-1: Intensity of the second harmonic generated wave as a function of propagation length. Highlighted in red is the coherence length distance l_c , which is the length in which the wave vectors of the driving and induced wave accumulate a phase-shift of π | 12 |
| Figure 2-2: Schematic of planar waveguide structure used to describe the propagation of TM electromagnetic modes. Three layers with different refractive index n_i are displayed. | 15 |
| Figure 2-3: Electric field amplitude of the second harmonic wave as a function of propagation length for three different phase matching scenarios. | 21 |
| Figure 2-4: Intensity of the second harmonic wave as a function of propagation length for three different phase matching scenarios. | 21 |
| Figure 2-5: Illustration of a formation energy diagram of a point defect X for various charged states q (+2, +1, 0, -1) as a function of Fermi energy referenced to the valence band maximum (the bandgap energy of AlN was chosen as an example). | 29 |
| Figure 2-6: Illustration of a formation energy diagram of a point defect, with its thermodynamic transition energies highlighted. | 30 |
| Figure 2-7: Configuration coordinate diagram illustrating the shift in energy between the peak absorption and emission bands, due to electron-phonon coupling. An optoelectronic transition involving a point defect X in the -1 charged state leading to a free electron in the conduction band and a neutral charged state is shown and the respective recombination process. | 31 |
| Figure 3-1: Experimental setup for photoluminescence spectroscopy measurements. | 34 |
| Figure 3-2: Schematic of the photoluminescence excitation spectroscopy setup. | 35 |

| | |
|---|----|
| Figure 3-3: Schematic of experimental setup used for testing the AlN and GaN based waveguides for second harmonic generation..... | 36 |
| Figure 3-4: Experimental setup for temperature dependent transmission spectra up to 900 °C. | 37 |
| Figure 3-5: Micrometer spatially resolved photoluminescence excitation spectroscopy setup. | 38 |
| Figure 3-6: Picture of the metal organic chemical vapor deposition reactor during vacuum annealing at 1100 °C (left). Clockwise starting at the top left, picture of the cooling systems containing the metalorganic sources (TMA and TEG), liquid nitrogen tank which provides the N ₂ gas source, ammonia gas source and hydrogen gas source. | 39 |
| Figure 3-7: Lloyd's mirror configuration setup..... | 40 |
| Figure 3-8: Laser interference intensity profile at the sample surface..... | 41 |
| Figure 4-1: Schematic displaying the crystal structure for different polar growth directions and mixed polar growth | 43 |
| Figure 4-2: Growth run temperature profile of an AlN nucleation layer..... | 46 |
| Figure 4-3: AFM image of the surface of a typical AlN nucleation layer. | 47 |
| Figure 4-4: AFM measurements of the surface morphology of a Ga-polar GaN (left) and Al-polar AlN (right) epitaxial layer. | 48 |
| Figure 4-5: AFM measurements of the surface morphology of N-polar GaN (left) and AlN (right) respectively with high (top) and low (bottom) magnification. | 49 |
| Figure 4-6: Tilted cross section SEM image displaying the etched surface of a III-polar (top) and N-polar (bottom), GaN (left) and AlN (right) epitaxial layer. | 51 |
| Figure 5-1: Schematic of mask design used for photolithography. The mask contains 8 different regions of 1 cm ² areas with different stripe structures. The stripe structures are composed of equally spaced covered and uncovered stripes. The periodicity of the stripe structures are 10, 20, 40 and 100 μm. Every periodic structure is available in two orientations at a 90° angle from each other in order to study the influence of the substrate orientation on the grown structures. The center region is half covered and half uncovered to achieve 0.5 x 1 cm ² single polar domains and compare with the corresponding polar domains in the lateral polar structures. | 54 |

-
- Figure 5-2: AFM image of a 20 μm periodic stripe pattern of an AlN nucleation layer deposited on a sapphire substrate with color coated height scale (left). Line scan across the periodic structure showing the height profile.....55
- Figure 5-3: AFM image of a 20 μm periodic AlN lateral polar structure55
- Figure 5-4: DIC optical microscope images of a 100 μm periodic AlN LPS as grown (left) and after wet etching for 30 seconds in 1M KOH at 70 $^{\circ}\text{C}$56
- Figure 5-5: SEM images of a 10 μm periodic AlN LPS as grown (left). On the right a 100 μm periodic AlN LPS after wet etching in a 1M KOH solution in DI water at 70 $^{\circ}\text{C}$ for 30 s.57
- Figure 5-6: SEM measurements of a wet etched 100 μm periodic AlN LPS. (Left) The wet etched N-polar domain where the remaining low density of large conical features are highlighted. (Center) high magnification of the inversion domain boundary with highlighted high density of conical features.57
- Figure 5-7: SEM image of a wet etched N-polar AlN film in a 0.5 M KOH solution in DI water for 20 s at 70 $^{\circ}\text{C}$. The apparent Al-polar inversion domains are encircled.58
- Figure 5-8: AFM amplitude images of the patterned AlN nucleation layer on a sapphire substrate prior to the growth of an AlN LPS (Top images). SEM images of wet etched AlN LPS showing a series of aligned Al-polar inversion domains in a similar pattern to the polishing scratches (Bottom images).59
- Figure 5-9: SEM image displaying a magnified view of the residual hexagonal pyramids after wet etching. Vertical AlN wires located at the top of the hexagonal pyramids are highlighted.....60
- Figure 5-10: Calculated coherence length in bulk AlN single crystal as a function of fundamental (driving) wavelength.62
- Figure 5-11: Both sides of equation (5.1.2) are plotted. In red, the effective refractive index for the 0th order mode of the fundamental wave. In purple, the effective refractive index for the 0th order mode of the second harmonic wave reduced a term given by the periodicity of the AlN LPS with $\Lambda = 1.2 \mu\text{m}$63
- Figure 5-12: Nanoscale polarity control process scheme. Step 1: MOCVD deposition of AlN nucleation layer on c-plane sapphire. Step 2: Photoresist and ARC are spin coated onto the substrate. Step 3: Photoresist layer is

| | |
|--|----|
| exposed to the laser interference periodic pattern and developed. Step 4: Pattern is transferred to the AlN nucleation layer by reactive ion etching. Step 5: The residual photoresist and ARC are removed by O ₂ plasma. Step 6: The patterned substrate is reinserted in the MOCVD chamber, where the AlN film is deposited leading to the AlN periodic lateral polar structure. ⁹⁵ | 64 |
| Figure 5-13: Differential interference contrast optical microscope image of 1.2 μm periodic pattern of the photoresist layer..... | 65 |
| Figure 5-14: Reflected intensity at the ARC-photoresist interface as a function of ARC thickness. | 66 |
| Figure 5-15: Atomic force microscopy image and height profile line scan of the patterned substrate, displaying domains of 25 nm thick AlN layers and domains with the sapphire substrate exposed. | 67 |
| Figure 5-16: Height profile AFM images of the patterned substrate before (left) and after the AlN thin film growth (right). In the right image, domains with a rough hexagonal columnar surface, characteristic of the N-polar domain, is observed as well domains with a smooth (sub-nanometer RMS roughness) Al-polar surface with similar domain sizes as the patterned substrate, pointing at the vertical inversion domain boundaries. | 68 |
| Figure 5-17: Tilted view SEM image of the AlN LPS as grown (a) and after being submerged in a 1 molar KOH solution in deionized water for 1 minute at 70 °C (b)..... | 68 |
| Figure 5-18: Cross-sectional SEM images of AlN LPS samples with varying thicknesses. The inversion domain boundaries are highlighted with yellow dashed lines. Complete coalescence at the IDBs is observed. | 70 |
| Figure 5-19: AFM image of a 1.2 μm periodic AlN LPS before (top left) and after (bottom left) mechanical polishing with comparable sclaes. The respective height profile linescans across the periodic structure are shown on the top right and bottom right. | 72 |
| Figure 5-20: SEM images showing the AlN LPS-based waveguides at a low (left) and high (right) magnification respectively. | 73 |
| Figure 5-21: Surface morphology of N-polar AlN thin films grown at different temperatures. The growth temperatures for the displayed samples is 1250 °C, 1400 °C, 1500 °C and 1550 °C for a)-d) respectively. | 74 |
| Figure 5-22: Al vapor supersaturation as a function of growth temperature..... | 75 |

| | |
|---|----|
| Figure 5-23: Temperature and pressure dependence of measured growth rates for Al- and N-polar AlN epitaxial films. | 76 |
| Figure 5-24: Al vapor supersaturation as a function of total pressure inside the growth chamber. | 76 |
| Figure 5-25: AlN LPS for a series of growth runs, where the growth temperature was varied to reduce the Al vapor supersaturation. | 78 |
| Figure 5-26: Amplitude AFM images of a grown AlN LPS sample before (top left) and after (top right) KOH etching in a 1M solution at 70 °C for 30 s. (bottom) Height profile line scans for the corresponding amplitude AFM image. | 79 |
| Figure 5-27: Amplitude AFM images of AlN LPS before (top left) and after (top right) KOH etching in a 1M concentrated solution at 70 °C for 30 s. | 80 |
| Figure 5-28: Polar domain thickness difference and Al vapor supersaturation as a function of temperature. | 81 |
| Figure 5-29: (left) AFM images of 550 nm thick (top) and 250 nm thick AlN LPS-based waveguides with 10 μm periodicity. (right) Height profile line scans across and along the waveguide corresponding to their respective AFM images. | 82 |
| Figure 5-30: (left) AFM image of 1.2 μm periodic AlN LPS grown at 1500 °C. (right) Optical DIC image of the same sample after being submerged in KOH, displaying inhomogeneous etching, indicating that the AlN LPS contained mixed polar domains. | 83 |
| Figure 5-31: Amplitude AFM image of 1.2 μm AlN LPS samples grown at 1500 °C. Regions where one polarity is overgrowing the neighboring polarity are encircled. A few inversion domain boundaries (IDB's), as determined by the surface morphologies characteristic of the respective polarities, are marked with yellow dashed lines. | 83 |
| Figure 5-32: AFM height images for 1.2 μm AlN LPS grown at $\sigma \approx 5-10 \times 10^3$ (left) and $\sigma \approx 1 \times 10^5$ (right) Al vapor supersaturation values. | 84 |
| Figure 5-33: AFM height images of 1.2 μm AlN LPS grown by a two-step temperature process. The first step growth temperature for all samples was 1250 °C. In the second step the temperature was increased to 1400 °C (top), 1500 °C (center) and 1550 °C (bottom) in order to achieve a smooth surface morphology of the 1.2 μm AlN LPS. | 85 |

| | |
|---|----|
| Figure 5-34: Tilted SEM images of a KOH wet-etched 1.2 μm AlN LPS sample grown in a two-step temperature process..... | 86 |
| Figure 5-35: AFM height (top) and amplitude (bottom) image of two different 1.2 μm periodic AlN LPS, where thicker Al-polar domains compared to the N-polar domains are measured..... | 86 |
| Figure 5-36: AFM height (top) and amplitude (bottom) image of the 1.2 μm periodic AlN LPS displayed in Figure 5-35 after regrowth at x temperature for x minutes, where higher deposition rates for the N-polar domains compared to the Al-polar domains were determined..... | 87 |
| Figure 5-37: AFM amplitude images of the IDB in AlN LPS samples with periodicities along the a-direction (top) and along the m-direction (bottom). The left images, are taken from a sample where the stripe pattern is well aligned with the crystallographic orientations and the samples on the right are taken from a sample where the stripe pattern is slightly misaligned with respect to the crystallographic orientations..... | 89 |
| Figure 5-38: AFM image with corresponding height profile line-scans of a GaN LPS grown at a V/III ratio of 250. | 91 |
| Figure 5-39: DIC optical microscope images for a GaN LPS before (top left) and after different polishing times..... | 91 |
| Figure 5-40: 75 min long mechanically polished GaN LPS with 0.3 μm alumina particles in DI water solution..... | 92 |
| Figure 5-41: Calculated coherence length for bulk GaN as a function of fundamental wavelength..... | 93 |
| Figure 5-42: (left) AFM amplitude image of a 1.2 μm periodic GaN LPS showing N-polar GaN being overgrown by Ga-polar GaN. (right) AFM height image where the N-polar GaN areas that have been etched away are highlighted.. | 94 |
| Figure 5-43: Tilted cross-section SEM image of a 1.2 μm GaN LPS before (left) and after (right) wet etching in a KOH solution..... | 94 |
| Figure 5-44: Calculated Ga vapor supersaturation as a function of temperature. For comparison the values are calculated for H_2 and N_2 diluent gas (left) and for different total reactor pressures (right). | 95 |
| Figure 5-45: Calculated Ga vapor supersaturation as a function of V/III ratio for different temperatures under N_2 diluent gas (left) and under H_2 diluent gas (right). | 95 |

| | |
|---|-----|
| Figure 5-46: AFM height image of the surface of an N-polar GaN thinfilm grown under the conditions described in the text. A scan area of $5 \times 5 \mu\text{m}^2$ (left) and $90 \times 90 \mu\text{m}^2$ (right) is presented. | 96 |
| Figure 5-47: AFM height (left) and amplitude (right) image of a GaN LPS grown at relatively low Ga vapor supersaturation values ($\sigma \approx 100$). | 96 |
| Figure 5-48: Cross section SEM images displaying a GaN LPS grown at a Ga vapor supersaturation value of 100. | 97 |
| Figure 5-49: AFM amplitude images (top) and height profile linescans (bottom) of a $1.2 \mu\text{m}$ periodic GaN LPS grown at a Ga vapor superseaturation of 100 before (left) and after (KOH) etching. | 98 |
| Figure 6-1: Point defect formation energy as a function of fermi level energy for various likely point defects present in PVT grown AlN. | 103 |
| Figure 6-2: Schematic displaying the thermodynamic transition energy sates for the respective point defects, as horizontal lines, referenced to the valence band maximum. | 103 |
| Figure 6-3: Photoluminescence spectra (black) overlapped with the absorption spectra (red) of a PVT grown AlN single crystal. | 104 |
| Figure 6-4: Color coded logarithmic intensity 2D map photoluminescence excitation spectroscopy measurements of an AlN single crystal recorded at 5 K. The vertical lines correspond to PLE spectra for a fixed detection energy and are displayed as red curves in Figure 6-5. Horizontal lines correspond to PL spectra at a fixed excitation energy and are displayed in Figure 6-5 as black curves. | 106 |
| Figure 6-5: Photoluminescence spectra (black) for various excitation energies, overlapped with photoluminescence excitation spectra (red) for various detection energies. | 107 |
| Figure 6-6: Power dependent photoluminescence measurements for above bandgap excitation. | 108 |
| Figure 6-7: Temperature dependent transmission spectra for an epitaxial GaN layer deposited on a sapphire substrate. The absorption spectra are not corrected for reflection. | 110 |
| Figure 6-8: Temperature dependence of absorption coefficient spectra. The spectra are not corrected for reflection. | 110 |

| | |
|--|-----|
| Figure 6-9: Tauc relation for temperature dependent transmission spectra measured for a GaN epitaxial thinfilm. | 111 |
| Figure 6-10: Bandgap energy of a GaN epitaxial film as a function of temperature, compared with the Varshni model fitted with literature values. | 112 |
| Figure 6-11: Absorption spectra for an AlN single crystal with higher oxygen concentration than carbon for different temperatures in the range from 295 K to 1063 K. For comparison a “UV non-transparent” sample containing higher carbon impurities than oxygen and silicon is displayed. | 113 |
| Figure 6-12: Absorption spectra for an AlN single crystal with a higher carbon concentration than oxygen and silicon for a temperature range from 296 K to 1070 K. | 114 |
| Figure 7-1: DIC microscope image of Al-polar AlN waveguides for MDPM SHG. | 117 |
| Figure 7-2: Dispersion relation of the fundamental and second harmonic waveguide modes for a 10 μm wide and 550 nm thick Al-polar AlN waveguide, taken from a publication by Troha et al. ⁴⁷ | 117 |
| Figure 7-3: MDPM SHG measurements using a 10 μm wide and 550 nm thick Al-polar AlN waveguide. ⁴⁷ | 118 |
| Figure 7-4: 3D AFM image with color-coated height scale of 500 nm - 550 nm thick and 4 μm wide AlN LPS-based waveguides. | 120 |
| Figure 7-5: Dispersion relation for the fundamental (red) and second harmonic (purple) TM ₀₀ wave mode for a 220 nm thick waveguide. | 121 |
| Figure 7-6: 2D top view grayscale scattering intensity profile of the fundamental laser light propagating through the 10 μm periodic AlN LPS-based waveguide (Top). 1D scattering intensity profile for a line-scan section along the waveguide surface. | 122 |
| Figure 7-7: QPM SHG spectra at two different fundamental wavelengths for a 500 nm – 550 nm thick and 10 μm periodic AlN LPS-based waveguide. | 123 |
| Figure 7-8: QPM SHG spectra at two different fundamental wavelengths for a 200 nm – 250 nm thick and 10 μm periodic AlN LPS-based waveguide. | 123 |
| Figure 7-9: 1.2 μm periodic AlN LPS-based waveguides fabricated via SiO ₂ hard mask deposition and subsequent RIE. ⁹⁵ | 124 |

| | |
|---|-----|
| Figure 7-10: 1.2 μm periodic AlN LPS-based waveguides fabricated by standard masked photolithography using negative photoresist and subsequent RIE etching. | 124 |
| Figure 7-11: Top view 2D grayscale scattering intensity profile at the coupling facet of 1.2 μm periodic AlN LPS-based waveguides. | 125 |

List of Tables

| | |
|---|-----|
| Table 1-1: Lattice parameter and spontaneous polarization field for III-Nitrides. ^{6,21} | 4 |
| Table 1-2: Material properties relevant for optoelectronic devices. ^{15,16,21,23-28} | 5 |
| Table 2-1: Nonlinear properties of prominent nonlinear crystals used for SHG in the UV-C spectral range and AlN for comparison. ³⁶⁻⁴¹ | 14 |
| Table 2-2: Experimentally determined vapor pressure equation constants for the metalorganic precursors trimethylaluminum (TMA) and triethylgallium (TEG)..... | 23 |
| Table 2-3: III-Nitrides coefficients for the equilibrium constant equation in (2.2.7). | 24 |
| Table 4-1: Etch rates of N- and III-polar GaN and AlN crystals in 1wt% KOH solution in deionized water at 70 °C. ⁸⁵ | 50 |
| Table 6-1: Calculated point defect concentration accounting for charge balance conservation and for a given measured concentration of C, O and Si. | 102 |

1 Introduction

1.1 Group III-Nitrides: History and Their Role in Current Technologies

The group III-Nitrides commonly refers to the compound semiconductors including indium-, gallium- and aluminum nitride (InN, GaN and AlN) and their ternary and quaternary alloys. Initial reports claiming to have obtained AlN crystals from direct reaction of aluminum vapor and nitrogen gas at high temperatures, were published in the late 1800's and early 1900's.¹⁻⁴ These conclusions were based on the fact that the investigated crystals decomposed into ammonia and other aluminum compounds containing oxides when submerged in alkali solutions. In a more detailed study in 1924, Heinrich Ott⁵, by means of X-ray diffraction determined that AlN crystallizes in a wurtzite structure and measured the lattice constants a and c to be 3.11 Å and 4.98 Å respectively, in agreement with current measured values on state of the art AlN crystals.⁶ GaN was first reported by Johnson et al.⁷ in 1932, where gallium metal was heated up to 1200 °C in ammonia atmosphere and InN was reported in 1938 by Juza and Hahn⁸, where $(\text{NH}_4)_3\text{InF}_6$ was heated up to 600 °C also in ammonia atmosphere. The latter authors, using X-ray diffraction, determined the crystal structure of GaN and InN to be wurtzite and calculated the lattice constants a and c to be 3.18 Å and 5.16 Å respectively for GaN and 3.53 Å and 5.69 Å respectively for InN in agreement with current measured values^{6,9}. The aforementioned methods for obtaining III-Nitride crystals, leads to high impurities concentrations which inhibited an accurate measurement of their respective electro-optical properties. The development of vapor phase epitaxy for III-Nitrides compound semiconductors using III-chlorides and ammonia as precursors, led to the realization of thin films with low impurities concentrations and superior optical quality.¹⁰⁻¹² In the early 1970's III-Nitride epitaxial layers deposited on sapphire substrates were optically characterized and a direct bandgap energy of 3.5 eV and 6.2 eV was determined for GaN and AlN respectively.¹²⁻¹⁴ These results and the possibility to control their electrical properties through dopants, intensified research on the material system due to their potential applications in lighting and photodetectors in the blue, violet and UV spectral range. Since the early 1970's, InN

was thought to have a direct bandgap energy close to 2 eV, however Davydov et al.¹⁵ published a work in 2002, where the bandgap energy of InN was measured to be closer to 0.9 eV. These results expanded the potential wavelengths for III-Nitrides emitters into the visible and near infra-red which further motivated research of the material system. Furthermore, the Baliga's figure of merit¹⁶ for GaN and AlN is superior when compared to prominent semiconductors like silicon and silicon carbide (SiC), making them very attractive for efficient, high power, high frequency and high temperature stable electronic devices. After the demonstration of AlGaIn/InGaIn based LEDs and laser diodes (LDs) by Nakamura et al.^{17,18} many commercial applications were developed in a variety of markets including efficient lighting, displays, high density storage media and UV detectors. In the field of electronics, GaN based power converters and RF devices have been recently made commercially available, exhibiting superior performance characteristics to Si and SiC based devices. Noteworthy, is the recent demonstration of GaN based vertical p-n junction diodes with breakdown voltages above 4 kV.¹⁹ III-Nitride based optoelectronic devices are a key component in most lighting applications and their market share in electronic applications is rapidly expanding. While record breaking performance has been demonstrated for many devices using the III-Nitride material system, point defects and dislocations still limit their theoretical potential. Large efforts towards the development of higher purity III-Nitride thin films and substrates is being conducted, which are expected to significantly improve device performance and enable novel devices such as UV-C LDs. Other challenges include p-type doping (particularly in high Al-content AlGaIn), surface passivation and contact design. In summary, the III-Nitrides technology has revolutionized the lighting industry and is already replacing current technologies in high power, high temperature and high frequency electronics. With much room for improvement, they will undoubtedly become a major player in the semiconductor based electronic industry.

1.2 Material Properties and Potential Future Applications

Two primary crystallization phases are observed in the III-Nitrides material system. At ambient conditions, the thermodynamically stable phase is their hexagonal wurtzite structure (space group $P6_3mc$) which is the structure of all samples studied

in this work.²⁰ Alternatively, their metastable zincblende phase can be obtained by heteroepitaxy on a cubic substrate. In *Figure 1-1* a schematic diagram displaying the III-Nitride wurtzite structure is presented.

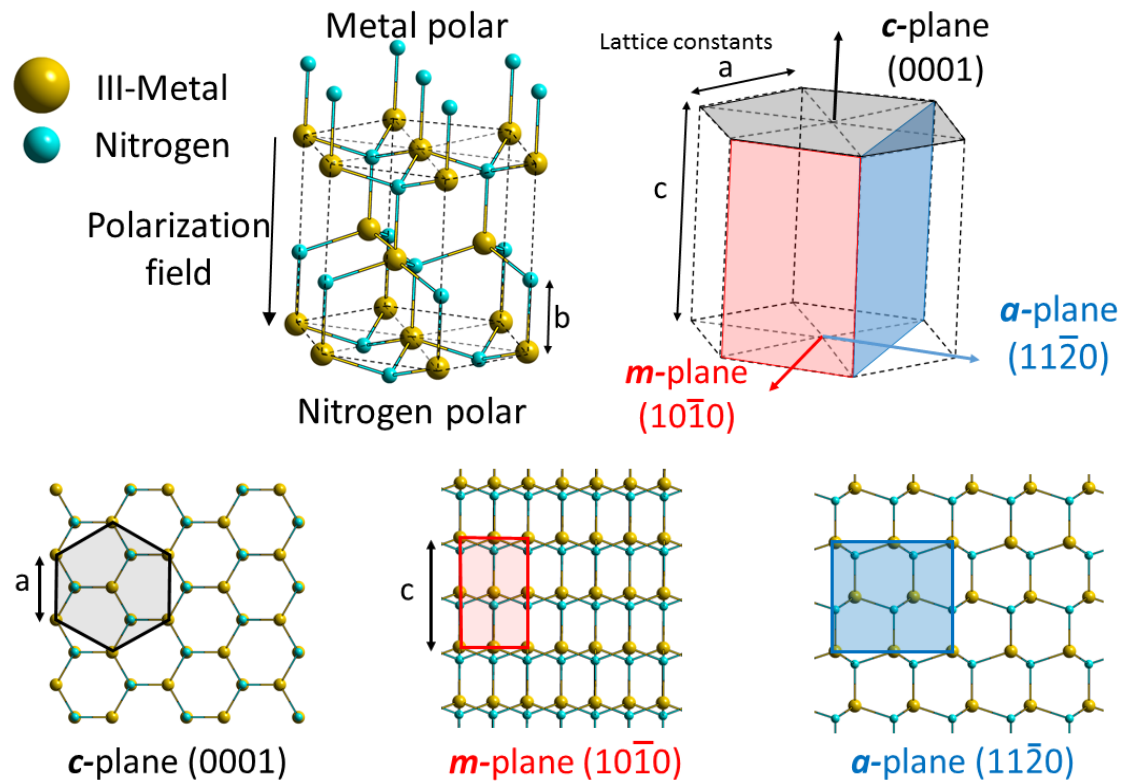


Figure 1-1: Schematic of the III-Nitride wurtzite structure, where the basal plane (c-plane) and the primary (m-plane) and secondary (a-plane) prismatic planes are highlighted.

The III-Nitrides can be classified as non-centrosymmetric polar crystals, giving rise to their piezoelectricity and pyroelectricity. Their lattice parameters are slightly distorted from the ideal tetrahedral arrangement in that the c/a ratio deviates from the value of 1.633 for the ideal wurtzite structure. The observed distortion in the lattice structure has been found to correlate with the u parameter in such manner that the tetrahedral bond lengths are kept nearly constant. The u parameter being the ratio between the bond length b and the c lattice constant, where b is the bond length between the two nearest neighbors along the c -axis (see *Figure 1-1*)^{20,21}. The u parameter in term correlates with the electronegativity of the respective atoms as well as the spontaneous polarization field \mathbf{P}_0 . The lattice parameters of the III-Nitrides and their respective spontaneous polarization field are displayed in *Table 1-1* for comparison.

Table 1-1: Lattice parameter and spontaneous polarization field for III-Nitrides.^{6,21}

| | AlN | GaN | InN | Ideal Tetrahedral |
|---|--------|--------|-------|----------------------|
| Lattice constant a (Å) | 3.112 | 3.189 | 3.585 | |
| Lattice constant c (Å) | 4.982 | 5.186 | 5.80 | |
| c/a | 1.601 | 1.626 | 1.618 | 1.633 |
| u (Å) | 0.382 | 0.377 | 0.379 | 0.375 |
| | | | - | |
| Spontaneous polarization \mathbf{P}_0 (C/m ²) | -0.081 | -0.029 | 0.032 | |

The III-Nitrides have a direct bandgap spanning from 0.7 eV for InN to 6.2 for AlN.^{12,15} Additionally, the bandgap can be tuned throughout the entire energy range by varying the composition of the III-metals in their ternary and quaternary alloys making them very attractive for light emitting diodes (LEDs) and laser diodes (LDs) (*Figure 1-2*). For LEDs and LDs, the tunable bandgap energy covers the entire visible spectra, the near IR up to 1.7 μm and the ultraviolet down to 200 nm. Other material properties relevant for high power and high frequency optoelectronic devices are listed in Table 1-2 and compared to prominent materials.

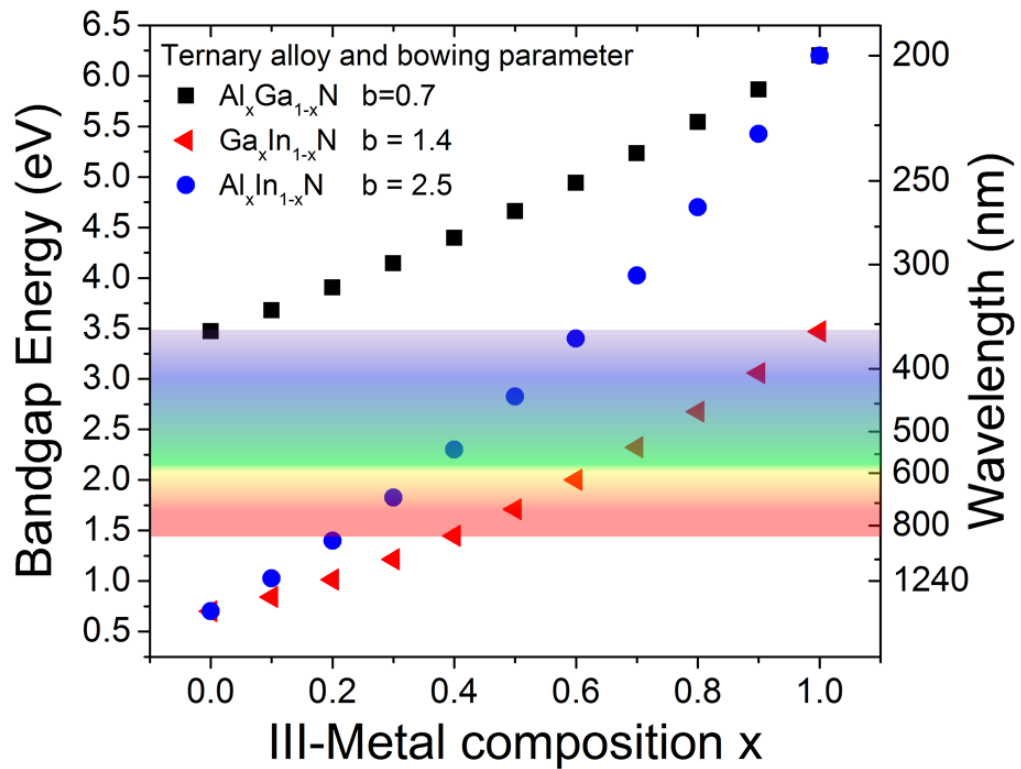


Figure 1-2: Calculated bandgap energy as a function of III-Metal composition x for the III-Nitrides ternary alloys using Vegard's law. Bowing parameters b are taken from Pelá et al.²²

Table 1-2: Material properties relevant for optoelectronic devices.^{15,16,21,23-28}

| | Si | 4H-SiC | GaAs | AlN | GaN | InN |
|---|------|--------|------|-------|------|------|
| Bandgap (eV) | 1.1 | 3.3 | 1.4 | 6.0 | 3.5 | 0.7 |
| Thermal conductivity (W/cm K) | 1.5 | 3.7 | 0.5 | 3.4 | 2.3 | |
| Electric breakdown E_c field (MV/cm) | 0.3 | 3.0 | 0.4 | 15 | 3.75 | |
| Electron mobility μ ($\text{cm}^2/\text{V s}$) | 1350 | 1000 | 8500 | 300 | 1400 | 4400 |
| Relative dielectric constant | 11 | 9.7 | 12.9 | 9.14 | 8.9 | 18.4 |
| Baligas high frequency figure of merit (μE_c^2) | 1 | 74 | 11 | 555 | 162 | |
| Baligas high voltage figure of merit ($\epsilon_r \mu E_c^3$) | 1 | 653 | 17 | 23080 | 1638 | |

1.3 Objectives of this work

Lasers emitting in the ultraviolet spectrum below 300 nm are desired for a variety of applications, including radiation sterilization, photochemical labeling, bio-sensing, nanolithography, medical surgery, micromachining and satellite communication. Currently available deep UV laser systems are expensive, inefficient, stationary, large, and require frequent maintenance, limiting their applications. Semiconductor based LEDs and LDs are compact (micrometer scale), robust, reliable and efficient, allowing for their low production cost, and wide range of applications. AlGaInN based LEDs and LDs in the spectral range between 370 nm and 520 nm are now widely available and have revolutionized the lighting industry. Advances have been made toward the fabrication of electrically injected AlGaInN based UV-C LDs, however doping, carrier injection, and defect control are still challenging.²⁹⁻³¹ Alternatively, UV-C lasers can be obtained through frequency doubling via second harmonic generation (SHG). In fact, diode-pumped solid state lasers with 266 nm emission wavelength are commercially available. These systems, typically involve two stages of frequency doubling (frequency quadrupling) after pumping a solid state crystal with a laser diode, which makes them very inefficient. Furthermore, they require complex optics, are large and degradation of the utilized nonlinear crystals leads to short lifetimes. The III-Nitrides are attractive for frequency conversion and nonlinear optical applications due to their relatively large nonlinear optical coefficients, wide transparency window and high power damage threshold. Their weak birefringence does not allow for birefringence phase matching making a quasi-phase matching approach necessary for second harmonic generation. Challenges in polarity control and the fabrication of periodically poled III-Nitrides crystals, have limited their implementation in nonlinear optical applications. It is reasonable to envision, AlGaInN-based integrated optics where periodically poled nitride-based waveguides serve as quasi-phase matching structures for frequency conversion of the laser light emitted from an AlGaInN LD.

In this work a process is developed for the fabrication of high quality AlN and GaN lateral polar structures-based waveguides, suitable for quasi-phase matched nonlinear optical processes. Furthermore, point defects in AlN, leading to absorption centers at energies lower than the bandgap energy are identified. Finally, quasi-

phase matched second harmonic generation of UV laser light in periodic AlN lateral polar structures-based waveguides is demonstrated for the first time.

In section 2, the theoretical background relevant for this work is summarized, including second order nonlinear optical processes, where some phase matching techniques are described, a thermodynamic supersaturation model describing the surface kinetics in low-pressure metalorganic chemical vapor deposition and a brief description on how to relate photoluminescence excitation spectra to calculated thermodynamic transition energies of point defects under the Franck-Condon approximation. Details on the growth, processing and characterization setups are described in section 3. In section 4, a polarity control process scheme for epitaxial AlN and GaN layers deposited on sapphire substrates via MOCVD is presented. In section 5 GaN and AlN periodic lateral polar structures with periodicities ranging from 1.2 μm to 100 μm are demonstrated and characterized, where the shorter periodicities of 1.2 μm are achieved, by introducing a laser interference lithographic process. Subsequently, two approaches for reducing the surface roughness of the lateral polar structures are described, namely post-growth mechanical polishing and surface roughness reduction during growth by promoting step flow growth at the nitrogen polar surface through control of the vapor phase supersaturation. Next, mass transport between the adjacent opposite-polar domains at reduced supersaturation values is demonstrated and growth conditions for equal deposition rate for both polar domains are established. Section 6 focuses on identifying point defects which lead to below bandgap energy absorption centers in single crystal AlN substrates. A novel approach to determine the impurities type and concentrations in the crystal is presented, where PL, PLE, absorption spectra and SIMS data is used in combination with a DFT based theoretical model which accounts for charge balance conservation in the crystal and the formation energy of defects. Absorption and PL measurements on AlN and GaN thin films are also presented and discussed. In section 7, modal dispersion phase matched second harmonic generation of laser light in single polar AlN and GaN waveguides are presented. Following, quasi-phase matched second harmonic generation of UV laser light is demonstrated for the first time in III-Nitride periodic lateral polar structures-based waveguides. Section 8 will summarize and discuss the bulk of the results, followed by an outlook for III-Nitride quasi-phase matching structures.

2 Theoretical background

2.1 Second Order Nonlinear Optical Processes

Second order nonlinear optical phenomena are well understood and a large pool of literature containing a thorough theoretical analysis and a broad review on nonlinear materials and applications is available.^{32–34} This section will briefly describe the theoretical framework relevant for this work, including second harmonic generation, propagation of waveguide-modes in planar waveguides, modal dispersion phase matching and quasi-phase matching.

2.1.1 Second Harmonic Generation (SHG)

Nonlinear optical phenomena in non-centrosymmetric polar crystals are described in the framework of the macroscopic Maxwell equations (also known as Maxwell equations in matter). Assuming no external charges and current, the Maxwell equations for the electric field $\vec{E}(\vec{r}, t)$, and the magnetic flux density field, $\vec{B}(\vec{r}, t)$, can be reduced to the following form (international system (SI) units):

$$\nabla \times \vec{E} = -\frac{d\vec{B}}{dt}, \quad (2.1.1)$$

$$\nabla \times \vec{B} = \frac{d\vec{D}}{dt}, \quad (2.1.2)$$

$$\nabla \cdot \vec{D} = 0, \quad (2.1.3)$$

$$\nabla \cdot \vec{B} = 0. \quad (2.1.4)$$

With

$$\vec{D} = \varepsilon_0 \vec{E} + \vec{P} \quad (2.1.5)$$

in the electric dipole approximation. Here, ε_0 is the vacuum permittivity, $\vec{D}(\vec{r}, t)$ is the electric displacement field, and $P(\vec{r}, t)$ is the electric dipole polarization density. In the regime of weak fields, namely for electric field amplitudes lower than that of the characteristic atomic electric field $E_a = 5.14 \times 10^{11}$ V/m, corresponding to laser intensities below $\sim 3.5 \times 10^{16}$ W/cm²,³² the standard linear relation describing $P(\vec{r}, t)$ in terms of $\vec{E}(\vec{r}, t)$ can be expanded by a Taylor series in $\vec{E}(\vec{r}, t)$ which in addition to the linear relation, also describes nonlinear relations between $\vec{E}(\vec{r}, t)$ and $P(\vec{r}, t)$ with.³³

$$P(\vec{r}, t) = \int \chi^{(1)}(t - t_1) \vec{E}(\vec{r}, t_1) dt_1 + \iint \chi^{(2)}(t - t_1, t - t_2) \vec{E}(\vec{r}, t_1) \vec{E}(\vec{r}, t_2) dt_1 dt_2 + \iiint \chi^{(3)}(t - t_1, t - t_2, t - t_3) \vec{E}(\vec{r}, t_1) \vec{E}(\vec{r}, t_2) \vec{E}(\vec{r}, t_3) dt_1 dt_2 dt_3 + \dots \quad (2.1.6)$$

When representing the electric field \vec{E} and the polarization density \vec{P} in the form of elementary monochromatic plane waves,

$$\vec{E} = \vec{E}(\omega) e^{i(\vec{k}\vec{r} - \omega t)} + c. c. \quad \text{and} \quad \vec{P} = \vec{P}(\omega) e^{i(\vec{k}\vec{r} - \omega t)} + c. c. \quad , \quad (2.1.7)$$

an expression for $P(\omega)$ can be derived from the Fourier transform of the relation between $P(\vec{r}, t)$ and $\vec{E}(\vec{r}, t)$ in equation (2.1.6) with:³³

$$\vec{P}(\omega) = \varepsilon_0 \chi^{(1)}(\omega) \vec{E}(\omega) + \varepsilon_0 \chi^{(2)}(\omega; \omega_i, \omega_j) \vec{E}(\omega_i) \vec{E}(\omega_j) + \varepsilon_0 \chi^{(3)}(\omega; \omega_i, \omega_j, \omega_k) \vec{E}(\omega_i) \vec{E}(\omega_j) \vec{E}(\omega_k) + \dots \quad , \quad (2.1.8)$$

$$\vec{P}(\omega) = \vec{P}^1(\omega) + \vec{P}^2 + \vec{P}^3 + \dots \quad . \quad (2.1.9)$$

Here $\chi^i(\omega)$ represent the i -th order susceptibility tensor with

$$\chi^{(1)}(\omega_i) = \int \chi^1(t_1) e^{i\omega_i t_1} \quad , \quad \chi^{(2)}(\omega_i, \omega_j) = \iint \chi^{(2)}(t_1, t_2) e^{i(\omega_i t_1 + \omega_j t_2)} \quad (2.1.10)$$

The first term in equation (2.1.8), describes the linear relation between the polarization field and the electric field. The following terms describe the second order nonlinear relation, the third order nonlinear relation and so on. The second term, $\vec{P}^2(\omega)$, describes three wave mixing processes, where setting $\omega_i = \omega_j = \omega_0$ corresponds to the second harmonic generation process leading to $\omega = 2\omega_0$. The focus of this work is on second harmonic generation hence all other terms of the polarization density are neglected. The second order susceptibility tensor $\chi^{(2)}(\omega; \omega_i, \omega_j)$ contains the constants of proportionality relating the amplitude of the second order polarization density field $\vec{P}^2(\omega)$ with the amplitude product of the electric fields $\vec{E}(\omega_i) \vec{E}(\omega_j)$ of the driving waves according to³²

$$P_l^{(2)}(\omega_i, \omega_j) = \varepsilon_0 \sum_{i,j} \sum_{lmk} \chi_{lmk}^{(2)}(\omega; \omega_i, \omega_j) E_m(\omega_i) E_k(\omega_j) \quad , \quad (2.1.11)$$

where l, m and k can take any x, y and z value. In general, for $\omega = \omega_i + \omega_j$ there exists 12 tensors of the form $\chi_{lmk}^{(2)}$ which describe all interactions between the waves, where each tensor contains 27 Cartesian components.³² In a specific case, namely for second harmonic generation ($\omega_i = \omega_j = \omega_0$ and $\omega = 2\omega_0$) in wurtzite crystal structures, uniaxial propagation and polarization of the driving waves (polarization along optical axis), due to symmetry constraints $\chi_{lmk}^{(2)}(\omega; \omega_0, \omega_0)$ is reduced to one dimension with³²

$$\chi^{(2)} = 2\varepsilon_0 d_{33} \quad (2.1.12)$$

For more details on the theoretical framework describing the second order nonlinear susceptibility tensor refer to the literature.^{32,35}

From Maxwell equations (2.1.1)-(2.1.4) and using the identity $\nabla \times (\nabla \times \vec{E}) = \nabla(\nabla \cdot \vec{E}) - \nabla^2 \vec{E}$ the following wave equation can be derived:

$$-\nabla^2 \vec{E} + \frac{\varepsilon^{(1)}}{c^2} \frac{\partial^2 \vec{E}}{\partial t^2} = -\frac{1}{\varepsilon_0 c^2} \frac{\partial^2 P^{(2)}}{\partial t^2}, \quad (2.1.13)$$

where $\varepsilon^{(1)}$ is the relative permittivity and c the speed of light in vacuum. Assuming the electromagnetic waves propagate along one direction (z-direction), the monochromatic plane waves describing the electric fields can take the following form:³³

$$\vec{E}(\vec{r}, t) = \text{Re}[\vec{e}A(z, t)\exp(ikz - \omega t)], \quad (2.1.14)$$

where k and $A(z, t)$ are the wave vector and the envelope function of the electric field.

For slowly varying envelope functions it follows $\frac{\partial^2 A}{\partial z^2} \ll \left|k \frac{\partial A}{\partial z}\right|$ and $\frac{\partial^2 P^{(2)}}{\partial t^2} \cong -\omega^2 P^{(2)}$, thus inserting equation (2.1.14) into (2.1.13), by neglecting higher order derivatives, with $k^2 = \frac{\varepsilon^{(1)}\omega^2}{c^2}$ and with $\chi^{(2)}(\omega; \omega_i, \omega_j) = 2\varepsilon_0 d_{\text{eff}}$ equation (2.1.13) can be reduced to:

$$2ik_\omega \frac{\partial A}{\partial z} = \frac{-2\omega^2}{c^2} d_{33} |A_0|^2 \exp(i\Delta kz) \quad (2.1.15)$$

where $\Delta k = 2k_{\omega_0} - k_\omega$ is the wave vector mismatch between the induced and driving waves and A_0 is the field amplitude of the driving waves. Note that ω is the frequency of the second harmonic generated wave with $\omega = 2\omega_0$. In the un-depleted pump approximation (A_0 constant), integrating equation (2.1.15) then leads to an expression for the amplitude $A(L)$ of the second harmonic generated wave as a function of propagation length L .³²

$$A(L) = \frac{i\omega^2}{k_\omega c^2} d_{33} |A_0|^2 \left(\frac{e^{i\Delta kL} - 1}{i\Delta k} \right). \quad (2.1.16)$$

With the intensities given by³²

$$I = 2n_\omega \varepsilon_0 c |A(L)|^2, \quad I_0 = 2n_{\omega_0} \varepsilon_0 c |A_0|^2 \quad (2.1.17)$$

where n_ω is the refractive index for the second harmonic wave and with the following relations

$$\left| \frac{e^{i\Delta k L} - 1}{i\Delta k} \right|^2 = L^2 \text{sinc}^2\left(\frac{\Delta k L}{2}\right) \quad \text{and} \quad k_\omega^2 = \frac{\omega^2 n_\omega^2}{c^2}, \quad (2.1.18)$$

we obtain the following expression for the intensity of the second harmonic wave.

$$\begin{aligned} I(L) &= \frac{2n_\omega \varepsilon_0 \omega^4}{k_\omega^2 c^3} d_{33}^2 |A_0|^2 |A_0|^2 \left| \frac{e^{i\Delta k L} - 1}{i\Delta k} \right|^2 \\ &= \frac{2\varepsilon_0 \omega^2}{n_\omega c} d_{33}^2 |A_0|^2 |A_0|^2 L^2 \text{sinc}^2\left(\frac{\Delta k L}{2}\right) \\ &= \frac{\omega^2 d_{33}^2}{2\varepsilon_0 c^3 n_\omega n_0^2} |I_0|^2 L^2 \text{sinc}^2\left(\frac{\Delta k L}{2}\right). \end{aligned} \quad (2.1.19)$$

From equation (2.1.19) we see that for a wave vector mismatch $\Delta k \neq 0$ and all other values held constant, the propagation length dependence of the second harmonic intensity follows a normalized sinusoidal function (see *Figure 2-1*). From *Figure 2-1* it is clear that in order to continuously increase the intensity of the second harmonic wave, the wave vectors of the driving and induced waves have to be matched ($\Delta k = 0$). Commonly, the optical birefringence of nonlinear polar materials is exploited to achieve phase matching, however the birefringence in III-Nitrides is weak and other phase matching techniques are necessary, such as quasi phase matching (QPM) or modal dispersion phase matching (MDPM).

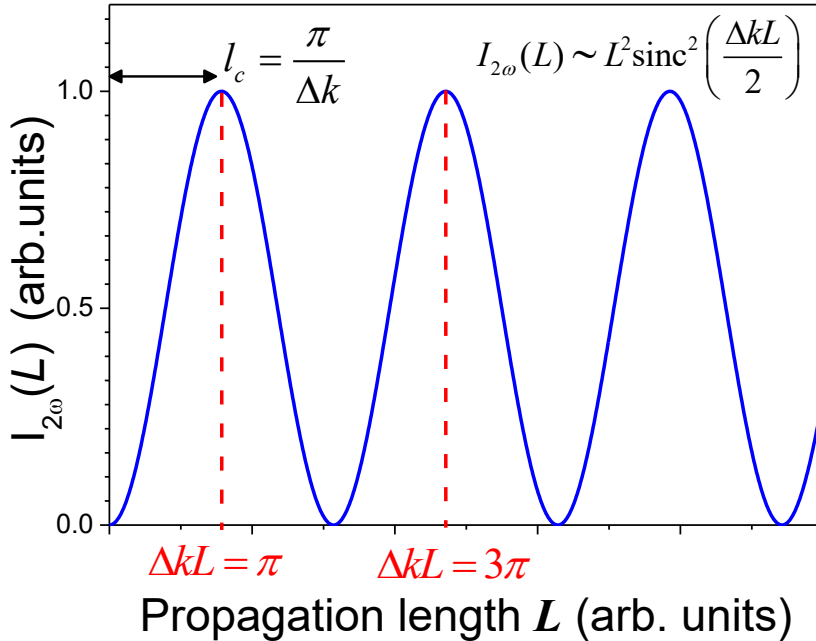


Figure 2-1: Intensity of the second harmonic generated wave as a function of propagation length. Highlighted in red is the coherence length distance l_c , which is the length in which the wave vectors of the driving and induced wave accumulate a phase-shift of π .

Additionally, equation (2.1.19) indicates that the intensity of the second harmonic wave (or alternatively, the conversion efficiency) is directly proportional to the square of the nonlinear susceptibility coefficient d_{33} of the nonlinear crystal. Being a constant material property, its value will determine the potential conversion efficiency that can be achieved for a given nonlinear crystal material. In fact, the quantity $(d_{xy}^2 / n_{2\omega} n_{\omega}^2)$ is often used as a figure of merit to classify the potential conversion efficiency of nonlinear crystal materials. *Table 2-1* displays the second order nonlinear coefficients for the most prominent nonlinear crystals used for SHG in the UV-C spectral range. It is clear that AlN has the potential for an order of magnitude greater conversion efficiency, when compared to other nonlinear crystals.

Table 2-1: Nonlinear properties of prominent nonlinear crystals used for SHG in the UV-C spectral range and AlN for comparison.³⁶⁻⁴¹

| Material | Second order Nonlinear coefficient (pm/V) | Refractive index @ 275 nm | Refractive index at 550 nm | $(d_{xy}^2 / n_{2\omega} n_{\omega}^2)$ |
|---|---|---------------------------|----------------------------|---|
| β -BaB ₂ O ₄ | $d_{11} = 1.84$ | 1.75 | 1.67 | 0.69 |
| CsLiB ₆ O ₁₀ | $d_{36} = 0.95$ | 1.54 | 1.5 | 0.26 |
| KBe ₂ BO ₃ F ₂ | $d_{11} = 0.8$ | 1.52 | 1.48 | 0.19 |
| KH ₂ PO ₄ (KDP) | $d_{36} = 0.46$ | 1.55 | 1.51 | 0.06 |
| AlN | $d_{33} = 7.4$ | 2.32 | 2.16 | 5.06 |

In the following sections, first, the theory describing the propagation of electromagnetic waveguide modes will be presented, followed by a brief discussion of modal dispersion phase matching (MDPM). Then a more detailed description of quasi-phase matching (QPM) will be presented, being the more relevant phase matching technique for this work.

2.1.2 Waveguide Modes

The intensity of second harmonic generation can be described by equation (2.1.19), when describing the propagation of electromagnetic waves in bulk material. However if waveguide structures are employed, it is necessary to consider the propagation of transverse-electric (TE) and transverse-magnetic (TM) modes. In AlN and GaN, the second order nonlinear susceptibility ($\chi_{r_m q}^2(\omega; \omega_i, \omega_j)$) along the c-axis exhibits the largest value. This translates into higher conversion efficiencies for TM modes when compared to TE modes. For this reason, this section will focus on describing the propagation of TM modes. Literature with a broader and more detailed description of coupled-mode theory for guided wave optics is available.^{34,42-}

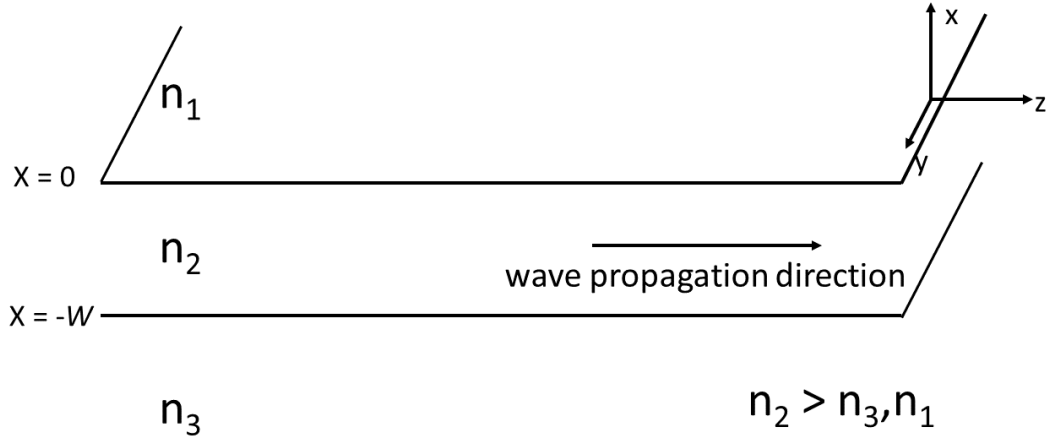


Figure 2-2: Schematic of planar waveguide structure used to describe the propagation of TM electromagnetic modes. Three layers with different refractive index n_i are displayed.

TE polarization refers to electromagnetic waves where the only non-zero electric field components is along the y -axis (see *Figure 2-2*) while TM polarization refers to electromagnetic waves where the only non-zero magnetic field components is along the y -axis. Hence, from Maxwell's wave equation in vacuum, the electromagnetic field components of the TM waves are reduced to:³⁴

$$H_y(x, z, t) = \mathcal{H}_y(x) e^{i(\omega t - \beta z)}, \quad (2.1.20)$$

$$E_x(x, z, t) = \frac{\beta}{\omega \epsilon_r \epsilon_0} \mathcal{H}_y(x) e^{i(\omega t - \beta z)}, \quad (2.1.21)$$

$$E_z(x, z, t) = -\frac{i}{\omega \epsilon_r \epsilon_0} \frac{\partial \mathcal{H}_y}{\partial x}. \quad (2.1.22)$$

Note that $E_x(x, z, t)$, the relevant field component for SHG, is directly proportional to the magnetic field amplitude $\mathcal{H}_y(x)$ which varies as a function of x . $\mathcal{H}_y(x)$ is different for each of the three layers described in *Figure 2-2*. From continuity requirement at the layer boundaries, an expression for $\mathcal{H}_y(x)$ can be derived for each of the layers with four unknowns (C , q , p and h).³⁴

$$\begin{aligned} & -\frac{h}{q} C e^{-qx}, & 0 \leq x \\ \mathcal{H}_y = C & \left[-\frac{h}{q} \cos(hx) + \sin(hx) \right], & -W \leq x \leq 0 \\ & C \left[\frac{h}{q} \cos(hW) + \sin(hW) \right] e^{p(x+W)}. & x \leq -W \end{aligned} \quad (2.1.23)$$

C is a normalization constant and the parameters q , p and h can be expressed in terms of the unknown propagation constant β . This is done by substituting each of the expressions for $\mathcal{H}_y(\mathbf{x})$ in (2.1.23) into (2.1.20) and rearranging the wave equation (2.1.24) which must be satisfied.

$$\nabla^2 \vec{H} = \frac{\varepsilon^{(1)}}{c^2} \frac{\partial \vec{H}}{\partial t^2}. \quad (2.1.24)$$

The following relations are determined:

$$\begin{aligned} q &= (\beta^2 - n_1^2 k^2)^{\frac{1}{2}} \\ p &= (\beta^2 - n_3^2 k^2)^{\frac{1}{2}} \\ h &= (n_2^2 k^2 - \beta^2)^{\frac{1}{2}} \end{aligned} \quad (2.1.25)$$

where

$$k \equiv \frac{2\pi}{\lambda}, \quad \tilde{p} \equiv \frac{n_2^2}{n_3^2} p \quad \text{and} \quad \tilde{q} \equiv \frac{n_2^2}{n_1^2} q \quad (2.1.26)$$

Here λ is the vacuum wavelength of the propagating electromagnetic wave and n_i is the refractive index of the respective layers. Additionally, from the requirement that $\frac{\partial \mathcal{H}_y}{\partial x}$ at $x = -t$ is continuous, a transcendental equation can be derived for the unknown variable β which must be satisfied.³⁴

$$\tan(hW) = \frac{h(\tilde{p} + \tilde{q})}{h^2 - \tilde{p}\tilde{q}}. \quad (2.1.27)$$

Since only the case for total internal reflection is considered, the value of the propagation constant β is limited by the surrounding layer with the largest refractive index and the refractive index of the waveguiding layer, with:

$$kn_3 < \beta < kn_2, \quad (2.1.28)$$

Equation (2.1.27) can be solved graphically or numerically, where a discrete number of solutions for the value of the propagation constant β^m are obtained. From the solutions β^m a relation describing an effective refractive index n_{eff}^m can be derived with

$$n_{eff}^m = \frac{\beta^m}{k}. \quad (2.1.29)$$

In summary, we realize that the boundary conditions of the waveguiding layer, do not allow for β to take any arbitrary value which satisfies the condition in (2.1.28). Only values are allowed which also satisfy the transcendental equation (2.1.27)

giving rise to the multiple TM modes. Note that the allowed modes are dependent on the waveguide layer thickness W , the refractive index n_i of the three layers and the vacuum wavelength λ of the propagating electromagnetic wave.

2.1.3 Modal Dispersion Phase Matching

As determined in section 2.1.1, the intensity of the second harmonic generated wave will not monotonically increase as a function of the propagation length if the wave vectors of the driving and induced waves are mismatched (Figure 2-1). In modal dispersion phase matching (MDPM) the dispersion relation of the material in combination with the different propagation constant values β^m for the different waveguide modes m is utilized to match the wave vectors of the driving and the induced second harmonic waves. Using the expression (2.1.21) which describes the electric field along the x -direction in waveguides, equation (2.1.16) is modified to

$$A_{\omega}^s(L) \left(\frac{\beta_{\omega}^s}{\omega n_{\omega}^2} \mathcal{H}_y^{\omega,s}(x) \right) = \frac{i\omega^2}{\beta_{\omega}^s c^2} d_{eff} |A_{\omega_0}^m|^2 \left(\frac{\beta_{\omega_0}^m}{\omega_0 n_{\omega_0}^2} \mathcal{H}_y^{\omega_0,m}(x) \right)^2 \left(\frac{e^{i\Delta\beta L} - 1}{i\Delta\beta} \right), \quad (2.1.30)$$

where β_{ω}^s and $\beta_{\omega_0}^m$ are the waveguide modes for the second harmonic and the driving waves respectively and $\omega = 2\omega_0$. In general $\mathcal{H}_y^{\omega,s}(x) \neq \mathcal{H}_y^{\omega_0,m}(x)$ and the amplitude $A(L)$ of the second harmonic electric field, will depend on the overlap integral Γ_{ω,ω_0} between the driving and second harmonic waves, with:

$$A_{\omega}^s(L) = \left(\frac{2\omega n_{\omega}^2}{\beta_{\omega}^s} \right) \left(\frac{\beta_{\omega_0}^m}{\omega n_{\omega_0}^2} \right)^2 \frac{i\omega^2}{\beta_{\omega}^s c^2} d_{eff} |A_{\omega_0}^m|^2 \left(\frac{e^{i\Delta\beta L} - 1}{i\Delta\beta} \right) \sqrt{\Gamma_{\omega,\omega_0}} \quad (2.1.31)$$

and where

$$\Gamma_{\omega,\omega_0} = C' \int (\mathcal{H}_y^{\omega_0,m}(x))^2 \mathcal{H}_y^{\omega,s}(x) dx. \quad (2.1.32)$$

C' is a normalization constant referenced to a perfect overlap between $\mathcal{H}_y^{\omega}(x)$ and $\mathcal{H}_y^{\omega_0}(x)$. The expression for the intensity $I_{\omega}(L)$ of the second harmonic wave can then be derived with:

$$I_{\omega}(L) = \left(\frac{2\omega\epsilon_{\omega}}{\beta_{\omega}^s} \right)^2 \left(\frac{\beta_{\omega_0}^m}{\omega\epsilon_{\omega_0}^2} \right)^4 \frac{\omega^2 d_{eff}^2}{2\epsilon_0 c^3 n_{\omega}^s (n_{\omega_0}^m)^2} |I_0|^2 L^2 \Gamma_{\omega,\omega_0} \text{sinc}^2 \left(\frac{\Delta\beta L}{2} \right). \quad (2.1.33)$$

Again, $\Delta\beta$ is the wave vector mismatch between the driving and second harmonic waves with:

$$\Delta\beta = 2\beta_{\omega_0}^m - \beta_{\omega}^s, \quad (2.1.34)$$

where it is possible to find values for $2\beta_{\omega_0}^m$ and β_{ω}^s , such that $\Delta\beta = 0$. More details on how to determine ω, ω_0, W, s and m such that $\beta_{\omega}^s = 2\beta_{\omega_0}^m$ are described elsewhere.⁴⁷ In that case, the intensity of the second harmonic wave simply follows

$$I_{\omega}(L) \sim \Gamma L^2 |I_0|^2. \quad (2.1.35)$$

Note that in this section MDPM is only considered for equal propagation modes of the driving waves $A_{\omega_0}^m$, where $\Delta\beta = 2\beta_{\omega_0}^m - \beta_{\omega}^s$. However, it is possible to achieve phase matching when different propagation modes m and p of the driving waves $A_{\omega_0}^m$ and $A_{\omega_0}^p$ are found so that the condition $\Delta\beta = \beta_{\omega_0}^m + \beta_{\omega_0}^p - \beta_{\omega}^s = 0$ is satisfied. More details on MDPM for mixed modes of the fundamental waves are detailed in a work by Troha et. al.⁴⁷

In summary, phase matching is accessible through MDPM and some experimental results will be presented in section 7. The drawback of this technique lies in that the mode order numbers s and m required to achieve equal propagation constants for the driving and second harmonic waves, in general, lead to small overlap integrals which decrease the conversion efficiency.

2.1.4 Quasi-Phase Matching in III-Nitride Waveguide Structures

An alternative for achieving phase matching between the driving and the second harmonic waves was proposed in 1962 by Armstrong et al. and is now commonly addressed as the quasi-phase matching (QPM) technique.⁴⁸ A detailed theoretical analysis of QPM is described by Fejer et al..⁴⁹ In this approach the sign of the second order nonlinear coefficient χ^2 is inverted after a propagation distance l_c , called the coherence length, by inverting the nonlinear crystal (equivalent to inverting the polarity of the III-Nitride film). The coherence length l_c is the distance for which the driving waves and the second harmonic wave accumulate a phase shift value of π , with

$$l_c = \frac{\pi}{\Delta k}. \quad (2.1.36)$$

For a phase shift larger than π ($2\pi > l_c \Delta k > \pi$), the electric field amplitude $A_\omega^s(L)$ of the second harmonic wave decreases as the cardinal sine function (Figure 2-3 Figure 2-1). Inverting the nonlinear crystal after every coherence length l_c and with it, the sign of the nonlinear susceptibility coefficient, effectively corrects the phase mismatch between the driving and second harmonic waves allowing for the amplitude of the second harmonic wave to continue increasing. Mathematically, this translates into a propagation length (z-direction) dependence of the nonlinear susceptibility coefficient $\chi^{(2)}(z)$. For a square-wave modulation of the nonlinear susceptibility coefficient (equivalent to a periodically poled III-Nitride crystal) from $+\chi^{(2)}$ to $-\chi^{(2)}$ with duty cycle D , it follows^{49,50}

$$\chi^{(2)}(z) = \sum_m \frac{2}{m\pi} d_{33} \sin(\pi D) e^{iK_m z}. \quad (2.1.37)$$

where $D = \frac{l}{\Lambda}$, $K_m = \frac{2\pi m}{\Lambda}$, Λ is the period of the modulation and l (not to be confused with l_c) is the length of the defined positive direction of the crystal (i.e domain length of Al-polar section in AlN LPS). Equation (2.1.31), which describes the amplitude $A_\omega^s(L)$ of the second harmonic wave, is thus modified to:

$$A_\omega^s(L) = \left(\frac{2\omega n_\omega^2}{\beta_\omega^s} \right) \left(\frac{\beta_{\omega_0}^r}{\omega n_{\omega_0}^2} \right)^2 \frac{i\omega^2}{\beta_\omega^s c^2} e^{-i\frac{\Delta K L}{2}} \frac{2}{m\pi} d_{33} \sin(\pi D) |A_{\omega_0}^r|^2 L \operatorname{sinc}\left(\frac{\Delta K L}{2}\right) \sqrt{\Gamma_{\omega, \omega_0}}, \quad (2.1.38)$$

where $\Delta K = 2\beta_{\omega_0}^r - \beta_\omega^s + K_m$. K_m represents an extra parameter, directly related to the periodicity of the lateral polar structure, which can be modified to achieve $\Delta K = 0$. Note that as in MDPM we are considering the allowed propagation TM modes r and s in the waveguide, as well as the overlap integral between the driving and second harmonic waves. In contrast to MDPM, in QPM using waveguides, it is possible to find $\beta_{\omega_0}^r$ and β_ω^s so that the overlap integral $\Gamma_{\omega, \omega_0}$ is unity. If the parameters are chosen so that $\Delta K = 0$, equation (2.1.38) is reduced to

$$A_\omega^s(L) = \left(\frac{2\omega n_\omega^2}{\beta_\omega^s} \right) \left(\frac{\beta_{\omega_0}^r}{\omega n_{\omega_0}^2} \right)^2 \frac{i\omega^2}{\beta_\omega^s c^2} \frac{2}{m\pi} d_{33} \sin(\pi D) |A_{\omega_0}^r|^2 L. \quad (2.1.39)$$

The intensity $I_\omega(L)$ of the TM polarized second harmonic wave then follows

$$I_\omega(L) \sim \left(\frac{2}{m\pi} \sin(\pi D) \right)^2 d_{33}^2 |I_{\omega_0}|^2 L^2. \quad (2.1.40)$$

From equation (2.1.40) it can be seen that the conversion efficiency in QPM is decreased by the factor $\left(\frac{2}{m\pi}\sin(\pi D)\right)^2$ when compared with perfect phase matching.

It is easy to see that the largest conversion efficiency is achieved for $m=1$ (first order QPM) and when the duty cycle is $D=0.5$. Note that m here is not the waveguide mode number. For this case $I_\omega(L)$ is reduced to:

$$I_\omega(L) \sim \left(\frac{2}{\pi}\right)^2 d_{33}^2 |I_{\omega_0}|^2 L^2. \quad (2.1.41)$$

This corresponds to approximately 40% conversion efficiency compared to an ideal case (see *Figure 2-4*). Alternatively, higher order QPM ($m > 1$) is also possible, allowing for flexibility when choosing the periodicity of the nonlinear crystal lateral polar structure (III-Nitride LPS). Surprisingly also for even numbered QPM orders, SHG can be achieved if the duty cycle $D \neq 0.5$ and is most efficient for $D=0.25$ or $D=0.75$, as can be deduced from equation (2.1.40).

In summary, the theory describing the QPM approach to achieve second harmonic generation is presented, where the phase mismatch between the driving and the second harmonic waves is periodically corrected through inverting the nonlinear crystal every coherence length distance. Details on the fabrication of periodic structures necessary for this approach are presented and discussed in section 4 and 5. Furthermore, results showing QPM second harmonic generation of UV laser light are presented and discussed in section 7.2.

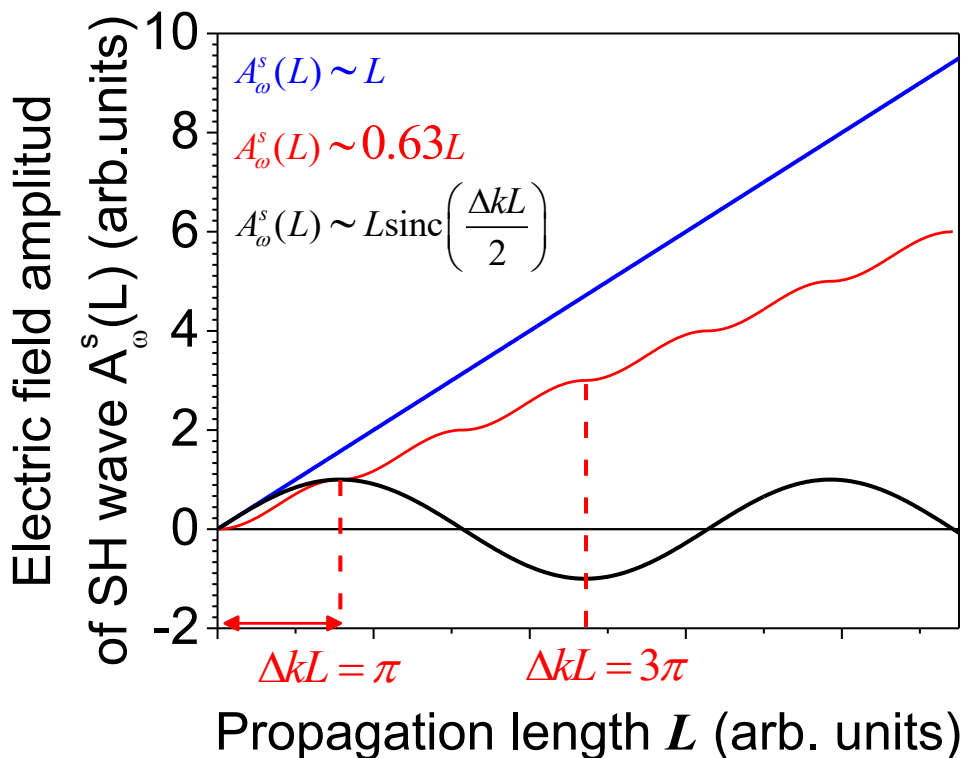


Figure 2-3: Electric field amplitude of the second harmonic wave as a function of propagation length for three different phase matching scenarios.

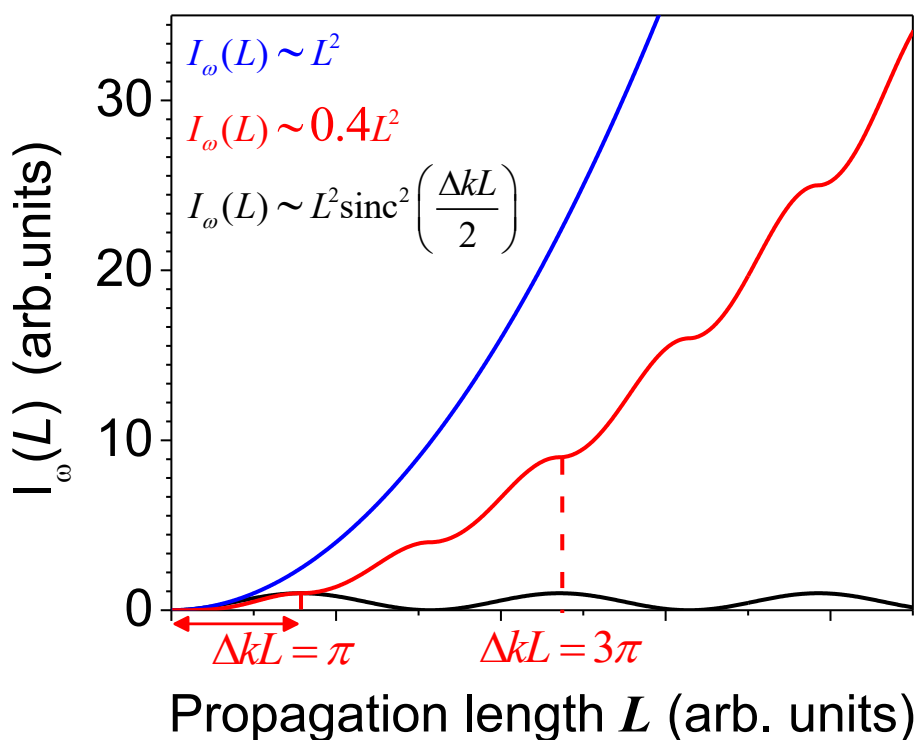


Figure 2-4: Intensity of the second harmonic wave as a function of propagation length for three different phase matching scenarios.

2.2 Surface Kinetics in III-Nitride Growth

An extensive study relating the vapor supersaturation to the growth mode and morphology of crystal surfaces was published in 1950 by Burton, Cabrera and Frank (BCF).⁵¹ The BCF model has been used extensively to describe the growth of semiconductor materials.⁵²⁻⁵⁵ This section will briefly describe the concepts relevant to this work and relies heavily on the work published by Mita et al. and Bryan et al.^{29,54,55}

Chemical vapor epitaxial processes are non-equilibrium processes with a driving force towards thermodynamic equilibrium of the system. The driving force for growth is determined by the change in the Gibbs free energy ΔG where

$$\Delta G = -RT \ln(1 + \sigma). \quad (2.2.1)$$

Here, R is the ideal gas constant, T is the temperature and σ is the vapor supersaturation. For typical growth conditions of III-Nitrides in metal organic chemical vapor deposition (MOCVD), the deposition reaction is governed by the supersaturation of the III metal species. The vapor supersaturation is defined by

$$\sigma = \frac{P_{III}^0 - P_{III}}{P_{III}}, \quad (2.2.2)$$

where P_{III}^0 is the input partial pressure of the III metal species and P_{III} is the equilibrium vapor pressure of the III species over the III-Nitride crystal at growth conditions. To obtain the vapor supersaturation value σ , it is necessary to calculate P_{III}^0 and P_{III} . In MOCVD, metal-organics are used as precursors for the III metal species (i.e. triethylgallium (TEG) for Ga and trimethylaluminum (TMA) for Al). The metal-organics are kept at constant temperature in an enclosure (typically referred to as the bubbler). A carrier gas is flowed through the bubbler to “carry” the metal-organic molecules into the growth chamber. The employed metal-organics have a low pyrolysis temperature (<400 °C) and typical growth temperatures are above 1000 °C, thus the assumption of Al vapor in the growth reaction is justified. The input partial pressure of the III species, P_{III}^0 , can be calculated from the vapor pressure of the III metal precursor $p_{III-precursor}$ in the bubbler, the carrier gas flow $f_{Carrier}$, the total reactor gas flow f_{Total} and the total chamber pressure P_{Total} . With

$$p_{III-precursor} = 10^{\left(D - \frac{Q}{T_{Precursor}}\right)}, \quad (2.2.3)$$

where D and Q are the experimentally determined constants of the vapor pressure equation (see *Table 2-2*) and $T_{Precursor}$ is the temperature of the III species precursor in the bubbler.

Table 2-2: Experimentally determined vapor pressure equation constants for the metalorganic precursors trimethylaluminum (TMA) and triethylgallium (TEG).

| Vapor pressure equation constants | | |
|-----------------------------------|-------|---------|
| | D | Q |
| TMA | 8.224 | 2134.83 |
| TEG | 8.083 | 2162 |

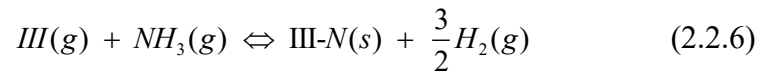
The III species flow f_{III} into the growth chamber is calculated from

$$f_{III} = \frac{f_{carrier} P_{III-precursor}}{P_{precursor}}, \quad (2.2.4)$$

where $P_{precursor}$ is the pressure inside the precursor enclosure. After obtaining f_{III} , P_{III}^0 can be calculated from

$$P_{III}^0 = \frac{P_{Total} f_{III}}{f_{Total}}, \quad (2.2.5)$$

where P_{Total} is the total chamber pressure and is set by the experimental conditions. The equilibrium vapor pressure P_{III} can be obtained by considering the following chemical reaction at or near the growth surface:



The corresponding equilibrium equation is

$$K_{III-N} = \frac{a_{III-N} P_{H_2}^{3/2}}{P_{III} P_{NH_3}} = T^C 10^{\left(\frac{A+B}{T}\right)} \quad (2.2.7)$$

where K_{III-N} is the equilibrium constant, P_{H_2} and P_{NH_3} are the equilibrium vapor pressures of H_2 and NH_3 respectively and a_{III-N} is the activity of the III-Nitride. Koukitu et al. calculated the equilibrium constants for AlN, GaN and InN where the coefficients A, B and C for equation (2.2.7) are given in *Table 2-3*.⁵⁶

Table 2-3: III-Nitrides coefficients for the equilibrium constant equation in (2.2.7).

| | Equilibrium constant coefficients | | |
|-----|-----------------------------------|--------------------|------|
| | A | B | C |
| AlN | 14.2 | 3.17×10^4 | 2.33 |
| GaN | 12.2 | 1.78×10^4 | 1.79 |
| InN | 13.1 | 1.13×10^4 | 2.29 |

The relevant gasses for the reaction are H_2 , NH_3 , and $III(g)$, therefore, the total pressure is composed by their respective equilibrium partial pressures with:

$$P_{Total} = P_{III} + P_{NH_3} + P_{H_2} \quad (2.2.8)$$

The molar conservation constraints dictate that

$$P_{III}^0 - P_{III} = P_{NH_3}^0 - P_{NH_3} \quad (2.2.9)$$

where $P_{NH_3}^0$ is the input partial pressure of NH_3 . Expressions for P_{NH_3} and $P_{H_2}^{3/2}$ can be obtained from (2.2.9) and (2.2.7) respectively with

$$P_{NH_3} = P_{III} - P_{III}^0 + P_{NH_3}^0 \quad (2.2.10)$$

$$P_{H_2} = \left(\frac{K_{III-N} P_{III} P_{NH_3}}{a_{III-N}} \right)^{\frac{2}{3}} = \left(\frac{K_{III-N} P_{III} (P_{III} - P_{III}^0 + P_{NH_3}^0)}{a_{III-N}} \right)^{\frac{2}{3}} \quad (2.2.11)$$

with $a_{III-N} = 1$, substituting (2.2.11) and (2.2.10) into (2.2.8) leads to a 4th order polynomial equation for the equilibrium vapor pressure of the III metal species with:⁵⁴

$$P_{III}^4 + \left(2A + \frac{8}{K_{III-N}^2} \right) P_{III}^3 + \left(A^2 - 12 \frac{B}{K_{III-N}^2} \right) P_{III}^2 + \left(6 \frac{B^2}{K_{III-N}^2} \right) P_{III} - \frac{B^3}{K_{III-N}^2} = 0, \quad (2.2.12)$$

where

$$A \equiv P_{NH_3}^0 - P_{III}^0 \quad \text{and} \quad B \equiv P_{Total} - A. \quad (2.2.13)$$

P_{III} is the only unknown in equation (2.2.12) which can be solved numerically. Once the values for P_{III} and P_{III}^0 are known the vapor supersaturation σ can be calculated.

The vapor supersaturation can then be used to describe a variety of growth modes including different types of step bunching, bilayer step flow, spiral growth, 2D

nucleation and a mixed growth mode of the 2D nucleation and step flow growth.⁵⁵ In this work we are interested in the transition from 2D nucleation growth to step flow growth and its relation to the vapor supersaturation since the latter growth mode leads to a reduced nitrogen polar surface roughness (see section 5.1.2).

The BCF theory states that for a “perfect” crystal surface, free of steps and dislocations, growth will only proceed when the vapor supersaturation exceeds a critical value σ^* for which the formation of 2D nuclei is favored. For 2D nuclei to form, the change in Gibbs free energy ΔG_{2D} must be favored with

$$\Delta G_{2D} = 2\pi r h \gamma_s - \frac{\pi r^2}{A} \Delta \mu \quad (2.2.14)$$

where r , h , γ_s , A and $\Delta \mu$ are the nucleus radius, nucleus height, surface free energy of the step, projected area of an adatom and change in chemical potential, respectively. $\Delta G_{2D}(r)$ increases with r reaching a maximum at a critical radius r^* where the formation of nuclei becomes stable. For larger values of r , $\Delta G_{2D}(r)$ decreases and the formation of 2D nuclei becomes more favorable. The critical radius r^* is related to the critical surface supersaturation σ_s^* (not to be confused with the vapor supersaturation σ) by

$$r^* = \frac{h A \gamma_s}{k_B T \ln(\sigma_s^* + 1)}, \quad (2.2.15)$$

from which an expression for the critical free energy for 2D nucleation can be derived.²⁹

$$\Delta G_{2D}^* = \frac{\pi A h^2 \gamma_s^2}{k_B T \ln(\sigma_s^* + 1)} \quad (2.2.16)$$

For the growth mode and the corresponding surface morphology, this translates into mixed step flow and 2D nucleation growth for surface supersaturation values above this critical value and solely step flow growth for values lower than σ_s^* . An expression for σ_s^* can be derived

$$\sigma_s^* = \frac{\pi h^2 A \gamma_s^2}{e^{(k_B T)^2 [65 - \ln(R_{2D}^*)]}}, \quad (2.2.17)$$

where R_{2D}^* is the critical nucleation rate and is related to ΔG_{2D}^* by⁵⁵

$$R_{2D}^* \approx e^{\left[65 - \frac{\Delta G_{2D}^*}{k_B T}\right]}. \quad (2.2.18)$$

In general, the surface supersaturation varies as a function of its position in relation to the step edges. The maximum value of the surface supersaturation is related to the vapor supersaturation through

$$\sigma_{s,\max} = \sigma \left(1 - \frac{1}{\cosh\left(\frac{\lambda_0}{2\lambda_s}\right)} \right), \quad (2.2.19)$$

where λ_s is the surface diffusion length of the ad-atoms and λ_0 is the terrace width. This expression shows the relation between the input growth parameters (contained in σ) and the surface supersaturation. The growth parameters can then be modified to decrease the surface supersaturation and promote step flow growth. This leads to a significant reduction of the nitrogen polar surface roughness as it will be shown and discussed in section 5.1.2.

The relation presented in equation (2.2.19) is representative of the maximum value that the surface supersaturation can take, however it does not account for pre-reaction or other possible losses. Alternatively, the effective value of $\sigma_{s,\max}$ can be described by the growth rate R with⁵⁵

$$\sigma_{s,\max} = \frac{R\tau_s\lambda_0n_0}{2h\lambda_s n_{S0}} \tanh\left(\frac{\lambda_0}{4\lambda_s}\right), \quad (2.2.20)$$

where τ_s is the mean residence time of the adatom at the surface, n_0 is the adatom site density and h is the monolayer step height. The expression in (2.2.20) is used to highlight the fact that pre-reaction losses, which lead to a reduced growth rate R , also imply a decrease on the surface supersaturation. In section 5.1.2 results showing pressure and temperature dependent pre-reaction losses in AlN growth will be presented, indicative of a lower surface supersaturation value than the calculated vapor supersaturation.

In summary, a method for calculating the Al vapor supersaturation with a given set of growth conditions is described. The vapor supersaturation is related to the maximum value of the surface supersaturation. Finally, a critical surface supersaturation value describing the transition from step flow growth to mixed 2D nucleation and step flow growth is presented. This theoretical background motivated the work presented in section 5.1.2 and 5.2.2 to achieve smoother surfaces of the

epitaxial nitrogen polar thin films as well as the GaN and AlN lateral polar structures.

2.3 Point Defects

Ideally, the III-Nitride crystals contain only III-metal and nitrogen atoms (also referred as native atoms) in a 1:1 ratio forming a wurtzite crystal structure. In reality, the crystals contain atoms of other elements which can incorporate in various manners. Substitutional point defects incorporate by replacing either the III-metal or the nitrogen atom. Atoms which incorporate in-between occupied lattice sites are called interstitial point defects. Multiple impurity atoms can incorporate in the crystal forming a complex with or without native atoms and are typically addressed as point defect complexes. Note that point defects are not necessarily composed of foreign elements but can also refer to native atom interstitials, unoccupied lattice sites (also known as vacancies) and native atoms occupying anti-sites, which are typically addressed as native point defects. The materials optoelectronic properties, such as transparency, photoluminescence spectra, mobility and carrier concentration, are dependent on the concentration and type of point defects. In this chapter, a brief overview of the theoretical model utilized to estimate the point defect types and concentration in AlN and their respective thermodynamic transition energy is presented. Next, the theoretical background for relating theoretically obtained thermodynamic transition energies with absorption, photoluminescence and photoluminescence-excitation spectra under the Franck-Condon approximation is described. Using these tools, the developed theoretical model can then be tested experimentally by means of optical characterization.

2.3.1 Energy of Formation for Point Defects

All density functional theory (DFT) calculations were performed by Dr. Irving's research group in the Materials Science and Engineering department at North Carolina State University. In particular, I would like to thank J. Harris and Dr. Gaddy, who developed the code and carried out the calculations. For a thorough description of the theory and methods, refer to Dr. Gaddy's, doctoral dissertation.⁵⁷

The energy of formation for point defects is useful for identifying the point defect types present in wide bandgap semiconductors. This energy is directly related to the

likelihood that the point defect will incorporate in the crystal during growth. Furthermore, the thermodynamic transition energies of a point defect can be directly extracted from the energy of formation for the different charged states and compared with photoluminescence and absorption spectra.^{58,59}

The formation energy E_{X^q} for a particular point defect X in a charge state q is calculated by

$$E_{X^q} = E_{Defective}^{DFT}(X^q) - E_{Bulk}^{DFT} - \sum_i n_i \mu_i - q(E_F - E_V + \Delta V_q), \quad (2.3.1)$$

where E_{Bulk}^{DFT} and $E_{Defective}^{DFT}(X^q)$ are the total ground state energy of an ideal crystal and that of a crystal containing a single point defect X^q respectively. The following term, $\sum_i n_i \mu_i$, describes the change in energy due to the interaction between the involved species n_i and their respective chemical potential μ_i . The last term, $q(E_F - E_V + \Delta V_q)$, describes the interaction between the charge state q of the point defect X and the Fermi level energy E_F with respect to the valence band energy E_V and a potential correction term ΔV_q . To mention some details, the Heyd, Scuseria and Ernzerhof (HSE) semi-local hybrid method is implemented for calculating the exchange and correlation potential, where a 0.32 fraction of the Hatree-Fock exact-exchange was chosen to match the 6.09 eV bandgap energy of AlN.⁶⁰ The Kohn and Sham approach is then used to obtain a solution for the Hohenberg and Kohn functional.⁶¹ Using this functional the ground state energy can be calculated as described by Hohenberg and Kohn.⁶² For all calculations a 96-atom supercell was chosen and a plane wave basis set, as implemented in the *Vienna ab initio simulation package* (VASP) was used.

The calculated formation energy of a point defect determines the probability of it being incorporated into the crystal during growth. The point defect concentration in the crystal, C_{X^q} , is related to the formation energy by

$$C_{X^q} = u N_s e^{\frac{-E_{X^q}}{k_B T}} \quad (2.3.2)$$

where N_i and u are the number of sites and possible configurations respectively, normalized to counts per unit volume (cm^{-3}).⁵⁷ From this relation it is clear that the lower the formation energy of a point defect, the higher its concentration. Additionally, the formation energy of a point defect varies as a function of the Fermi

energy E_F (see equation (2.3.1)). It is useful to plot this relation for a point defect with different charged states q (see example in *Figure 2-5*). The different slopes represent the different charged states of the point defect. Commonly, only the charged state with the lowest formation energy is displayed for a given Fermi energy (see *Figure 2-6*).

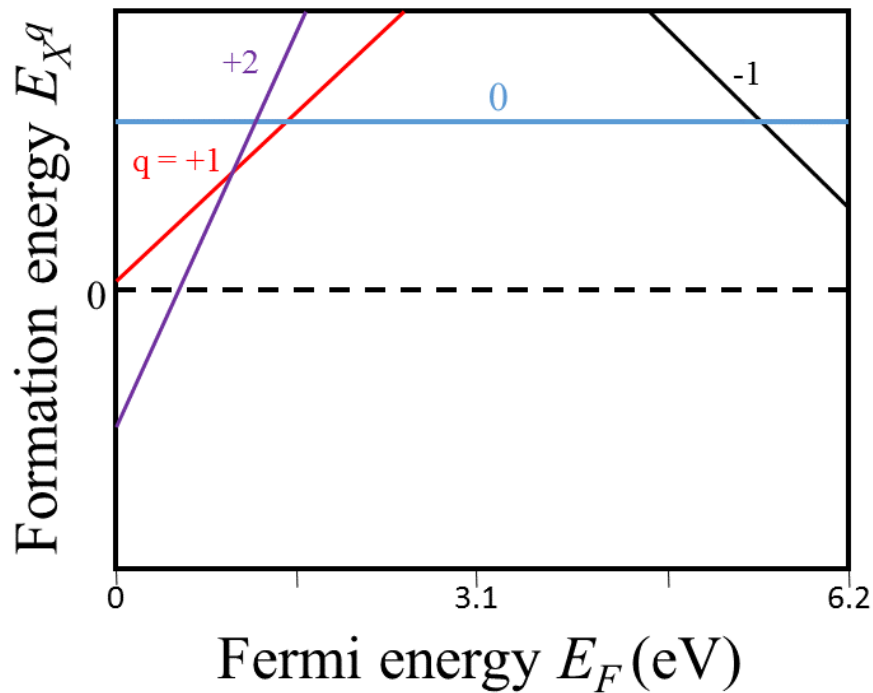


Figure 2-5: Illustration of a formation energy diagram of a point defect X for various charged states q (+2, +1, 0, -1) as a function of Fermi energy referenced to the valence band maximum (the bandgap energy of AlN was chosen as an example).

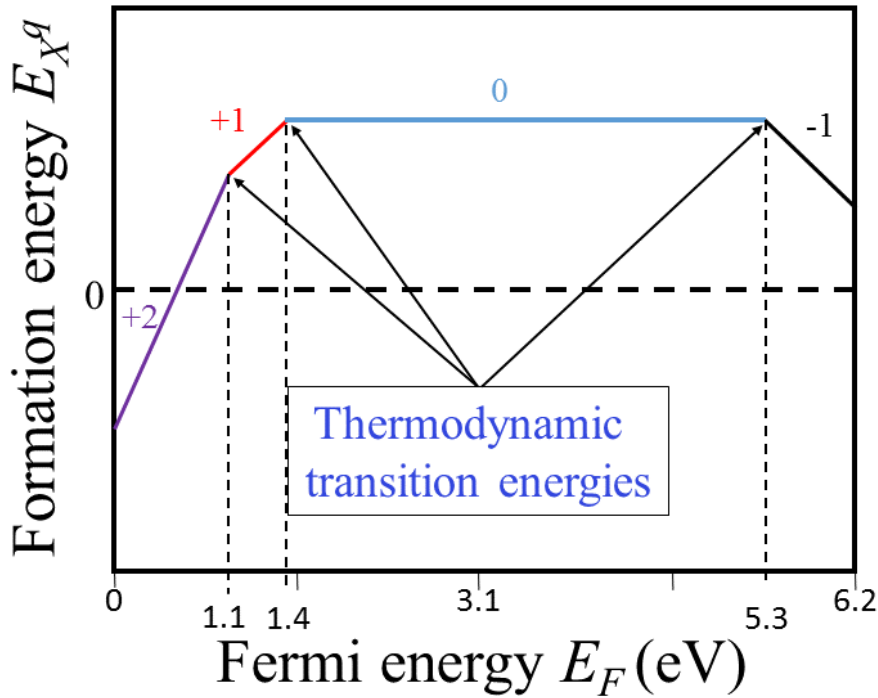


Figure 2-6: Illustration of a formation energy diagram of a point defect, with its thermodynamic transition energies highlighted.

The kinks where the changes in slope are observed in *Figure 2-6* mark the thermodynamic transitions between two charged states of a point defect. These thermodynamic transition energies are related to optical spectra and are useful for identifying the point defect types present in the crystal (section 6). In the next section (2.3.2) a more detailed description on how the thermodynamic transitions are related to optical spectra is given. It is important to highlight that DFT calculations using the HSE hybrid functional, have been established to estimate thermodynamic transition levels of impurities within the bandgap of the host semiconductor material more accurately than methods using the local density approximation (LDA) method or the general gradient approximation (GGA)^{63,64}. The latter significantly underestimate the bandgap energy as well as the electron/hole localization. Nevertheless, even when using the HSE hybrid functional, finite size correction schemes for charged defects lead to inaccuracies in the calculations. Typical claims for the accuracy of DFT calculations using the HSE hybrid functional are in the order of 0.1 eV,⁶³ however the accuracy varies for different charged states of the impurities and a higher error is predicted for native point defects such as native vacancies.^{57,64}

2.3.2 Franck-Condon Approximation

In the presence of point defects, energy states within the bandgap of the III-Nitride semiconductor may exist and their energy level is determined by the thermodynamic energy required for a point defect to transition from one charged state to another (Figure 2-6). These defect energy states can participate in optoelectronic transitions leading to below bandgap energy absorption and luminescence bands. The transitions include conduction band to defect state (or vice versa), valence band to defect state (or vice versa) and defect state to defect state (commonly referred to as donor acceptor pair transitions). At equilibrium, the charged state of point defects is determined by the Fermi level. The equilibrium coordinate of a point defect is dependent on its charged state, thus the equilibrium coordinate for the ground state may defer from that of the excited state, leading to energy shifts between the observed absorption maxima and the photoluminescence maxima (see Figure 2-7).

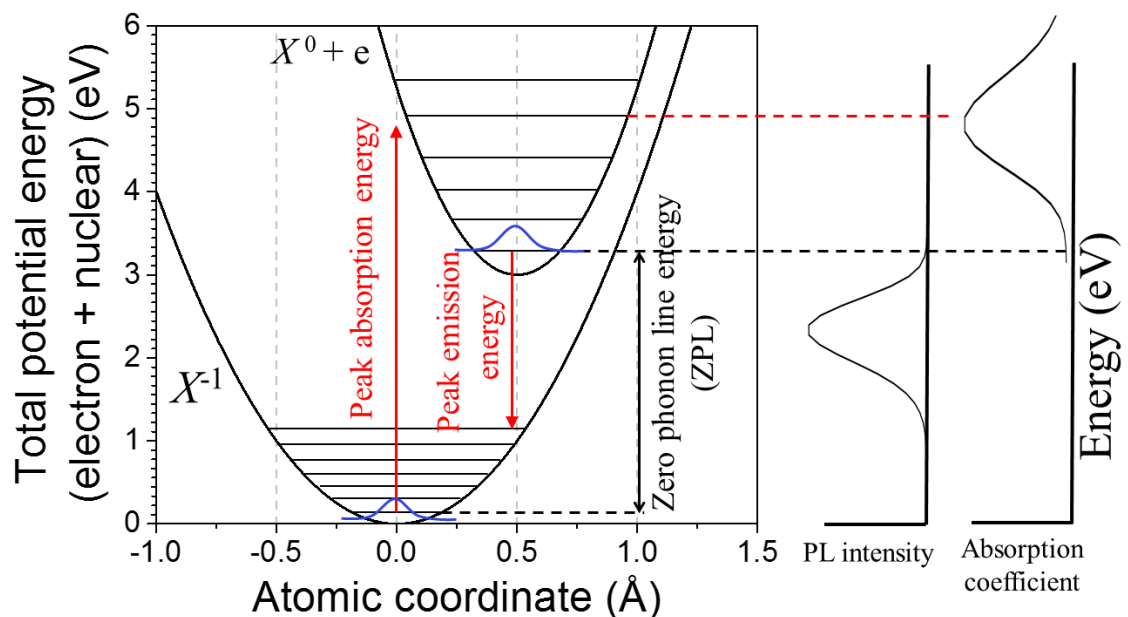


Figure 2-7: Configuration coordinate diagram illustrating the shift in energy between the peak absorption and emission bands, due to electron-phonon coupling. An optoelectronic transition involving a point defect X in the -1 charged state leading to a free electron in the conduction band and a neutral charged state is shown and the respective recombination process.

In the Franck-Condon approximation it is assumed that the optoelectronic transition occurs in a short time scale, when compared to the nuclear motion of the point defect, so that the transition probability can be calculated at a fixed nuclear coordinate.⁶⁵ Assuming the initial state is at equilibrium, from conservation of

momentum, the probability of an optoelectronic transition will be proportional to the overlap between the 0th quantum number vibrational wave function in the initial state with the nth (n = 0, 1, 2, 3 ...) quantum number vibrational wave function in the final state of the point defect. More generally, Fermi's golden rule states, the transition probability P_{Tran} is proportional to the square of the transition dipole moment which under the Franck-Condon approximation can be separated into the electronic transition dipole moment μ_e and a nuclear term μ_{FC} , with⁶⁶

$$P_{Tran} \sim |\mu_e|^2 \mu_{FC}. \quad (2.3.3)$$

In this section we are interested on the effects the nuclear term has on the shape of the absorption and photoluminescence spectra. For this reason, the electronic transition is assumed to be allowed, and μ_e is normalized and assumed to be independent of the coordinate position. The transition probability P_{Tran} , which determines the shape of the spectra, from the 0th vibrational state of the ground state into the nth vibrational state of the excited state can be described by the following equation.⁵⁹

$$P_{Tran}(\hbar\omega, T) = \sum_n w(T) |\langle \chi_{ne} | \chi_{0g} \rangle|^2 \delta(E_{Thermodynamic} + n\hbar\omega_v - \hbar\omega_{photon}). \quad (2.3.4)$$

here $w(T)$ is the thermal occupation factor of the vibrational energy state, ω_v is the vibrational frequency, ω_{photon} the photon frequency, $E_{Thermodynamic}$ is the thermodynamic transition energy and $\langle \chi_{ne} | \chi_{0g} \rangle$ are the Franck-Condon overlap integrals of the vibrational wave functions. Assuming the potential for both charged states in their respective equilibrium coordinate are identical, then one can assume the nuclear vibrational energy quanta of the initial and final state to be equal ($\hbar\omega_i = \hbar\omega_f = \hbar\omega_v$). It follows for low temperatures.^{59,67}

$$|\langle \chi_{ne} | \chi_{0g} \rangle|^2 = \frac{e^{-S} S^n}{n!}, \quad (2.3.5)$$

where S is the electron phonon coupling strength (also known as the Huang-Rhys factor). The electron-phonon coupling strength is given by

$$S = \frac{|E_{Peak} - E_{Thermodynamic}|}{\hbar\omega_v} = \frac{E_{FC}}{\hbar\omega_v}. \quad (2.3.6)$$

Here E_{Peak} is the peak absorption/emission energy. This difference in energy E_{FC} is typically addressed as the Franck-Condon energy shift. The energy E_{Peak} can be measured by absorption, photoluminescence and photoluminescence excitation spectroscopy techniques and $E_{Thermodynamic}$ is obtained from the energy of formation diagrams (see section 2.3.1). From this the absorption and PL spectra can be fitted in order to obtain a value for S and hence the vibrational energy quanta $\hbar \omega$.

Alternatively, at thermal energies $k_B T$ much higher than the vibrational energy quanta $\hbar \omega$, the full width at half maximum $W_{PL}(T)$ of the photoluminescence band is a function of temperature with⁵⁹

$$W_{PL}(T) = W_0 \coth\left(\frac{\hbar\omega}{k_B T}\right). \quad (2.3.7)$$

Here W_0 is the full width at half maximum for $T = 0$ and k_B is the Boltzmann constant. An expression for W_0 can be derived with

$$W_0 = \hbar\omega\sqrt{8 \ln(2S)} \quad (2.3.8)$$

From temperature dependent measurements one can obtain the vibrational energy quanta $\hbar \omega$ and the Huang-Rhys parameter S .⁵⁹

In summary, this chapter describes the DFT theoretical model utilized for calculating the energy of formation of point defects as a function of Fermi level. From these diagrams, the thermodynamic transition energies of point defects can be extracted. The thermodynamic transition energies can then be tested experimentally, where the shape of the measured PL and absorption bands are described under the Franck-Condon approximation. A method for obtaining the electron-phonon coupling strength and the vibrational frequencies of the point defect is described.

3 Experimental Setup

3.1 Optical Spectroscopy

3.1.1 Photoluminescence and Photoluminescence Excitation Spectroscopy

The photoluminescence (PL) setup for above bandgap excitation is displayed in *Figure 3-1*. Two laser sources are available in the setup. A 193 nm emission wavelength argon fluoride excimer laser system with 5 ns pulse width, where the repetition can be tuned from 10 Hz to 500 Hz and the energy per pulse from 0.05 mJ to 6 mJ. Alternatively a 325 nm emission wavelength helium-cadmium continuous wave (cw) laser system is available with a maximum output power of 50 mW.

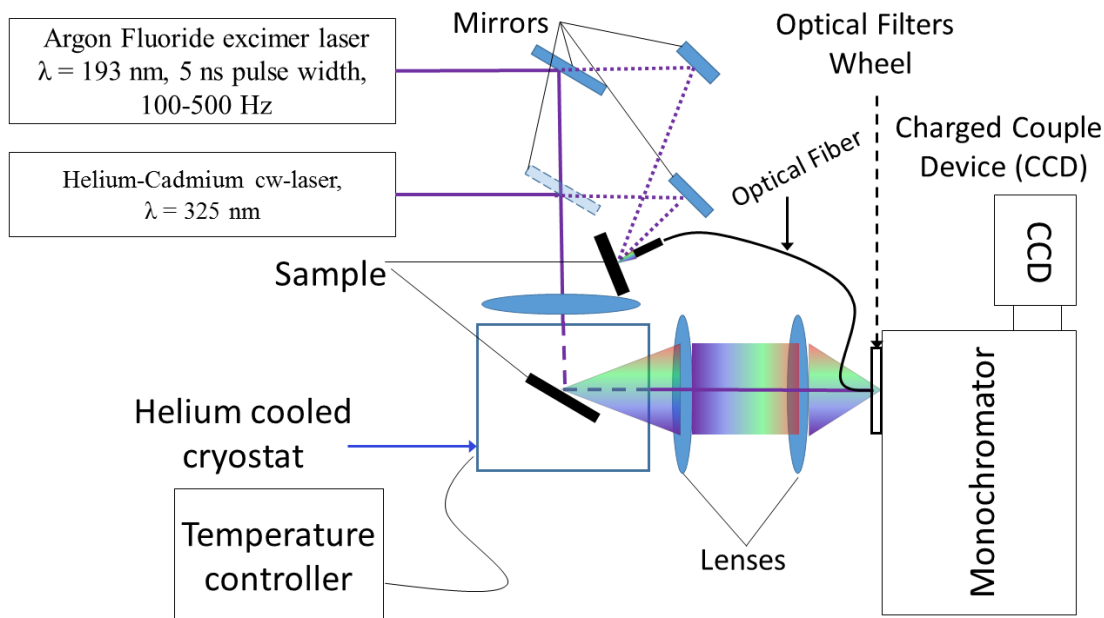


Figure 3-1: Experimental setup for photoluminescence spectroscopy measurements.

Two different methods for detecting the sample's photoluminescence signal were used. In one setup, the sample signal was coupled into a UV-grade optical fiber cable which is then coupled to the detection monochromator. Alternatively the sample was placed inside a cryostat chamber and the signal was collected using a system of lenses. The cryostat is cooled by flowing helium in a closed cycle system using an "F-70L Sumitomo Helium Compressor", reaching temperatures as low as 3 K. The temperature of the cryostat is controlled by adjusting the power of a heating element, allowing for temperature dependent PL measurements up to 350 K. The monochromator in the detection system is a 0.75 m focal length "Acton series SP-

2750” grating monochromator. The signal is detected by a “Pixis-XO: 2KB” charged couple device (CCD) with a 2048 x 512 imaging array of 13.5 μm by 13.5 μm pixels. The CCD is thermoelectrically cooled to $-75\text{ }^\circ\text{C}$.

The photoluminescence excitation spectroscopy measurements were conducted in a separate setup (*Figure 3-2*). The excitation light source used is a 450 W xenon arc lamp, where the light was collimated with an elliptical mirror. The broadband light is then coupled to a double 0.3 m focal length monochromator, containing UV blazed 3600 grooves mm^{-1} gratings, to select the excitation wavelength (energy). Optical filters are placed in the optical path after the monochromators to block second order artifacts. The light is then guided and focused onto the sample surface at a 45° - 60° angle. Silver paste is used to adhere the sample to a cold finger in a high vacuum enclosure. The sample is cooled to as low as 6 K by flowing liquid helium through the cold finger. The temperature of the cold finger can be adjusted between 6 K and 273 K by adjusting the flow rate of the liquid helium.

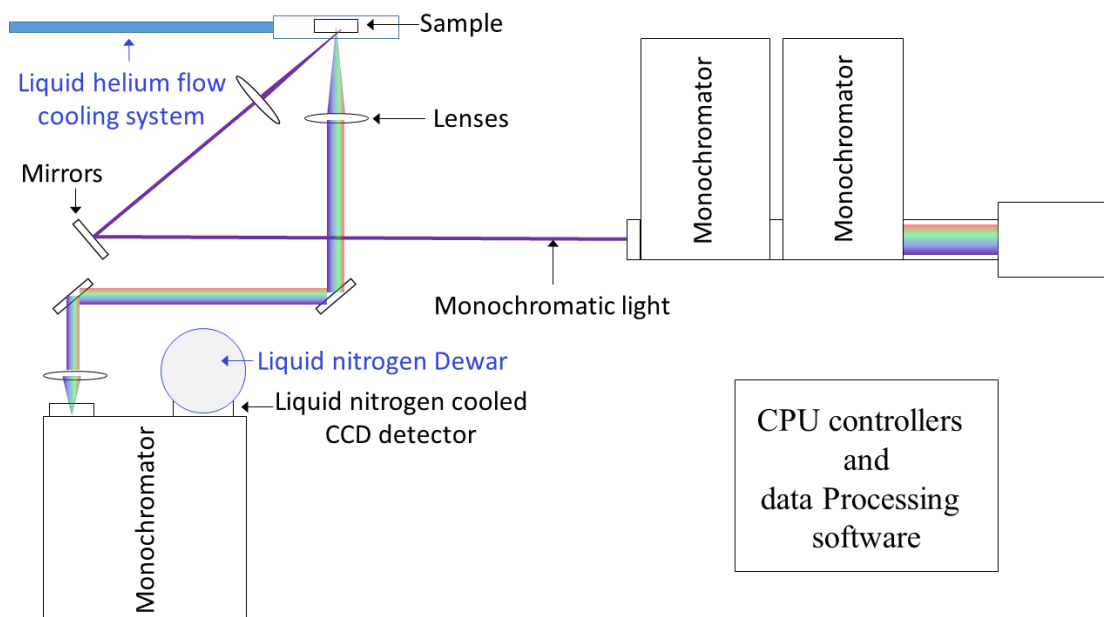


Figure 3-2: Schematic of the photoluminescence excitation spectroscopy setup.

The sample signal is then collimated with a lens and guided to the detection monochromator. A filter holder is placed before the entrance slit of the monochromator to allow for filters which block the excitation wavelength and second order artifacts. A 150 grooves mm^{-1} diffraction grating is used in the detection monochromator. The diffracted light is then detected by a liquid nitrogen cooled CCD detector.

3.1.2 Second Harmonic Generation Spectroscopy

To test the AlN LPS-based waveguides as well as the single polar AlN and GaN waveguides for QPM SHG and MDPM SHG respectively, a tunable wavelength (600 nm - 1100 nm) 40 femtosecond pulse length laser system was used with a 1 KHz repetition rate and 30 nm spectral width (FWHM). The energy per pulse varied with the wavelength and ranged from 1 μ J to 100 μ J. A 10 mm focal length lens was used to focus the laser beam onto the front face of the waveguide, where the beam diameter at the waveguide coupling facet was 10 μ m. The polarization was chosen so that TM modes were coupled into the waveguide. The SH signal together with the remaining fundamental signal was collected from the output waveguide facet with a lens. The fundamental signal was filtered allowing to guide the SH signal to the detection system, consisting of a monochromator and a photon counting camera synchronized with the femtosecond laser system. A schematic of the experimental setup is displayed in *Figure 3-3*.

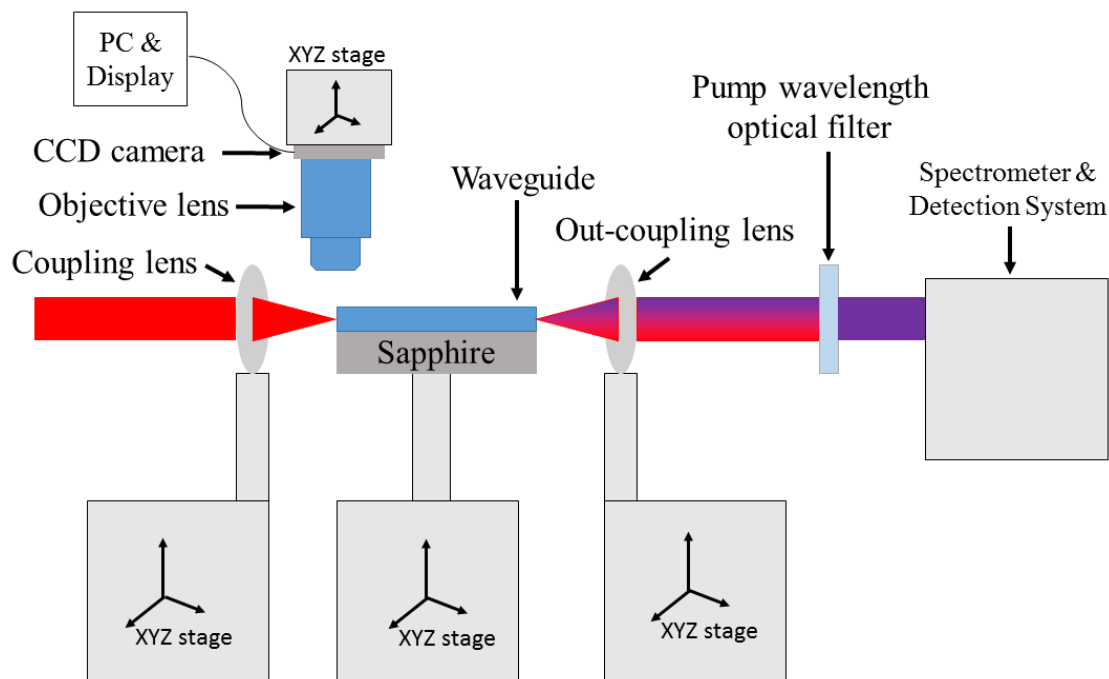


Figure 3-3: Schematic of experimental setup used for testing the AlN and GaN based waveguides for second harmonic generation.

3.1.3 Transmission Spectroscopy

Temperature dependent transmission spectroscopy measurements were conducted up to 870 $^{\circ}$ C. The setup employed for the temperature dependent measurements was built in-house and is displayed in *Figure 3-4*.

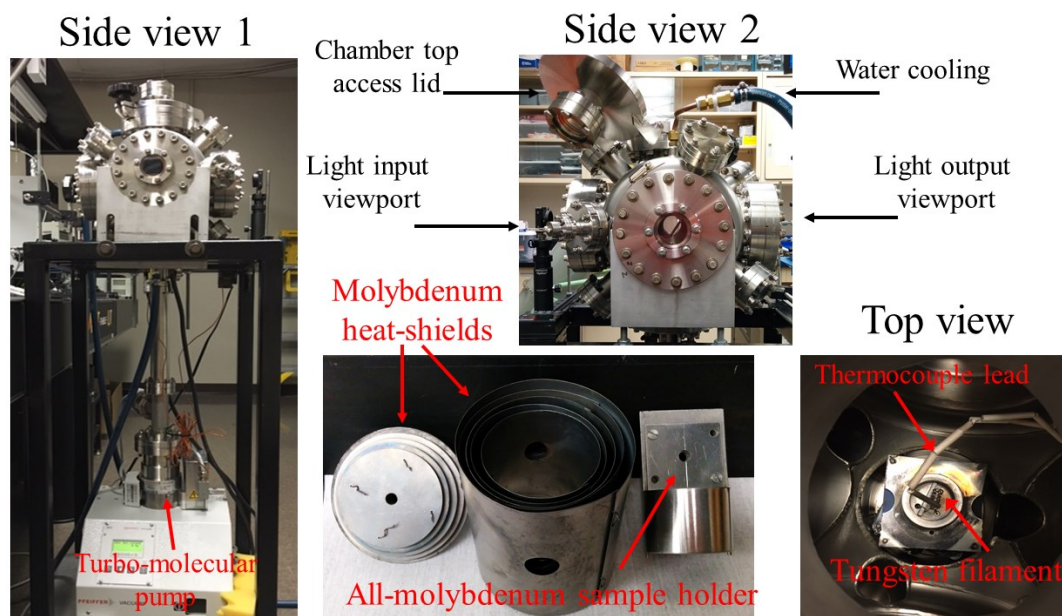


Figure 3-4: Experimental setup for temperature dependent transmission spectra up to 900 °C.

A turbo-molecular pump is attached to the chamber to keep the pressure below 10^{-4} mbar. The temperature is increased using a coiled tungsten wire as a resistive heating element. The current and voltage across the wire is manually controlled with an external power supply where powers up to 200 W are applied. To achieve temperatures as high as 900 °C, five concentric heat-shields, with circular openings to allow for the transmission of light, were machined to reduce the radiative heat transfer out of the sample enclosure. Not only higher temperatures can be achieved by the introduction of heat-shields, but also a more homogenous temperature within the sample enclosure is maintained. The stainless steel vacuum chamber wall is water cooled to keep the ambient temperature constant and to avoid any damage to vulnerable components due to overheating. The sample temperature is measured using a thermocouple which is placed in contact with the sample holder inside the concentric heat-shields. A 150 Watt UV-enhanced xenon arc lamp is used as a broad spectrum light source with an emission spectra ranging from 225 nm to above 800 nm. UV-grade fused silica viewports were attached for the transmission measurements. The transmitted light is focused onto the optical fiber and coupled to the detection system described above. A spectra at 800 °C was taken with no excitation light source to measure the background intensity due to heat radiation and determined to be negligible in the spectral range of interest.

3.1.4 Micro-photoluminescence Spectroscopy Setup

In this setup an argon ion laser system is used as the excitation light source. Nonlinear crystals for frequency doubling are available, allowing for discrete excitation wavelengths in the range between 227 nm and 264 nm according to the laser lines of the argon ion laser. The laser light is guided and focused onto the sample surface using a UV-compatible micro-objective lens with 1 μm resolution, which is positioned normal to the sample surface. The sample is placed on a piezo translation stage allowing for selective nano-positioning of the sample. The sample signal is collected using the same objective lens as the excitation lens, however it is separated by placing a beam splitter in the optical path. An additional beam splitter can be placed allowing for the sample surface to be displayed by a camera on a screen. The sample signal is then guided to a triple monochromator system where it is spectrally separated and detected by a liquid nitrogen cooled CCD detector (Figure 3-5).

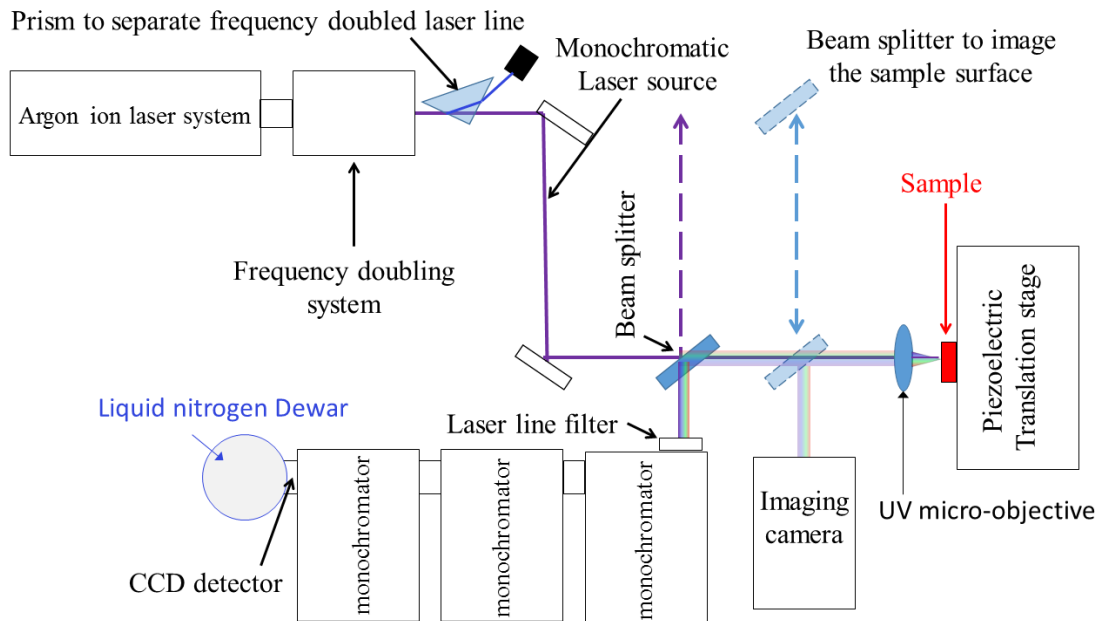


Figure 3-5: Micrometer spatially resolved photoluminescence excitation spectroscopy setup.

3.2 Growth Setup

The epitaxial AlN, GaN and AlGaN layers investigated in this work are grown via metal organic chemical vapor deposition (MOCVD) in a low pressure (20 – 100 Torr) vertical showerhead reactor with a water cooled quartz tube (see Figure 3-6). Inductively coupled graphite susceptors are used to heat the up to 2-inch substrates which are placed at their top surface. Two different material coatings of the graphite susceptors are available, silicon carbide and tantalum carbide, where the latter is used when temperatures above 1250 °C are required and with which temperatures up to 1550 °C can be achieved. For the III-metal aluminum and gallium, trimethylaluminum (TMA) and triethylgallium (TEG) metalorganic liquid sources are used as precursors. Ammonia gas is used as the nitrogen precursor. Hydrogen and nitrogen gas sources are available to serve as the carrier gas and/or as a diluent gases. The reactor background pressure is in the high 10^{-7} Torr range. Epi-ready LED quality 0.4 mm thick c-plane sapphire single crystals with 0.2 ° offcut (unless specified otherwise) were used as the starting substrate material.

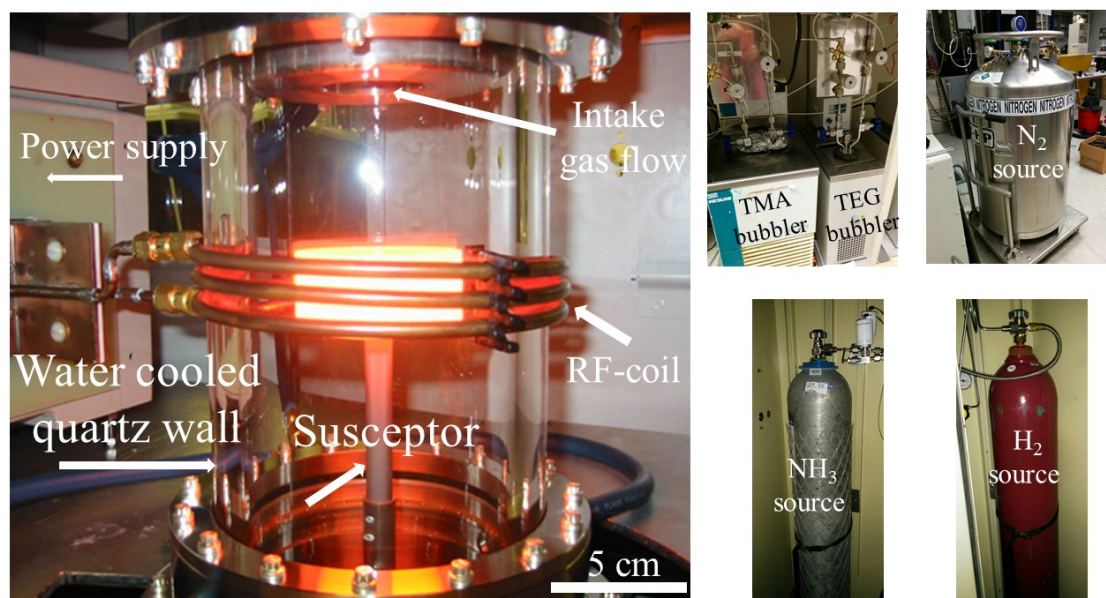


Figure 3-6: Picture of the metal organic chemical vapor deposition reactor during vacuum annealing at 1100 °C (left). Clockwise starting at the top left, picture of the cooling systems containing the metalorganic sources (TMA and TEG), liquid nitrogen tank which provides the N₂ gas source, ammonia gas source and hydrogen gas source.

3.3 Laser Interference Lithography

For the laser interference lithography, a Lloyd's mirror configuration setup was employed, developed by A. Bagal (*Figure 3-7*).⁶⁸ In this setup, a helium-cadmium laser is focused onto a pinhole to obtain a wave front of parallel plane waves with a Gaussian intensity profile as a function of the radial distance from the optical axis. If the sample is then placed at a large enough distance (>1 m), a nearly uniform intensity across the sample is obtained. The sample is paced adjacent to a mirror at a 90° angle. The angle of incidence can then be rotated to obtain the desired periodicity.

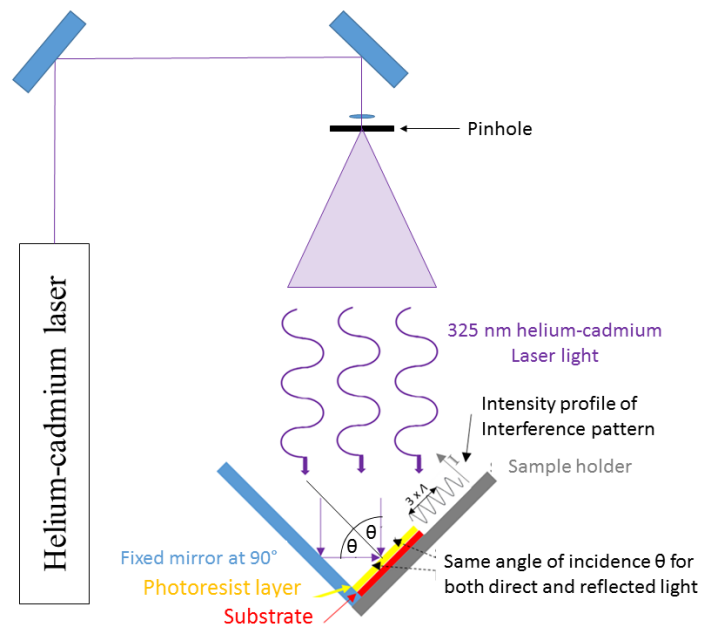


Figure 3-7: Lloyd's mirror configuration setup.

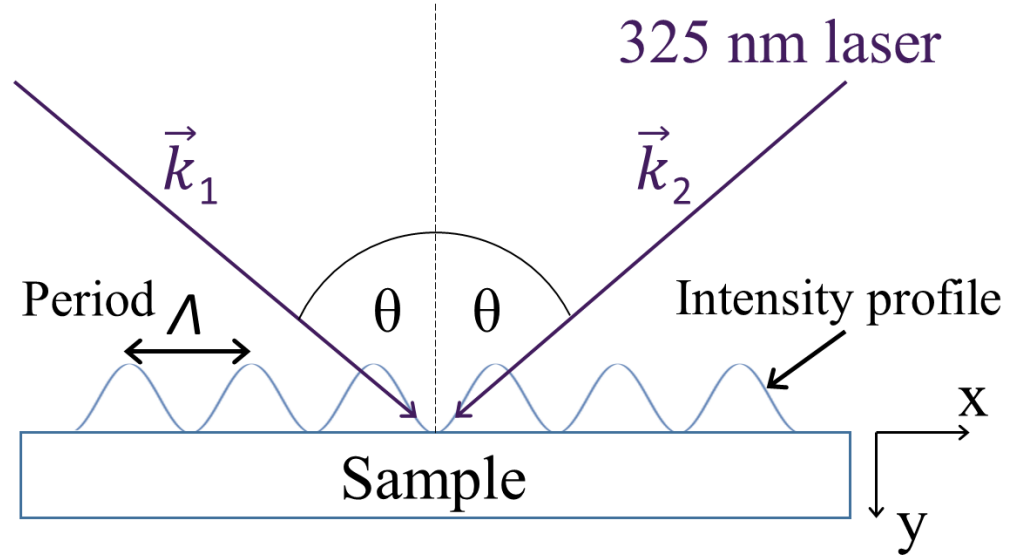


Figure 3-8: Laser interference intensity profile at the sample surface.

The periodic intensity of the laser at the sample surface is a result of the phase-shift between the two incident waves with wave vectors \vec{k}_1 and \vec{k}_2 (Figure 3-8). Since both waves originate from the same light source, their wave vector components in the y and z direction are equal. Only the direction of the wave vector in the x-direction is opposite while the magnitude is equal with

$$\vec{k}_1 e_x = k_{1x} = -k_{2x} = -\vec{k}_2 e_x. \quad (3.3.1)$$

The magnitude of the wave vector in the x-direction k_{1x} will be a function of the incidence angle with

$$|\vec{k}_1| \sin(\theta) = \frac{2\pi n}{\lambda} \sin(\theta) \quad (3.3.2)$$

Where n is the refractive index of the medium. The total phase-shift $\Delta\varphi$ accumulated at the sample surface after a translation distance r along the x-direction will be

$$\Delta\varphi = r\Delta k = r(k_{1x} - k_{2x}) = r(k_{1x} - (-k_{1x})) = 2rk_{1x}. \quad (3.3.3)$$

The period is given by the translation distance at which a phase-shift value of $\Delta\varphi = 2\pi$ is accumulated. From (3.3.2) and (3.3.3) it follows the relation between the angle of incidence θ and the interference period Λ , with

$$\Delta\varphi = 2\pi = 2rk_{1x} \equiv 2\Lambda k_{1x} \quad (3.3.4)$$

and

$$\Lambda = \frac{2\pi}{2k_{1x}} = \frac{\lambda}{2n\sin(\theta)}. \quad (3.3.5)$$

With the wavelength λ and refractive index n known, it is straight forward to calculate the angle of incidence θ necessary to obtain the calculated periodicity Λ required for quasi-phase matched frequency doubling in the UV-spectra (section 2.1.4).

4 Polarity Control

As discussed in section 1.1, the III-Nitrides semiconductors are polar materials. Epitaxial layers can exhibit either nitrogen polarity, III-metal polarity or mixed polar growth where both polarities grow side by side simultaneously (*Figure 4-1*). This section focuses on how the polarity of III-Nitride epitaxial films can be controlled in MOCVD systems, when using c-plane sapphire substrates.

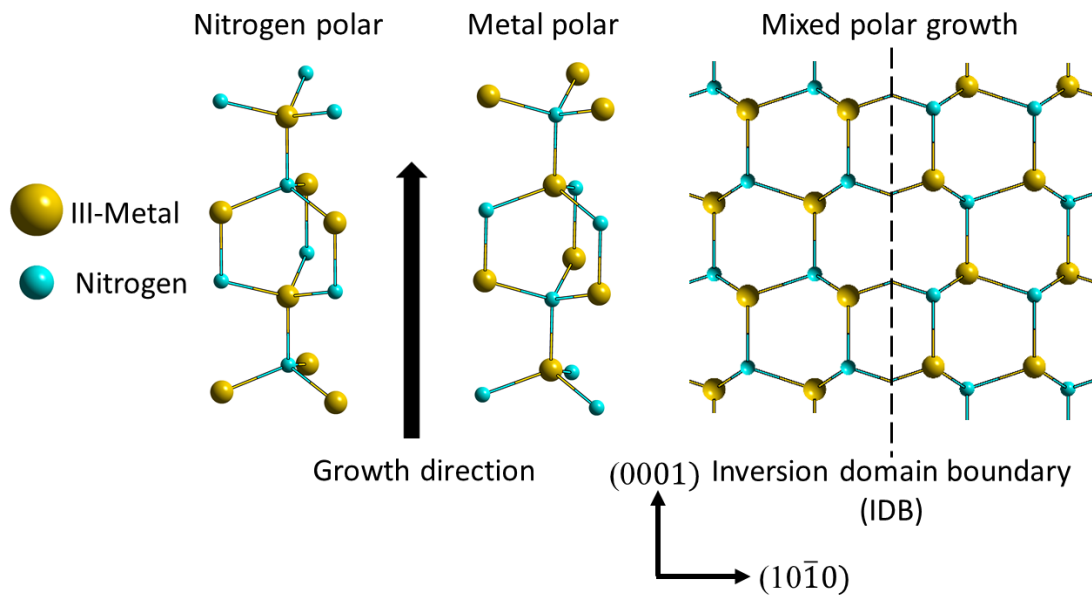


Figure 4-1: Schematic displaying the crystal structure for different polar growth directions and mixed polar growth

4.1 Historical Perspective

Single crystal AlN and GaN epitaxial layers on sapphire substrates by chemical vapor deposition, were reported for the first time by Yim et al.¹² and Maruska et al.¹¹ respectively. Their optical and electrical properties as well as their crystal structure were characterized, however no studies on the polarity of the grown films were performed. Yoshida et al.⁶⁹ reported on the first epitaxial AlN layers on sapphire by reactive molecular beam epitaxy (MBE). In 1983 Yoshida et al. using reactive MBE showed that if an AlN layer is deposited prior to the deposition of a GaN layer, the surface roughness is significantly reduced and the electrical and optical properties of the GaN layer are significantly improved. The study, related the result to the reduced lattice mismatch and thermal expansion mismatch between GaN and AlN compared to that of sapphire.⁷⁰ Similarly, in a later study by Amano et al. using metal organic

chemical vapor deposition, superior quality GaN layers were achieved by prior deposition of an AlN layer under adequate growth conditions and was also related to the reduced lattice and thermal expansion mismatch.^{71,72} It is now assumed that the improved quality of the reported GaN films, was likely due to uniform Ga-polar growth as opposed to N-polar or mixed-polar growth. In 1988, Sasaki and Matsuoka, reported on MOCVD GaN epitaxial films using SiC polar substrates, where both the C-face and the Si-face of the (0001) plane were used as well as sapphire substrates.⁷³ The work showed that previously observed differences in the surface morphology (atomically smooth Vs hexagonal hillocks) and optical properties of GaN epitaxial films arise due to polarity dependent growth surface kinetics and impurities incorporation. The study showed nearly identical photoluminescence spectra and surface morphology (hexagonal hillocks) for GaN films grown directly on sapphire substrates and on the C-face of the SiC substrates. Meanwhile, the properties of the GaN film grown on the Si-face of SiC were similar to the GaN films grown on AlN layers on sapphire substrates reported by Yoshida et al, and Amano et al.. The results by Sasaki and Matsuoka, uncovered the implications of different polar growth directions, however the polarity of the films remained unknown. Nakamura and Mukai, similarly to Amano et al. and Yoshida et al., observed an improvement on the optical and structural quality of InGaN epitaxial layers on sapphire when introducing a low temperature (500 °C) GaN buffer layer prior to the InGaN deposition.⁷⁴ It wasn't until 1996 that Daudin et al., using ion channeling diffraction and convergent beam electron diffraction (CBED), determined that MOCVD GaN layers exhibiting a smooth surface were uniformly Ga-polar and that films exhibiting hexagonal hillocks at the surface were predominantly N-polar with a high density of narrow Ga-polar domains.⁷⁵ The study highlights the importance of an optimized low temperature GaN buffer layer in obtaining uniform Ga-polarity. In parallel, Hwang et al. studied the effect of nitridation of the sapphire surface prior to depositing the GaN film and concluded that under certain conditions, nitridation of the sapphire surface leads to films exhibiting a rough surface covered with hexagonal hillocks, now known to be typical for N-polar GaN films.⁷⁶ Dimitrov et al. reported that a low temperature AlN nucleation layer leads to Ga-polar GaN films (similar to the GaN buffer layer reported by Daudin et al.), while direct growth on sapphire leads to N-polar GaN films.⁷⁷ Collazo et al. developed a process for controlling the polarity of GaN

epitaxial layers using MOCVD, where N-polar films are achieved by proper nitridation of the sapphire substrate prior to growth of the GaN layer and Ga-polar films are achieved by introducing a low temperature AlN nucleation layer which is properly annealed.⁷⁸ An extensive review summarizing growth techniques, growth procedures and the resulting polarity of the GaN film was reported by Sumiya and Fuke.⁷⁹ The epitaxial processes developed over the past decades which use an AlN or GaN nucleation layer, to control the polarity of the III-Nitride film, have been empirically established with no detailed description available on the precise mechanism leading to a particular polarity. A recent study by Mohn et al. has shone light on the subject, where high resolution transmission electron microscopy measurements of the AlN low temperature buffer layer, indicate that a rhombohedral aluminum-oxynitride interlayer is responsible for the polarity inversion from the “N-polar” AlN of the nitridated sapphire surface to the Al-polar face AlN.⁸⁰

As an alternative to controlling the polarity of III-Nitride epitaxial films, there are reports demonstrating polarity inversion from the III-polar face to the N-polar face through high concentration magnesium doping in both GaN and AlN.^{81,82} This polarity control process scheme has been employed to fabricate submicron GaN and AlN lateral polar structures with limited success.^{82,83} This approach has proven successful in achieving periodic poling of GaN, while little success has been demonstrated for periodic poling of AlN, typically resulting in no growth at the interfaces between the polar domains, inhibiting their use in nonlinear optical applications. In this work we employ the previously described polarity control process scheme, where an AlN nucleation layer is used (or not) to achieve III-polar (N-polar) growth of the III-Nitride film and is described in detail in the following section.

4.2 III-Polar AlN and GaN

As described in the former subsection (4.1) III-Polar III-Nitride epitaxial films can be achieved on sapphire substrates by depositing an optimized AlN or GaN nucleation layer. In this subsection the process developed by Collazo et al. where an AlN nucleation layer is used to achieve uniform III-polar films is described.

An LED quality c-plane sapphire substrate with a 0.2° offcut towards the m-plane is introduced to the MOCVD system described in section (3.2). The reactor is pumped down to a pressure in the order of 10^{-6} Torr to high 10^{-7} Torr. The substrate is then vacuum annealed at 1100°C for 10 minutes and subsequently backfilled with a 1:1 ratio of 1 slm H_2 and 1 slm N_2 to a total chamber pressure of 20 Torr, where it is annealed for additionally 7 minutes. Following, ammonia is introduced to the reactor at a flow rate of 0.3 slm together with 1 slm of N_2 diluent gas for 4 minutes at 950°C . Next, the 20-30 nm AlN layer is deposited by flowing $5.5\ \mu\text{mol}/\text{min}$ of TMA into the reactor for 3 minutes at 650°C under 3 slm flow of N_2 and 3 slm flow of NH_3 . Next, the AlN nucleation layer is annealed at 1040°C for 15 minutes under 1.6 slm flow of N_2 and 0.2 slm flow of NH_3 . A typical temperature profile of the growth run for an AlN nucleation layer is displayed in *Figure 4-2*.

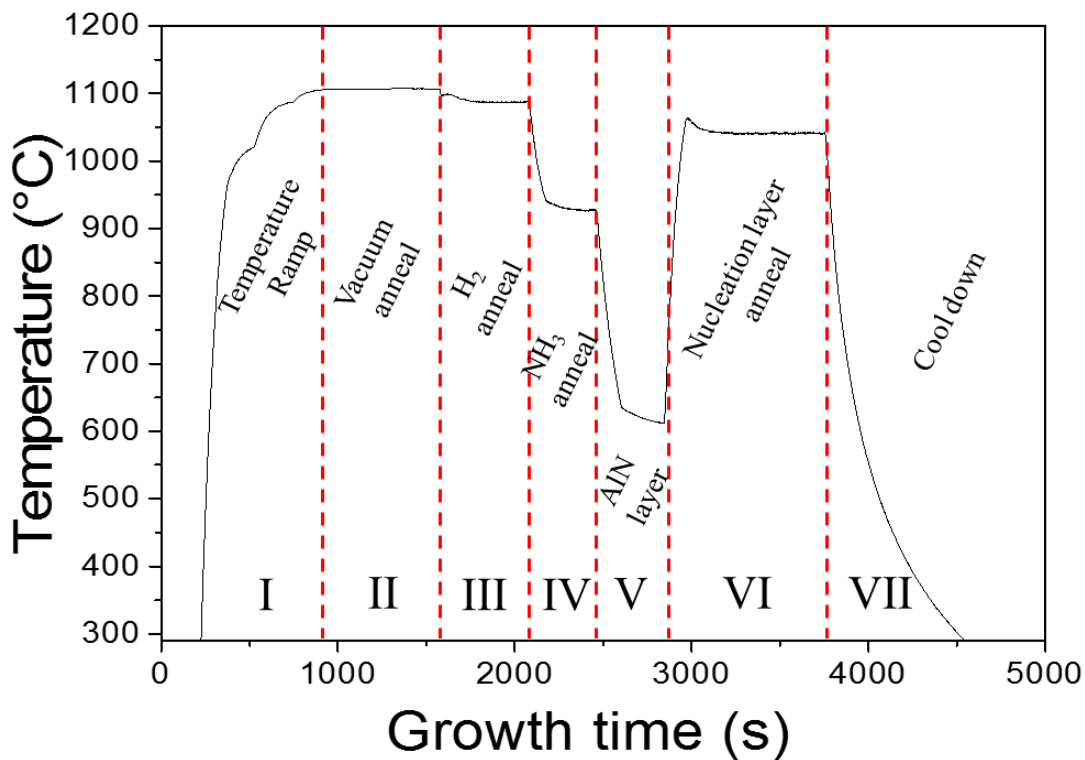


Figure 4-2: Growth run temperature profile of an AlN nucleation layer.

In *Figure 4-3* the surface morphology of a typical AlN nucleation layer as measured by AFM is displayed.

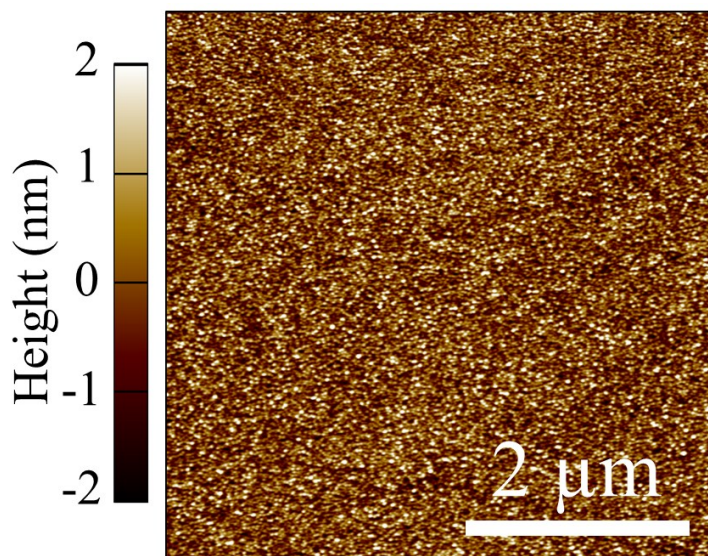


Figure 4-3: AFM image of the surface of a typical AlN nucleation layer.

For single polar films, instead of cooling down and removing the sample from the reactor (step VII in Figure 4-2), the growth of the GaN (AlN) film is started. The subsequent growth conditions for the III-Nitride layers depend strongly on the objective at hand. There are however standard growth runs for GaN and AlN layers, which are used to troubleshoot the MOCVD system. In a “standard” growth run for a 1.2 μm thick GaN layer, following the annealing of the AlN nucleation at 1040 $^{\circ}\text{C}$ (step VI in Figure 4-2), TEG is flown into the reactor at a flow rate of 36 $\mu\text{mol}/\text{min}$ for 33 minutes in a mixture of 0.3 slm of NH_3 and 6.9 slm of N_2 at 20 Torr total chamber pressure. The growth is then finished by stopping the TEG flow and the reactor is cooled down under NH_3 atmosphere. For a “standard” 300 nm AlN layer, following the annealing of the AlN nucleation layer, the temperature is increased to 1150 $^{\circ}\text{C}$ where growth is started by flowing 7.1 $\mu\text{mol}/\text{min}$ of TMA for 6 minutes under 10 slm of H_2 and 0.3 slm of NH_3 . Under continued growth and otherwise constant conditions, the temperature is increased to 1200 $^{\circ}\text{C}$ and left there for 24 minutes followed by an additional temperature increase to 1250 $^{\circ}\text{C}$ for 15 minutes of additional growth. The growth is then terminated by stopping the TMA flow and the reactor is cooled under NH_3 atmosphere. The surface morphology of a “standard” III-polar GaN and AlN film is displayed in Figure 4-4.

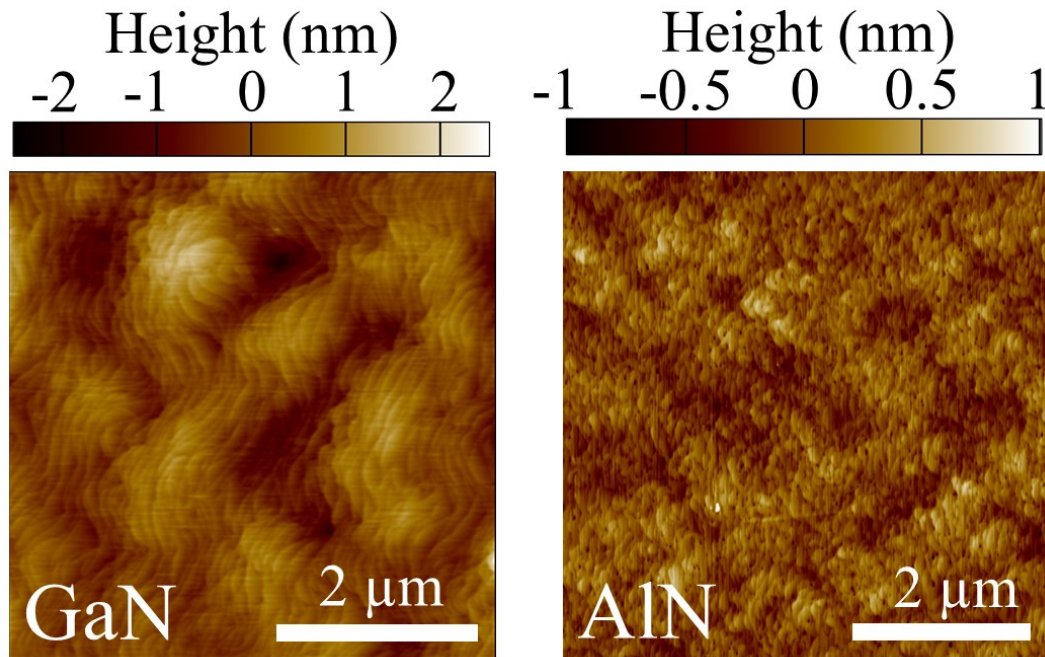


Figure 4-4: AFM measurements of the surface morphology of a Ga-polar GaN (left) and Al-polar AlN (right) epitaxial layer.

Typical III-polar GaN films grown as described above, exhibit step flow growth, are highly resistive ($>M\Omega$) and are inert to KOH wet-etching. Typically point defect concentrations (mainly carbon) in the high 10^{17} cm^{-3} to low 10^{18} cm^{-3} is measured for these films. Standard III-polar AlN films also exhibit step flow growth, are inert to KOH etching and have point defect concentrations in the low 10^{18} cm^{-3} .

4.3 N-Polar AlN and GaN

To obtain Nitrogen polar III-Nitride films, the first three steps are identical to those used for the deposition of an AlN nucleation layer (section 4.2). The sapphire substrate is vacuum annealed at 1040°C , followed by annealing in H_2 and is subsequently annealed in NH_3 at 950°C as described in the previous section (section 4.2). Following the annealing step in NH_3 , the substrate temperature is increased to the desired growth temperature at which the III-Nitride layer is to be deposited. Typical starting growth temperatures for GaN and AlN are 1040°C and 1100°C respectively. AFM measurements of the surface of N-polar GaN and AlN are shown in *Figure 4-5*.

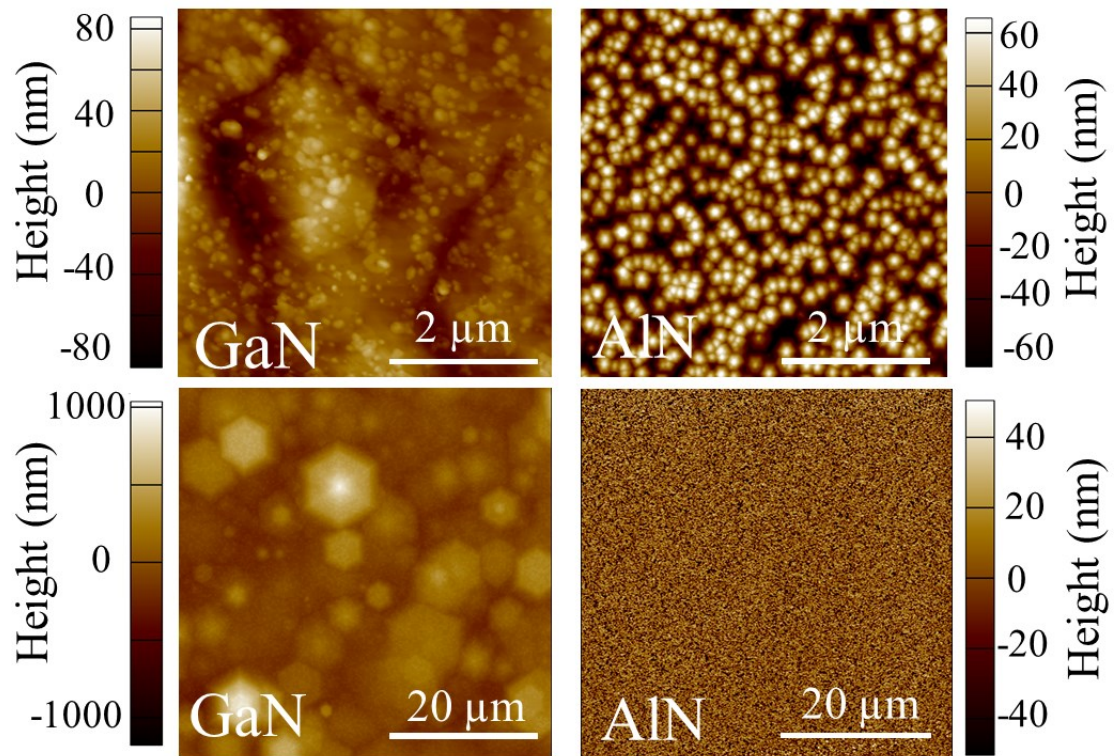


Figure 4-5: AFM measurements of the surface morphology of N-polar GaN (left) and AlN (right) respectively with high (top) and low (bottom) magnification.

In contrast to III-polar GaN, N-polar GaN exhibits 2D nucleation growth leading to a rough surface morphology with a high density of hexagonal hillocks with diameters reaching tens of micrometers. The unintentionally incorporated oxygen impurities, reach concentrations in the order of $6 \times 10^{19} \text{ cm}^{-3}$ and account for the majority of the point defects, leading to conductive n-type GaN layers.⁸⁴ The N-polar AlN face, is reactive to KOH wet-etching and more details on the polarity dependent etching will be described in the next sub-section (4.4). The surface of the N-polar AlN epitaxial layer also exhibits a rough surface with a high density of columnar-like hexagonal hillocks in contrast to Al-polar AlN. The diameter of the columnar hexagonal hillocks is typically in the hundreds of nanometers, where an aspect ratio in the range 0.3 to 0.6 is measured, significantly higher than the range measured for GaN of 0.03 to 0.1. The concentration of oxygen impurities in the epitaxial N-polar AlN layers is in the high 10^{19} cm^{-3} to low 10^{20} cm^{-3} range, however in contrast to GaN the films are highly resistive. The oxygen impurity as a nitrogen substitutional point defect in AlN is expected to have a stable DX^- state at 550 meV below the conduction band, explaining the highly resistive nature of the N-polar AlN layers, event at such high oxygen concentrations.⁵⁷

4.4 Polarity Dependent Wet Etching in KOH

The polarity of epitaxial GaN and AlN films grown via MOCVD under the process conditions described above, has been extensively studied using convergent beam electron diffraction (CBED), conventional transmission electron microscopy (CTEM) and scanning transmission electron microscopy (STEM).^{85,86} These characterization techniques require complex sample preparation procedures making it impractical for characterizing a large number of samples. Alternative techniques have been developed to determine the polarity of the films including reflection high energy electron diffraction (RHEED), X-ray photoelectron spectroscopy (XPS) and chemical stability analysis in alkali solutions.⁷⁹ The latter is found to be the most convenient technique, where the polarity dependent chemical properties of the III-Nitrides are used to determine the polarity of the films.⁸⁷ In this work the polarity of the epitaxial films or that of particular polar domains in the samples, is determined by wet etching in KOH solutions. In *Table 4-1* the polarity dependent etch rates for AlN and GaN are summarized as determined by Guo et al..⁸⁷

Table 4-1: Etch rates of N- and III-polar GaN and AlN crystals in 1wt% KOH solution in deionized water at 70 °C.⁸⁷

| Material | Etch rate (nm/min), 1wt% KOH @ 70 °C. | | Etch selectivity (N-polar/III-polar) |
|----------|---------------------------------------|-----------|--------------------------------------|
| | N-polar | III-polar | |
| GaN | 40 | 1.9 | ~20 |
| AlN | 1400 | 1.6 | ~900 |

As can be seen from *Table 4-1* the etch rate for the N-polar surface is around one and three orders of magnitude larger than that of the III-polar surface, for GaN and AlN respectively. From cross sectional SEM measurements before and after wet etching, the polarity of the films can be determined based on the established etch rates. In addition, the III-polar surface remains atomically smooth after wet etching, with the exception of regions containing pits where the etch rate of the exposed r (1-102) and s (1-101) planes (and possibly others) is larger, leading to increased pit sizes. In contrast, the N-polar surface roughness significantly increases after wet etching in alkali solution, leaving a high density of hexagonal hillocks exposed (*Figure 4-6*).⁸⁷ Often, examining the sample surface with an optical microscope before and after wet etching is sufficient to estimate the polarity of the sample. In

Figure 4-6 the chemically etched N-polar and III-polar surface of a GaN and AlN layer are presented for comparison. The III-polar surface for both GaN and AlN remains featureless, while the N-polar surface of both GaN and AlN exhibit a rough surface filled with hexagonally shaped pyramidal features.

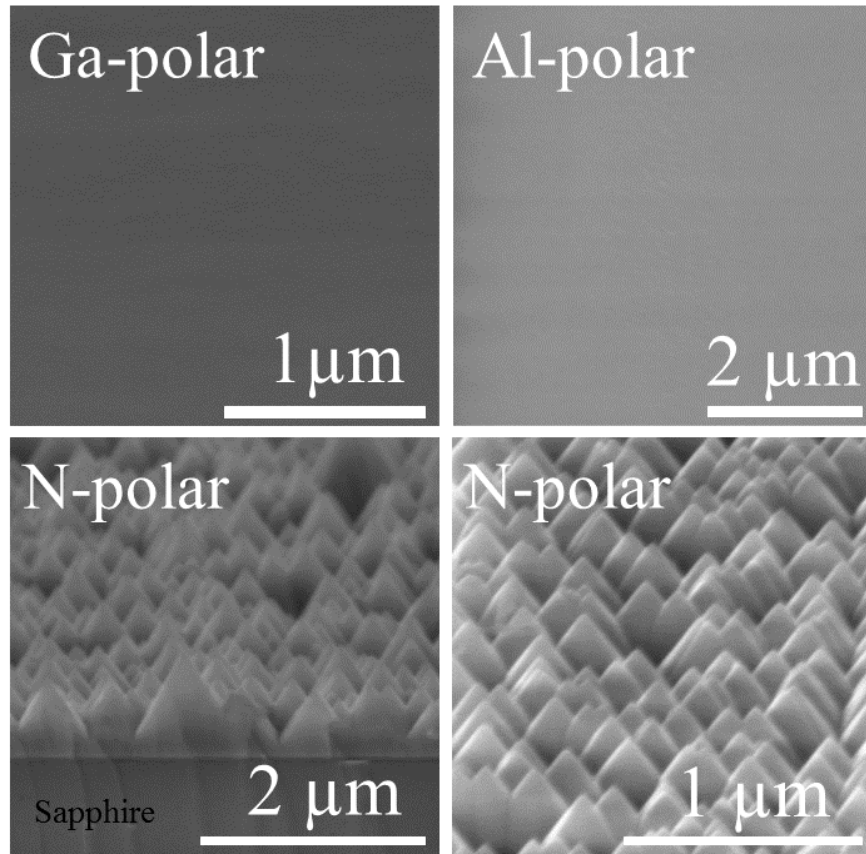
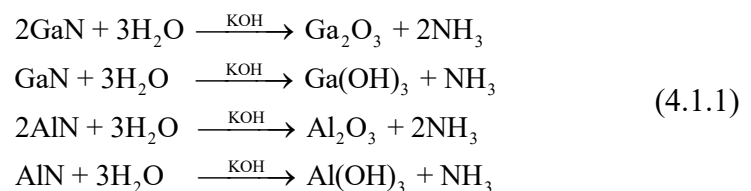


Figure 4-6: Tilted cross section SEM image displaying the etched surface of a III-polar (top) and N-polar (bottom), GaN (left) and AlN (right) epitaxial layer.

The chemical reactions leading to the formation and dissolution of III-Nitrides into III-oxides and ammonia when submerged in a KOH solution is well known with:^{88–}

90



Guo et al.⁸⁸ calculated a Gibbs free energy for the latter chemical reactions of 1399 KJ/mol, 723 KJ/mol, -350 KJ/mol and -334 KJ/mol respectively indicating the more favorable formation of Al-oxide/-hydroxide over Ga-oxide/hydroxide, which is reflected in the increased etch rates for AlN over GaN. The polarity etch selectivity favoring the N-polar face over the III-polar face, has been attributed to the different

number of nitrogen dangling bonds for the respective polarities, where the N-polar face will exhibit three nitrogen dangling bonds, shielding the III-atoms from reacting with the OH^- molecules, while the III-polar face will only exhibit a single nitrogen dangling bond allowing for a reaction with the OH^- molecules.⁸⁹ However, none of the studies consider polarization induced charge compensation and its relation to polarity dependent oxidation potential, which may also play a role on the etch selectivity between the polarities of the III-Nitrides.

In summary, the polarity control process is described in detail for III- and N-polar GaN and AlN thinfilms deposited via MOCVD on sapphire. The surface morphologies for the respective polar films are characterized via AFM, where step flow growth is observed for both III-polar III-Nitrides and a rough surface is measured for both N-polar III-Nitrides plagued with hexagonal hillocks. The etch behavior for both polarities in a KOH solution at 70 °C is presented where the III-polar films are inert and the N-polar films are etched, exhibiting a high density of hexagonal hillocks at the surface after wet etching. This method for determining the polarity of the III-Nitrides is practicle when characterizing a large number of samples, and is the main characterization technique employed for the lateral polar structures fabricated in this work.

5 Lateral Polar Structures

5.1 AlN Lateral Polar Structures

A novel concept for devices based on lateral polarity structures was introduced by Stutzman et al., where Ga-face and N-face GaN films were deposited simultaneously sided by side.⁹¹ For this, an MBE system was used, where a low temperature AlN layer deposited on a sapphire substrate was lithographically patterned leaving alternating regions of exposed sapphire substrate and AlN. The subsequently deposited GaN films were N-polar on the regions where the sapphire substrate was exposed and Ga-polar on the regions where the AlN layer remained. Similarly, Collazo et al. demonstrated polarity control via MOCVD and realized GaN lateral polar structures by lithographically patterning a previously deposited AlN buffer layer.⁹² Using the same concept, MOCVD grown AlN lateral polar structures were demonstrated by Kirste et al..⁹³ In this work, we employ the procedure described by the latter study to fabricate III-Nitride lateral polar structures.

The AlN lateral polar structures are fabricated using a multi-step process. First an AlN nucleation layer is deposited on an LED quality c-plane sapphire substrate as described in section 4.2. The substrate coated with a 20-30 nm AlN nucleation layer (*Figure 4-3*) is then removed from the reactor and spin-coated with a 3 μm thick positive photoresist layer (S1813). A photolithography mask was designed for the growth and study of lateral polar structures and is displayed in *Figure 5-1*. The photoresist layer is exposed to 130 mJ/cm^2 using the mask displayed in *Figure 5-1* and developed for 1 min in MF-319 developer. After rinsing the sample with deionized water and blow drying it with N_2 , the pattern is transferred to the III-Nitride epitaxial layer by RIE in a Cl_2 and BCl_3 anisotropic plasma in a “Tryon Minilock II” RIE system. The samples are etched at an RF power of 100 W in a 1:1 ratio gas mixture of 25 sccm of Cl_2 and BCl_3 at a 75 mTorr total reactor pressure.

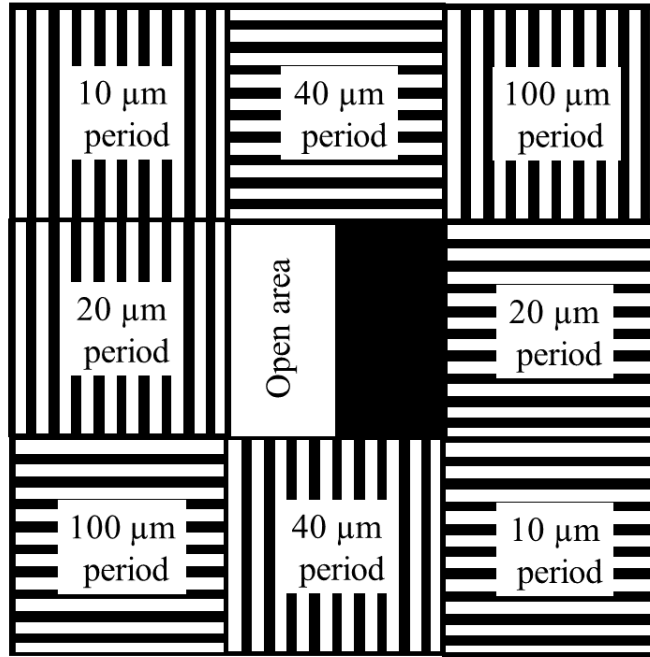


Figure 5-1: Schematic of mask design used for photolithography. The mask contains 8 different regions of 1 cm^2 areas with different stripe structures. The stripe structures are composed of equally spaced covered and uncovered stripes. The periodicity of the stripe structures are 10, 20, 40 and $100 \mu\text{m}$. Every periodic structure is available in two orientations at a 90° angle from each other in order to study the influence of the substrate orientation on the grown structures. The center region is half covered and half uncovered to achieve $0.5 \times 1 \text{ cm}^2$ single polar domains and compare with the corresponding polar domains in the lateral polar structures.

The remaining photoresist residue was then removed by submerging the sample in heated N-Methyl-2-Pyrrolidone (NMP) followed by isotropic O_2 plasma in a PM-600 system. An AFM image at the $20 \mu\text{m}$ periodic structure region of a patterned substrate, is displayed in *Figure 5-2*. The patterned substrate is then introduced to the MOCVD reactor, which is pumped to a pressure in the high 10^{-7} to low 10^{-6} Torr. The sample is vacuum annealed at a temperature of 1040°C for 10 minutes and then backfilled with 1 slm of H_2 and 1 slm of N_2 at a total chamber pressure of 20 Torr where it is kept for 7 minutes. Next, the temperature is lowered to 950°C and the sample is exposed to a mixture of 1 slm N_2 and 1 slm NH_3 for 4 min. The substrate temperature is then increased to 1100°C where the AlN growth is started by flowing $6.7 \mu\text{mol}/\text{min}$ of trimethylaluminium (TMA) and 0.3 slm NH_3 for 10 min using N_2 as the precursor carrier gas and 10 slm of H_2 as a diluent gas in a reactor total pressure of 80 Torr. Finally, the temperature and the TMA flow are increased to 1250°C and $13.4 \mu\text{mol}/\text{min}$, respectively. In this process, N-polar AlN grows on

the exposed sapphire regions and Al-polar AlN on top of the AlN nucleation layer^{93,94}.

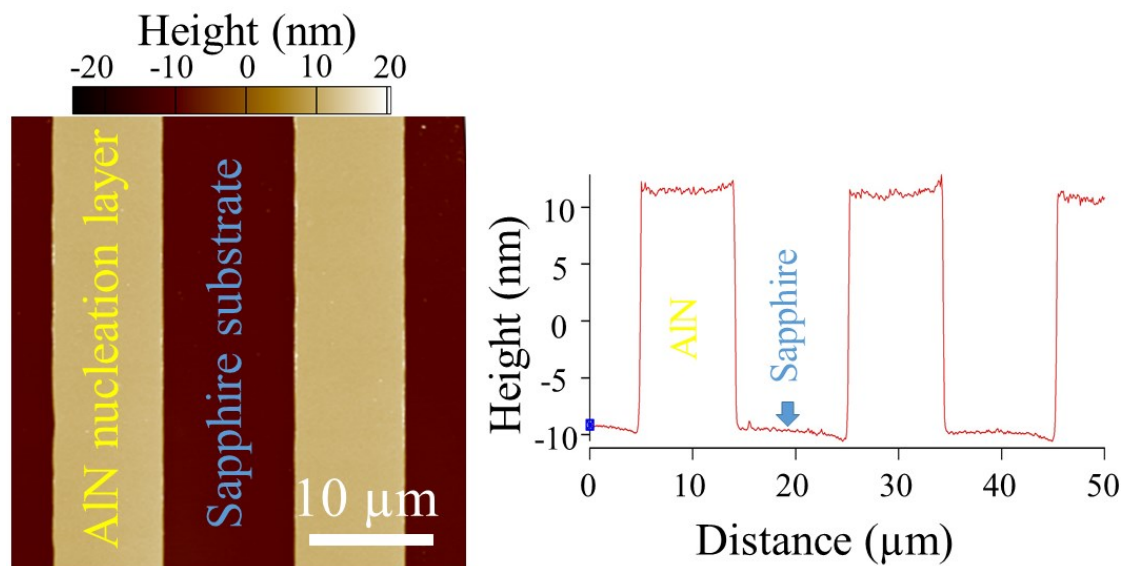


Figure 5-2: AFM image of a 20 μm periodic stripe pattern of an AlN nucleation layer deposited on a sapphire substrate with color coated height scale (left). Line scan across the periodic structure showing the height profile.

Figure 5-3 displays the surface morphology of an AlN lateral polar structure at a 20 μm periodically patterned region, where one N-polar domain can be seen in the center region surrounded by two Al-polar domains at each side.

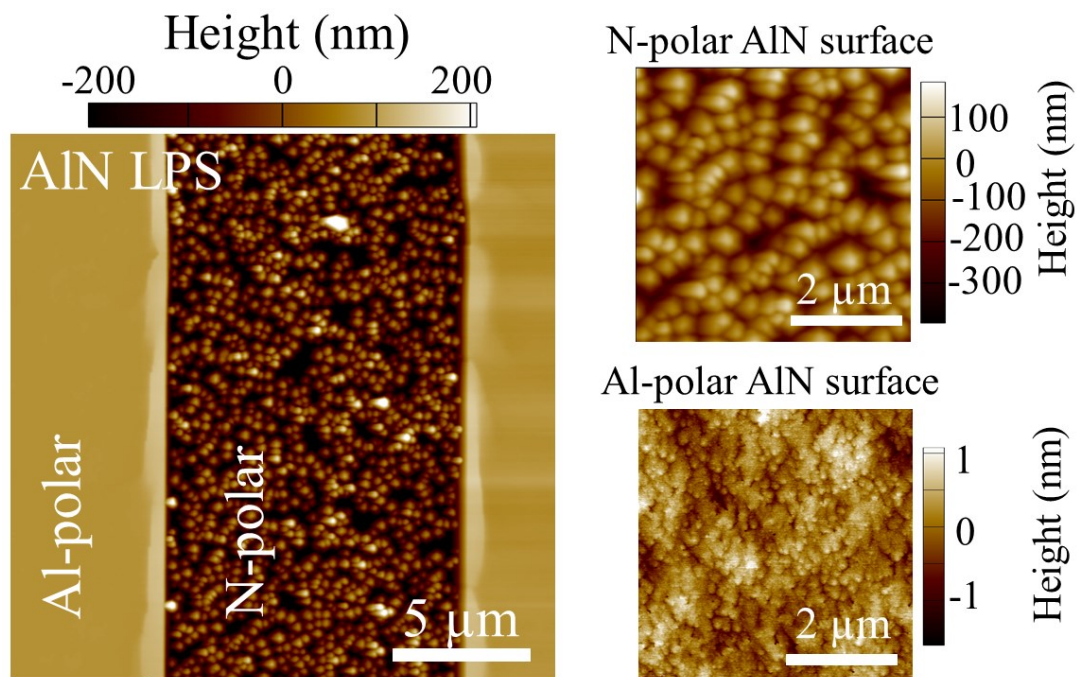


Figure 5-3: AFM image of a 20 μm periodic AlN lateral polar structure

An expanded view of the Al-polar domain (bottom right in *Figure 5-3*) shows a smooth surface with an RMS value of 0.3 nm, similar to that shown in *Figure 4-4*. In contrast a rough surface, exhibiting hexagonal hillocks is observed for the expanded view of the N-polar domain (top right in *Figure 5-3*), like the N-polar surface shown in *Figure 4-5*. To confirm the polarity of the respective domains, the samples were submerged in a 1 molar KOH solution in DI water at 70 °C. In *Figure 5-4*, DIC optical microscope images of a 100 μm periodic AlN LPS before and after 30 seconds of wet etching in KOH are presented for comparison.

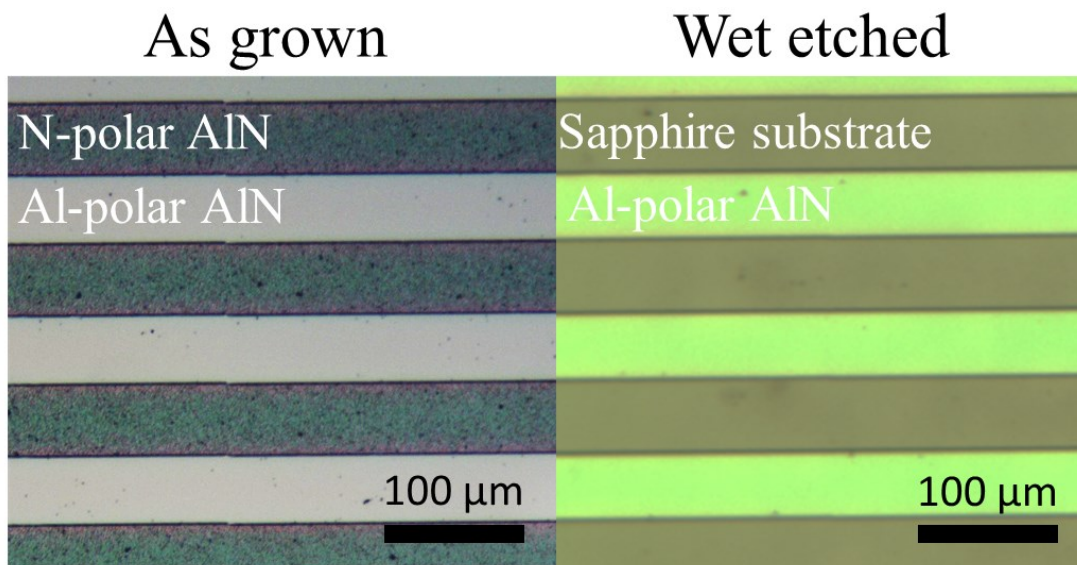


Figure 5-4: DIC optical microscope images of a 100 μm periodic AlN LPS as grown (left) and after wet etching for 30 seconds in 1M KOH at 70 °C.

In *Figure 5-4* the change in roughness at the N-polar regions, before and after etching is observed. The N-polar region seemingly becomes smooth after etching. This is due to the fact that the etch time was sufficient to remove the N-polar film and expose the smooth surface of the sapphire substrate as determined from cross section SEM measurements. For comparison SEM measurements of an AlN LPS before and after wet etching are shown in *Figure 5-5*. Note that the displayed images are taken from different patterned areas of the same sample.

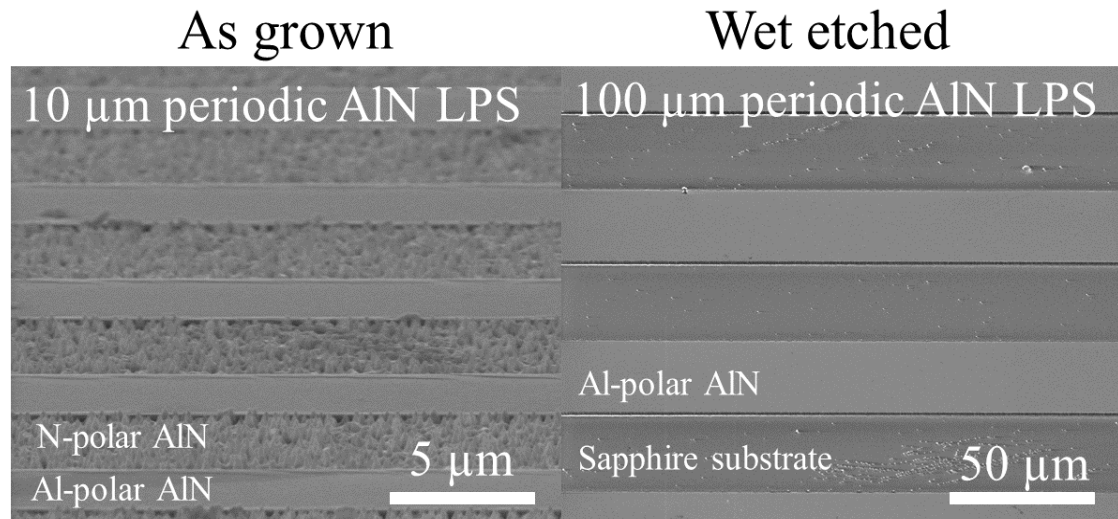


Figure 5-5: SEM images of a 10 μm periodic AlN LPS as grown (left). On the right a 100 μm periodic AlN LPS after wet etching in a 1M KOH solution in DI water at 70 $^{\circ}\text{C}$ for 30 s.

A more detailed inspection of the wet etched sample reveals that while the majority of the N-polar film has been removed, leaving a large area of exposed sapphire surface, a high density of hexagonally faceted pyramids of AlN domains remain on the surface (*Figure 5-6*). These features can be divided into two categories. A lower density of large pyramids with heights in the range between 300 - 500 nm and widths of 500 - 1000 nm, can be observed. Secondly, a higher density ($\sim 3 \times 10^9 \text{ cm}^{-2}$) of hexagonally faceted pyramids of significantly smaller size with heights ranging from 5 - 100 nm and widths between 50 nm and 200 nm remain on the surface.

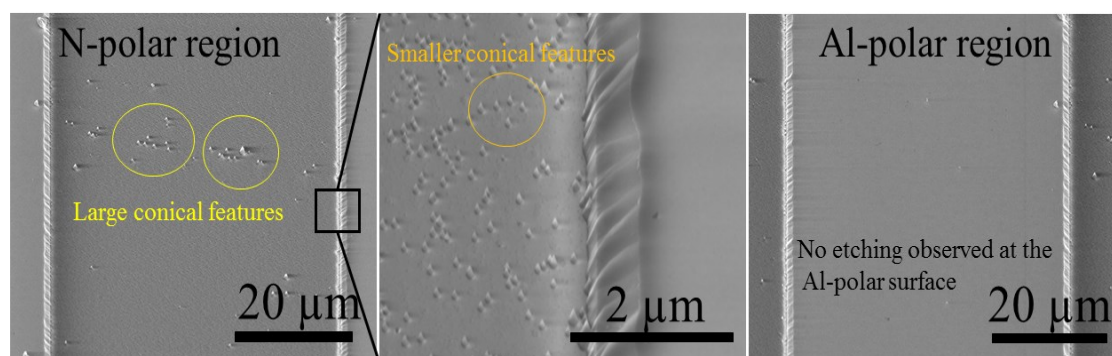


Figure 5-6: SEM measurements of a wet etched 100 μm periodic AlN LPS. (Left) The wet etched N-polar domain where the remaining low density of large conical features are highlighted. (Center) high magnification of the inversion domain boundary with highlighted high density of conical features.

The origin of the residue material is unclear. On one hand, a study by Guo et al., showed that wet etching the N-polar surface of PVT grown AlN single crystals, where no inversion domains are expected and have a low dislocation density ($\sim 10^3 -$

10^4 cm^{-2}), leads to a rough surface full of hexagonally faceted pyramids with a density $\sim 10^7 \text{ cm}^{-2}$, suggesting that the remaining residue is likely the result of an inhomogeneous etch rate.⁸⁷ However, the observed density of remaining hexagonally faceted features in *Figure 5-6* is two to three orders of magnitude higher than the density observed in the latter study. A more likely scenario based on a study by Hussey et al., is the presence of a high density of Al-polar inversion domains.⁸⁶ Through cross sectional high resolution TEM measurements on N-polar AlN samples in combination with low molarity KOH wet etching experiments, the study determined an inversion domains density $\sim 10^9 \text{ cm}^{-2}$, in agreement with the estimated density of the smaller features observed in this work. *Figure 5-7* shows a high magnification SEM image of a low molarity and short time wet-etched N-polar AlN domain, exhibiting vertically aligned AlN wires of varying widths between 5 – 40 nm located at the top of the hexagonally faceted pyramids.

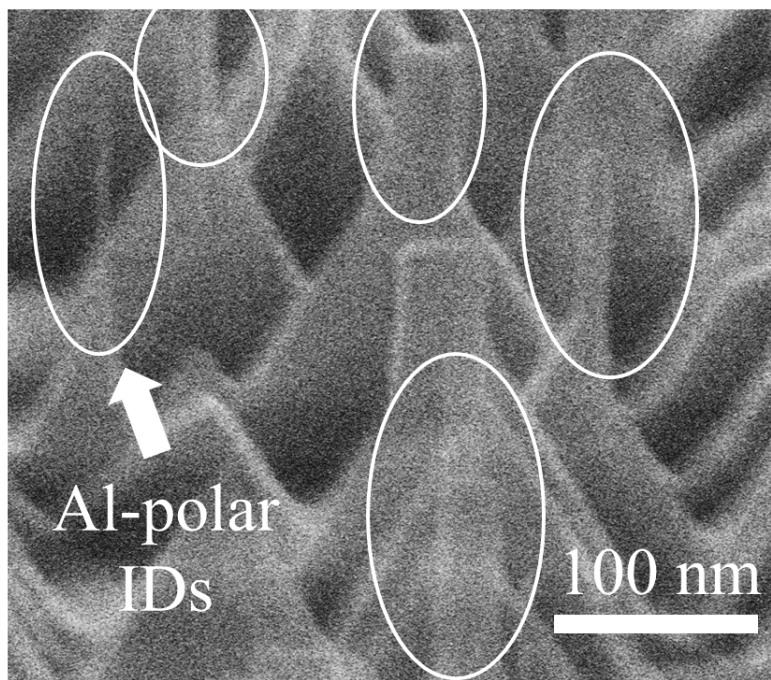


Figure 5-7: SEM image of a wet etched N-polar AlN film in a 0.5 M KOH solution in DI water for 20 s at 70 °C. The apparent Al-polar inversion domains are encircled.

The density of the vertically aligned AlN wires is estimated to be $\sim 3 \times 10^9 \text{ cm}^{-2}$ in agreement with the density measured by Hussey et al., as well as with the measured widths of the inversion domains. From these observations, a likely scenario is that the pyramidal shape of the base surrounding the Al-polar wires is given by the etching nature of N-polar AlN films as described by Guo et al., however, contrary to

the case of AlN single crystals, the hexagonal pyramids are pinned at their center by Al-polar inversion domains explaining the two to three orders of magnitude higher density observed. Note that such inversion domains have also been measured in N-polar GaN films on sapphire substrates.⁷⁵ Hussey et al. showed that regardless of the grown III-Nitride polarity, voids are formed at the sapphire surface into the sapphire substrate and suggest that these are formed during the H₂ and NH₃ annealing steps where H₂ participates in the sapphire decomposition. In addition the study shows that in both N-polar and Al-polar growth, these voids promote the growth of Al-polar domains, however the precise mechanism leading to Al-polar growth remains unexplained.

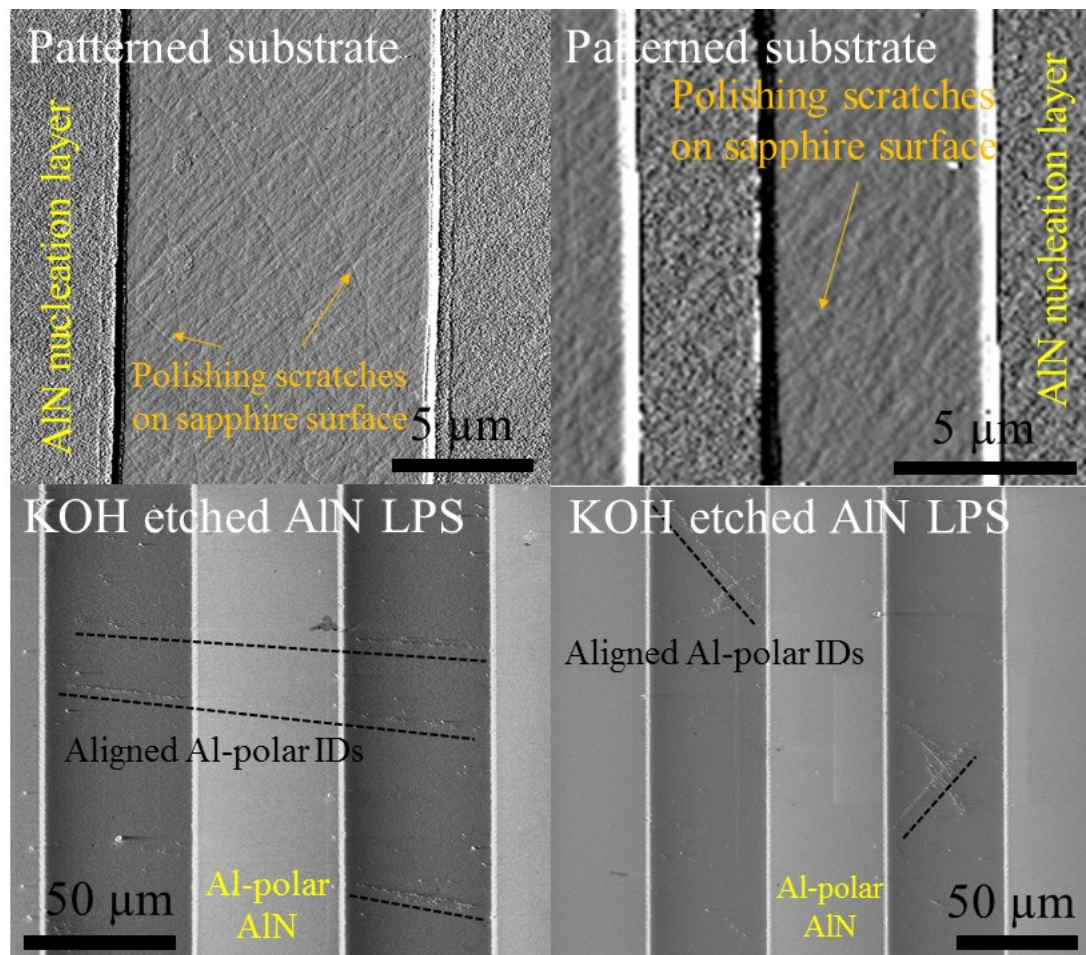


Figure 5-8: AFM amplitude images of the patterned AlN nucleation layer on a sapphire substrate prior to the growth of an AlN LPS (Top images). SEM images of wet etched AlN LPS showing a series of aligned Al-polar inversion domains in a similar pattern to the polishing scratches (Bottom images).

Takeuchi et al. has shown that a low density of large AlN hexagonal pyramids may remain on the sapphire surface even after prolonged wet etching in 10% wt. KOH

solution in DI water at 60 °C and attributes them to Al-polar inversion domains that may originate from residual polishing scratches on the as received sapphire substrates.⁹⁵ The top images in *Figure 5-8* display two different patterned AlN nucleation layers deposited on sapphire substrates, where the sapphire surface with residual polishing scratches can be observed. The bottom images are 60° tilted SEM measurements of a wet etched AlN LPS sample where rows of aligned Al-polar IDs in the N-polar domains are highlighted. In particular, two rows of aligned Al-polar IDs continue after crossing an entire Al-polar domain (bottom left image in *Figure 5-8*), indicating that the IDs originate from residual polishing scratches in agreement with the conclusion made by Takeuchi et al. An SEM image of the large IDs related to residual polishing scratches is presented in *Figure 5-9*, showing that vertical AlN wires extending from the top of the hexagonal pyramids are also present. A possible explanation is that the residual polishing scratches act as voids, similarly to decomposed sapphire, and promote Al-polar growth as suggested by Hussey et al.⁸⁶

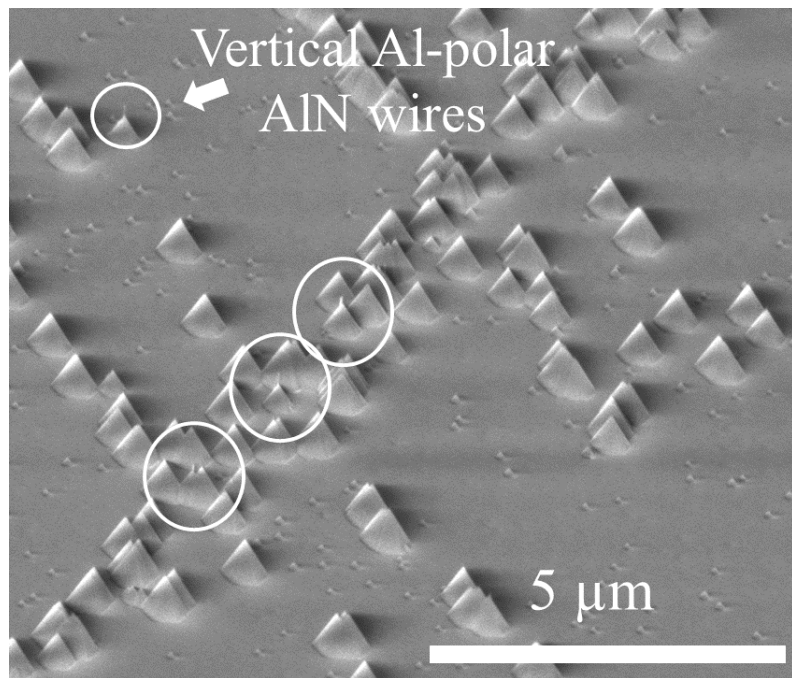


Figure 5-9: SEM image displaying a magnified view of the residual hexagonal pyramids after wet etching. Vertical AlN wires located at the top of the hexagonal pyramids are highlighted.

In summary, AlN LPS can be obtained using the process described in this section. Uniform Al-polar growth of AlN is obtained in the regions where an AlN nucleation layer remained. Predominantly N-polar growth can be achieved in the areas where the sapphire surface is exposed, however a density $\sim 10^9$ cm⁻² of Al-polar inversion

domains is estimated. The inversion domains are measured to be 5 – 40 nm in diameter. Assuming a 10 nm diameter average of the Al-polar inversion domains, this corresponds to <1% of the material volume which is not expected to significantly decrease the conversion efficiency in quasi-phase matching. Nevertheless, a detailed study on the influence of H₂ and NH₃ annealing in the decomposition of sapphire and how they promote Al-polar growth, is necessary for developing a process to achieve a reduced density of Al-polar inversion domains in N-polar AlN films. Finally, it is critical that the starting surface of the sapphire substrate is epi-ready, free of any residual polishing scratches, to minimize the density of Al-polar inversion domains in the N-polar AlN regions.

5.1.1 Nanometer Scale AlN Lateral Polar Structures

For frequency doubling of laser light into the UV spectral range via quasi-phase matching using AlN lateral polar structures, domain sizes in the nanometer scale are necessary. The coherence length (see section 2.1.4) in bulk material can be calculated with

$$l_c = \frac{\pi}{\Delta k} = \frac{\lambda_0}{4(n_{2\omega_0} - n_{\omega_0})}, \quad (5.1.1)$$

and is presented in *Figure 5-10* as a function of the fundamental wavelength, where the Sellmeier dispersion relation coefficients were taken from the literature.⁹⁶ It can be observed that for frequency doubling from 530 nm to 265 nm in bulk AlN, the coherence length is 645 nm, setting the periodicity of the required AlN LPS at 1.3 μm to achieve 1st order QPM.

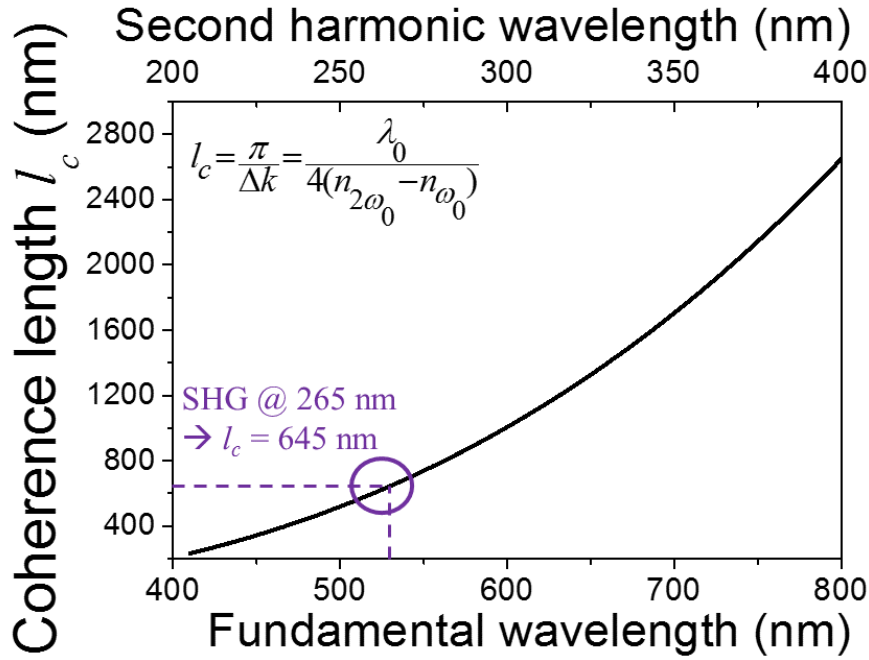


Figure 5-10: Calculated coherence length in bulk AlN single crystal as a function of fundamental (driving) wavelength.

Figure 5-10 gives an idea of the required periodicities for QPM in bulk AlN, however as discussed in section 2.1.4, when using waveguide structures, the propagation of TM modes need to be considered which lead to slightly different periodicities for 1st order QPM structures. The condition determined in section 2.1.4

$\left(\Delta K = 2\beta_{\omega_0}^r - \beta_{\omega}^s + \frac{2\pi m}{\Lambda} \equiv 0 \right)$ can be rearranged to the form

$$n_{\omega_0}^{r,eff} = n_{\omega}^{s,eff} - \frac{m\lambda_{\omega_0}}{2\Lambda}, \quad (5.1.2)$$

where $n_{\omega_0}^{r,eff} = \frac{\beta_{\omega_0}^r}{k_{\omega_0}}$ and $n_{\omega}^{s,eff} = \frac{\beta_{\omega}^s}{k_{\omega}}$ are the effective refractive index of the rth mode of the fundamental (driving) wave and the sth mode of the second harmonic wave. λ_{ω_0} , k_{ω_0} and k_{ω} are the vacuum wavelength and wave vectors for the respective wave frequencies ω_0 and ω . Using a Wolfram Mathematica code, both sides of equation (5.1.2) were plotted for a given waveguide dimension (Figure 5-11). In Figure 5-11 only the 0th TM modes for both driving and second harmonic waves were considered, the QPM order was set to $m=1$ and a 550 nm thick AlN LPS waveguide with 1.2 μm periodicity was assumed.

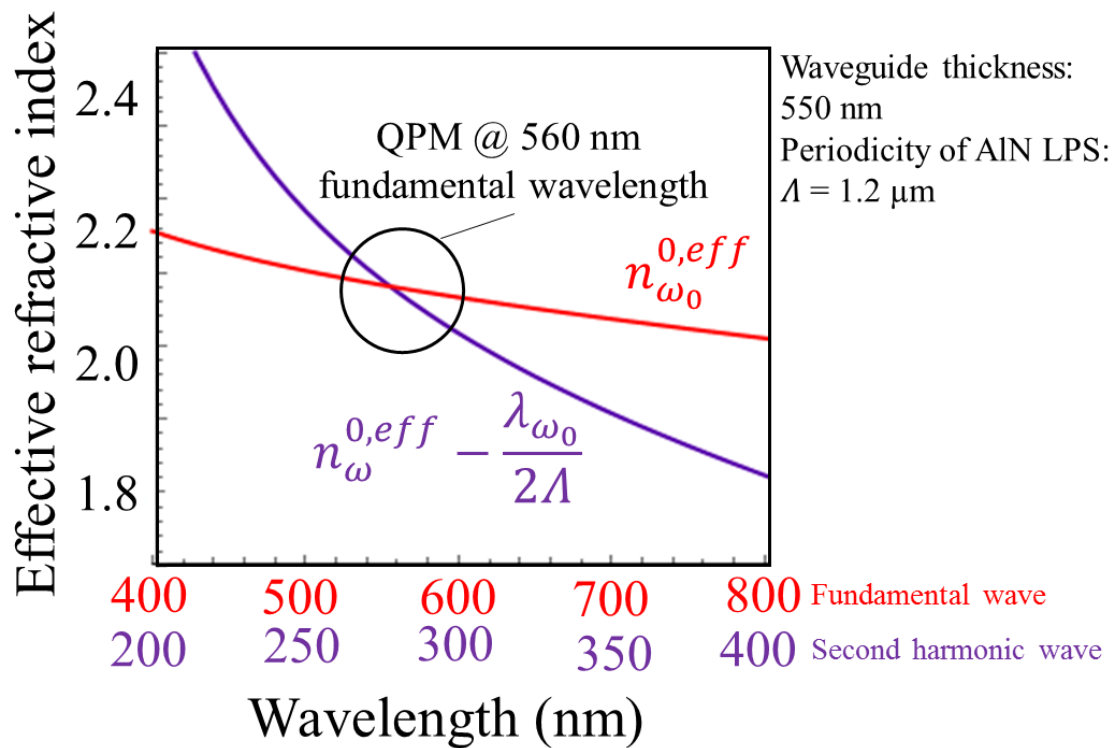


Figure 5-11: Both sides of equation (5.1.2) are plotted. In red, the effective refractive index for the 0th order mode of the fundamental wave. In purple, the effective refractive index for the 0th order mode of the second harmonic wave reduced a term given by the periodicity of the AlN LPS with $\Lambda = 1.2 \mu\text{m}$.

Standard, available, masked photolithography is limited to features in the order of $2 \mu\text{m}$ in size, making other patterning techniques necessary to achieve the periodicities required for QPM SHG in the UV-C spectral range. For this reason a novel process is developed, which uses laser interference lithography in combination with the previously established polarity control process scheme, to achieve sub-micrometer periodically poled AlN lateral polar structures (LPS) (Figure 5-12).

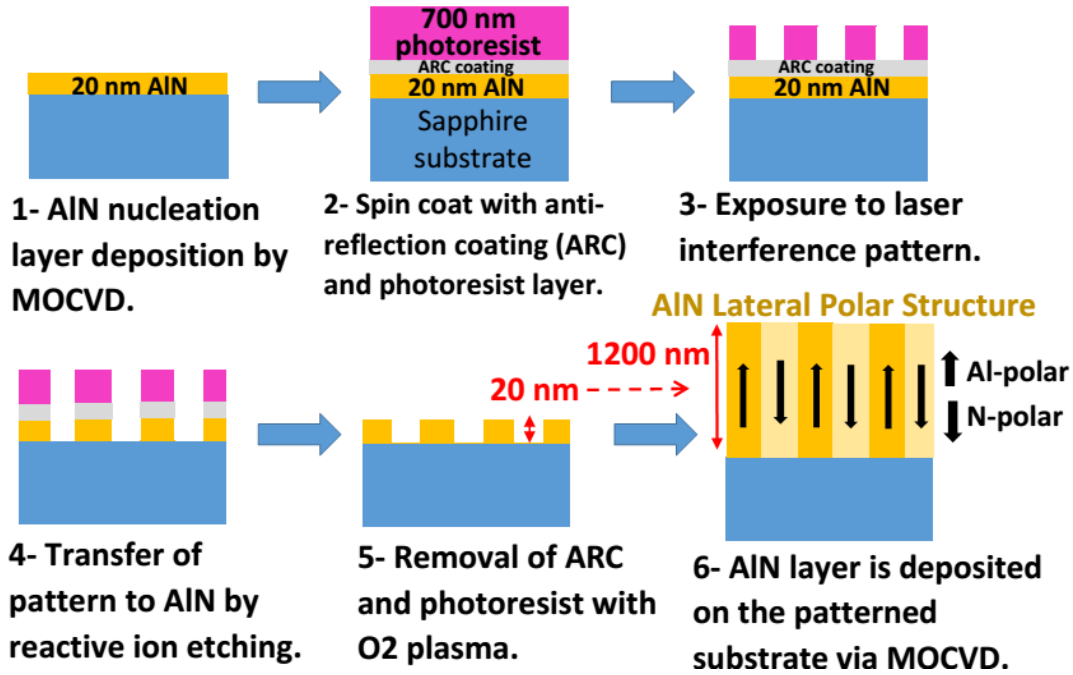


Figure 5-12: Nanoscale polarity control process scheme. Step 1: MOCVD deposition of AIN nucleation layer on c-plane sapphire. Step 2: Photoresist and ARC are spin coated onto the substrate. Step 3: Photoresist layer is exposed to the laser interference periodic pattern and developed. Step 4: Pattern is transferred to the AIN nucleation layer by reactive ion etching. Step 5: The residual photoresist and ARC are removed by O₂ plasma. Step 6: The patterned substrate is reinserted in the MOCVD chamber, where the AIN film is deposited leading to the AIN periodic lateral polar structure.⁹⁷

A low temperature nucleation layer as described in section 4.2 is deposited on an LED-quality c-plane sapphire substrate with 0.2° offcut towards the sapphire m-plane. The substrate is then removed from the reactor and spin-coated with a 100 nm thick anti-reflection coating (Brewer Science i-CON-16, $n=1.72-0.04j$) and a 630 nm thick photoresist layer (Sumitomo PFI-88). The laser interference pattern is obtained using a Lloyd's mirror configuration setup (section 3.3), developed by Bagal et al.⁹⁸, resulting in a highly periodic sub-micrometer pattern across the entire substrate. A He-Cd laser focused onto a pinhole is used as a monochromatic point light source. The sample is placed adjacent to a fixed mirror at a 90° angle, acting as the second light source with the same incidence angle θ . The periodicity, Λ , of the interference pattern is then defined by the angle of incidence θ with respect to the normal of the sample, the wavelength λ of the light source and the refractive index n of the medium as follows:

$$\Lambda = \frac{\lambda}{2n \sin \theta} \quad (5.1.3)$$

From this relation, the refractive index of air being $n=1$ and the wavelength of the laser $\lambda = 325 \text{ nm}$, the angle of incidence to achieve a $1.2 \mu\text{m}$ periodicity (necessary for 1st order quasi phase matching at 280 nm) can be calculated, which $\theta = 7.78^\circ$. The sample was exposed to a total energy of 47 mJ and was developed for 1 minute (*Figure 5-13*).

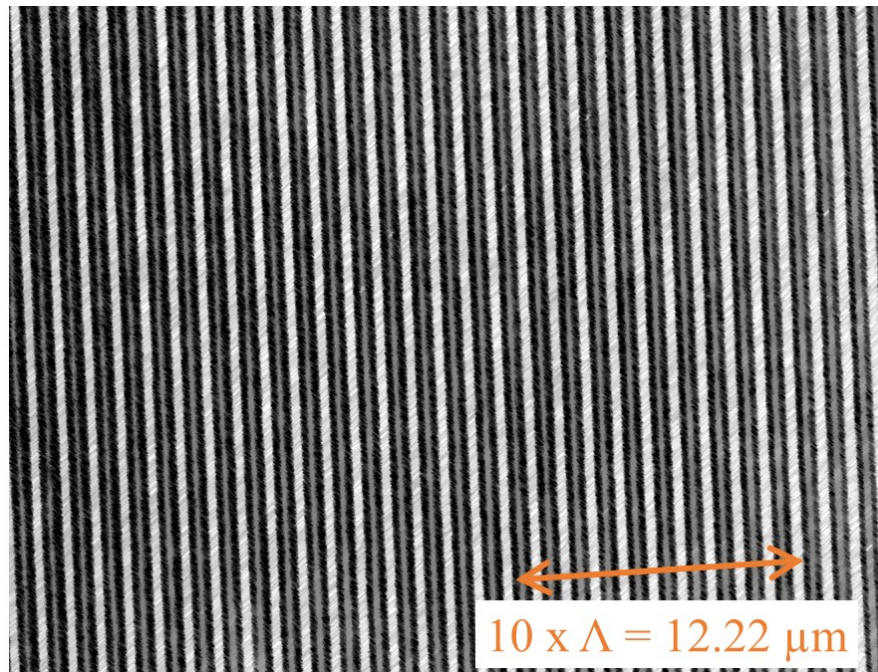


Figure 5-13: Differential interference contrast optical microscope image of $1.2 \mu\text{m}$ periodic pattern of the photoresist layer.

In addition to the standing wave intensity profile along the sample surface, a standing wave normal to the sample surface is created which deteriorates the sidewall profile of the exposed photoresist layer.⁹⁹ To suppress the vertical standing wave and achieve vertical sidewalls of the patterned photoresist, an additional layer between the sample and the photoresist layer is introduced typically addressed as the anti-reflection coating (ARC) layer. The purpose of the ARC layer, is to suppress the vertical standing wave by destructive interference between the reflected light at the sample-ARC interface and the reflection at the ARC-photoresist interface. For more details on types of ARC layers and their working principle, refer to the dissertation of M. Walsh.⁹⁹ In this work, a computer program, which considers the complete layer stack and their respective refractive indices (substrate, thin film, ARC, photoresist and air), is used to calculate the ARC thickness which will lead to

the maximum suppression of the vertical standing wave (see *Figure 5-14*). From the program, the optimal ARC thickness of 100 nm was obtained.

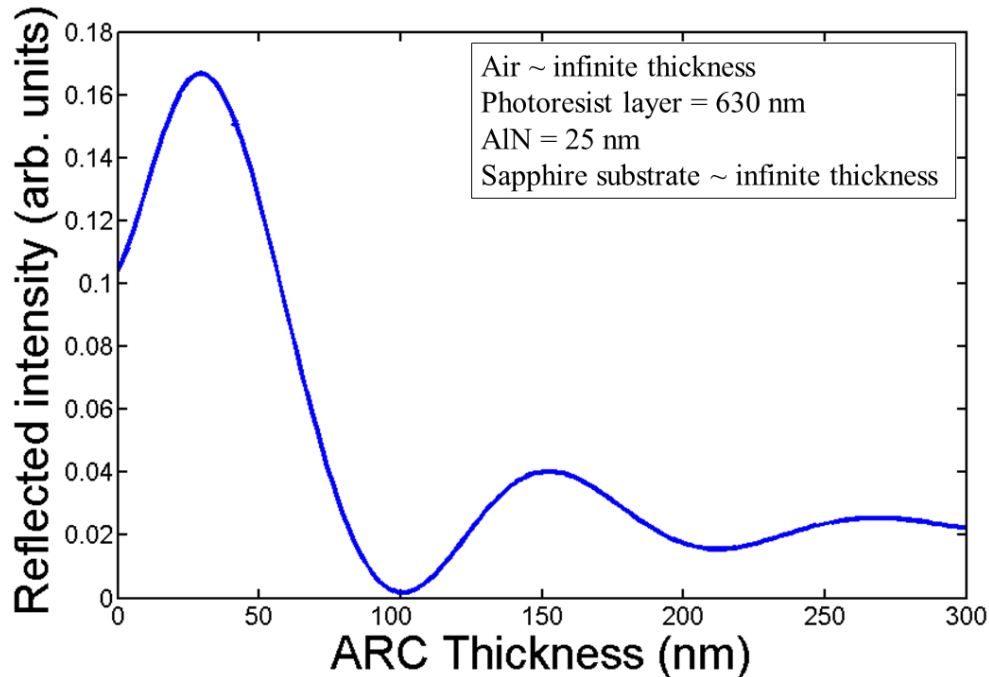


Figure 5-14: Reflected intensity at the ARC-photoresist interface as a function of ARC thickness.

The patterned obtained from developing the exposed photoresist layer is transferred to the ARC layer and then to the epitaxial layer in a two-step reactive ion etching (RIE) process. First the sample is introduced in a “Semigroup 1000TP” RIE system and is exposed to an anisotropic oxygen plasma for 3 minutes at an RF power of 54 W, in 30 sccm of O₂ flow and 30 mTorr total pressure. In a second step, the pattern is transferred to the III-Nitride epitaxial layer by RIE using the same conditions as described in the previous section (5.1). The remaining photoresist residue was then removed using heated NMP, followed by isotropic O₂ plasma. An AFM image, displaying such a patterned substrate is displayed in (*Figure 5-15*).

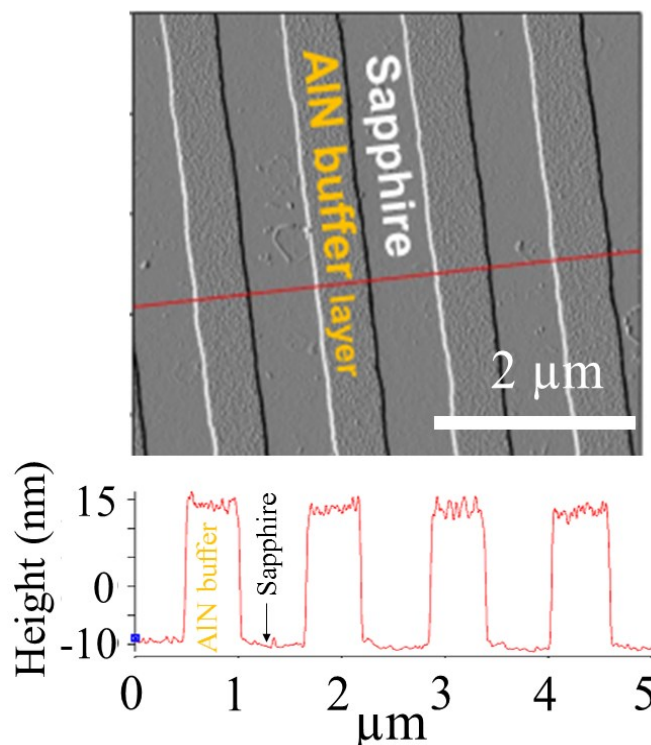


Figure 5-15: Atomic force microscopy image and height profile line scan of the patterned substrate, displaying domains of 25 nm thick AlN layers and domains with the sapphire substrate exposed.

The patterned substrate is then placed in the reactor and the AlN lateral polar structures are grown according to the procedure described in the previous section, where both polarities grow simultaneously. AFM images of a patterned substrate before and after the AlN film deposition are shown next to each other in Figure 5-16. Alternating stripes of low temperature AlN nucleation layer and bare sapphire substrate can be observed in *Figure 5-16* (left). *Figure 5-16* (right) shows an AFM image of the surface of an AlN film deposited on the patterned substrate. Two different domains of similar width to the initial pattern are observed and identified as Al- and N-polar domains from their characteristic surface morphology. The surface morphology for the Al-polar domains is smooth with a surface roughness RMS value of 0.3 nm, while columnar hexagonal structures are observed for the N-polar AlN with surface roughness RMS values in the order of 30 nm, which are typical surface morphologies for the respective polarities at these growth conditions.⁹³ The IDB between the Al- and N-polar domains is well defined and parallels the shape of the patterned AlN nucleation layer, which demonstrates the ability to control the polarity of the AlN layer down to the sub-micron regime using laser interference lithography.

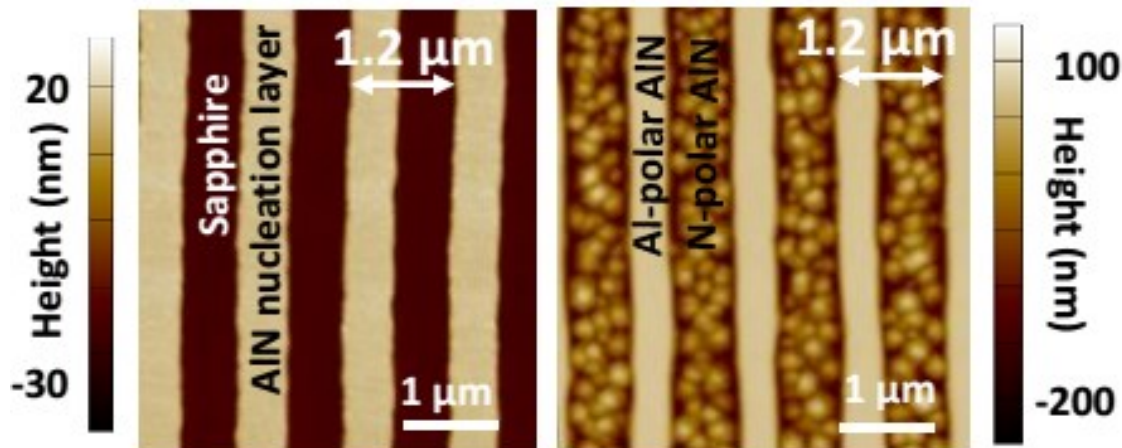


Figure 5-16: Height profile AFM images of the patterned substrate before (left) and after the AlN thin film growth (right). In the right image, domains with a rough hexagonal columnar surface, characteristic of the N-polar domain, is observed as well domains with a smooth (sub-nanometer RMS roughness) Al-polar surface with similar domain sizes as the patterned substrate, pointing at the vertical inversion domain boundaries.

To unambiguously identify the Al-polar and N-polar domains, KOH etching and subsequent SEM characterization were performed (*Figure 5-17*). The figure shows tilted cross-section SEM images of the AlN LPS film as grown (a) and the same sample after etching in a 1M KOH solution in deionized water for 1 minute at 70°C. For the wet etched sample, the N-polar domains were completely removed while the Al-polar domains remained unchanged, thereby confirming the polarity of the respective domains. Some lateral etching is observed at the Al-polar domains, however no vertical top-down etching is observed.

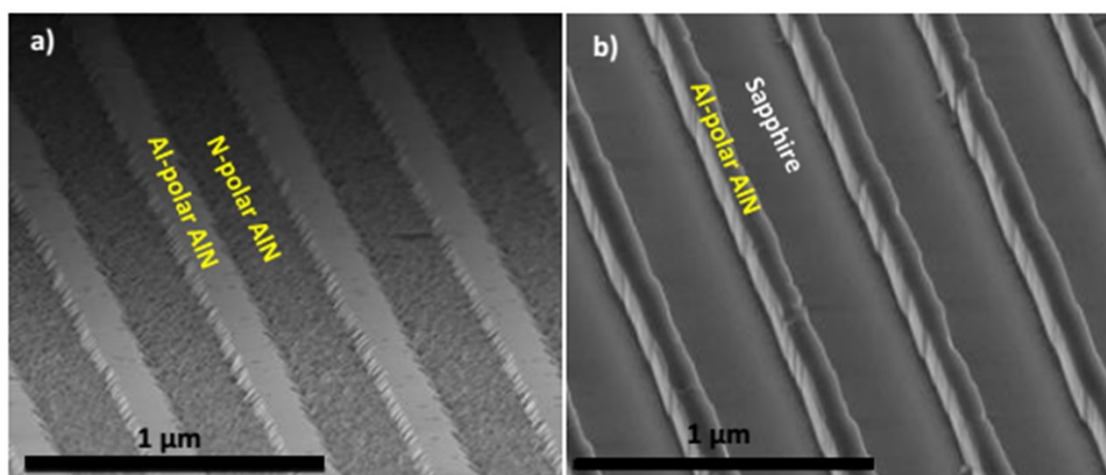


Figure 5-17: Tilted view SEM image of the AlN LPS as grown (a) and after being submerged in a 1 molar KOH solution in deionized water for 1 minute at 70 °C (b).

In a growth series, the deposition times were varied, to determine if there is mass transport between the polar domains leading to an increased deposition rate of one polarity over the other, and to establish if polarity overgrowth takes place at these growth conditions. From cross-section secondary electron microscopy (SEM) images (*Figure 5-18*), taken in a “Verios 460 L FEI system”, equal growth rate for both polarities is determined and vertical growth with no polarity overgrowth is observed. More significantly, fully coalesced inversion domain boundaries are observed, essential for the propagation of light, since any air gaps at the interface will lead to large scattering losses and/or reflection at each IDB inhibiting their use for second harmonic generation of laser light. The 20-30 nm patterned low temperature AlN nucleation layer can also be observed, which as expected, is present directly below the plateaus of the Al-polar domains.

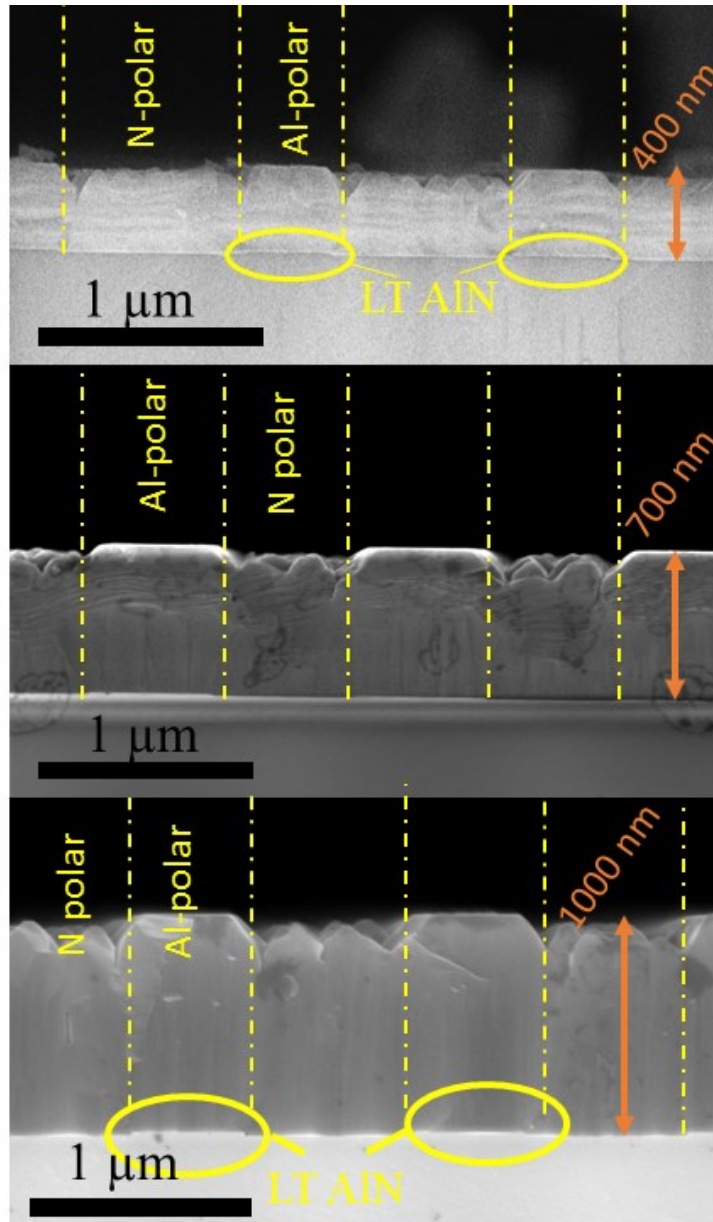


Figure 5-18: Cross-sectional SEM images of AlN LPS samples with varying thicknesses. The inversion domain boundaries are highlighted with yellow dashed lines. Complete coalescence at the IDBs is observed.

Using laser interference lithography well defined polarity control is demonstrated down to 600 nm domain sizes with fully coalesced inversion domain interfaces and equal growth rates for both polarities. However, scattering losses at the surface roughness remains a concern, particularly at the N-polar AlN surface. For QPM SHG, the excitation and second harmonic light will travel in the AlN waveguides and scattering losses will depend on surface roughness. Scattering losses due to random deviations at the waveguide boundaries have been investigated in detail.^{46,100} Under the Rayleigh criterion, a surface may be considered as optically smooth for

$$\sigma_s < \frac{\lambda}{8\cos(\theta)}, \quad (5.1.4)$$

where σ_s is the RMS surface roughness, λ is the wavelength in the material and θ the angle of incidence with respect to the surface normal. When considering the propagation of TM modes in AlN LPS-based waveguides, every mode r will have a corresponding angle of incidence θ_r and is related to the mode's propagation constant value β_ω^r by

$$\beta_\omega^r = kn_\omega \sin(\theta_r), \quad (5.1.5)$$

where k and n_ω are the vacuum wave vector and the refractive index of AlN at frequency ω respectively. The propagation constant values β_ω^r are obtained by graphically solving equation (2.1.27) as described in section 2.1.2. Considering an RMS surface roughness value of 30 nm (typical measured value for AlN LPS), a 650 nm thick waveguide and utilizing the method described by Tien et al.,⁴⁶ the calculated attenuation coefficient per unit length α_r at 550 nm wavelength for the 0th order TM mode is 102 cm⁻¹. It is clear that the scattering losses for such a surface roughness will not allow efficient propagation of the driving and second harmonic waves along the waveguide and thus efficient QPM SHG of UV laser light. Hence, it is necessary to reduce the surface roughness of the AlN LPS. One possible solution is to reduce the surface roughness by mechanical polishing. *Figure 5-19* displays an AFM image of a 1.2 μm periodic AlN LPS before and after mechanical polishing. Alumina particles of 0.3 μm in size dissolved in DI water were used as a polishing vehicle squirted on a "TexMet P" soft pad platform. The mechanically polished samples showed significantly improved RMS surface roughness values of 10-15 nm. Further reduction of the roughness seemed challenging as longer polishing times did not lead to further improvement. This may have been related to the polarity-dependent etching due to the pH of the polishing vehicle. However a more detailed study on mechanical polishing using various particle sizes and materials as well as different pH solutions may lead to further improvements of the surface roughness.

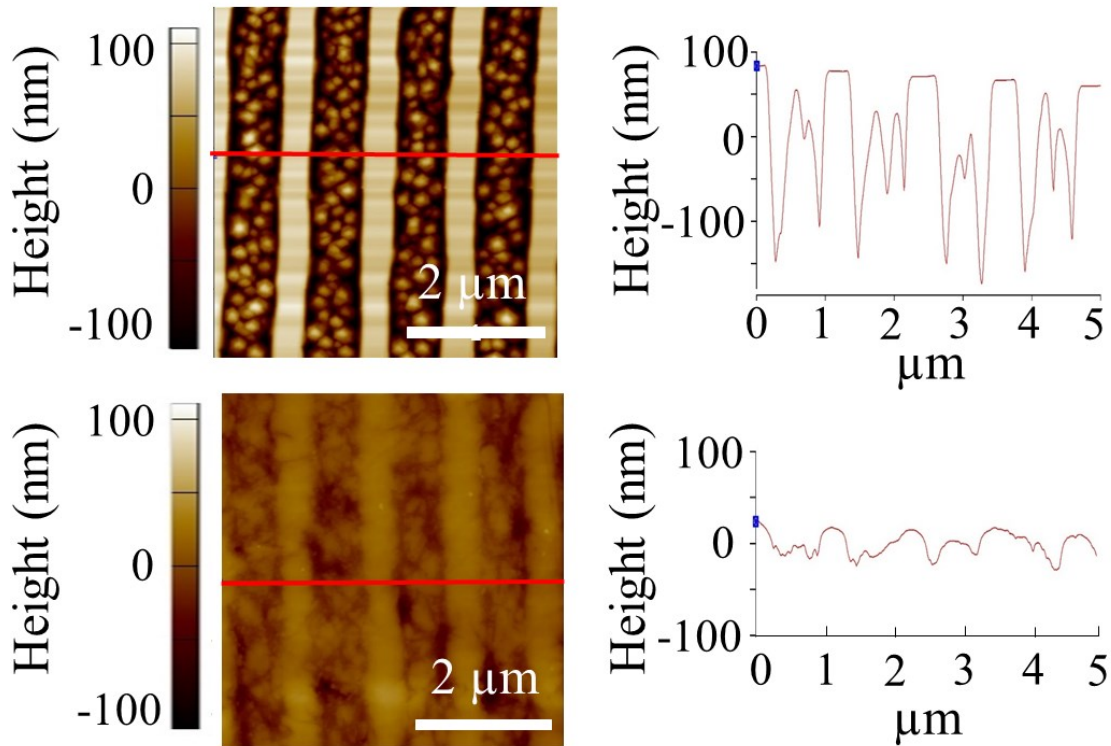


Figure 5-19: AFM image of a 1.2 μm periodic AlN LPS before (top left) and after (bottom left) mechanical polishing with comparable sclaes. The respective height profile linescans across the periodic structure are shown on the top right and bottom right.

Nevertheless, the achieved RMS roughness values of 10 nm lead to a calculated attenuation coefficient value, α_r , for the 0th order TM mode of 11 cm⁻¹ at 550 nm wavelength and 6 cm⁻¹ for the SHG wave at 275 nm. These values predict that the fabricated AlN LPS are suitable for SHG in the UVC spectrum [1] [2].

Waveguides were etched into a mechanically polished AlN LPS sample using standard masked photolithography and RIE, to test the AlN LPS for second harmonic generation. For this, a 3 μm thick negative photoresist (NFR 016 D2) layer was spin coated onto the sample and exposed to 110 mJ of UV light. After light exposure the sample was submerged in MF-319 developer for 1 min. The sample was subsequently placed on a 90 °C hot plate for 10 min to harden the photoresist. Following, the pattern is transferred to the AlN LPS by RIE for 50 minutes with 2.5 minutes of pause in between 2.5 minutes of etch time to avoid overheating of the photoresist, and using the same etching conditions as for the low temperature AlN nucleation layer (described in section 5.1).

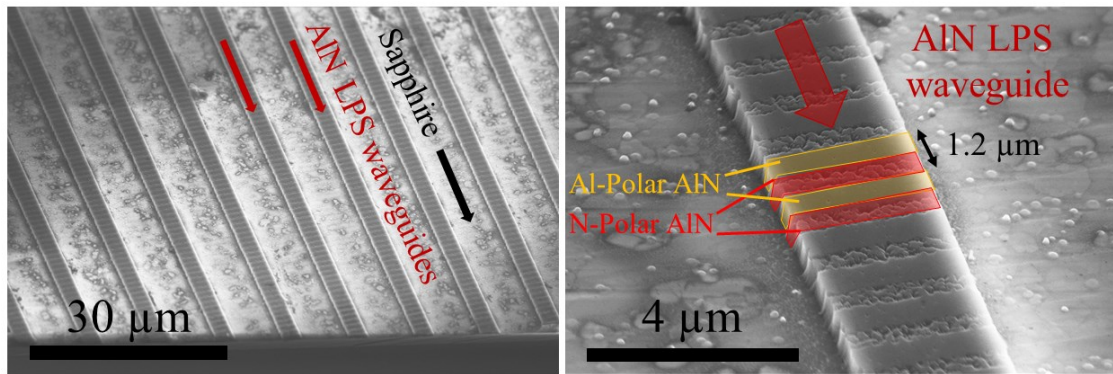


Figure 5-20: SEM images showing the AlN LPS-based waveguides at a low (left) and high (right) magnification respectively..

These waveguides were tested for QPM SHG, where more details are presented in section 7.2.2.

5.1.2 Promoting Step Flow Growth through Control of Al Vapor Supersaturation

An alternative to mechanical polishing for reducing the surface roughness of the AlN LPS is to promote step flow growth for both AlN polarities. The Burton, Cabrera and Frank (BCF) theory of crystal growth has been used to describe the growth kinetics leading to distinct surface morphologies of prominent epitaxial semiconductor materials.^{51–53,55,101} In epitaxial N-polar GaN thin films a high density of hexagonal hillocks are frequently observed. The formation of hillocks in GaN can be suppressed by promoting step flow growth. In general, this is achieved by decreasing the surface supersaturation σ_s below a critical value σ_s^* as described in section 2.2.^{52,53,55,101} Studies have demonstrated the growth of smooth N-polar GaN thin films by MOCVD either by increasing the off-cut angle of the substrate with respect to the (0001) sapphire plane, substituting the nitrogen diluent gas with hydrogen or increasing the V/III ratio of the precursors under nitrogen diluent gas, all resulting in a reduced surface supersaturation σ_s directly or indirectly through a reduction of the vapor phase supersaturation σ .^{101–104} In analogy to previous work done on N-polar GaN, the vapor phase supersaturation is reduced in order to promote step flow growth at the N-polar surface of the AlN thin films. For this, a growth series was conducted where the Al vapor supersaturation σ was decreased step wise by increasing the growth temperature (*Figure 5-21*).

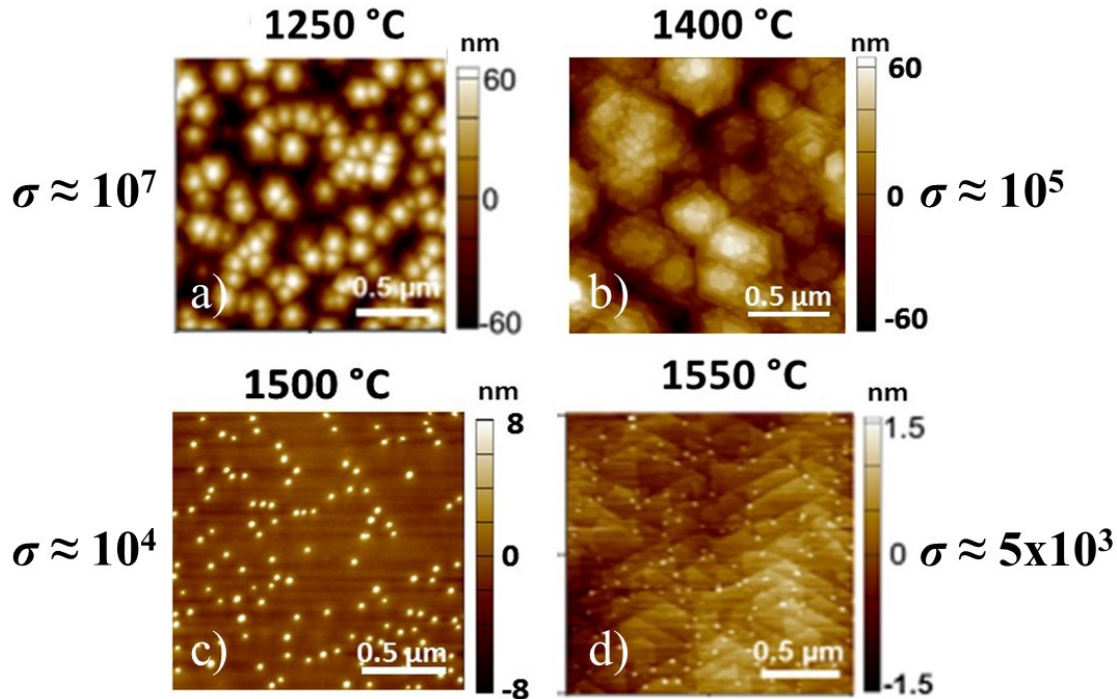


Figure 5-21: Surface morphology of N-polar AlN thin films grown at different temperatures. The growth temperatures for the displayed samples is 1250 °C, 1400 °C, 1500 °C and 1550 °C for a)-d) respectively.

For the sample grown at the highest vapor supersaturation (1250 °C), the typical rough surface morphology exhibiting a high density of hexagonal hillocks is observed. As the vapor supersaturation is decreased, the hillock aspect ratio decreases as well as the surface roughness RMS value (22 nm at 1400 °C). Also the AlN nuclei increase in size and decrease in density, and step terraces become resolvable with AFM (Figure 5-21-b)), indicating a mixed growth mode of step flow and 2D nucleation. Further decreasing the surface supersaturation, results in a drastic decrease of the RMS surface roughness value to 1.6 nm. Interestingly, 30-50 nm wide and ~10 nm tall columns with a density of $\sim 3 \times 10^9 \text{ cm}^{-2}$ can be observed (Figure 5-21-c)) in agreement with the previously established density of Al-polar inversion domains in epitaxial N-polar films (section 5.1). For the regions in between the columns, the surface roughness is below 1 nm indicating step flow growth. Finally, the N-polar film grown at the lowest vapor supersaturation (Figure 5-21-d)), clearly displays step flow growth, where the surface roughness RMS value is measured to be 0.5 nm. Here a density of $\sim 3 \times 10^9 \text{ cm}^{-2}$ of the 30-50 nm diameter wide columns can also be observed, however their height only ranges from 0.5 nm to 1 nm.

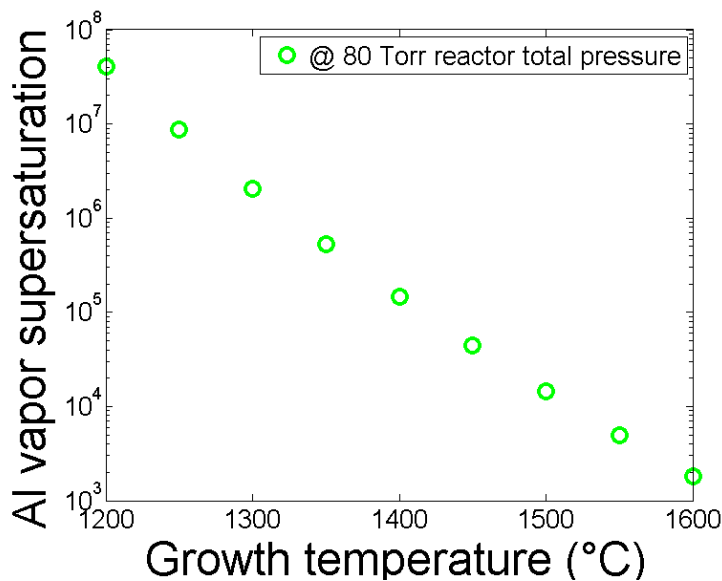


Figure 5-22: Al vapor supersaturation as a function of growth temperature

From these observations, the estimated Al vapor supersaturation necessary for step flow growth of N-polar AlN is $\sim 10^4$ or lower. Note that the critical surface supersaturation will depend on the surface diffusion length of the adatoms. In this temperature range, the diffusion length is expected to decrease with temperature. Since we observe a transition from 2D nucleation to step flow growth with increasing temperature, it is evident that the vapor supersaturation plays a dominating role. Also, the calculated Al vapor supersaturation values (*Figure 5-22*) do not include pre-reaction or other transport losses specific to the reactor design and represent the maximum expected vapor supersaturation values. It is more likely that the critical surface supersaturation is actually lower than the estimated value from the calculated Al vapor supersaturation values, because pre-reaction losses of TMA are significant in AlN MOCVD growth, as can be seen in *Figure 5-23*. As determined in section 2.2, the surface supersaturation is directly proportional to the growth rate (see equation (2.2.20)), thus from *Figure 5-24*, where an increase in the total reactor pressure is expected to lead to a higher Al vapor supersaturation, but actually a reduced growth rate is measured (*Figure 5-23*), it is clear that the vapor-phase reaction of TMA is significant and leads to a lower surface supersaturation than the calculated Al vapor supersaturation, since in the mass transport limited regime, the growth rate is not expected to change if the TMA flow is kept constant. *Figure 5-23* shows that at 1250 °C growth temperature, varying the total reactor pressure from 20 Torr to 80 Torr and otherwise maintaining equal growth

parameters, results in a decreased growth rate by a factor of $\frac{1}{2}$. Similar observations have been reported in the literature, where vapor-phase pre-reaction between TMA and NH_3 are studied.^{105–107}

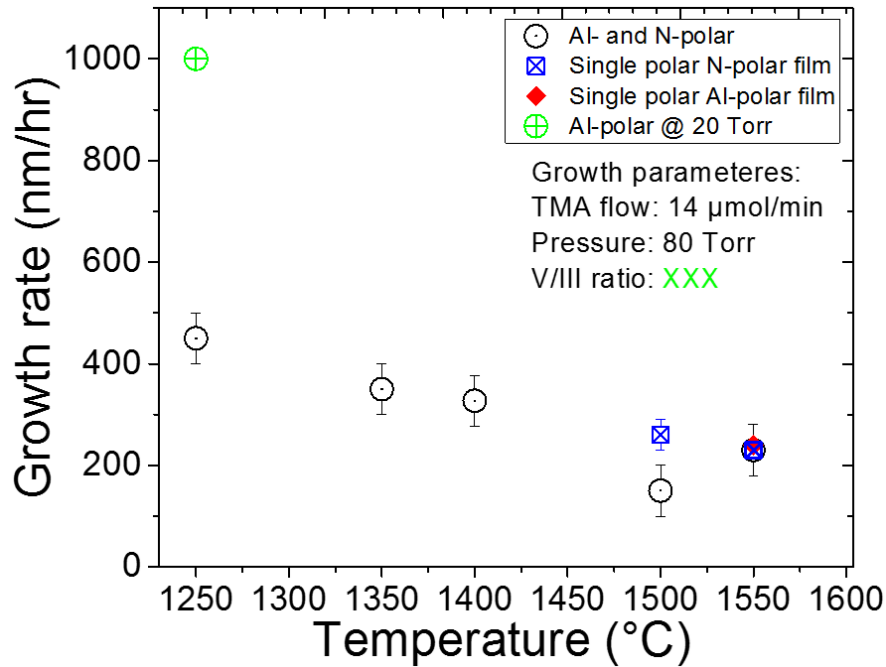


Figure 5-23: Temperature and pressure dependence of measured growth rates for Al- and N-polar AlN epitaxial films.

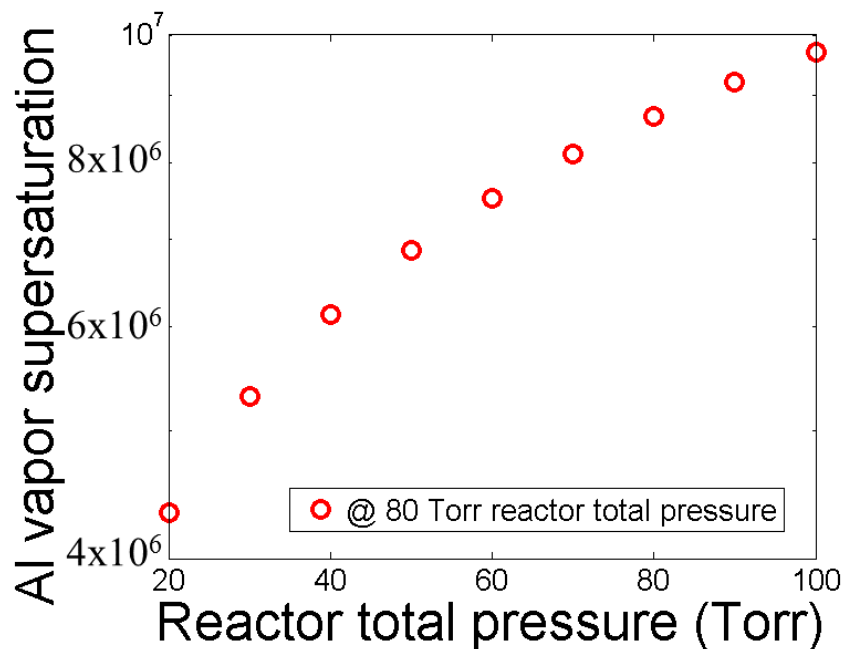


Figure 5-24: Al vapor supersaturation as a function of total pressure inside the growth chamber.

Also, increasing the temperature from 1250 °C to 1550 °C resulted in a decreased growth rate by an additional factor of $\frac{1}{2}$, reflecting the temperature dependence of the pre-reaction of NH₃ with TMA.

In summary, step flow growth of N-polar AlN can be achieved by decreasing the Al vapor supersaturation, where the critical surface supersaturation σ_s^* is estimated to be $<10^4$ at a growth temperature of 1500 °C. The surface roughness RMS value is reduced by two orders of magnitude from 50 nm to 0.5 nm. In addition, a pressure dependent vapor-phase reaction between NH₃ and TMA is measured where an increase from 20 Torr to 80 Torr leads to a decrease in growth rate by a factor of $\frac{1}{2}$. Similarly at 80 Torr reactor pressure, the vapor-phase reaction of TMA with NH₃ is measured to be dependent on temperature, where an increase from 1250 °C to 1550 °C leads to a decrease in growth rate by a factor of $\frac{1}{2}$.

5.1.3 Mass Transport between Polar Domains

Having achieved step flow growth for N-polar AlN at low supersaturation values, a growth series was conducted where the supersaturation was stepwise decreased, through increasing the growth temperature, to achieve smooth AlN LPS (*Figure 5-25*).

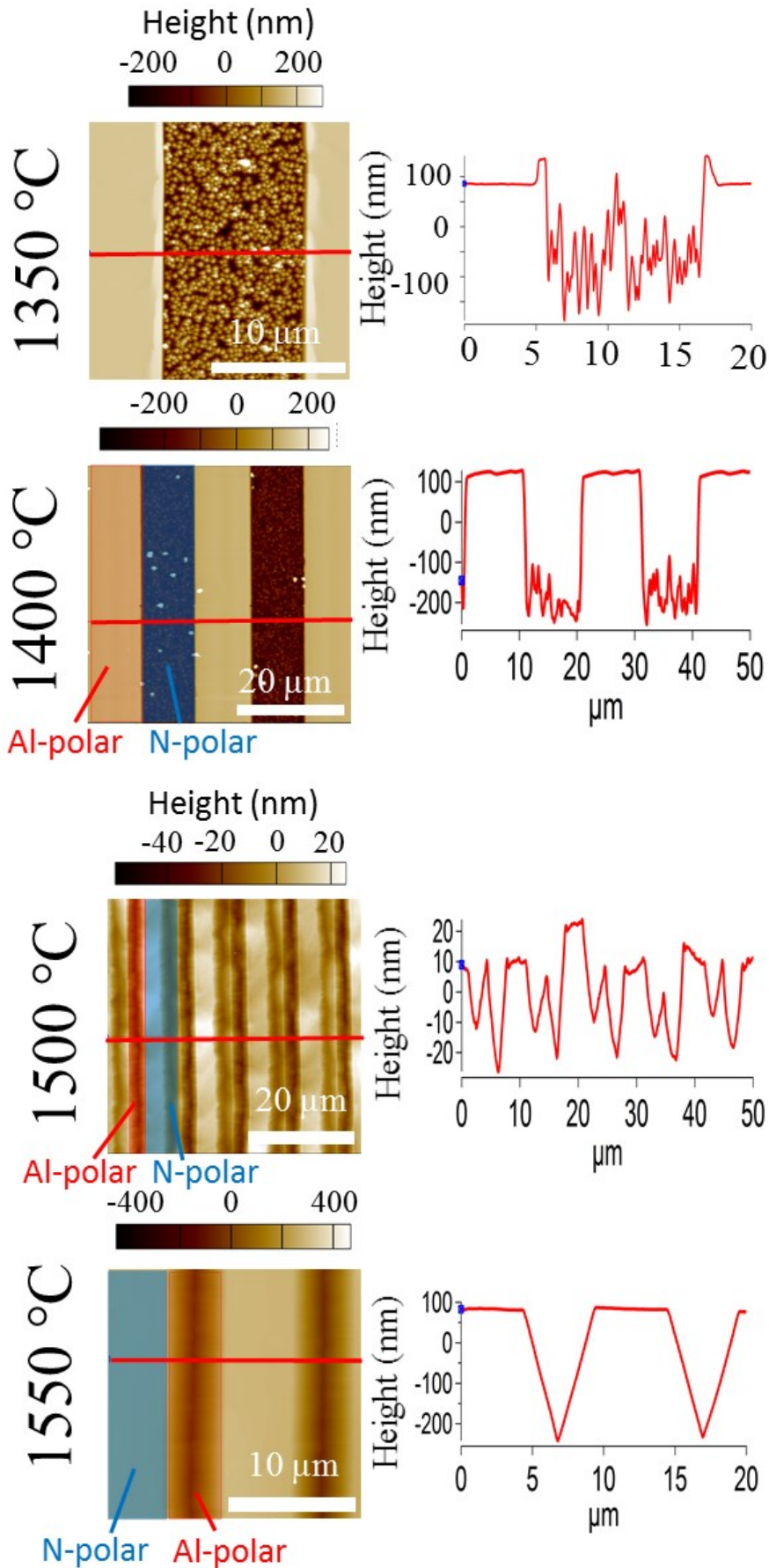


Figure 5-25: AlN LPS for a series of growth runs, where the growth temperature was varied to reduce the Al vapor supersaturation.

In contrast to the AlN LPS grown at 1250 °C (*Figure 5-16* and *Figure 5-18*), a temperature dependent growth rate difference is observed for the alternating polar domains in *Figure 5-25*. At 1250 °C growth temperature, similar deposition rates are measured for both polarities (*Figure 5-18*). Increasing the temperature leads to an increased deposition rate at the Al-polar domains compared to the N-polar domains, reaching a maximum growth rate difference between 1400 °C and 1450 °C. For growth temperatures above 1450 °C the growth rate of the Al-polar domains decreases reaching a crossover temperature around 1475 °C, where similar growth rate for both polar domains is determined. For higher temperatures the N-polar growth rate exceeds that of the Al-polar domains. The polarities of the respective domains were confirmed by KOH etching and subsequent AFM and/or SEM characterization. Amplitude AFM images of samples before and after KOH etching are displayed in *Figure 5-26* and *Figure 5-27*.

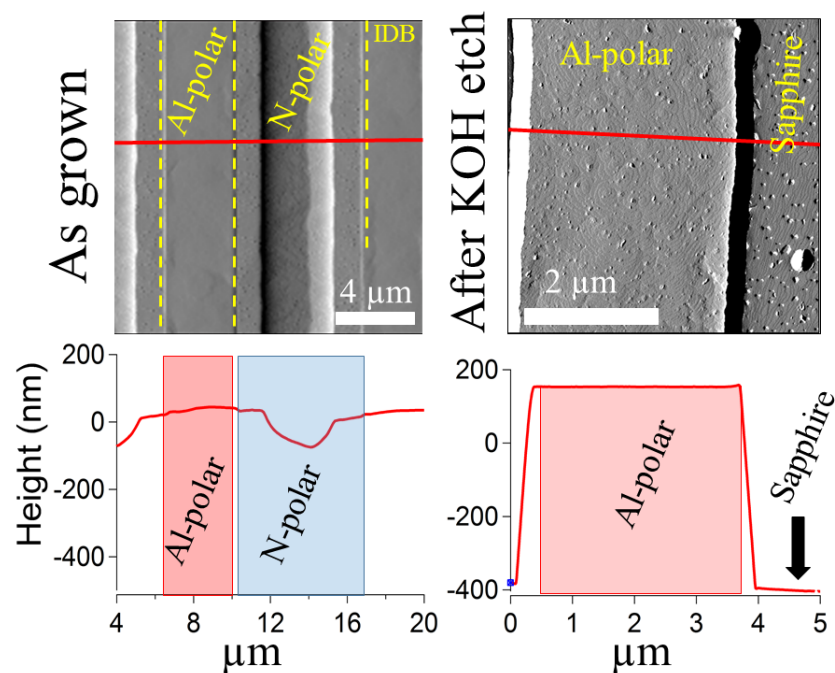


Figure 5-26: Amplitude AFM images of a grown AlN LPS sample before (top left) and after (top right) KOH etching in a 1M solution at 70 °C for 30 s. (bottom) Height profile line scans for the corresponding amplitude AFM image.

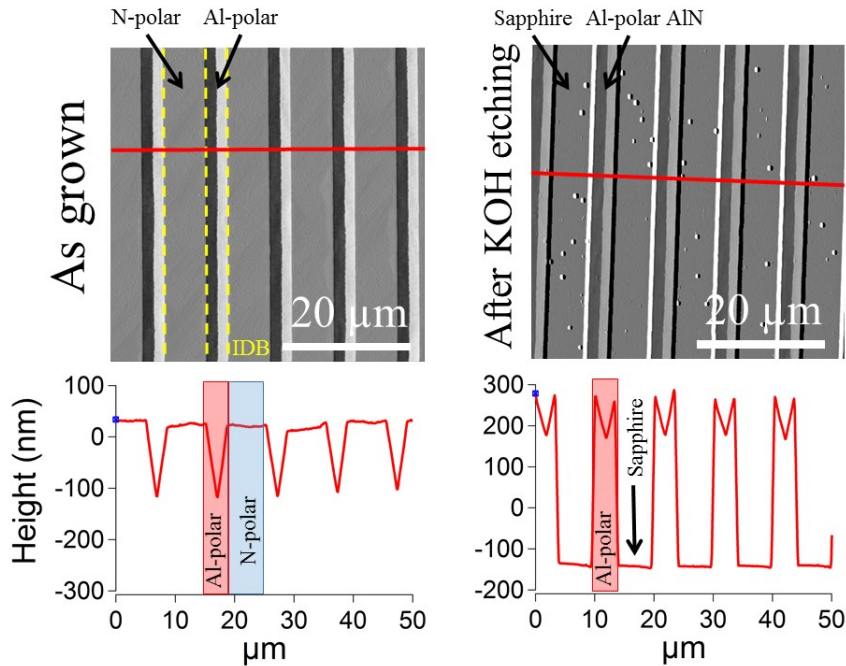


Figure 5-27: Amplitude AFM images of AlN LPS before (top left) and after (top right) KOH etching in a 1M concentrated solution at 70 °C for 30 s.

Figure 5-26 displays an AlN LPS with smooth Al-polar domains with surface roughness RMS values ~ 3 nm and relatively rough N-polar domains with V-shaped valleys within the polar domains. In contrast Figure 5-27 displays smooth N-polar domains with ~ 3 nm RMS values and rough Al-polar domains with V-shaped valleys. Regardless of the surface morphology, in both cases the N-polar domains are completely etched away while the Al-polar domains remain unaltered. Vertical sidewalls are revealed after KOH etching, which is critical for the fabrication of QPM structures. Deviations from vertical growth will lead to duty cycle variations and in extreme cases, to polarity overgrowth, resulting in a reduced QPM SHG conversion efficiency.

Because the measured growth rates for single polar AlN films are independent of polarity (Figure 5-23), the growth rate differences observed in Figure 5-25 are attributed to mass transport between the adjacent and opposite polar domains. This conclusion is also supported by the fact that the total volume is conserved when the volume of both polar domains is added, which is equal to that measured for single polar AlN films. To date, there is no theoretical model detailing the mechanism leading to polar domain thickness differences in III-Nitrides. Experiments indicate that the mechanism is related to multiple growth parameters including temperature, the choice of diluent gas, V/III ratio and total chamber pressure, suggesting a dependence on the Al vapor supersaturation. Furthermore, thickness differences

between the polar domains are dependent on the distance relative to the inversion domain boundary, extending up to tens of μm , hinting towards mass transport in the vapor-phase. A more detailed study is necessary to develop a theoretical model that precisely describes the experimental observations.

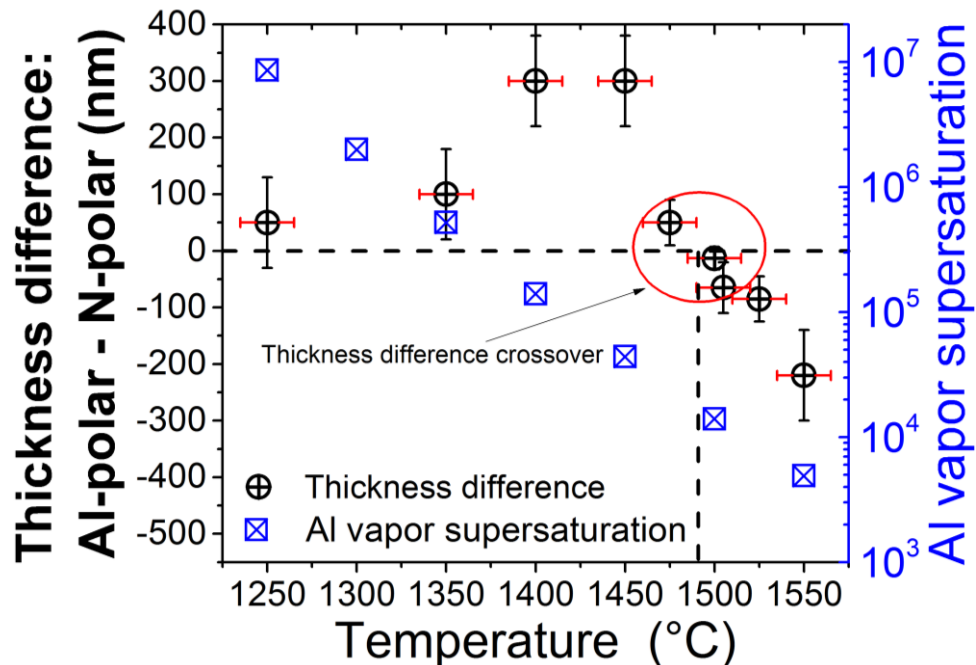


Figure 5-28: Polar domain thickness difference and Al vapor supersaturation as a function of temperature.

Figure 5-28 displays the measured thickness difference between the polar domains as a function of temperature. The corresponding Al vapor supersaturation values are superimposed for comparison. The values are obtained by measuring the $10\ \mu\text{m}$ periodic AlN LPS and taking the difference between the average value of the respective polar domains. For the error bar, the sum of the RMS values for the respective polar domains is taken. Similar growth rates for both polar domains are achieved at $1500\ \text{°C}$ growth temperature or perhaps more relevant, at Al vapor supersaturation values $\sigma \approx 1-3 \times 10^4$ as can be observed in Figure 5-25. The measured AlN LPS surface roughness RMS value for $10\ \mu\text{m}$ periodic AlN LPS grown at $1500\ \text{°C}$ is $11\ \text{nm}$ over a $90\ \mu\text{m}^2$ area. Additionally, the surface roughness correlation length is obviously larger compared to that of AlN LPS where the N-polar surface exhibits a high density of hexagonal hillocks. A larger correlation length in addition to the reduced surface roughness RMS will lead to lower scattering losses for the propagating laser light. $550\ \text{nm}$ thick and $250\ \text{nm}$ thick, $10\ \mu\text{m}$ periodic AlN LPS were grown at $1500\ \text{°C}$ and $\sim 5\ \mu\text{m}$ wide waveguides were

etched into the film, using masked photolithography and RIE (*Figure 5-29*). While such large periodicities cannot be used for 1st order QPM SHG, lower efficiency higher order QPM SHG can be achieved as it will be demonstrated in section 7.2.1.

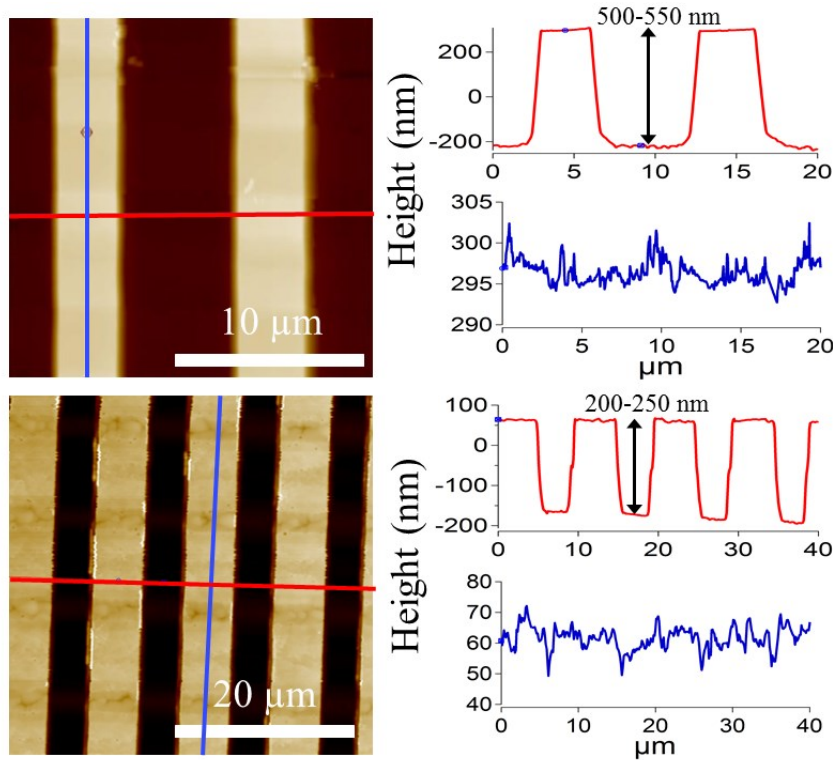


Figure 5-29: (left) AFM images of 550 nm thick (top) and 250 nm thick AlN LPS-based waveguides with 10 μm periodicity. (right) Height profile line scans across and along the waveguide corresponding to their respective AFM images.

Growing AlN LPS with shorter periodicities, to achieve 1st order QPM SHG in the UV-C spectral range (i.e. 1.2 μm periodicity), at low Al vapor supersaturation values ($\sigma \approx 1-3 \times 10^4$), necessary for equal deposition rate at both polar domains and step flow growth at the N-polar domains, results in a highly pitted surface and mixed polar growth within the polar domains. An AFM image of such an AlN LPS is displayed in *Figure 5-30*. For comparison, an optical DIC image of the sample after etching in a KOH solution for 30 s at 70 °C is displayed.

1.2 μm periodic AlN LPS

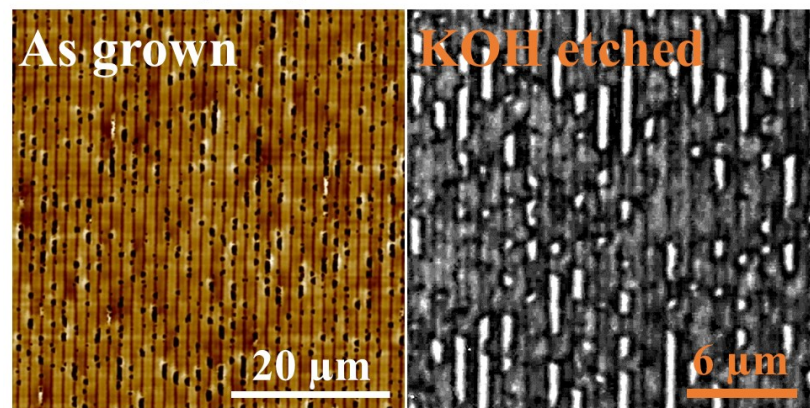


Figure 5-30: (left) AFM image of 1.2 μm periodic AlN LPS grown at 1500 $^{\circ}\text{C}$. (right) Optical DIC image of the same sample after being submerged in KOH, displaying inhomogeneous etching, indicating that the AlN LPS contained mixed polar domains.

A higher magnification amplitude AFM image, highlighting the surface morphology of 1.2 μm periodic AlN LPS grown at 1500 $^{\circ}\text{C}$, is displayed in *Figure 5-31*.

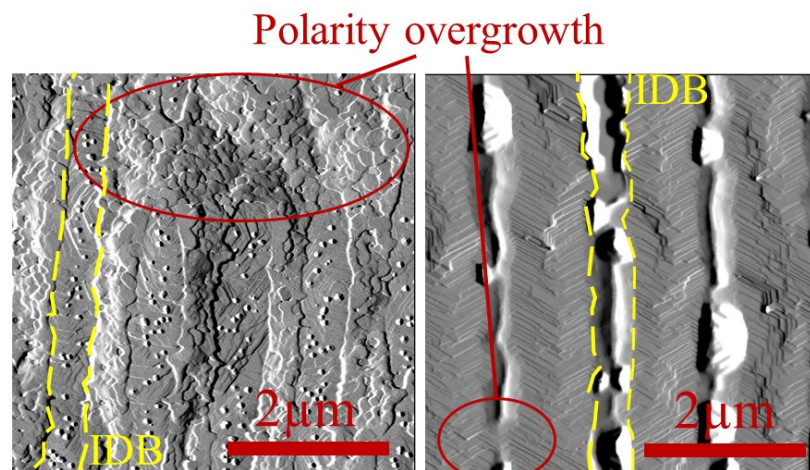


Figure 5-31: Amplitude AFM image of 1.2 μm AlN LPS samples grown at 1500 $^{\circ}\text{C}$. Regions where one polarity is overgrowing the neighboring polarity are encircled. A few inversion domain boundaries (IDB's), as determined by the surface morphologies characteristic of the respective polarities, are marked with yellow dashed lines.

Regions where one polar domain has overgrown the neighboring opposite-polar domain are encircled. Moreover, the Al-polar domains are plagued with a high density of pits with depths up to 200 nm as well as with protrusions of up to 150 nm in height. The scattering losses for such a rough structure will not allow for the propagation of laser light inhibiting their use for QPM SHG. Additionally, for QPM, alternating polarity domains are necessary, hence polarity overgrowth will not allow for the phase mismatch correction of the driving and second harmonic waves at

every coherence length distance and QPM will not take place. Polarity overgrowth seems mainly a concern for growth conditions leading to similar growth rates for both polarities ($\sigma \approx 1-3 \times 10^4$). This conclusion is based on the fact that if the growth parameters are selected, such that one polarity has a significant larger deposition rate compared to the opposing polarity (*Figure 5-28*), no polarity overgrowth is observed as well as vertical growth at the respective polar domains (*Figure 5-32*). It is worth noting that, thus far, polarity overgrowth in 1.2 μm periodic AlN LPS has only been observed for geometries where the IDBs are placed parallel to the crystallographic a-plane of the AlN. However a more detailed study is necessary to make a substantiated conclusion.

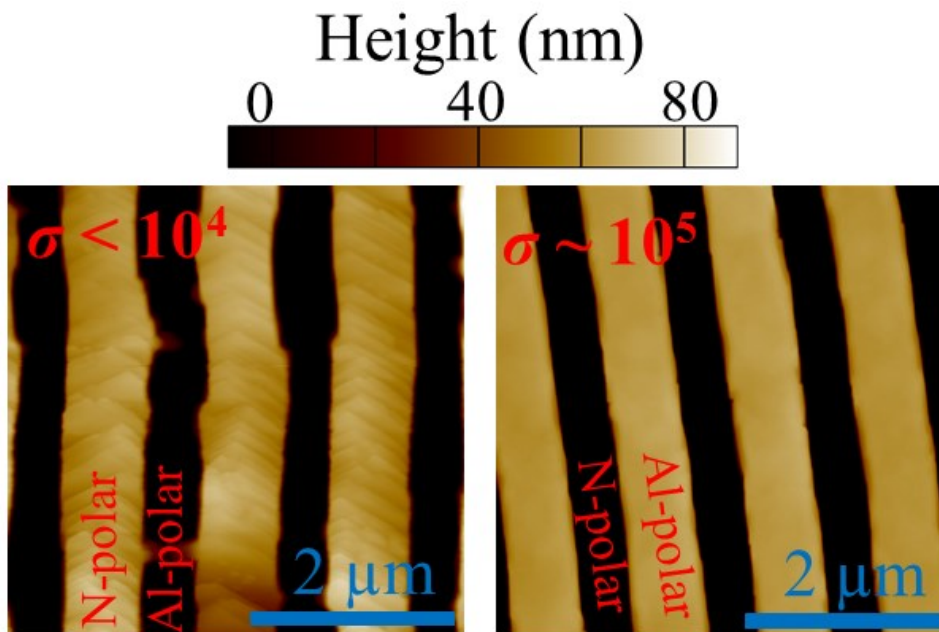


Figure 5-32: AFM height images for 1.2 μm AlN LPS grown at $\sigma \approx 5-10 \times 10^3$ (left) and $\sigma \approx 1 \times 10^5$ (right) Al vapor supersaturation values.

To circumvent the issue of polarity overgrowth, a growth process was developed where different growth modes are combined. First the 1.2 μm periodic AlN LPS is grown at high Al vapor supersaturation values, where well defined IDB's and polar domains are obtained (*Figure 5-16*), until the desired film thickness is achieved. In a second step a “capping” AlN layer is deposited, where the Al vapor supersaturation is decreased (i.e. by increasing the temperature) to promote step flow growth at the N-polar surface and reduce its surface roughness. At this point, polarity overgrowth will only influence a thin layer near the surface of the AlN LPS, which will not significantly affect the QPM SHG conversion efficiency, since the electric field amplitude of the wave-guided TM_0 mode is predominantly confined in the center

region of the waveguide. *Figure 5-33* shows AFM height images of the surface of a series of 1.2 μm AlN LPS, grown in a two-step temperature process, where the temperature of the second step was varied from 1400 $^{\circ}\text{C}$ to 1550 $^{\circ}\text{C}$.

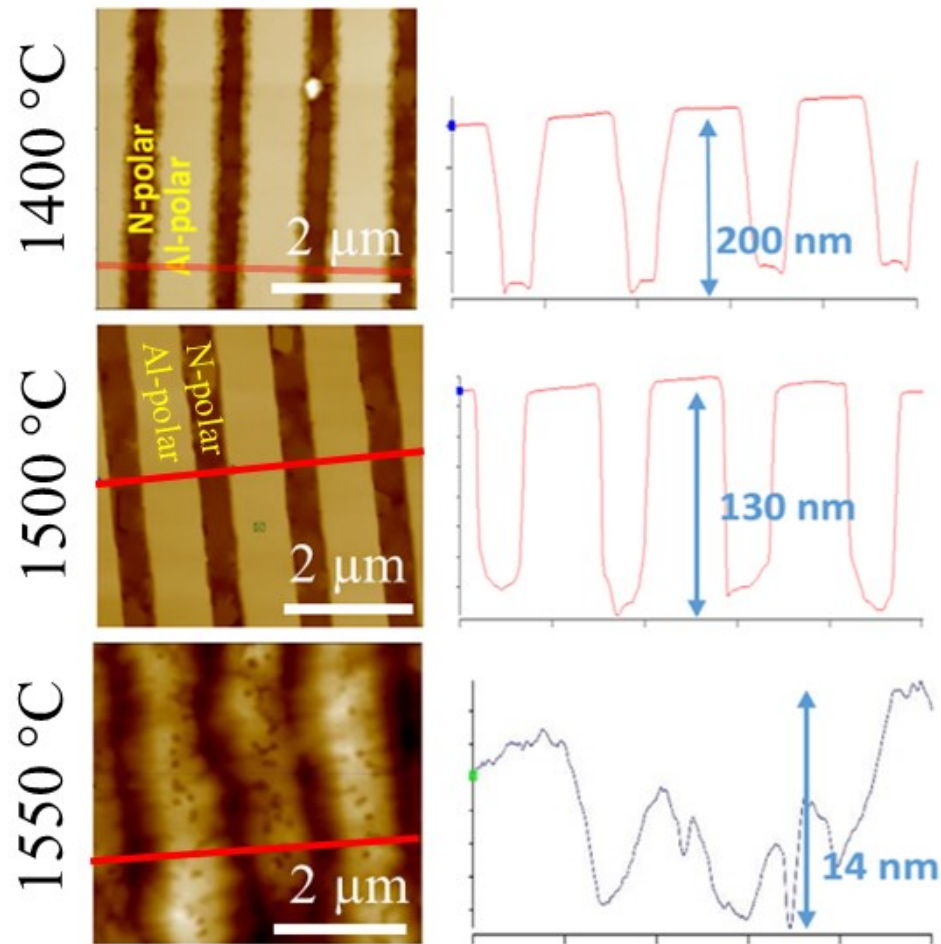


Figure 5-33: AFM height images of 1.2 μm AlN LPS grown by a two-step temperature process. The first step growth temperature for all samples was 1250 $^{\circ}\text{C}$. In the second step the temperature was increased to 1400 $^{\circ}\text{C}$ (top), 1500 $^{\circ}\text{C}$ (center) and 1550 $^{\circ}\text{C}$ (bottom) in order to achieve a smooth surface morphology of the 1.2 μm AlN LPS.

A clear decrease in the domain height difference is observed as the temperature is increased for the second growth step, in agreement with previous observations (*Figure 5-28*). A representative tilted SEM image of a 1.2 μm periodic AlN LPS grown in a two-step temperature process, after KOH etching is presented in *Figure 5-34*.

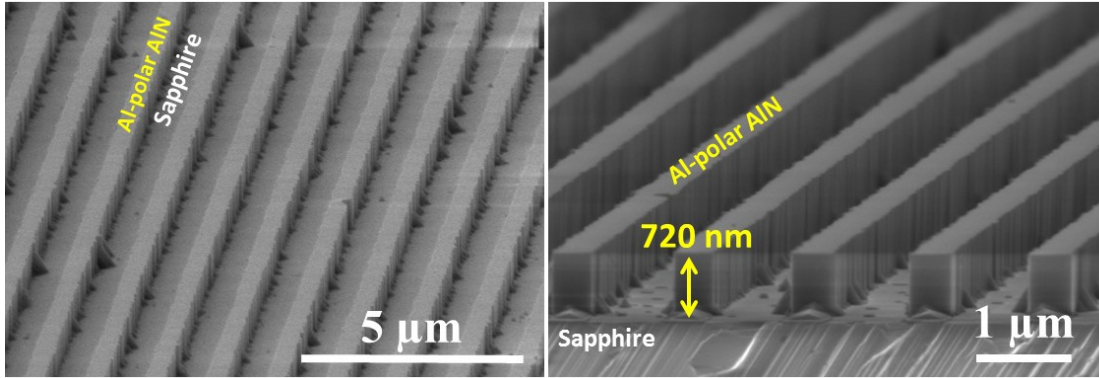


Figure 5-34: Tilted SEM images of a KOH wet-etched 1.2 μm AlN LPS sample grown in a two-step temperature process.

The two step temperature process can also be implemented in separate growth runs. *Figure 5-35* shows two different AlN LPS where thicker Al-polar domains compared to the N-polar domains are measured.

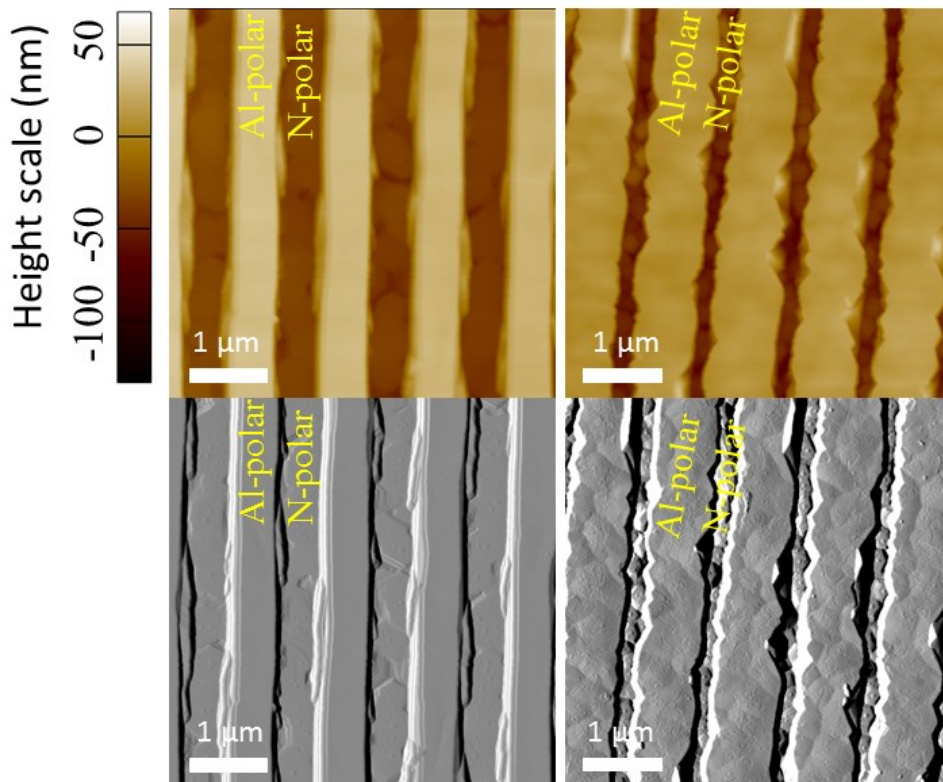


Figure 5-35: AFM height (top) and amplitude (bottom) image of two different 1.2 μm periodic AlN LPS, where thicker Al-polar domains compared to the N-polar domains are measured.

After characterizing the samples, they were cleaned in an ultrasound bath in acetone, methanol and deionized water and subsequently subjected to an acid clean in a 5% HF solution in deionized water followed by rinsing with only deionized water. The samples were then introduced to the MOCVD reactor where they were vacuum and

H₂ annealed following the standard procedure described in section 5.1. Following the annealing steps, the samples were heated up to 1550 °C at 80 Torr total chamber pressure, 10 slm and 0.3 slm flow of H₂ and ammonia respectively. AlN was then deposited for 30 minutes by flowing 13.4 μmol/min of TMA. The calculated vapor supersaturation for these growth parameters is $\sigma = 5 \times 10^3$, where higher deposition rates at the N-polar domains are established (*Figure 5-28*).

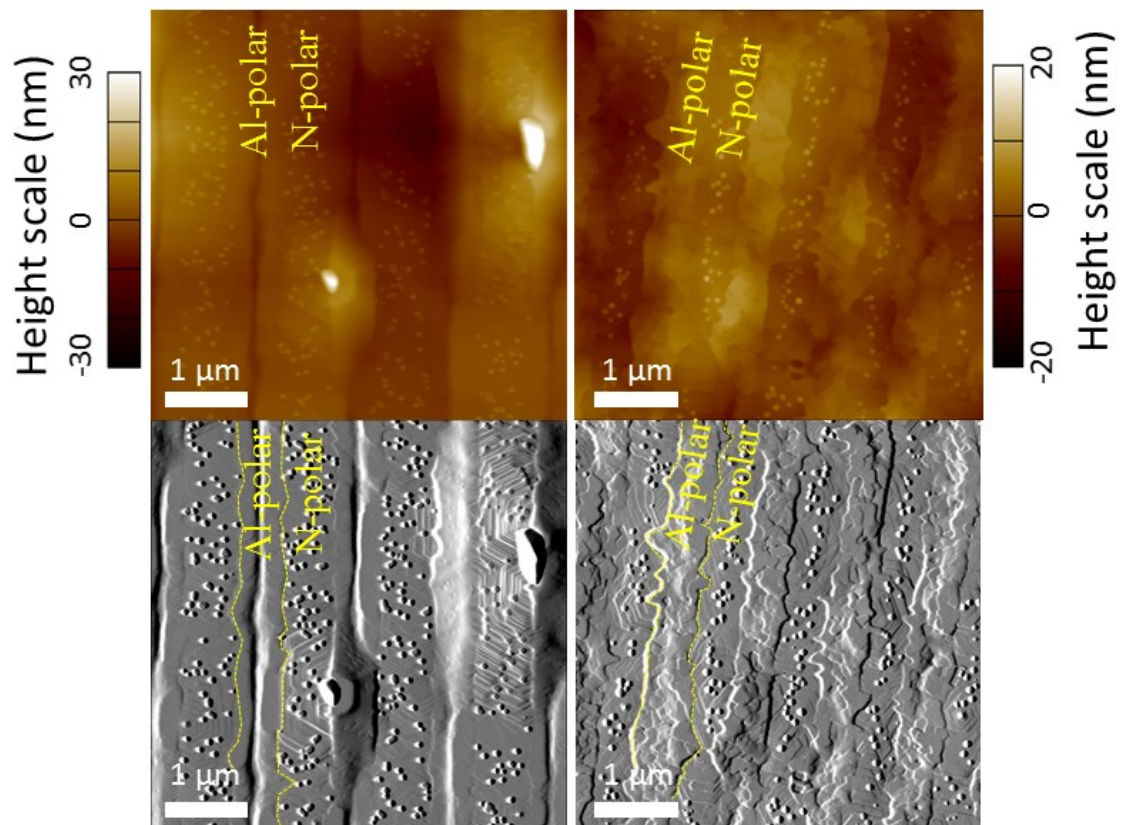


Figure 5-36: AFM height (top) and amplitude (bottom) image of the 1.2 μm periodic AlN LPS displayed in Figure 5-35 after regrowth at x temperature for x minutes, where higher deposition rates for the N-polar domains compared to the Al-polar domains were determined.

Figure 5-36 shows AFM height and amplitude images of the AlN LPS samples after regrowth. In both samples the thickness difference between the opposite polar domains has virtually disappeared while still maintaining the polarity of the respective domains. The N-polar domains are evident from the m-plane faceted step flow morphology, as well as the inversion domains with a density $\sim 10^9 \text{ cm}^{-2}$. As evident in *Figure 5-36* this method can be used to achieve 1.2 μm periodic AlN LPS with a smooth surface morphology. Additionally, the possibility to control deposition rates for the respective polarities when grown side by side will be useful for other applications.

In summary, when growing AlN LPS at vapor supersaturation values $\sigma < 10^8$, mass transport between the opposite polar domains is observed as the Al vapor supersaturation σ is decreased. For $10^8 > \sigma > 3 \times 10^4$ mass transport from the N-polar to the Al-polar domains, leads to thicker Al-polar domains. For $\sigma \approx 1-3 \times 10^4$ similar growth rates for both polarities is measured, indicating no net mass transport between the adjacent polarities. Finally, for $10^4 > \sigma$ mass transport from the Al-polar to the N-polar domains is measured leading to thicker N-polar domains. For AlN LPS with periodicities $\Lambda \approx 1.2 \mu\text{m}$, polarity overgrowth takes places when grown at Al vapor supersaturation values where similar growth rates are determined. Alternatively, a two-step temperature process can be utilized to avoid polarity overgrowth and achieve $1.2 \mu\text{m}$ periodic AlN LPS with a 6-10 nm surface roughness RMS value. Finally, $5 \mu\text{m}$ wide waveguides were etched into $10 \mu\text{m}$ AlN LPS waveguides of two different thicknesses (550 nm and 250 nm) to test them for QPM SHG in the UV spectral range.

5.1.4 Influence of Crystallographic Orientation on the IDB

A closer examination of the IDB with AFM, reveals that the IDB's preferentially facet along the crystallographic m-plane of AlN, giving rise to different IDB patterns for LPS with different crystallographic orientations (*Figure 5-37*). For AlN LPS with the IDB aligned along the crystal's (11-20) plane, a jigsaw pattern for the IDB can be observed. In contrast, the AlN LPS where the IDB is aligned with the crystal's (10-10) plane, the IDB is virtually a straight line. These results are in agreement with IDB's predicted and observed for GaN, where first principle calculations predict a comparably small formation energy for an IDB along the m-plane and shifted along the c-direction by a magnitude of $c/2 = 2.6 \text{ \AA}$.^{85,108}

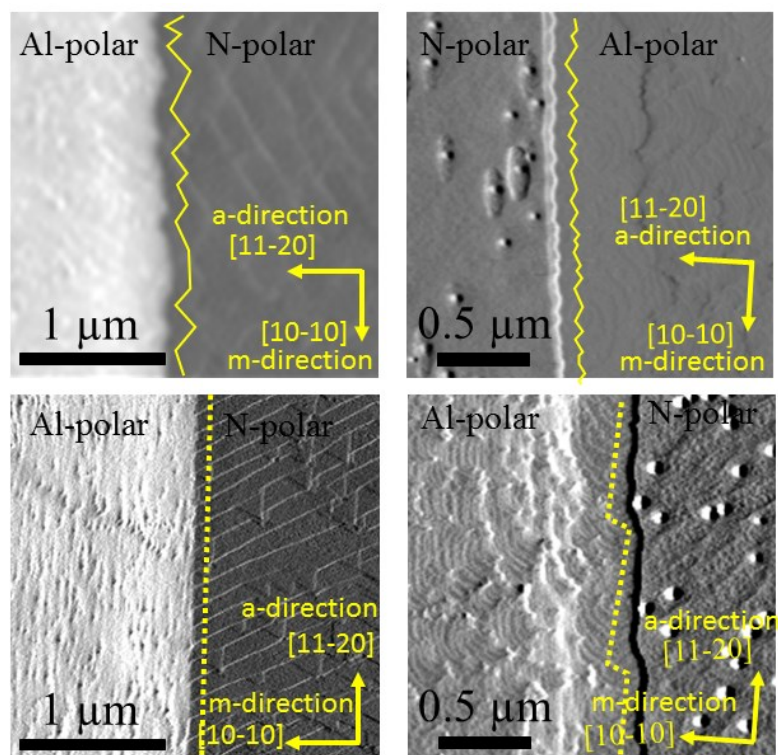


Figure 5-37: AFM amplitude images of the IDB in AlN LPS samples with periodicities along the a-direction (top) and along the m-direction (bottom). The left images, are taken from a sample where the stripe pattern is well aligned with the crystallographic orientations and the samples on the right are taken from a sample where the stripe pattern is slightly misaligned with respect to the crystallographic orientations.

This was later confirmed in a study through high resolution TEM characterization showing the expected shift along the c-direction at the IDB.¹⁰⁹ From these observations, it is evident that in order to achieve an abrupt IDB along the periodicity of the AlN LPS, it is necessary to align the IDBs with the (10-10) crystallographic plane. Note that the quality of the IDB will also depend on the sidewall roughness of the patterned AlN nucleation layer which is used to selectively grow Al-polar AlN. For AlN LPS where the IDB is aligned the (11-20) plane, where the IDB is not abrupt but rather displays a jigsaw pattern, the position of the IDB is measured to vary in a range thinner than 50 nm. While it is not ideal, small changes in the duty cycle of the periodic structure will not have a significant impact on conversion efficiency, becoming more relevant as the periodicity of the AlN LPS decreases.

5.2 GaN Lateral Polar Structures

In contrast to AlN based LPS, numerous studies on GaN based LPS have been published.^{78,84,85,91,110–115} In particular, the doctoral dissertation of S. Mita and M. Hoffmann,^{84,114} have a detailed description of studies on GaN based LPS with periodicities $\Lambda \geq 5\mu\text{m}$ using the same polarity control process scheme as described in section 4. The focus of this section includes promoting step flow growth at the N-polar GaN surface to achieve smooth GaN LPS and avoid polarity overgrowth for GaN LPS with 1.2 μm periodicity. It will be shown that the effects observed and described in section 5.1 for AlN LPS, largely parallel those observed in GaN LPS, only shifted towards lower temperatures.

Like for AlN and as described in sections 4 and 5.1, patterned low temperature AlN nucleation layers deposited on sapphire substrates are used to control the polarity of GaN epitaxial layers and fabricate GaN LPS, where the only difference lies in the growth conditions for the GaN layer deposited on the patterned substrate. After vacuum annealing the patterned substrate at 1040 °C, followed by H₂ anneal and NH₃ anneal at 1040 °C (section 5.1), the GaN growth is started by flowing 133 $\mu\text{mol}/\text{min}$ of TEG and 0.6 slm of NH₃ (equivalent to a V/III ratio of 250) in 6.6 slm of N₂ diluent gas. These growth conditions were chosen as a starting point, based on results presented by Hoffmann et al.¹¹⁶, which show similar growth rates for both polarities and the smallest polar domain height difference. *Figure 5-38*, shows AFM images of a 2.4 μm thick GaN LPS grown under the conditions described above. While no polarity overgrowth is observed, and the average height values for the N-polar and Ga-polar domains differ from each other by 50 nm, the surface roughness RMS value for the N-polar domains is measured to be 85 nm. Such high values for the surface roughness, would lead to significant scattering losses in GaN LPS-based waveguides, inhibiting their implementation for QPM applications. Note that while the surface roughness of the GaN LPS is critical for LPS-based waveguides, it has no implications for thick bulk GaN LPS where waveguiding modes need not be considered.

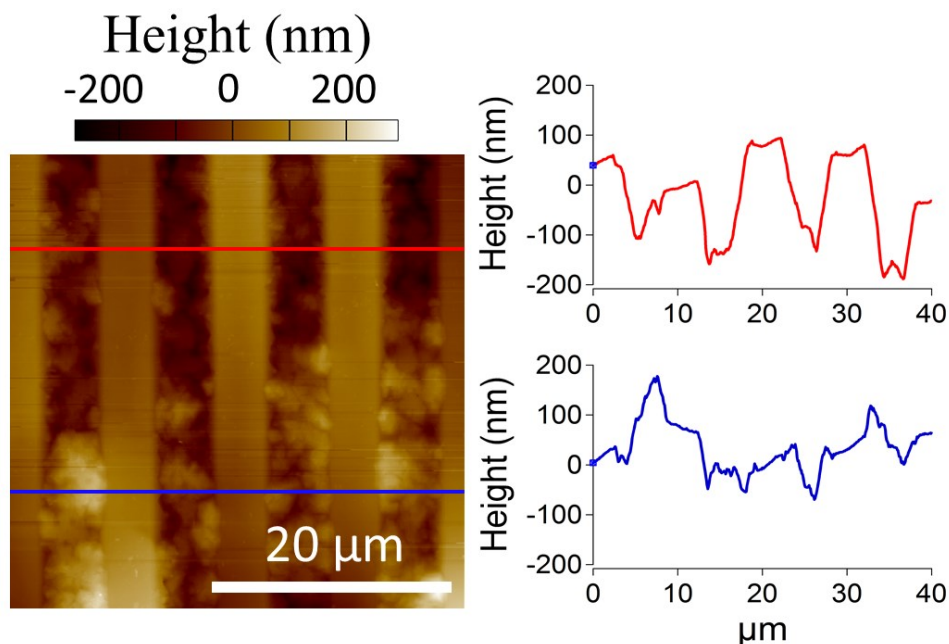


Figure 5-38: AFM image with corresponding height profile line-scans of a GaN LPS grown at a V/III ratio of 250.

The surface roughness can be reduced, as with the AlN LPS, by mechanical polishing with alumina particles of 0.3 μm in size dissolved in DI water, squirted on a “TexMet P” soft pad platform. A sequence of optical DIC microscope images of a GaN LPS after different polishing times is presented in *Figure 5-39*.

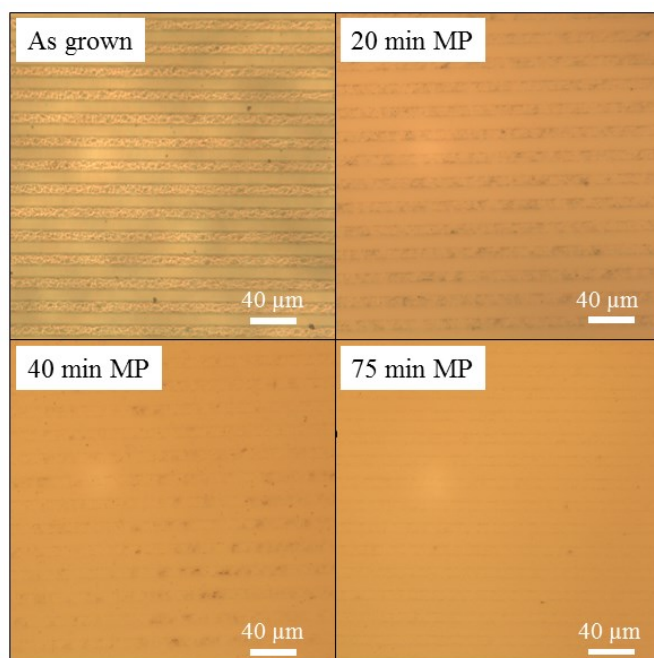


Figure 5-39: DIC optical microscope images for a GaN LPS before (top left) and after different polishing times.

Polishing times longer than 75 minutes did not result in a further reduction of the surface roughness RMS value. The surface of a 75 minute long mechanically polished GaN LPS sample was studied in more detail by AFM.

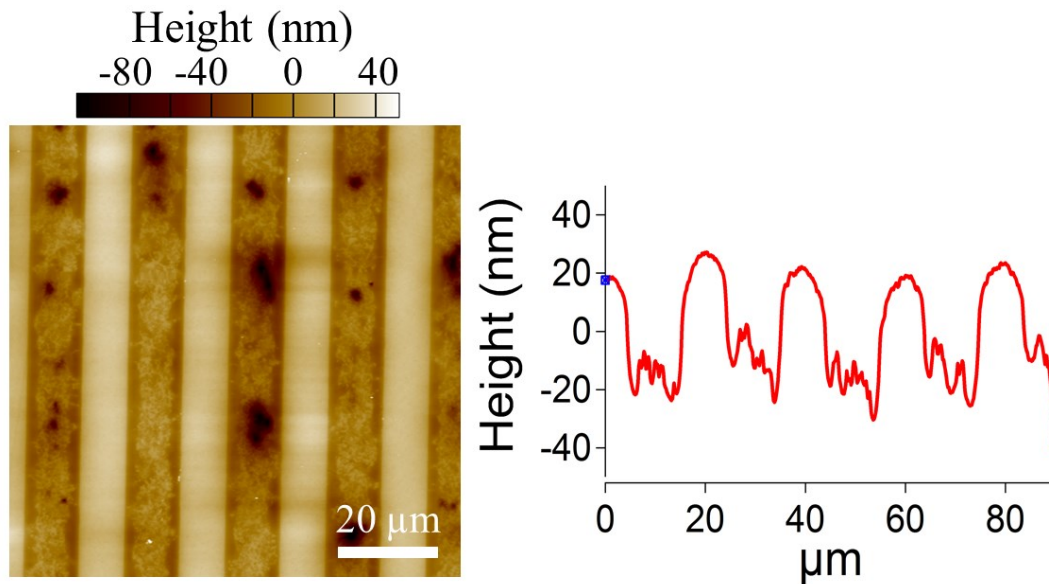


Figure 5-40: 75 min long mechanically polished GaN LPS with 0.3 μm alumina particles in DI water solution.

Through mechanical polishing the GaN LPS surface roughness RMS value was reduced from 66 nm to 25 nm. A constant height difference between the polar domains of 40 nm is measured independent of further polishing times. As suggested for AlN LPS, the reason for the obtained height differences after polishing, may be related to polarity dependent etching due to the pH of the polishing solution. Further polishing studies are necessary to determine the mechanism leading to the polar domain height differences measured. Some parameters that could be modified include, different pH polishing vehicles, the polishing particles type and size and the polishing pad. However, there are a variety of other parameters that can be studied. In this work an alternative approach is pursued where the surface roughness of the GaN LPS is reduced by promoting step flow growth at the N-polar domains during growth with the goal to eliminate the need for post-processing steps to reduce the GaN LPS surface roughness (section 5.2.2).

5.2.1 Nanometer Scale GaN Lateral Polar Structures

For first order QPM SHG using GaN LPS in the UV-visible spectral range, periodicities below 10 μm are required (*Figure 5-41*).

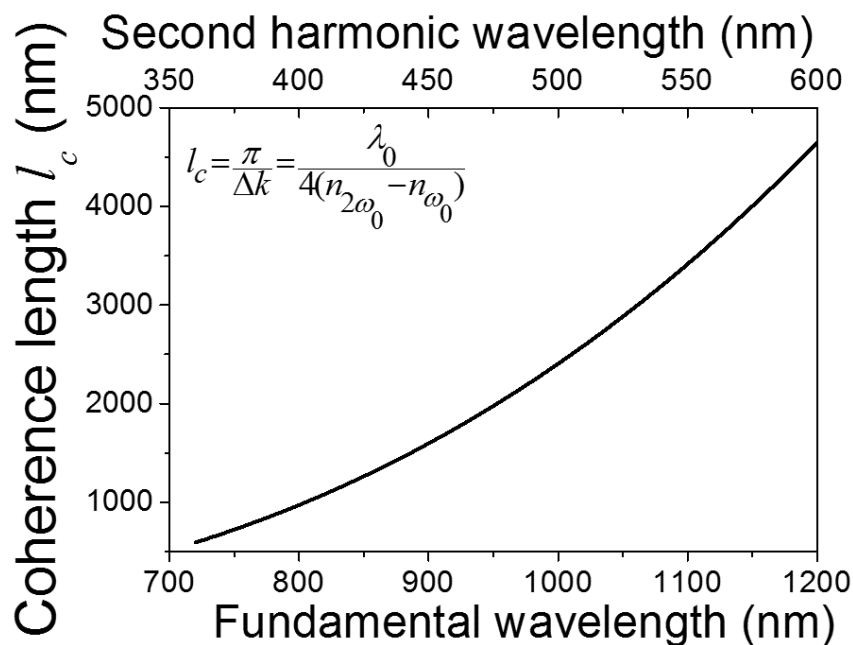


Figure 5-41: Calculated coherence length for bulk GaN as a function of fundamental wavelength.

Figure 5-41 displays the calculated coherence length for bulk GaN as a function of the driving (fundamental) wave. The fundamental absorption edge of GaN limits QPM SHG to photon energies above 3.47 eV (360 nm wavelength). While QPM SHG into the UV-C spectra is not accessible for GaN LPS, there are interesting potential applications including down conversion from InGaN-based high power LD's into the IR communication wavelengths. The lower coherence length limit for QPM SHG in GaN LPS, from 720 nm to 360 nm, requires LPS with periods in the order of 1.2 μm . Figure 5-42 shows AFM images of an intended 1.2 μm GaN LPS, before and after KOH etching. From the surface morphology, it is clear that Ga-polar GaN has partially overgrown the N-polar GaN domains which is then confirmed by the AFM height image of the KOH etched sample. Moreover, tilted cross-section SEM images of a 1.2 μm GaN LPS (Figure 5-43) shows electron charge accumulation in the sapphire substrate, localized below the N-polar domains. This is typically observed in epitaxial N-polar GaN and is likely related to the fact the N-polar GaN is intrinsically conductive due to its high oxygen incorporation in contrast to the intrinsically insulating Ga-polar GaN. The observed polarity overgrowth for periodicities $\Lambda \sim 1.2 \mu\text{m}$ parallels the observations made for 1.2 μm periodic AlN LPS grown at Al-vapor supersaturation values ($\sigma \approx 1\text{-}3 \times 10^4$) where similar growth rates for both polar domains was determined.

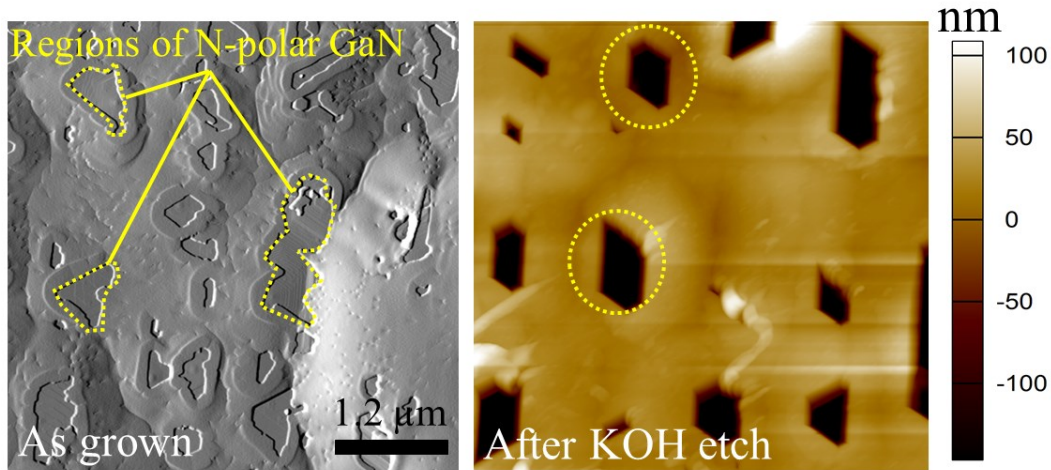


Figure 5-42: (left) AFM amplitude image of a 1.2 μm periodic GaN LPS showing N-polar GaN being overgrown by Ga-polar GaN. (right) AFM height image where the N-polar GaN areas that have been etched away are highlighted.

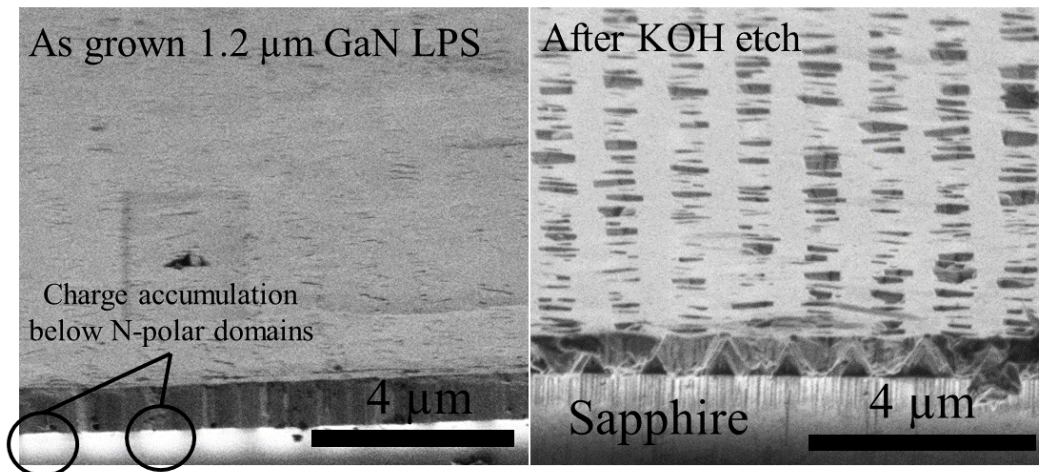


Figure 5-43: Tilted cross-section SEM image of a 1.2 μm GaN LPS before (left) and after (right) wet etching in a KOH solution.

Clearly polarity overgrowth is also a challenge in GaN when the periodicity of the GaN LPS is $\sim 1.2 \mu\text{m}$. The Ga vapor supersaturation value for the growth conditions used for the GaN LPS described in *Figure 5-43* is $\sigma \sim 5 \times 10^3$. In the next section, it will be shown that for Ga vapor supersaturation values $\sigma \sim 100$, polarity overgrowth can be avoided and similar growth rates for both polar domains are achieved.

5.2.2 Promoting Step Flow Growth for Smooth GaN LPS

Numerous studies have demonstrated step flow growth of N-polar GaN.^{101–104} This has been achieved by increasing the off-cut angle of the substrate, substituting the nitrogen diluent gas with hydrogen or by increasing the V/III ratio of the precursors under nitrogen diluent gas, all resulting in a reduced surface supersaturation σ_s .

directly or indirectly through a reduction of the Ga vapor supersaturation σ . As a guide, *Figure 5-44* and *Figure 5-45* display the calculated Ga vapor supersaturation for multiple growth conditions with the goal to illustrate general trends when varying specific growth parameters, such as temperature, pressure, V/III ratio and exchanging the N₂ diluent gas with H₂.

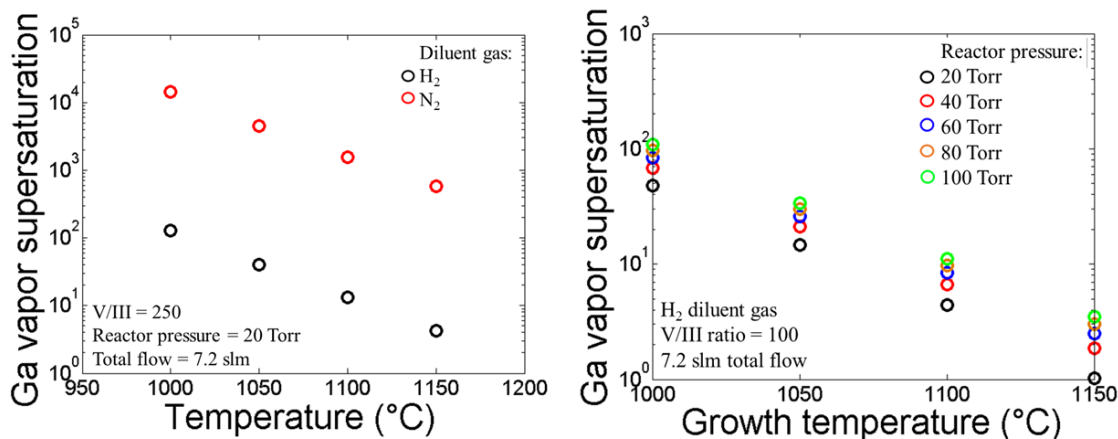


Figure 5-44: Calculated Ga vapor supersaturation as a function of temperature. For comparison the values are calculated for H₂ and N₂ diluent gas (left) and for different total reactor pressures (right).

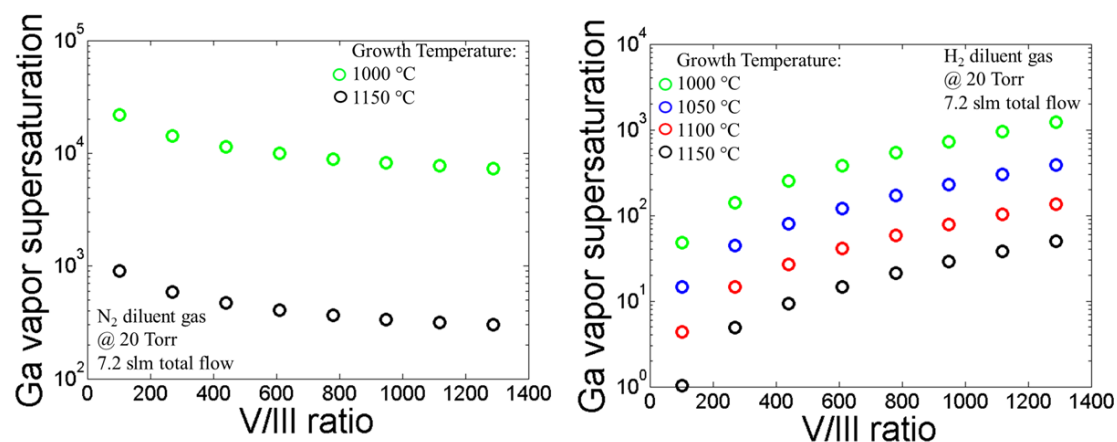


Figure 5-45: Calculated Ga vapor supersaturation as a function of V/III ratio for different temperatures under N₂ diluent gas (left) and under H₂ diluent gas (right).

To achieve a smooth surface morphology for N-polar GaN thin films, in this work, sapphire substrates with 2° off-cut towards the m-plane are used. Following the standard substrate annealing steps in vacuum, H₂ and NH₃ (section 4.2) a GaN nucleation layer is deposited at 950 °C by flowing 133 μmol/min of TEG and 6 slm of NH₃ under 1.2 slm of N₂ diluent gas for 30 seconds at 20 Torr total reactor pressure. The GaN nucleation layer is annealed for 6 min at 1100 °C under the same conditions, with the exception that no TEG is flown into the reactor. Subsequently the growth of GaN is commenced, where TEG is reintroduced into the reactor at 133

$\mu\text{mol}/\text{min}$, the N_2 diluent gas is exchanged with 4.2 slm of H_2 gas and the ammonia flow is decreased to 3 slm to maintain a constant total flow rate of 7.2 slm. The calculated Ga vapor supersaturation for these growth conditions is $\sigma \approx 100$.

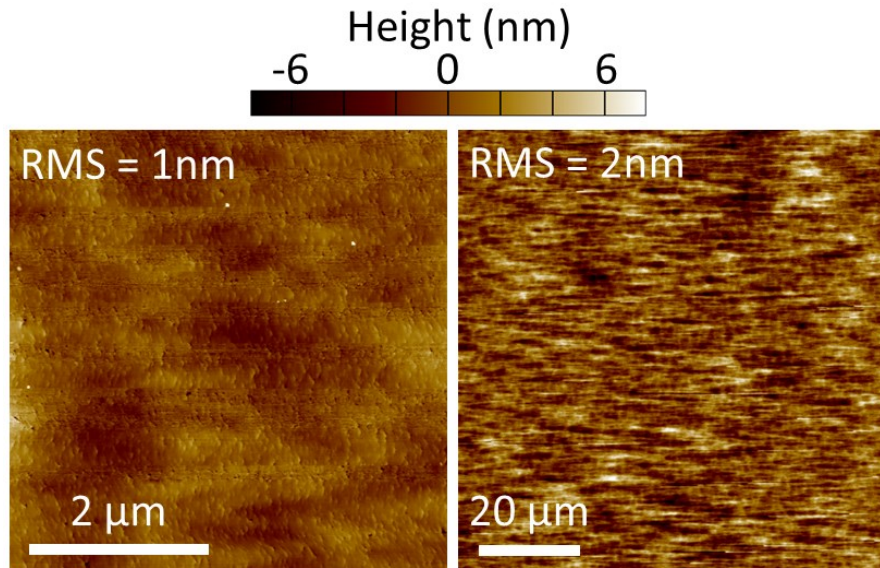


Figure 5-46: AFM height image of the surface of an N-polar GaN thinfilm grown under the conditions described in the text. A scan area of $5 \times 5 \mu\text{m}^2$ (left) and $90 \times 90 \mu\text{m}^2$ (right) is presented.

Figure *Figure 5-46* shows AFM height images of an N-polar GaN film grown using the conditions described above. Clear step flow growth is observed and a surface roughness RMS value of 2 nm over a $90 \times 90 \mu\text{m}^2$ area is achieved. Using the same parameters for the growth of GaN LPS, leads to a significant improvement of the surface roughness, where step flow growth is clearly observed and an RMS value of 36 nm over a $50 \times 50 \mu\text{m}^2$ area is achieved (*Figure 5-47*).

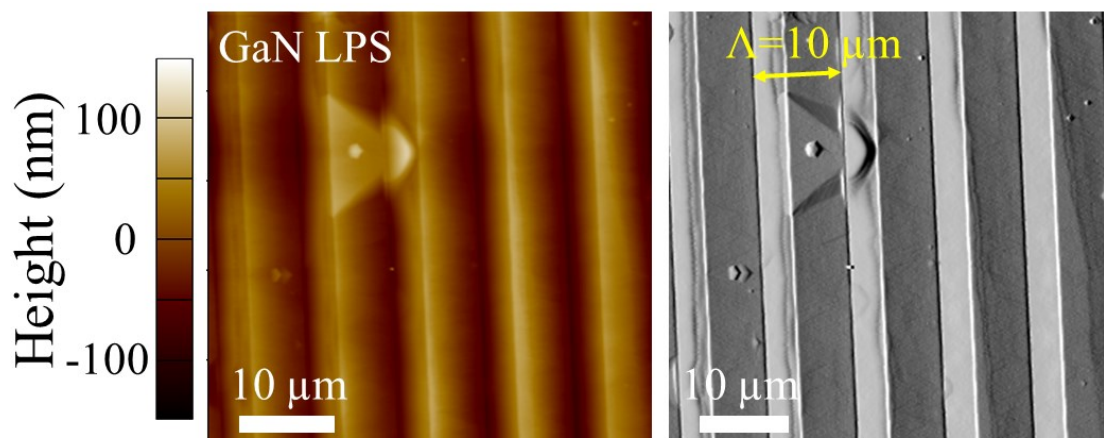


Figure 5-47: AFM height (left) and amplitude (right) image of a GaN LPS grown at relatively low Ga vapor supersaturation values ($\sigma \approx 100$).

Cross section SEM images of the GaN LPS show a fully coalesced film and equal polar domain height at the IDB's (*Figure 5-48*). Charge accumulation is observed below the N-polar GaN domains, in agreement with previous observations. Low scattering losses at the surface interface are expected for the propagating wave, allowing for their implementation in QPM SHG applications.

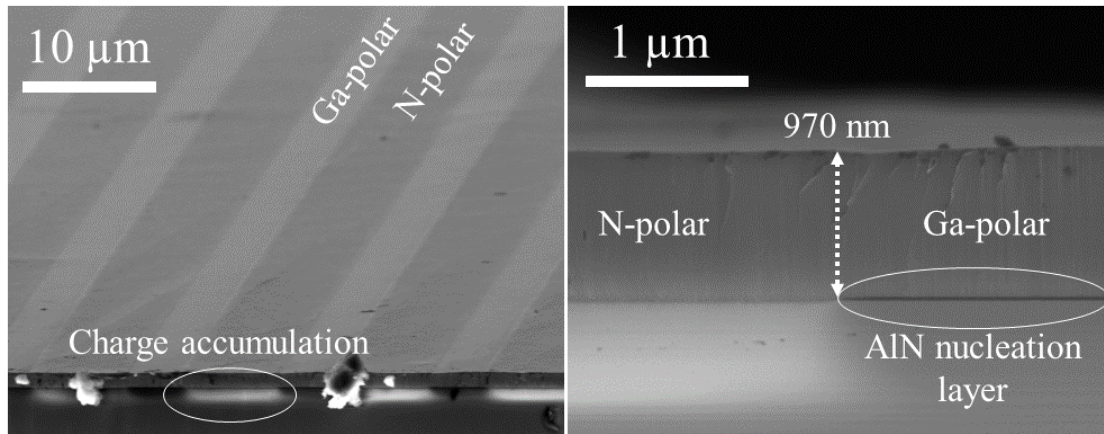


Figure 5-48: Cross section SEM images displaying a GaN LPS grown at a Ga vapor supersaturation value of 100.

Furthermore, in contrast to 1.2 μm periodic GaN LPS grown at high Ga vapor supersaturation values (*Figure 5-42*), at a Ga vapor supersaturation value of 100, no polarity overgrowth is observed as evidenced from the AFM height images presented in *Figure 5-49* for a 1.2 μm GaN LPS before and after etching in KOH etching.

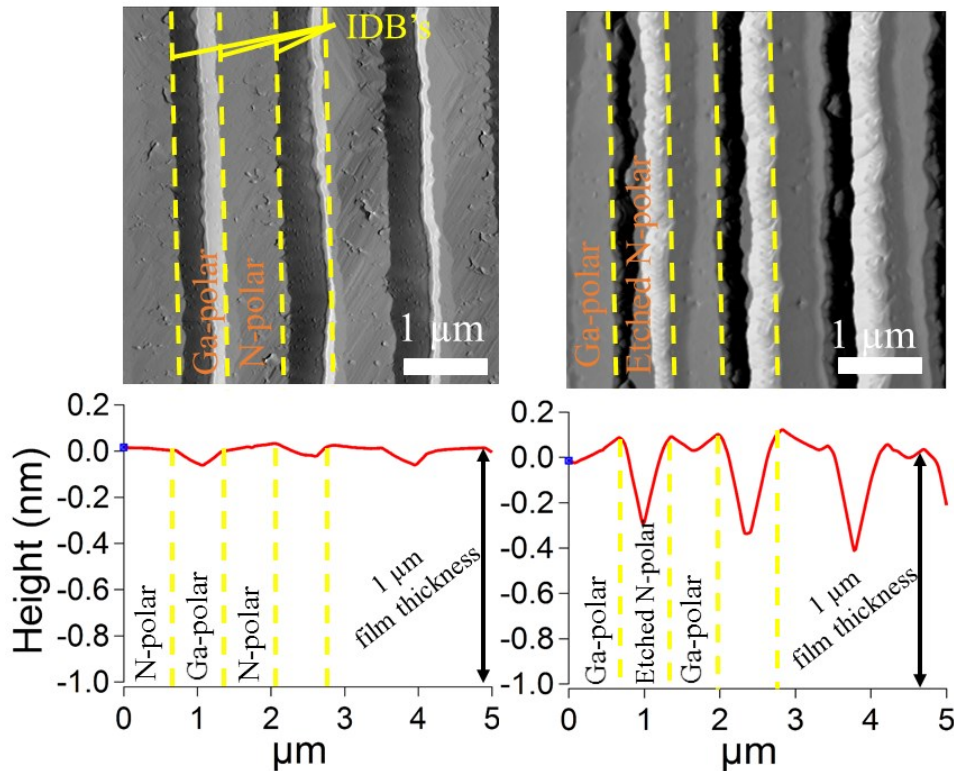


Figure 5-49: AFM amplitude images (top) and height profile linescans (bottom) of a 1.2 μm periodic GaN LPS grown at a Ga vapor supersaturation of 100 before (left) and after (KOH) etching.

From *Figure 5-49* it can be seen that the surface morphology of the Ga-polar domains remains unaltered after submerging the sample in KOH for 3 minutes at 80 $^{\circ}\text{C}$ in a 3M concentration solution, while 320 nm to 520 nm of etch depth is measured at the N-polar domains, confirming the polarity of the respective domains.

In summary, the GaN polarity control process scheme, which utilizes a patterned low temperature AlN nucleation layer, is extended to the nanometer scale by means of laser interference lithography. A smooth surface of the GaN LPS is achieved by inducing step flow growth at the N-polar surface through controlling surface supersaturation. At the same time, polarity overgrowth in 1.2 μm periodic GaN LPS is prevented by growing at low supersaturation values, where step flow growth at the N-polar domains is observed.

6 Point Defects in AlN

For an ideal wurtzite AlN single crystal with a bandgap energy of 6.2 eV and optical phonon energies in the order of 0.1 eV,^{12,117} transparency is expected in the 205 nm – 12 μm spectral range. In reality, impurities are present in the AlN crystals, which introduce below bandgap energy absorption bands. These absorption bands are detrimental (in some cases even hinder) to applications where transparency is necessary, including UV LEDs designed in a geometry where the light is extracted through the substrate. Moreover, unintentionally introduced impurities, lead to doping compensation, below bandgap energy luminescent bands and a reduced mobility as well as thermal conductivity, resulting in an inferior performance of AlN-based optoelectronic devices. To improve the optical and electrical properties of the AlN crystals, it is critical to identify the impurities present in the crystal and understand their incorporation mechanism. This chapter will focus on identifying point defects leading to below bandgap energy luminescent bands and a commonly observed UV-C absorption band in AlN single crystals grown via physical vapor transport (PVT). A novel approach is presented to determine the impurities type and concentrations in single crystals, where PL, PLE, absorption spectra and SIMS data is used in combination with a DFT based defect solver program, which accounts for charge balance in the crystal and formation energies of the defects.

6.1 PVT Grown AlN Bulk Single Crystals

6.1.1 Historical Perspective

After initial reports, where AlN was incidentally synthesized as a byproduct when attempting to produce aluminum carbide by Briegleb and Geuther in 1862,¹ AlN gained significant interest in the early 1900's because it could be obtained using bauxite as the source material and decomposing it in alkali solutions produced aluminum oxide, aluminum hydroxide and ammonia, resulting in a series of patents by Ottokar Serpek^{118,119}. However, the high energy required to produce AlN, inhibited its commercialization as a process to produce ammonia. It later regained interest as a refractory material inert to reactions with aluminum at high temperatures (~ 1800 °C).¹²⁰ Fabrication methods to obtain AlN single crystals continued to be developed, where aluminum powder was heated up in a nitrogen

atmosphere leading to the reaction of aluminum vapor with nitrogen gas, forming a high density of small AlN single crystals^{120,121} Typical heating methods to reach temperatures above 1500 °C involved either arc lamp furnaces or resistive/inductive heating of a graphite crucible^{120–122} Further developments included the implementation of finely grinded AlN powder as the starting material in a sublimation condensation process.¹²³ Seeded growth on AlN single crystals was introduced resulting in increased single crystal size and reduced dislocation densities.^{124,125} Additionally, Herro et al. determined that seeded growth on the nitrogen polar face results in a more stable growth mode and allows for a more relaxed parameter window.¹²⁶

Currently, state of the art AlN bulk crystals are grown via physical vapor transport (PVT) in inductively heated vertical reactors, where the N-polar surface of AlN single crystals are implemented as seeds.^{127,128} For nitride based UV-C optoelectronic devices, single crystal AlN is the ideal substrate material. AlN substrates with dislocation densities in the low $\sim 10^3 \text{ cm}^{-2}$ are available.^{127,128} The latter and the low lattice mismatch to that of high aluminum content AlGaIn thin films of the highest quality.¹²⁹ However, point defects in the crystal lead to light absorption at energies lower than that of the bandgap energy which hinder their implementation in applications where transparency is necessary. In early studies the measured absorption and luminescence bands have been attributed to oxygen.^{130,131} Strassburg et al. and Bickermann et al., in separate studies, performed glow discharge mass spectrometry analysis on various PVT grown AlN single crystals and concluded that oxygen alone cannot explain the absorption and luminescent bands present in such samples.^{132,133} Carbon impurities in concentrations similar to that of oxygen were consistently measured in the AlN single crystals indicating that carbon must play a significant role in the optical properties of the crystals. A particularly strong absorption band centered at 4.7 eV is commonly measured in PVT grown AlN single crystals (*Figure 6-3*).^{130,131,134–139} The presence of photoluminescence peaks at 2.7 eV and 3.9 eV is observed in samples displaying the strong absorption band at 4.7 eV (*Figure 6-3*).^{134–137} The absorption band centered at 4.7 eV with an onset at 4.2 eV is only observed in AlN crystals which contain carbon concentrations higher than or comparable to the amount of oxygen and silicon.^{134–137,139} Hartmann et al determined that the oxygen to carbon concentration ratio needs to be equal or larger than 3 in order for the absorption band to be

completely suppressed. Additionally, the absorption coefficient at 4.7 eV decreases with total concentration of C + O for a given concentration ratio of the two.^{128,135} These results clearly show that carbon impurities are present in PVT grown AlN single crystals at significant concentrations and lead to the commonly observed absorption band at 4.7 eV. This is in contrast to the conclusions made by Slack et al (2002) where the increase of the absorption coefficient at 4.7 eV is attributed to an increase in the oxygen impurities.¹³¹ However, in the latter study no other extrinsic impurities are considered such as carbon, and the oxygen concentration measurements are limited to one sample. Collazo *et al*, attribute this absorption band to the presence of negatively ionized carbon impurities which incorporates as a nitrogen substitutional (C_N^-)¹³⁵. This conclusion is based on the calculations of defect formation energies as well as thermodynamic and optical transitions using density functional theory (DFT) which are in agreement with absorption and photoluminescence spectra as well as secondary ion mass spectroscopy (SIMS) measurements.^{135,136}

6.1.2 Absorption, PL and PLE Characterization

To identify point defects, it is necessary to consider the formation energy of all plausible point defects and defect complexes, while accounting for charge balance conservation. According to Van de Walle and Neugebauer, the chemical potentials can be related to partial pressures when growth conditions are near equilibrium.¹⁴⁰ This assumption is valid for AlN single crystals grown via physical vapor transport where growth temperatures are near the decomposition point of AlN. The partial vapor pressure of aluminum over AlN at 2100 °C under typical growth conditions is in the order of 50 mbar which is close to the Al vapor pressure over liquid aluminum of 120 mbar at the same temperature.^{141,142} Consequently, growth is expected to take place under aluminum rich conditions and accordingly assumed for the calculation of the formation energy of point defects in PVT grown AlN. A more detailed description on how the formation energies are calculated is discussed in section 2.3.1. If the concentration of the main impurities (i.e. carbon, oxygen and silicon in PVT grown AlN) in the crystal is known (i.e. via SIMS or GDMS), it is possible to estimate the concentration and type of point defects and defect complexes, based on charge balance conservation and their formation energy. These calculations were

performed in the research group of Dr. Irving at North Carolina State University and details on the methodology used for these calculations are published in part in the doctoral dissertation of B. Gaddy,⁵⁷ and the remaining details will be published in the doctoral dissertation of Joshua Harris. The larger the amount of possible point defects and defect complexes that are considered, the more representative the result of the actual AlN crystal. For the calculated defect concentrations in this work, a bulk of defect complexes are considered including, native point defects, substitutional carbon, oxygen and silicon in both Al and N lattice sites, and all first nearest neighbor complexes including the latter mentioned point defects (i.e. C_N-C_{Al} , C_N-O_{Al} , $Si_{Al}-O_N$, O_N-V_{Al} , etc...). The calculated point defect concentrations are listed in *Table 6-1*, where a fixed concentration of $8 \times 10^{18} \text{ cm}^{-3}$ oxygen, $7 \times 10^{18} \text{ cm}^{-3}$ silicon and $2 \times 10^{19} \text{ cm}^{-3}$ carbon is assumed as measured by SIMS. Only defect concentrations above $1 \times 10^{17} \text{ cm}^{-3}$ are listed since lower concentrations are not expected to contribute significantly to the optical properties of the crystal compared to defects in concentrations as high as $1 \times 10^{19} \text{ cm}^{-3}$. The results indicate that the main compensator for carbon point defects are oxygen and nitrogen vacancies, further supporting the conclusions made by Gaddy et al.¹³⁶ which attributed the 2.7 eV Luminescence to a DAP transition involving carbon and a nitrogen vacancy. The conclusion by Gaddy et al. is based on DFT calculations that show a relatively low formation energy of the nitrogen vacancy compared to other impurities and its charge compensating nature to the ionized carbon impurity.¹³⁶

Table 6-1: Calculated point defect concentration accounting for charge balance conservation and for a given measured concentration of C, O and Si.

| | C_N | V_N | O_N | Si_{Al} | $Si_{Al} + C_N$ |
|--|-------|-------|-------|-----------|-----------------|
| Defect Concentration ($\times 10^{19}/\text{cm}^3$) | 1.98 | 0.6 | 0.8 | 0.6 | 0.06 |

Theory predicts the presence of carbon on a nitrogen site (C_N), nitrogen vacancies (V_N), silicon on an aluminum site (Si_{Al}), oxygen on a nitrogen site (O_N) and a complex between carbon on a nitrogen site and silicon on an aluminum site ($Si_{Al} + C_N$). The calculated formation energy for the dominant point defects and defect complexes are displayed in *Figure 6-1* as a function of Fermi level energy. The charge state of the defect is represented by the slope and only the charge state with

the lowest energy of formation for a particular defect at a given Fermi level energy is displayed.

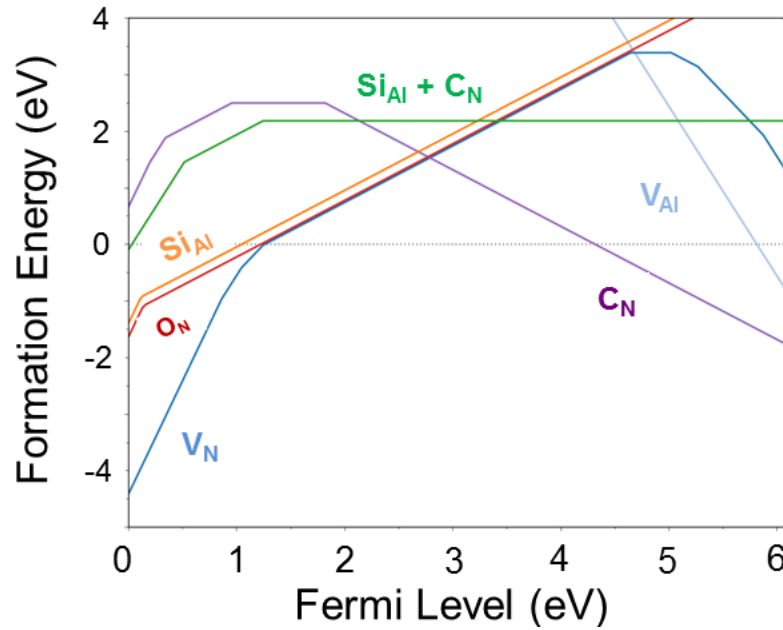


Figure 6-1: Point defect formation energy as a function of fermi level energy for various likely point defects present in PVT grown AlN.

From *Figure 6-1*, the thermodynamic transition energies for the respective point defects can be extracted, which correspond to the energy values, where changes in the slope of the formation energy are observed. Perhaps for a more intuitive perspective, the thermodynamic transition energies can be represented as energy states within the bandgap as illustrated in *Figure 6-2*.

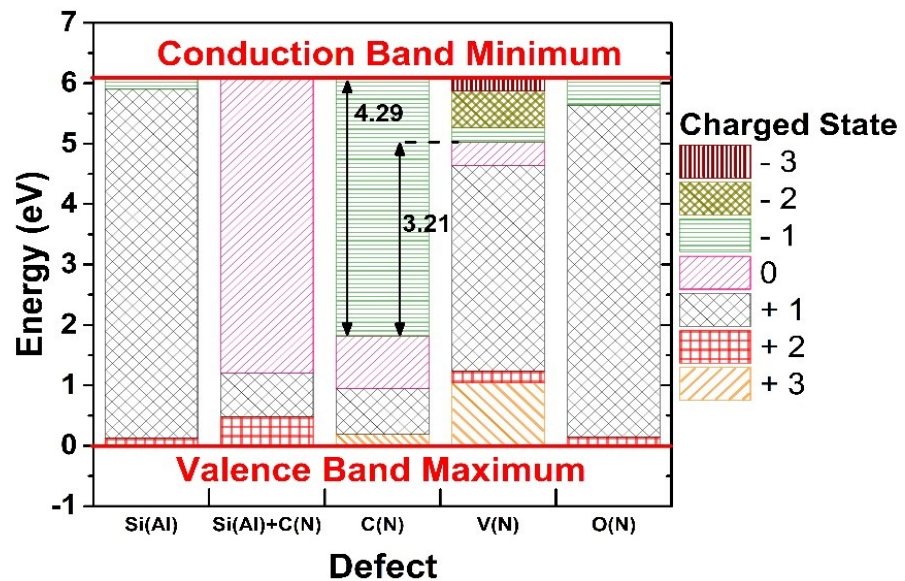


Figure 6-2: Schematic displaying the thermodynamic transition energy states for the respective point defects, as horizontal lines, referenced to the valence band maximum.

In *Figure 6-2* a bandgap energy of 6.1 eV is assumed for AlN and the calculated thermodynamic transition energies for $C_N^- \rightarrow C_N^0$ and $V_N^0 \rightarrow V_N^-$ are 1.81 eV and 5.02 eV above the valence band maximum (VBM) respectively. From *Figure 6-2* it is clear that the only band to defect transition with an energy difference close to 4.2 eV is the transition involving C_N^- to C_N^0 and the conduction band minimum (CBM). *Figure 6-3* displays the absorption coefficient spectra overlapped with the photoluminescence spectra of the studied PVT grown AlN single crystal. An absorption band centered at 4.7 eV is revealed with an onset at 4.2 eV. The absorption coefficient plateaus at 4.5 eV until 4.8 eV where it then decreases until 5.1 eV. For photon energies larger than 5.1 eV the absorption coefficient increases again. An excitation energy of 6.4 eV is utilized to record the photoluminescence spectra displayed in *Figure 6-3*. Two main luminescence bands centered at 3.9 eV and 2.7 eV are observed. When fitting the asymmetric band centered at 2.7 eV an overlapping lower energy luminescence band centered at 2.5 eV is estimated. An additional luminescent band centered at 4.5 eV is also present, where the intensity is significantly smaller in magnitude and will be discussed in more detail later in this section.

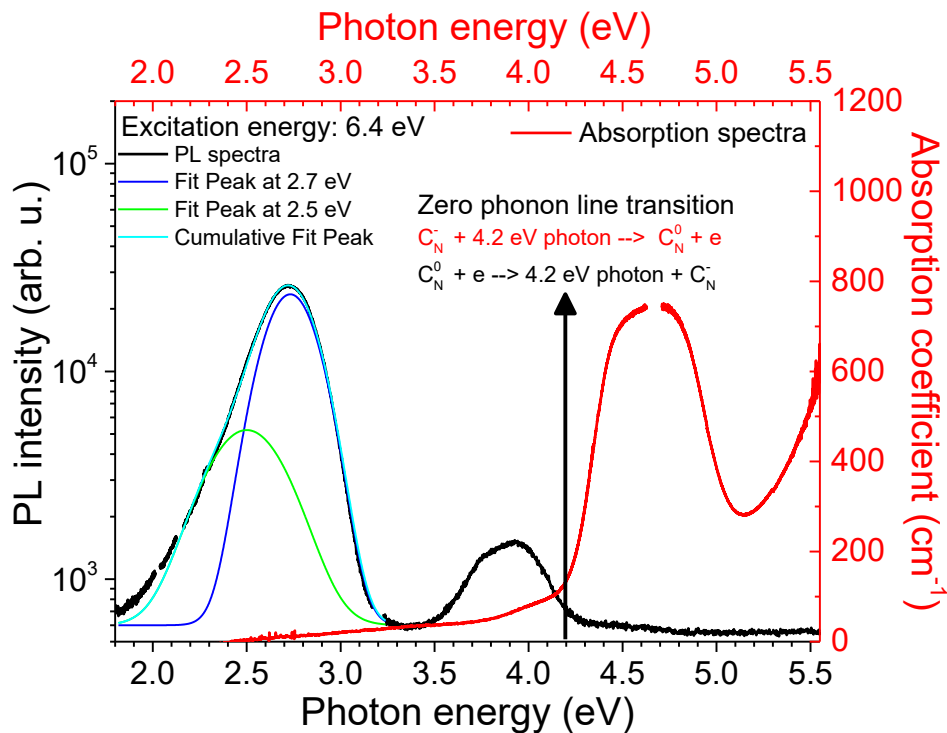


Figure 6-3: Photoluminescence spectra (black) overlapped with the absorption spectra (red) of a PVT grown AlN single crystal.

The minimum photon energy for the excitation of a point defect in a particular charged state and the maximum photon energy for the respective radiative recombination of the generated electron hole pair are expected to be equal to the thermodynamic transition energy of the point defect and it is typically addressed as the zero phonon line (ZPL) energy (section 2.3.2 and *Figure 2-7*).⁶⁷ According to the Franck-Condon approximation, the probability for the optoelectronic transition at this energy is proportional to the overlap between the 0th quantum number vibrational wave functions of the initial and final states at their equilibrium coordinate position.⁶⁵ For differing equilibrium coordinate positions of the initial and final state, the vibrational wave function overlap is expected to be small between the two charged states of a point defect in AlN, leading to a significantly reduced emission and absorption probability at this energy. When comparing the absorption with the PL spectra in *Figure 6-3*, indeed the estimated high energy edge of the PL band centered at 3.9 eV matches the calculated thermodynamic transition energy of 4.2 eV for the C_N^- point defect as well as the onset of the absorption band centered at 4.7 eV. In spite of these strongly suggestive observations, it is not possible to make a definite conclusion based on the above bandgap excitation PL spectra and the measured absorption spectra due to the large number of possible defects and their overlapping electro-optical transition energies. To precisely determine the electro-optical dynamics between the luminescence and absorption centers, photoluminescence excitation spectroscopy measurements were conducted. In *Figure 6-4* a color coded logarithmic intensity contour map is shown where the horizontal axis represents the detection energy of the sample's photoluminescence ranging from 1.95 eV to 4.5 eV while the vertical axis describes the energy of the excitation light source which spans from 3.6 eV to 5.5 eV. The PLE spectra shows the onset of the luminescence band centered at 3.9 eV at an excitation energy of 4.2 eV. This is in excellent agreement with the model where C_N^- is the point defect responsible for the UV absorption band as well as the luminescence band centered at 3.9 eV. This is more easily observed in *Figure 6-5* where single spectra were extracted from the contour map. The vertical lines in *Figure 6-4* correspond to the red PLE curves in *Figure 6-5* while the horizontal lines in *Figure 6-4* are displayed in black/grey curves in *Figure 6-5* and represent the PL spectra for a given excitation energy. Looking at the PLE spectra with the detection energy fixed at 3.93 eV in *Figure 6-5*, an exponential increase in the intensity is observed when the

excitation energy reaches 4.2 eV and peaks at 4.5 eV where it plateaus. Furthermore the PL spectra with 4.5 eV excitation energy shows that the high energy edge of the luminescence band centered at 3.9 eV matches the onset of the PLE spectra with 3.93 eV detection energy at 4.2 eV. This is expected under the Frank-Condon approximation as previously described. These results are direct evidence linking the 3.9 eV PL band and the 4.7 eV absorption band to a common defect with a thermodynamic transition energy of 4.2 eV.

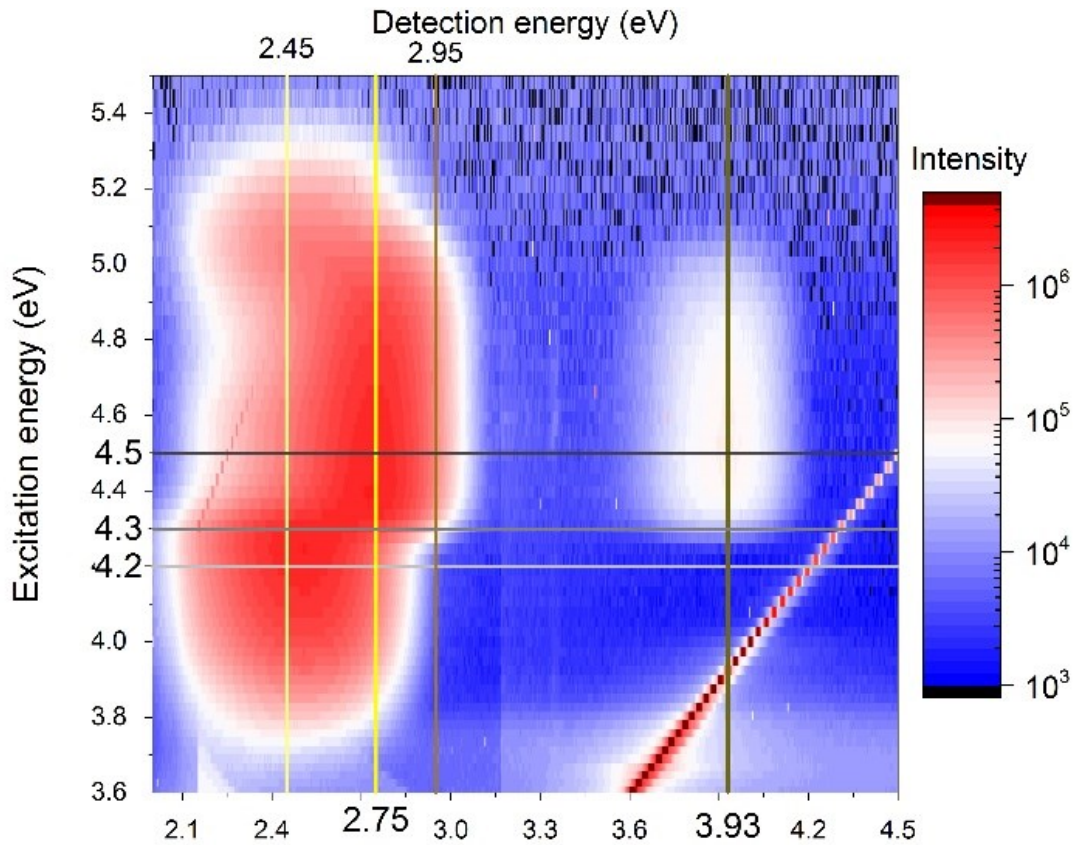


Figure 6-4: Color coded logarithmic intensity 2D map photoluminescence excitation spectroscopy measurements of an AlN single crystal recorded at 5 K. The vertical lines correspond to PLE spectra for a fixed detection energy and are displayed as red curves in Figure 6-5. Horizontal lines correspond to PL spectra at a fixed excitation energy and are displayed in Figure 6-5 as black curves.

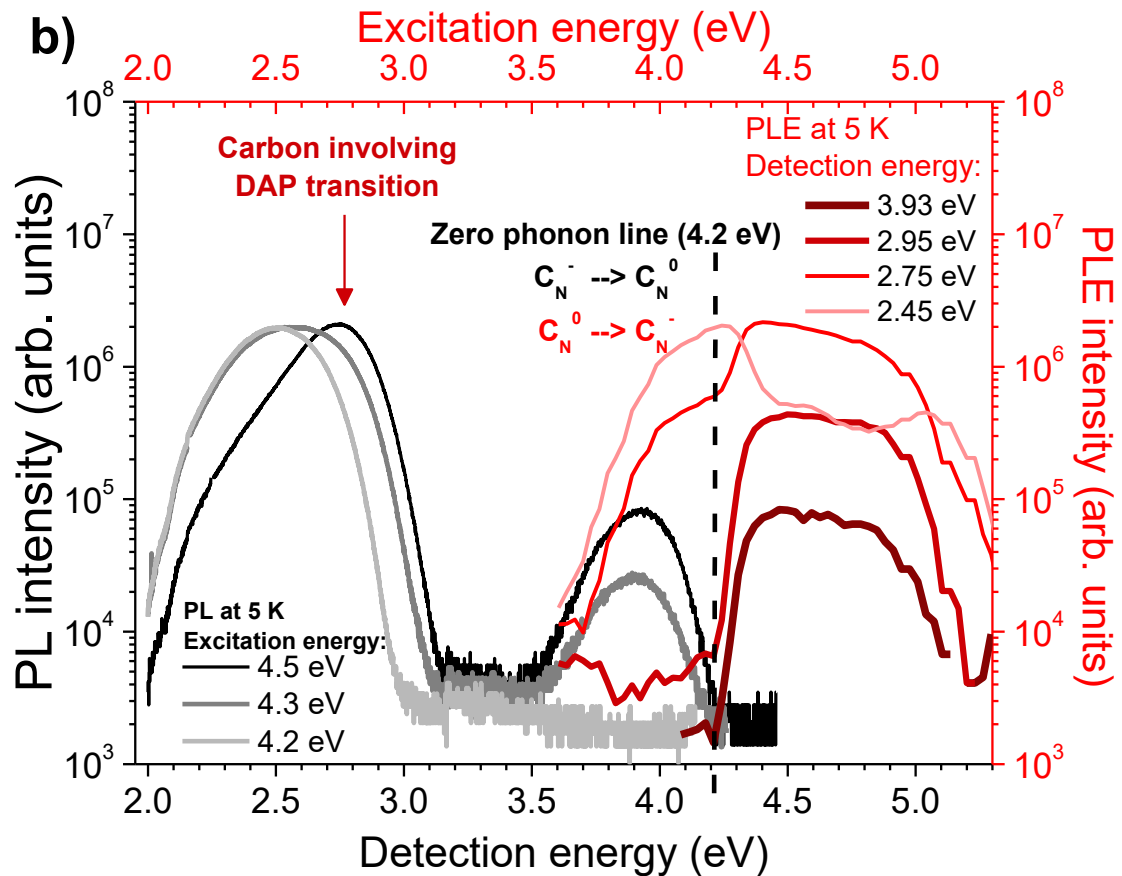


Figure 6-5: Photoluminescence spectra (black) for various excitation energies, overlapped with photoluminescence excitation spectra (red) for various detection energies.

The PLE measurements show that C_N^- is also involved in the radiative transition leading to the luminescence band centered at 2.7 eV. This is evident from the PLE curve in *Figure 6-5* with fixed detection energy at 2.95 eV which shows an identical excitation channel to that of the 3.9 eV luminescence band. The detection energy of this PLE spectra was purposely shifted from the peak emission at 2.7 eV to 2.95 eV in order to avoid any intensity originating from the overlapping luminescence sideband with peak emission at 2.5 eV as is observed in the PLE spectra with detection energy at 2.75 eV. The onset excitation energy for the 2.5 eV luminescence band is measured at 3.6 eV excitation energy, obtained from the PLE spectra with detection energy at 2.45 eV. The origin of this luminescence band is not clear and further studies are necessary. From the PL spectra in *Figure 6-5* with 4.5 eV excitation energy, the ZPL energy of the 2.7 eV luminescent band is estimated at 3.1 eV. Assuming the nature of this PL band to be a donor acceptor pair (DAP) transition involving carbon, a deep donor state at 5.0 eV above the valence band maximum is predicted based on the energy level of the C_N^- acceptor state at 1.9 eV

above the VBM. From the thermodynamic transition energy diagram (*Figure 6-2*) this is in good agreement with the calculated thermodynamic transition energy state at 5.0 eV for the nitrogen vacancy (V_N) from V_N^+ to V_N^0 . Furthermore, power dependent PL measurements reveal the presence of a luminescence band centered at 4.5 eV (*Figure 6-6*). As the pulse peak power density is increased and defect states are saturated a PL band centered at 4.5 eV appears, where the highest energy edge of this band is estimated at 5.0 eV in agreement with the predicted deep donor energy state involved in the DAP luminescence band centered at 2.7 eV.

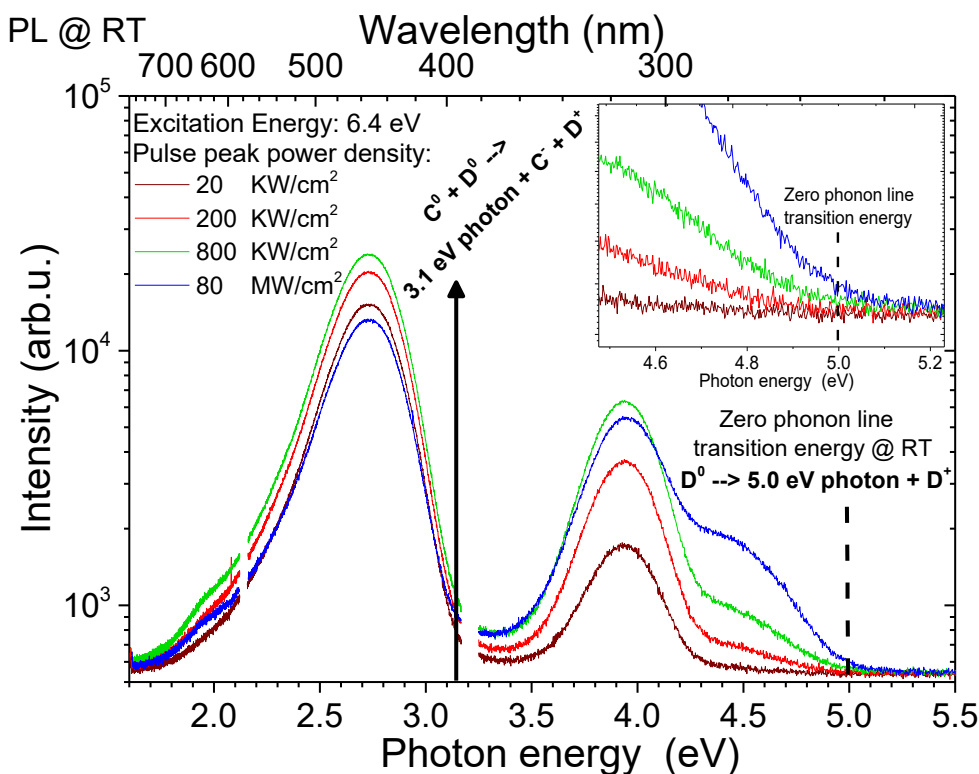


Figure 6-6: Power dependent photoluminescence measurements for above bandgap excitation.

In summary, the UV absorption band at 4.7 eV and the luminescence bands at 2.7 eV and 3.9 eV are linked to the same defect state with a thermodynamic transition energy of 4.2 eV through photoluminescence excitation spectroscopy (PLE). Power dependent photoluminescence (PL) measurements reveal the presence of an energy state within the bandgap with a 5.0 eV thermodynamic transition energy in agreement with the predicted energy state for the donor acceptor pair transition (DAP) leading to the 2.7 eV luminescence band and the calculated thermodynamic transition energy for the nitrogen vacancy (V_N). A novel approach is presented to determine the impurities type and concentrations in the crystal where PL, PLE, absorption spectra and SIMS data is used in combination with a DFT based defect

solver program which accounts for charge balance in the crystal and formation energies of the defects.

6.1.3 High Temperature Absorption Spectra

As part of my PhD program, I was responsible for building a setup for temperature dependence transmission spectroscopy, allowing for temperatures from room temperature up to at least 900 °C. A detailed description of the setup is given in section 3.1.3. The setup however, is not limited to transmission spectroscopy, but can also be used for temperature dependent photoluminescence spectroscopy.

6.1.3.1 GaN Epitaxial Layers

As an initial test of the experimental setup and to confirm the bandgap value of GaN near growth temperatures, a GaN epitaxial film deposited on a sapphire substrate was characterized. One interest in measuring the absorption edge energy of GaN near growth temperatures (1040 °C), was in establishing the viability to use an InGaN laser diodes with 445 nm (2.8 eV) emission wavelength (energy) for point defect reduction via defect quasi Fermi level control.^{143–145} *Figure 6-7* displays the measured lamp spectra when placing a GaN thin film sample in the optical path, where the temperature of the GaN sample is varied in the range from room temperature to 874 °C. The interference fringes expected for a heteroepitaxial thin film are observed and the absorption edge at room temperature near 3.4 eV is measured. From the interference fringes a film thickness of 2 μm is calculated, in agreement with growth rate calculations. Using the film thickness, the transmission spectra and the dispersion relation for GaN, the absorption coefficient can be calculated and plotted for different temperatures as a function of wavelength (*Figure 6-8*).

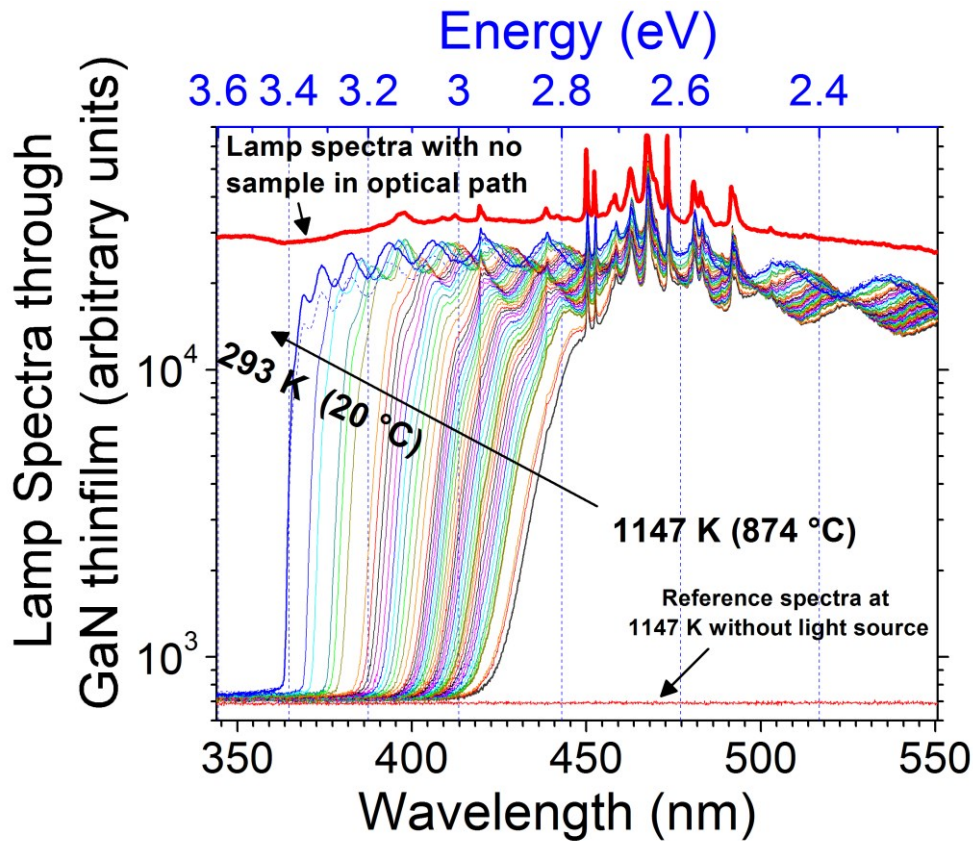


Figure 6-7: Spectra of a UV-enhanced Xenon Arc lamp measured after passing through an epitaxial GaN layer deposited on a sapphire substrate as a function of the GaN temperature.

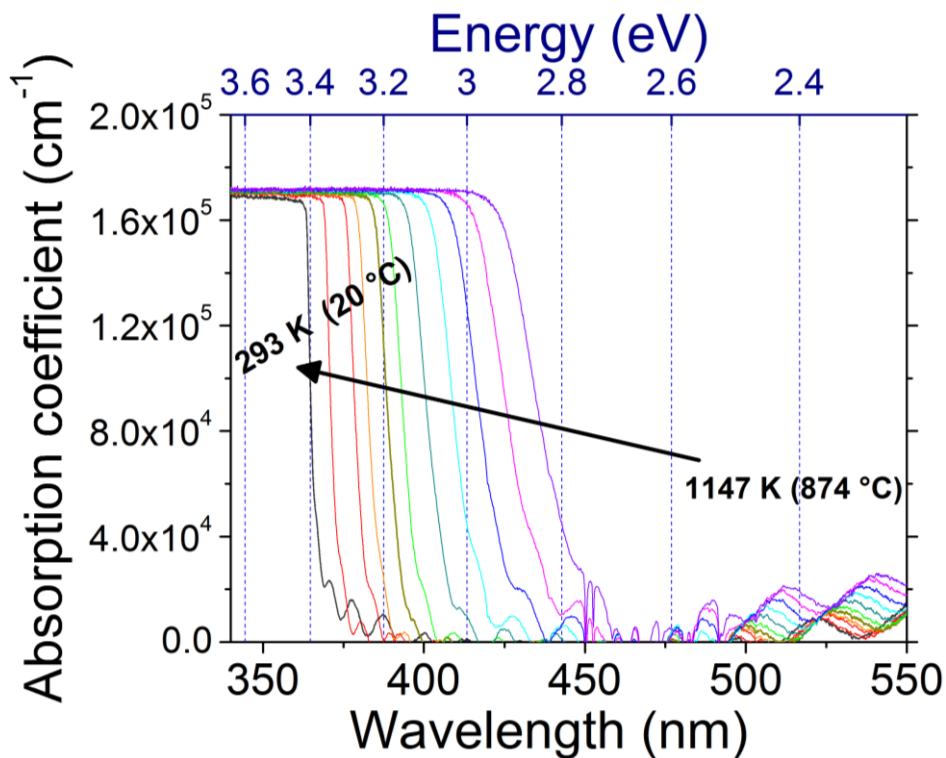


Figure 6-8: Temperature dependence of absorption coefficient spectra. The spectra are not corrected for reflection.

From *Figure 6-8* a clear red-shift of the absorption edge can be observed for increasing temperature following the Varshni-Shift.¹⁴⁶ An absorption coefficient value $> 1.6 \times 10^5 \text{ cm}^{-1}$ is measured for above bandgap photon energies. The measured constant value at $1.7 \times 10^5 \text{ cm}^{-1}$ is a measurement artifact due to the background noise level of the detector, indicating the light intensity from the lamp source was completely absorbed and does not represent a real absorption coefficient value. To precisely determine the GaN temperature dependent bandgap energy, the Tauc relation can be plotted (*Figure 6-9*), from which the bandgap energy can be extracted from the x-axis intersect with extrapolated linear fit near the band edge.^{147,148}

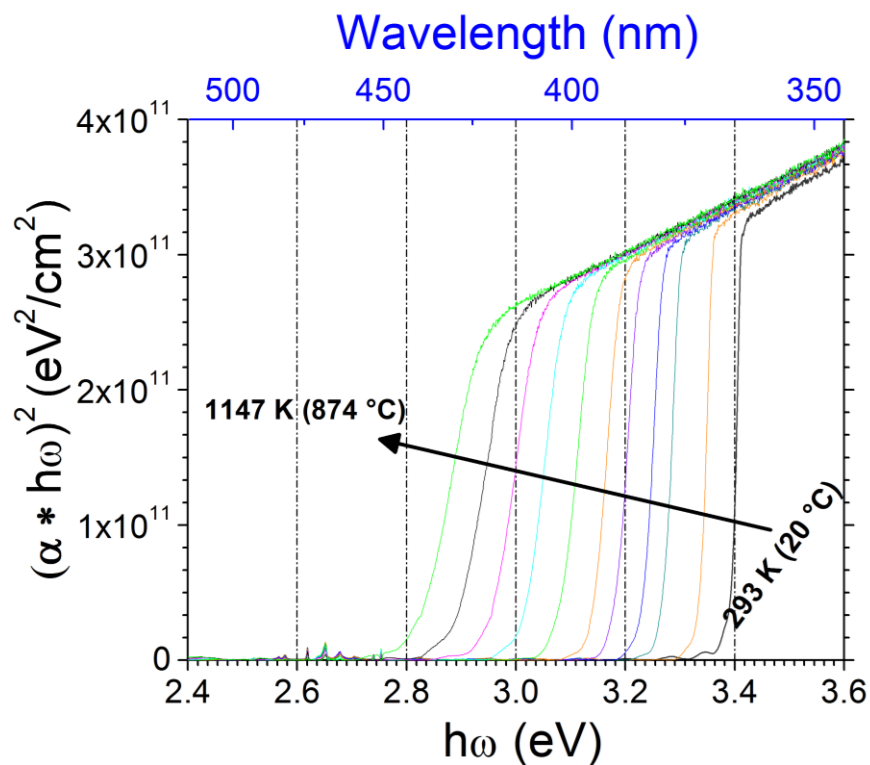


Figure 6-9: Tauc relation for temperature dependent transmission spectra measured for a GaN epitaxial thinfilm.

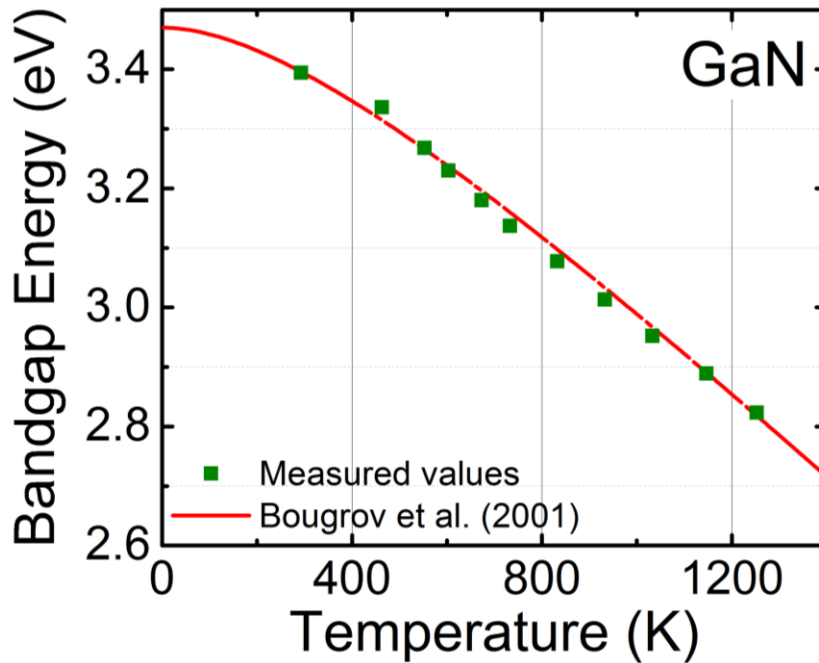


Figure 6-10: Bandgap energy of a GaN epitaxial film as a function of temperature, compared with the Varshni model fitted with literature values.

Once the bandgap energy has been determined for each temperature spectra, the values can be plotted as a function of temperature. The measured values are in excellent agreement with the Varshni energy shift model and agree with previously experimentally established values. A bandgap energy of 2.77 eV is calculated at growth temperatures (1040 °C), where an absorption coefficient $\alpha > 1.6 \times 10^5 \text{ cm}^{-1}$ demonstrating that a 445 nm (2.8 eV) emission wavelength InGaN laser diode can be used for carrier generation by photoexcitation.

6.1.3.2 PVT AlN Single Crystals

Having established that the experimental setup is well calibrated, an experiment was conducted where bulk AlN single crystals grown via PVT were investigated. In the previous section (section 6.1.2), the point defects in AlN single crystals exhibiting a strong absorption band in the UV-C spectra and a high carbon concentration were investigated. It has been found that by introducing silicon and/or oxygen such that their concentration exceeds that of carbon, the UV-C absorption band can be suppressed.^{128,137,149} DFT calculations, have predicted that silicon and oxygen substitutional point defects have a stable DX^- energy state which they populate for Fermi level energies near the conduction band, which is the case for AlN crystals with higher oxygen and/or silicon concentrations than carbon. It has been argued

that these states can act as long-lived traps inhibiting the recombination of photo-generated carriers from the C_N^- point defect back to its original state, and thereby quenching the UV-C absorption band. In this experiment a PVT grown AlN single crystal exhibiting UV-C transparency with a higher oxygen and/or silicon concentration than carbon, is heated up to 900 °C with the purpose of decreasing the lifetime of the possible long lived DX^- trap state. If such trap states are present in the crystal, it is expected that with increasing temperature the repopulation rate of the C_N^- will increase exponentially with temperature and thereby giving rise to the commonly observed UV-C absorption band. For a silicon in aluminum substitutional point defect, an ionization energy E_b of 0.25 eV has been determined for the Si DX^- and 0.34 eV calculated for the O DX^- state.^{57,150} For these ionization energies, an increase in temperature from 293 K to 1070 K corresponds to an increased transition probability by a factor of 1.3×10^3 for silicon and 1.8×10^4 for oxygen.

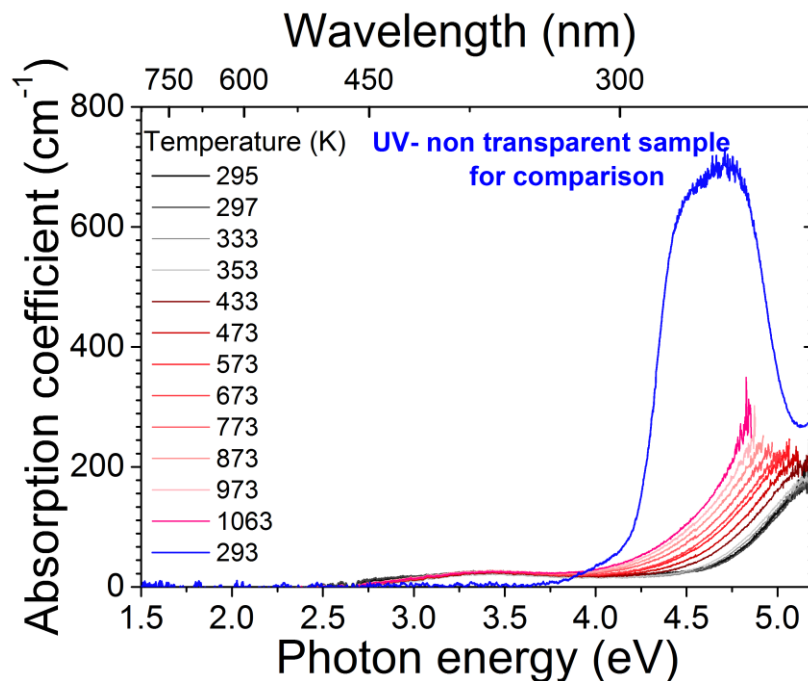


Figure 6-11: Absorption spectra for an AlN single crystal with higher oxygen concentration than carbon for different temperatures in the range from 295 K to 1063 K. For comparison a “UV non-transparent” sample containing higher carbon impurities than oxygen and silicon is displayed.

Figure 6-11 displays the absorption spectra for an AlN single crystal with a higher oxygen concentration than carbon. It is clear that the UV-C absorption band is not present in the AlN crystal with higher oxygen concentration and does not appear with increasing temperature. These results indicate that a long lived oxygen or silicon DX^- like trap state is not responsible for the suppression of the UV-C

absorption band, which is measured in crystals with a higher carbon concentration than oxygen and silicon. Moreover, the result suggests that for high oxygen and/or silicon concentrations, where a Fermi level energy near the conduction band is expected, the formation energy for a different carbon point defect configuration is more favorable than C_N^- . However, DFT calculations of the formation energy for nearest neighbor complexes involving carbon and substitutional point defects in both lattice sites, predict higher formation energies. Second nearest neighbor complexes including carbon remain a possibility among a vast pool of possible point defects, however no DFT calculations for such point defects have been performed to date.

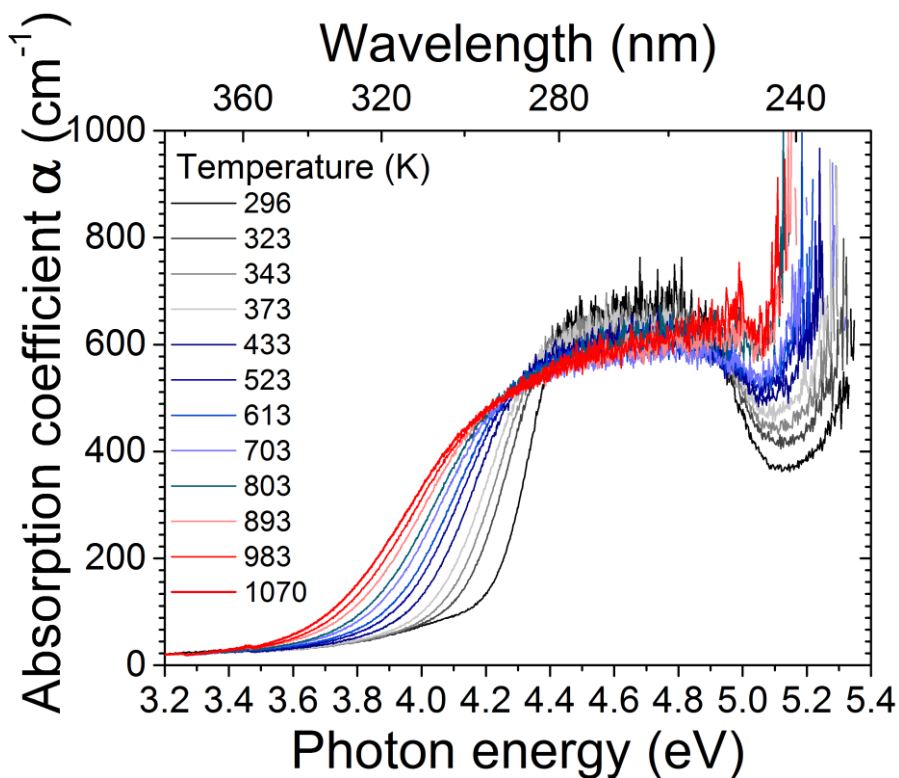


Figure 6-12: Absorption spectra for an AlN single crystal with a higher carbon concentration than oxygen and silicon for a temperature range from 296 K to 1070 K.

The absorption spectra for various temperatures for an AlN single crystal with a higher carbon concentration than oxygen and silicon, is displayed in *Figure 6-12*. At the high energy edge of the absorption spectra, the tail of the fundamental absorption edge is observed and the corresponding Varshni like red shift, where a bandgap energy of 5.2 eV at 1070 K is calculated when using literature parameters for the Varshni shift.¹⁵¹ A model explaining the increase in the FWHM of the width of the absorption band as well as the broadening towards lower energies of the absorption

onset is described in the literature.⁵⁹ Otherwise, no significant change in the absorption band is observed.

In summary, a transmission spectroscopy setup was built capable of measuring at temperatures, at least, up to 900 °C. The bandgap energy of GaN was measured up to 874 °C, where the parameters obtained from the measurements for the Varshni shift model are in agreement with literature. Finally, high temperature absorption spectra of AlN single crystals with a higher oxygen and/or silicon concentration than carbon, indicate long lived DX⁻ like states are not responsible for the quenching of the UV-C absorption band.

7 UV Laser Light as Second Harmonic Generation

Lasers emitting in the ultraviolet spectrum are desired for a variety of applications, including photochemical labeling, bio-sensing, nanolithography, medical surgery, micromachining, Bragg gratings, and many others.⁹⁷ Available UV laser systems are expensive inefficient, stationary, large, and require frequent maintenance. Although many advances have been made toward the fabrication of electrically injected AlGaIn semiconductor based UV-C laser diodes, doping, carrier injection, and defect control are still challenging.^{31,143} An alternative approach to compact UV-C lasers is to exploit frequency doubling via second harmonic generation (SHG). AlN is an excellent candidate for the generation of UV-C laser light via SHG and a variety of other nonlinear optical applications due to its large second order nonlinear susceptibility coefficient along the c-axis of 7.7 pm/V, high thermal conductivity (320 W/mK), and a wide transparency window (205 nm and above).^{132,152,153} This enables the possibility for high conversion efficiency, high power damage threshold and wide wavelength tunability. Birefringence phase matching is not accessible in III-Nitrides and other phase matching techniques need to be employed. In this chapter, SHG results in AlN waveguides using modal dispersion phase matching (MDPM) and quasi phase matching (QPM) are presented.

7.1 Modal Phase Matched SHG

An alternative approach to birefringence phase matching, which is not accessible for III-Nitrides, is modal dispersion phase matching, as described in section (2.1.3). Some benefits for employing this phase matching technique, include the facility to fabricate, high quality single polar AlN waveguides, only limited by lithography and dry etching, which are mature technologies. The drawback of this phase matching technique, lies in the lower conversion efficiency due to typically small overlap of the wave-guided modes for the fundamental and second harmonic waves (typically in single digit percent).⁴⁷ *Figure 7-1* displays a DIC optical microscope image of typical Al-polar AlN waveguides, where the AlN film was deposited via MOCVD as described in section 4.2 and where the waveguides were fabricated via standard masked photolithography using negative photoresist and reactive ion etching in BCl_3 and Cl_2 .

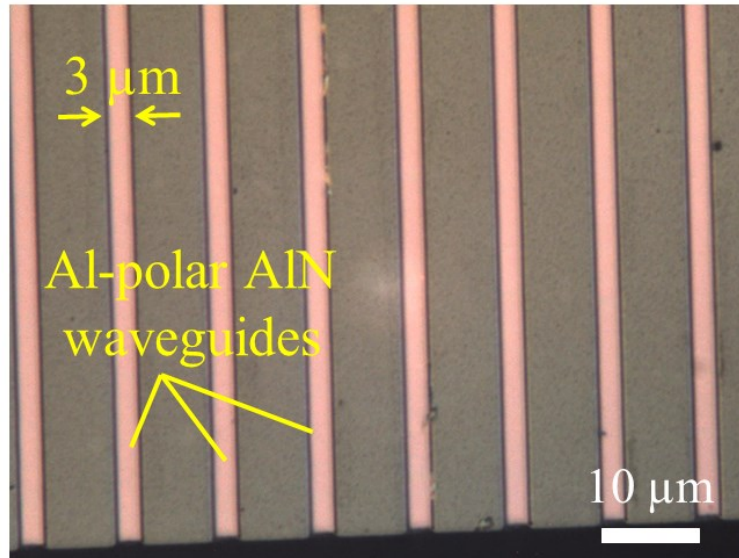


Figure 7-1: DIC microscope image of Al-polar AlN waveguides for MDPM SHG.

The calculated dispersion relation for the different waveguide modes of the fundamental and second harmonic waves in 10 μm wide and 550 nm thick Al-polar AlN waveguides were reported in a publication by Troha et al. and are displayed in. MDPM SHG measurements in the UV spectral range are displayed.

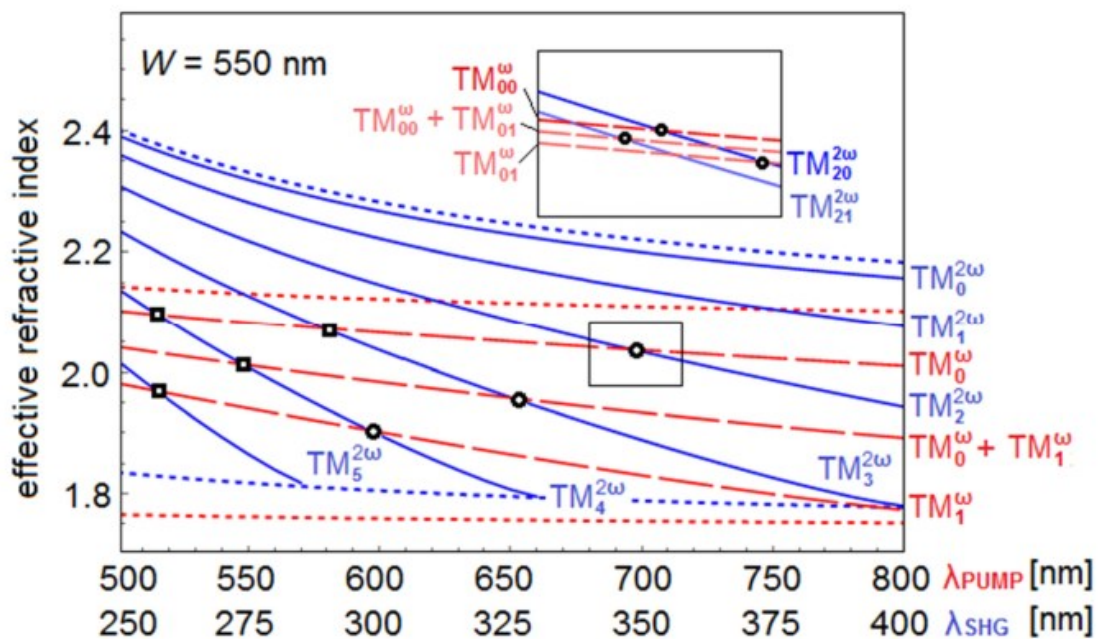


Figure 7-2: Dispersion relation of the fundamental and second harmonic waveguide modes for a 10 μm wide and 550 nm thick Al-polar AlN waveguide, taken from a publication by Troha et al.⁴⁷

The corresponding MDPM SHG measurements are displayed in Figure 7-3 where a good agreement between theory and experiment is measured.

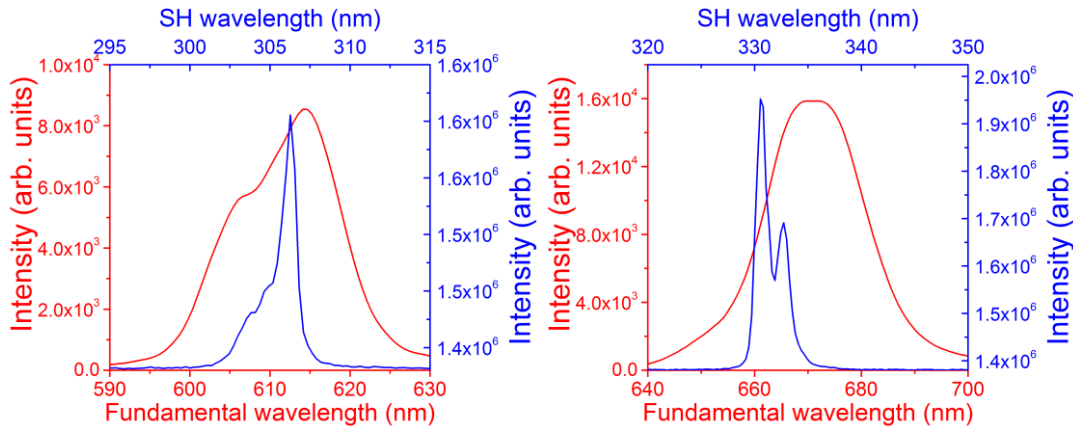


Figure 7-3: MDPM SHG measurements using a 10 μm wide and 550 nm thick Al-polar AlN waveguide.⁴⁷

More details on the MDPM SHG measurements are described by Troha et al.⁴⁷ and additional MDPM measurements including in GaN waveguides, will be published in her doctoral dissertation.

These results demonstrate the feasibility to employ AlN waveguides for UV laser light generation down to 305 nm, and where theoretical calculations indicate that MDPM SHG in the UV-C below 300 nm should be allowed in principle.

7.2 Quasi Phase Matched SHG in AlN LPS Waveguides

Quasi-phase matching, where the second order nonlinear coefficient of non-centrosymmetric crystals is periodically or aperiodically modulated, offers the widest range of accessible nonlinear interactions, is the most efficient phase matching technique and allows the use of nonlinear materials with weak birefringence.^{48–50,154} This technique had been limited due to difficulties in fabricating periodically inverted nonlinear crystals with periodicities down to the nanometer scale, and in achieving high quality interfaces between the inverted domains. After remarkable advances in lithography and processing technology since the late 1970's, periodically poled ferroelectric oxide crystals are now produced on a daily bases and periods as short as 1.4 μm are achieved.^{155–159} A wealth of quasi-phase matched nonlinear interactions have been demonstrated using such crystals.^{160–163} For integrated optics, thin wave-guiding layers, in the order of hundreds of nanometers, which can be obtained using the well-established semiconductor thinfilm technology are required. Progress is being made in ferroelectric oxides to meet these demands, however it still remains a challenge¹⁶⁴.

The III-V compound semiconductors are the obvious alternative, since they already make up a significant portion of electronics and optoelectronics, and have excellent nonlinear optical properties. Being non-ferroelectric, the main challenges for this material system lies in periodically inverting the crystal while maintaining high quality interfaces between the alternating polar domains and achieving an optically smooth surface. AlGaAs has pioneered the field with all-epitaxial periodically oriented GaAs based waveguides being demonstrated nearly two decades ago by Ebert et al.¹⁶⁵ The nonlinear properties of III-Arsenides excel in the 1 – 16 μm spectral region where, using thick ($> 450 \mu\text{m}$) periodically poled GaAs crystals, second-, sum- and difference-frequency generation have been demonstrated with efficiencies up to 50% and an output average power reaching 7.7 W at 100 kHz pulse repetition rate.^{166,167} The material system is limited to photon energies below 2 eV and still faces challenges in efficient waveguiding structures inhibiting their implementation in integrated optics. The III-Nitrides will provide semiconductor-based quasi-phase matching structures which can cover nonlinear optical processes from 14 μm down to 0.2 μm .^{97,112,113} This range covers all wavelengths used in telecommunication and allows for frequency conversion from/to wavelengths as short as 205 nm which significantly reduces the size limitation for photonic circuits. Already, efficiency, thermal stability and high power are moving the semiconductor industry towards AlGaN based electronic devices.^{168,169} Simultaneously, AlGaInN-based optoelectronics are reaching maturity and have revolutionized the lighting industry. It is reasonable to envision, AlGaInN-based integrated optics where periodically poled nitride-based waveguides serve as quasi-phase matching structures for nonlinear optical interactions.

In this section, quasi-phase matched UV second harmonic generation at 344 nm and 386 nm, using 500 nm and 250 nm thick, and 10 μm periodic AlN lateral polar structure-based waveguides, respectively, is demonstrated for the first time. These results mark the beginning of III-Nitride based waveguide structures for quasi phase matching applications and is a step towards the realization of on-chip and chip-to-chip optical interconnects.

7.2.1 10 μm Periodicity

The 3D plotted AFM image in *Figure 7-4* shows a small section of the waveguides which were etched into a 10 μm periodic AlN LPS grown at 1500 $^{\circ}\text{C}$ (section 5.1.3, *Figure 5-29*). The waveguides are 500-550 nm thick and $\sim 4 \mu\text{m}$ wide. The measured average RMS value for the waveguides surface is 11 nm.

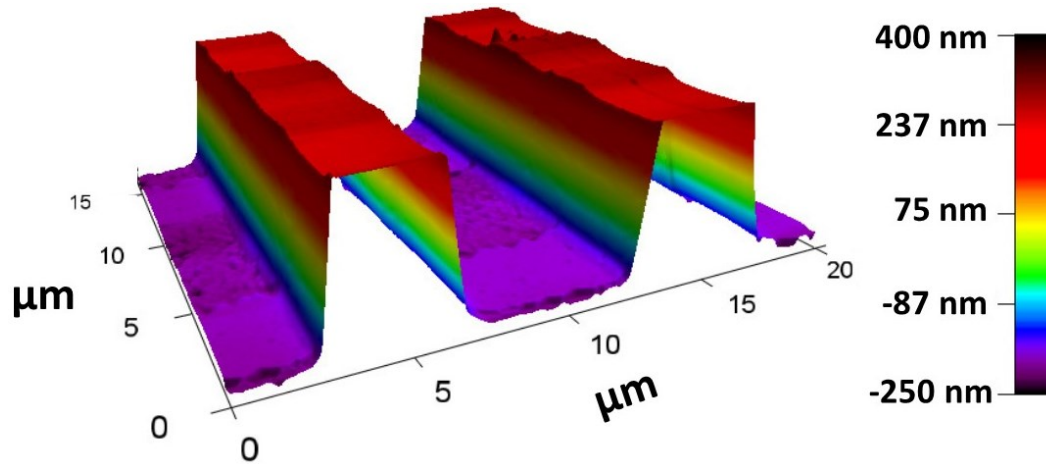


Figure 7-4: 3D AFM image with color-coated height scale of 500 nm - 550 nm thick and 4 μm wide AlN LPS-based waveguides.

Using a computer code developed by T. Troha, the dispersion relation for the fundamental and second harmonic waves are calculated for a given waveguide dimension. Each side of equation (5.1.2) is then plotted to illustrate the conditions for which QPM is expected (*Figure 7-5*). Theory predicts 3rd and 5th order QPM SHG at 340 nm and 473 nm respectively for the TM_0 modes of the fundamental and second harmonic waves in a 10 μm periodic 540 nm thick AlN LPS-based waveguide and 5th and 7th order QPM SHG at 377 nm and 453 nm respectively for a 10 μm periodic 220 nm thick AlN LPS-based waveguide. The model utilized to calculate the QPM conditions is according to the theory described in section 2.1.

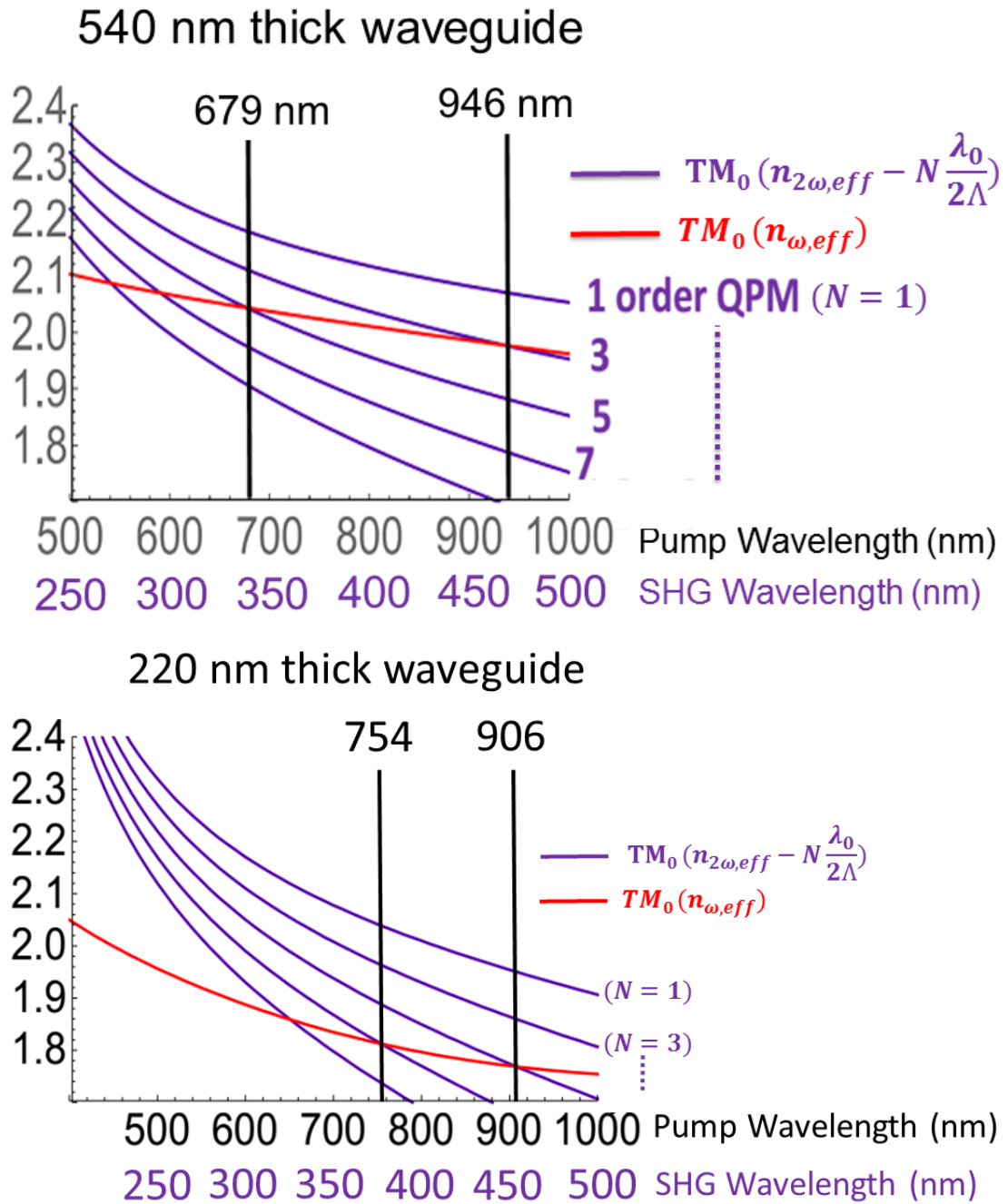


Figure 7-5: Dispersion relation for the fundamental (red) and second harmonic (purple) TM_{00} wave mode for a 220 nm thick waveguide.

Figure 7-6 shows a top view 2D grayscale scattering intensity image of the laser light traveling through a 1 mm long AlN LPS-based waveguide with 10 μm periodicity. Strong scattering is observed at the coupling facet and some appreciable amount of scattering is evident at the out-coupling facet. The scattering intensity profile along the waveguide is displayed in Figure 7-6 (bottom) for a 100 μm segment of the 1 mm long waveguide. An obvious periodic pattern in the scattering intensity profile along the waveguide is observed matching the AlN LPS periodicity of 10 μm , which highlights the importance of achieving a smooth waveguide surface

to minimize scattering losses. The remaining intensity of the fundamental laser light at the out-coupling facet, is filtered out and the SHG light laser light is guided to the detection system.

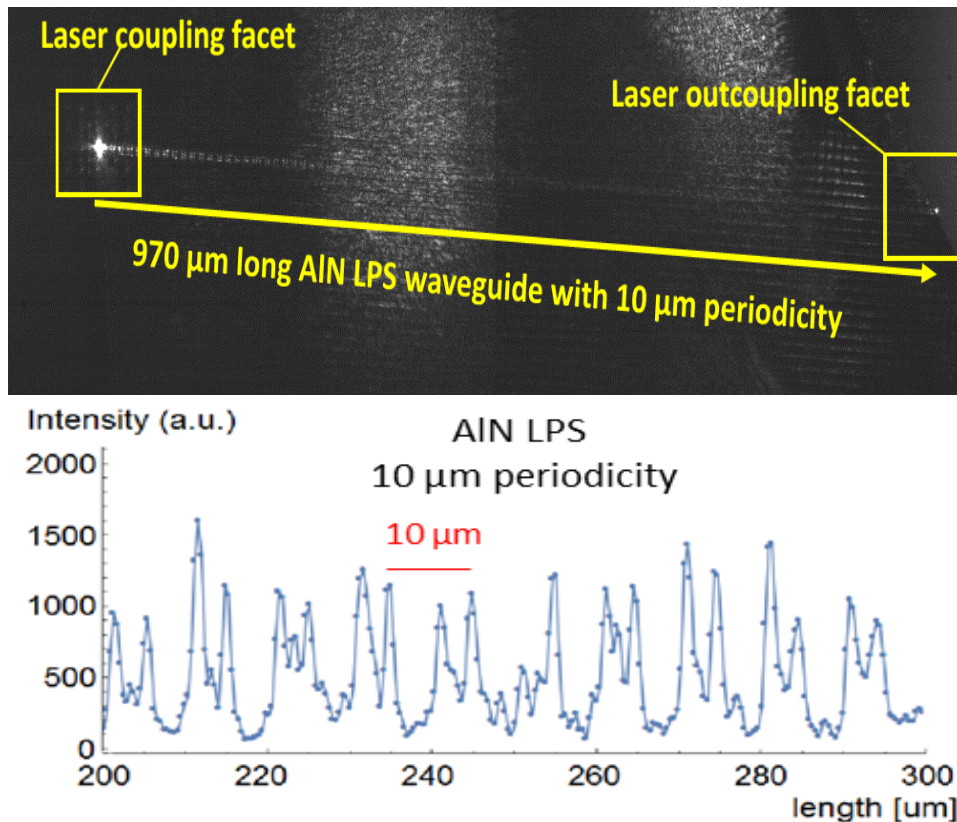


Figure 7-6: 2D top view grayscale scattering intensity profile of the fundamental laser light propagating through the 10 μm periodic AlN LPS-based waveguide (Top). 1D scattering intensity profile for a line-scan section along the waveguide surface.

QPM SHG is demonstrated at 344 nm and 471 nm (Figure 7-7) for the 500 nm – 550 nm thick AlN LPS –based waveguide and at 386 nm and 452 nm (Figure 7-8) for the 200 nm – 250 nm thick AlN LPS-based waveguide, in agreement with the calculated values (Figure 7-5). The LPS structures will be characterized and analyzed in more detail, where the results will be published in the doctoral dissertation of Tinkara Troha. Slight differences between theory and experiment may arise from the difficulty to define a waveguide thickness due to the surface roughness, and from the planar waveguide approximation, which neglects the propagation of lateral modes arising from the finite width of the waveguide. More significantly, according to theory, second harmonic generation for wavelengths above 375 nm is not accessible through MDPM for the fabricated waveguide dimensions.⁴⁷ Additionally, no MDPM SHG is observed experimentally for single polar AlN waveguides of the same thickness at wavelengths above 375 nm,

confirming the nature of the SHG measurements presented in this work to be QPM SHG.⁴⁷

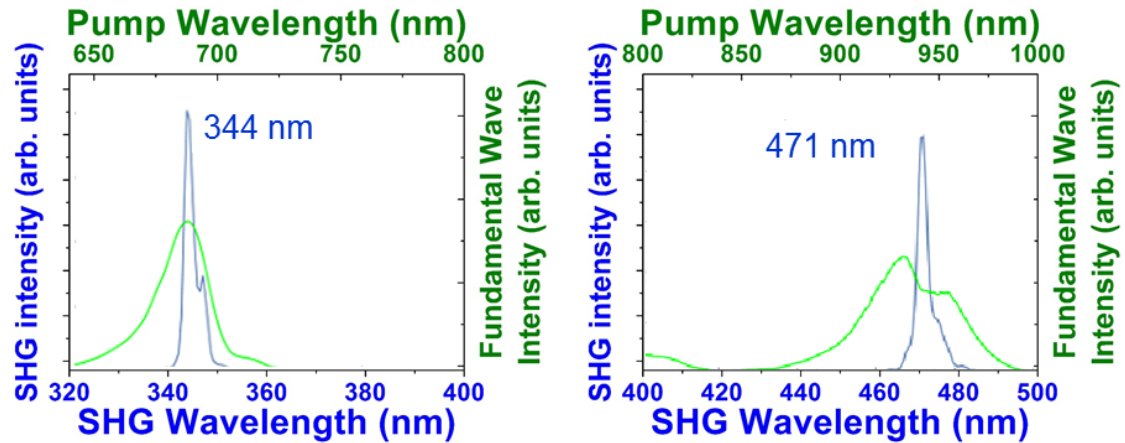


Figure 7-7: QPM SHG spectra at two different fundamental wavelengths for a 500 nm – 550 nm thick and 10 μ m periodic AlN LPS-based waveguide.

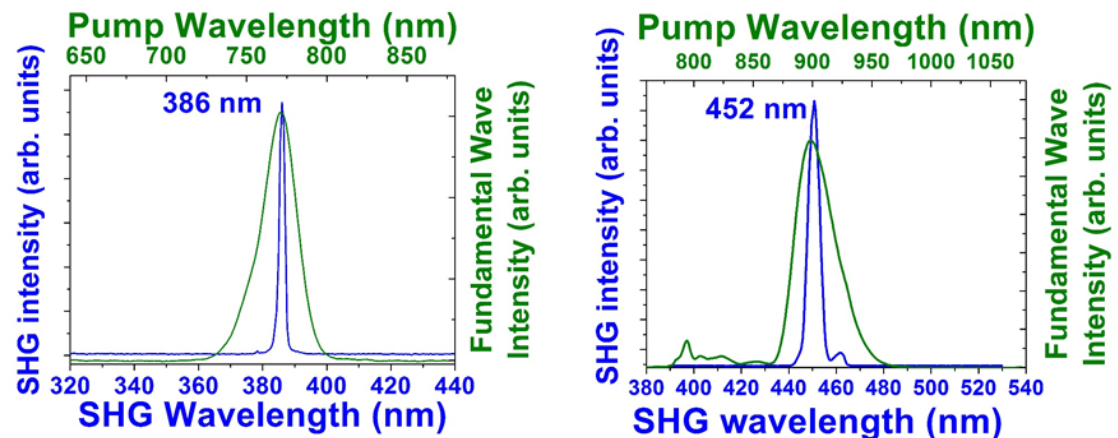


Figure 7-8: QPM SHG spectra at two different fundamental wavelengths for a 200 nm – 250 nm thick and 10 μ m periodic AlN LPS-based waveguide.

These results demonstrate the feasibility to use AlN LPS-based waveguides for UV-C laser generation via frequency doubling in compact integrated optics. Numerous other nonlinear optical processes, which are extensively described in the literature, may be exploited utilizing AlN LPS as the ones presented in this work. Note that the fabrication process can be extended to the entire III-Nitride material system, allowing to design a Nitride based LPS with optimal composition addressing specific nonlinear optical processes. On a broader scale, research towards epitaxial polarity control in other wide bandgap semiconductors with weak birefringence and promising nonlinear optical properties will be encouraged.

7.2.2 1.2 μm Periodicity

For 1st order QPM SHG in the UV-C spectral range, periodicities in the order of 1.2 μm are required (*Figure 5-11*). AlN LPS with 1.2 μm periodicity were fabricated according to the process described in chapter 5.1, where surface roughness RMS values in the order of 10 nm or lower were achieved either by mechanical polishing or two step temperature growth. Waveguides were etched into the 1.2 μm AlN LPS either by SiO₂ hard mask deposition and subsequent RIE (*Figure 7-9*),⁹⁷ or by standard masked photolithography using negative photoresist, followed by RIE (*Figure 7-10*).

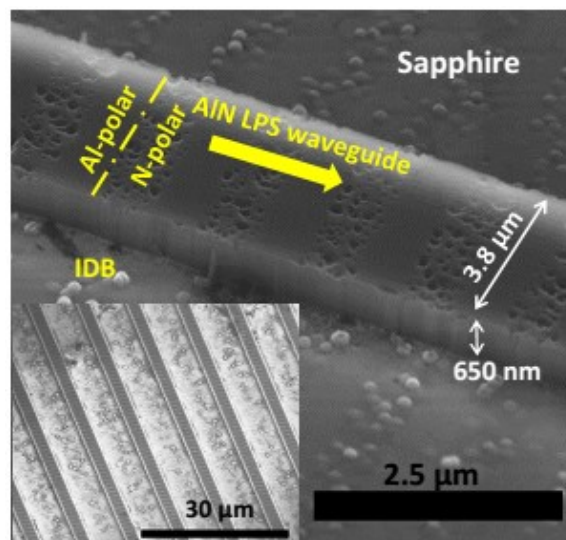


Figure 7-9: 1.2 μm periodic AlN LPS-based waveguides fabricated via SiO₂ hard mask deposition and subsequent RIE.⁹⁷



Figure 7-10: 1.2 μm periodic AlN LPS-based waveguides fabricated by standard masked photolithography using negative photoresist and subsequent RIE etching.

For the waveguides fabricated using a SiO₂ hard mask, straight sidewalls were obtained, however an increase of the surface roughness at the N-polar domains is observed, compared to the AlN LPS prior to the waveguide fabrication. The origin of the increased surface roughness at the N-polar domains arises from wet etching in the basic developing solution during the development of the photoresist mask, prior to the deposition of the SiO₂ hard mask. Hence, if a SiO₂ hard mask is desired to fabricate waveguides, a process needs to be implemented where the surface is not exposed to the basic developing solution.

For the waveguides fabricated using a negative photoresist, followed by RIE (Figure 7-10), the surface roughness is maintained, however rough sidewalls are observed. The reason for the observed sidewall roughness is unclear and a more detailed study is necessary. A possible explanation could be a crystallographic dependence of the RIE, where the misaligned waveguide sidewall from a crystallographic plane, exhibited two different facets, leading to a rough sidewall.

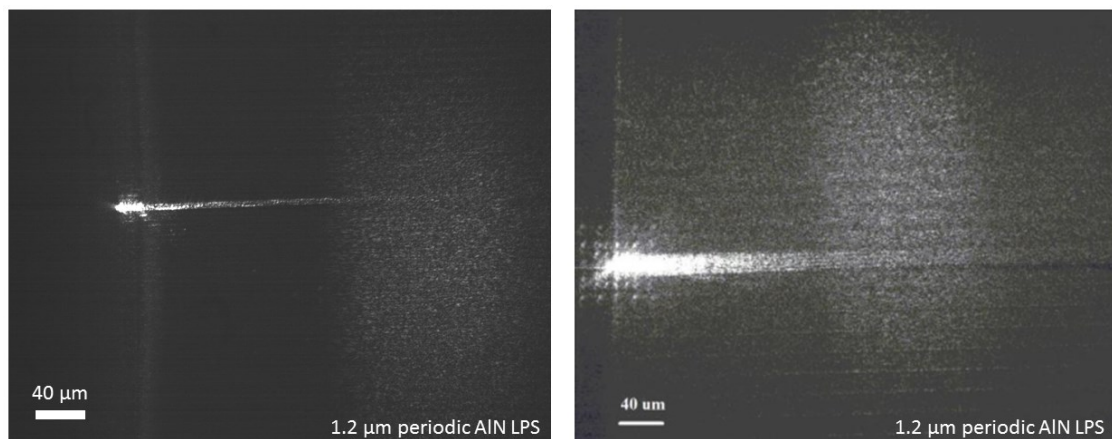


Figure 7-11: Top view 2D grayscale scattering intensity profile at the coupling facet of 1.2 μm periodic AlN LPS-based waveguides.

Figure 7-11 displays a top view 2D grayscale laser scattering intensity image, at the coupling facet of 1.2 μm periodic AlN LPS-based waveguides. Significant scattering intensity is observed, inhibiting the coupled laser light to reach the out-coupling facet. Clearly, the waveguide quality for 1.2 μm periodic AlN waveguides needs to be improved for 1st order QPM SHG in the UV-C spectral range.

In summary, using 10 μm periodic AlN LPS-based waveguides, 3rd, 5th and 7th order QPM SHG is demonstrated, where wavelengths as low as 344 nm are achieved. These are the first results demonstrating QPM SHG in AlN LPS-based waveguides,

laying the ground work for QPM nonlinear optics in III-Nitride based waveguide structures.

8 Conclusions and Future Work

8.1 Summary and Conclusions

The theory describing second harmonic generation via quasi phase matching and modal dispersion phase matching is presented. A brief introduction on the density functional theory-based theoretical model utilized for calculating the energy of formation of point defects as a function of Fermi level, is given. Following, a description on how the extracted thermodynamic transition energies can be related to optical spectroscopy characterization techniques is provided.

A polarity control process is described in detail for III- and N-polar GaN and AlN thin films deposited via MOCVD on sapphire. The etch behavior for both polarities in KOH solution is presented and is used for determining the polarity of the III-Nitride films fabricated in this work. Step flow growth of N-polar AlN is achieved by decreasing the Al vapor supersaturation below values of 10^4 , reducing the surface roughness RMS value by two orders of magnitude from 50 nm to 0.5 nm. In addition, mass transport between the adjacent opposite polar domains is measured when growing AlN LPS at vapor supersaturation values $\sigma < 10^8$, where an equal growth rate for both polarities is established at a vapor supersaturation value of $\sigma \approx 3 \times 10^4$. A two-step temperature process is utilized to avoid polarity overgrowth and achieve 1.2 μm periodic AlN LPS with a 6-10 nm surface roughness RMS value.

As with AlN LPS, using the same polarity control process scheme, a smooth surface of the GaN LPS is achieved by inducing step flow growth at the N-polar surface through controlling surface supersaturation and increasing the sapphire off-cut angle.

The optical properties of AlN single crystals are investigated, where the UV absorption band at 4.7 eV and the luminescence bands at 2.7 eV and 3.9 eV are linked to the same defect state with a thermodynamic transition energy of 4.2 eV through photoluminescence excitation spectroscopy (PLE). This thermodynamic transition energy is attributed to carbon as a nitrogen substitutional point defect. Power dependent photoluminescence (PL) measurements reveal the presence of an energy state within the bandgap with a 5.0 eV thermodynamic transition energy in agreement with the predicted energy state for the donor acceptor pair transition (DAP) leading to the 2.7 eV luminescence band and the calculated thermodynamic

transition energy for the nitrogen vacancy (V_N). A novel approach is presented to determine the impurities type and concentrations in the crystal where PL, PLE, absorption spectra and SIMS data is used in combination with a DFT based defect solver program which accounts for charge balance in the crystal and formation energies of the defects.

While PVT grown AlN single crystals contain point defect concentrations in the $\sim 10^{19} \text{ cm}^{-3}$ range, reducing their transparency in the UV-C spectral range, epitaxial thin films contain point defect concentrations 2 – 3 orders of magnitude lower (10^{16} - 10^{17} cm^{-3}), comparable to HVPE AlN crystals, where absorption coefficient values below 5 cm^{-1} are measured up to the near band edge energy of AlN. Hence, epitaxial AlN thin films are expected to be transparent in the UV-C spectral range, allowing for their implementation as frequency doubling crystals for UV-C laser generation.

Modal dispersion phase matched second harmonic generation down to 305 nm is demonstrated in single polar AlN waveguides, in agreement with theoretical calculations, showing the feasibility to employ AlN for UV laser light generation.

More significantly, 3rd, 5th and 7th order quasi phase matched second harmonic generation is demonstrated for the first time using 10 μm periodic AlN LPS-based waveguides, where wavelengths as low as 344 nm are achieved. These results lay the groundwork for QPM nonlinear optics in III-Nitride based waveguide structures.

8.2 Future Work

A series of studies are proposed based on the studies and conclusions of this work.

- While 1.2 μm periodic AlN LPS with surface RMS roughness values of 5 nm over a 90 x 90 μm^2 are achieved, second harmonic generation was not measured due to the scattering losses. A detailed study of the origin of the scattering losses will allow the development of an improved process for fabricating waveguide-structures of sufficient high quality suitable for second harmonic generation in the UV-C spectral range.
- A detailed understanding of the surface kinetics and thermodynamics leading to mass transport between the adjacent opposite polar domains in III-nitrides LPS, is essential for developing the theoretical framework which will allow for precise control of the polar domains thickness differences and achieve the smoothest surface morphology.
- Fabrication of AlN LPS using bulk AlN substrates will allow for thick structures ($> 500 \mu\text{m}$), eliminating the need for smooth surfaces, as well as the need to consider the propagation of waveguide modes
- A detailed study on the mechanism leading to the suppression of the UV-C absorption band at 4.7 eV in bulk AlN single crystals when the oxygen and/or silicon impurities concentrations are higher than carbon.
- The theory describing nonlinear optical interactions in quasi phase matching structures has been extensively studied in the literature. Exploring the possibility to employ III-nitride LPS for other nonlinear optical interactions relevant for integrated optics such as wavelength division multiplexing, optical time division multiplexing and optical amplifiers is of great interest. Initially, the structures dimensions and geometry necessary for the particular nonlinear process can be calculated, which can be then fabricated and experimentally tested.

9 Publications and Conference Contributions

9.1 Publications

Sections of the presented work includes results which have been published in peered review journals and are marked with an asterisk (*). The remaining listed publications are not directly related to the presented work but are rather the result of a wide range of collaborations.

[1]* **D. Alden**, W. Guo, R. Kirste, F. Kaess, I. Bryan, T. Troha, A. Bagal, P. Reddy, L.H. Hernandez-Balderrama, A. Franke, S. Mita, C.-H. Chang, A. Hoffmann, M. Zgonik, R. Collazo, and Z. Sitar, *Fabrication and structural properties of AlN submicron periodic lateral polar structures and waveguides for UV-C applications*. Applied Physics Letters **108**, 261106 (2016).

[2]* **D. Alden**, Z. Bryan, B. Gaddy, I. Bryan, G. Callsen, A. Koukitu, Y. Kumagai, A. Hoffmann, D. Irving, Z. Sitar, and R. Collazo, *On the Origin of the 4.7 eV Absorption and 2.8 eV Emission Bands in Bulk AlN Substrates*. ECS Trans. **72**, 31 (2016).

[3]* T. Troha, M. Rigler, **D. Alden**, I. Bryan, W. Guo, R. Kirste, S. Mita, M.D. Gerhold, R. Collazo, Z. Sitar, and M. Zgonik, *UV second harmonic generation in AlN waveguides with modal phase matching*. Optical Materials Express **6**, 2014 (2016).

[4] P. Reddy, S. Washiyama, F. Kaess, M. Hayden Breckenridge, L.H. Hernandez-Balderrama, B.B. Haidet, **D. Alden**, A. Franke, B. Sarkar, E. Kohn, R. Collazo, and Z. Sitar, *High temperature and low pressure chemical vapor deposition of silicon nitride on AlGaN: Band offsets and passivation studies*. Journal of Applied Physics **119**, 145702 (2016).

[5] F. Kaess, P. Reddy, **D. Alden**, A. Klump, L.H. Hernandez-Balderrama, A. Franke, R. Kirste, A. Hoffmann, R. Collazo, and Z. Sitar, *The effect of illumination power density on carbon defect configuration in silicon doped GaN*. Journal of Applied Physics **120**, 235705 (2016).

[6] Y. Abate, D. Seidlitz, A. Fali, S. Gamage, V.E. Babicheva, V.S. Yakovlev, M.I. Stockman, R. Collazo, **D.E. Alden**, and N. Dietz, *Nanoscopy of Phase Separation in $In_xGa_{1-x}N$ Alloys*. ACS Applied Materials & Interfaces (2016).

[7] R. Collazo, I. Bryan, Z. Bryan, M. Bobea, L. Hussey, **D. Alden**, S. Mita, B. Gaddy, J. Tweedie, R. Kirste, D. Irving, and Z. Sitar, *Advantages and limitations of UV optoelectronics on AlN substrates*. 2015 IEEE Summer Topicals Meeting Series (SUM). (2015), pp. 135–136.

9.2 Conference Talks

1. **D. Alden**, T. Troha, R. Kirste, F. Kaess, A. Franke, M. Gerhold, A. Hoffmann, M. Zgonik, R. Collazo, and Z. Sitar; *Second Harmonic Generation of UV Laser Light in AlN Periodic Lateral Polar Structures*. International Workshop on Nitride Semiconductors 2016; Oralndo, FL, USA (Oct. 2016).

2. **D. Alden**, J. Harris, Z. Bryan, I. Bryan, B. Gaddy, G. Callsen, A. Hoffmann, D. Irving, R. Collazo, Z. Sitar; *Detailed Photoluminescence Excitation Study of the 3.9 eV and 2.7 eV Defect Luminescence Bands and the Commonly Observed Deep UV Absorption at 4.7 eV*. International Workshop on Nitride Semiconductors 2016; Oralndo, FL, USA (Oct. 2016).

3. **D. Alden**, R. Kirste, T. Troha, W. Guo, F. Kaess, I. Bryan, A. Franke, M. Gerhold, M. Zgonik, R. Collazo, and Z. Sitar; *Sub-micron Polarity Control in AlN Periodic Lateral Polar Structures*. 58th Electronic Materials Conference, June 2016, Newark, Delaware, USA.

4. **D. Alden**, T. Troha, R. Kirste, F. Kaess, A. Franke, M. Gerhold, A. Hoffmann, M. Zgonik, R. Collazo, and Z. Sitar; *Second Harmonic Generation of UV Laser Light in AlN Periodic Lateral Polar Structures*. 2016 Society of Hispanic Professional Engineers Conference. November 2016, Seattle, USA.

10 References

1. Briegleb, F. & Geuther, A. Ueber das Stickstoffmagnesium und die Affinitäten des Stickgases zu Metallen. *Justus Liebigs Ann. Chem.* **123**, 228–241 (1862).
2. Zenghelis, C. Chemische Reaktionen bei Extrem Hohen Temperaturen. *Z. Für Elektrochem.* **9**, 109 (1903).
3. Matignon, M. C. & Williams, W. J. Formation and Preparation of Aluminum Carbide. *J. Frankl. Inst.* **166**, 203–212 (1908).
4. Fichter, F. Über Aluminiumnitrid. *Z. Für Anorg. Chem.* **54**, 322–327 (1907).
5. Ott, H. Das Gitter des Aluminiumnitrids (AlN). *Z. Für Phys.* **22**, 201–214 (1924).
6. Bobea, M. R. High Resolution X-ray Diffraction Characterization of III-Nitride Semiconductors: Bulk Crystals and Thin Films. (2015).
7. Johnson, W. C., Parson, J. B. & Crew, M. C. Nitrogen compounds of gallium. iii. *J. Phys. Chem.* **36**, 2651–2654 (1932).
8. Juza, R. & Hahn, H. Über die Kristallstrukturen von Cu₃N, GaN und InN Metallamide und Metallnitride. *Z. Für Anorg. Allg. Chem.* **239**, 282–287 (1938).
9. Dimakis, E., Iliopoulos, E., Tsagaraki, K., Adikimenakis, A. & Georgakilas, A. Biaxial strain and lattice constants of InN (0001) films grown by plasma-assisted molecular beam epitaxy. *Appl. Phys. Lett.* **88**, 191918 (2006).
10. Tietjen, J. J. & Amick, J. A. The Preparation and Properties of Vapor-Deposited Epitaxial GaAs(1-x)P_x Using Arsine and Phosphine. *J. Electrochem. Soc.* **113**, 724–728 (1966).
11. Maruska, H. P. & Tietjen, J. J. The Preparation and Properties of Vapor Deposited Single Crystalline GaN. *Appl. Phys. Lett.* **15**, 327–329 (1969).

12. Yim, W. M. *et al.* Epitaxially grown AlN and its optical band gap. *J. Appl. Phys.* **44**, 292–296 (1973).
13. Cox, G. A., Cummins, D. O., Kawabe, K. & Tredgold, R. H. On the preparation, optical properties and electrical behaviour of aluminium nitride. *J. Phys. Chem. Solids* **28**, 543–548 (1967).
14. Pankove, J. I., Maruska, H. P. & Berkeyheiser, J. E. Optical Absorption of GaN. *Appl. Phys. Lett.* **17**, 197–199 (1970).
15. Davydov, V. Y. *et al.* Absorption and Emission of Hexagonal InN. Evidence of Narrow Fundamental Band Gap. *Phys. Status Solidi B* **229**, r1–r3 (2002).
16. Baliga, B. J. Power semiconductor device figure of merit for high-frequency applications. *Electron Device Lett. IEEE* **10**, 455–457 (1989).
17. Nakamura, S., Mukai, T. & Senoh, M. Candela-class high-brightness InGaN/AlGaIn double-heterostructure blue-light-emitting diodes. *Appl. Phys. Lett.* **64**, 1687–1689 (1994).
18. Nakamura, S. *et al.* InGaIn-Based Multi-Quantum-Well-Structure Laser Diodes. *Jpn. J. Appl. Phys.* **35**, L74–L76 (1996).
19. Ohta, H. *et al.* Vertical GaN p-n Junction Diodes With High Breakdown Voltages Over 4 kV. *IEEE Electron Device Lett.* **36**, 1180–1182 (2015).
20. *Springer handbook of electronic and photonic materials.* (Springer, 2006).
21. Morkoç, H. *Nitride Semiconductor Devices.* (2013).
22. Pelá, R. R. *et al.* Accurate band gaps of AlGaIn, InGaIn, and AlInN alloys calculations based on LDA-1/2 approach. *Appl. Phys. Lett.* **98**, 151907 (2011).
23. Chin, V. W. L., Tansley, T. L. & Osotchan, T. Electron mobilities in gallium, indium, and aluminum nitrides. *J. Appl. Phys.* **75**, 7365–7372 (1994).
24. Ozbek, A. M. & Baliga, B. J. Planar Nearly Ideal Edge-Termination Technique for GaN Devices. *IEEE Electron Device Lett.* **32**, 300–302 (2011).

25. Rojo, J. C. *et al.* Single-crystal aluminum nitride substrate preparation from bulk crystals. in *MRS Proceedings* **680**, E2–7 (Cambridge Univ Press, 2001).
26. Baliga, B. J. *Fundamentals of power semiconductor devices*. (Springer, 2008).
27. Chu, T. L. & Kelm, R. W. The Preparation and Properties of Aluminum Nitride Films. *J. Electrochem. Soc.* **122**, 995–1000 (1975).
28. Davydov, S. Y. & Lebedev, A. A. Calculations of the Spontaneous Polarizations and Dielectric Constants for AlN, GaN, InN, and SiC. *Mater. Sci. Forum* **645–648**, 1203–1206 (2010).
29. Bryan, I. S. Al-rich AlGaN and AlN Growth on Bulk AlN Single Crystal Substrates. (North Carolina State University, 2016).
30. Bryan, Z. A. Point Defect Identification and Management for Sub-300 nm Light Emitting Diodes and Laser Diodes Grown on Bulk AlN Substrates. (North Carolina State University, 2015).
31. Hardy, M. T., Feezell, D. F., DenBaars, S. P. & Nakamura, S. Group III-nitride lasers: a materials perspective. *Mater. Today* **14**, 408–415 (2011).
32. Boyd, R. *Boyd Nonlinear Optics, Third Edition.pdf*. (2008).
33. *Springer Handbook of Lasers and Optics*. (Springer Berlin Heidelberg, 2012).
34. Hunsperger, R. G. *Integrated Optics*. (Springer New York, 2009).
35. Rigler, M. Second Harmonic Generation in Blue and Ultraviolet Region Using AlGaN Waveguides. (University of Ljubljana, 2014).
36. Sasaki, T., Mori, Y., Yoshimura, M., Yap, Y. K. & Kamimura, T. Recent development of nonlinear optical borate crystals: key materials for generation of visible and UV light. *Mater. Sci. Eng. R Rep.* **30**, 1–54 (2000).
37. Strite, S. & Morkoç, H. GaN, AlN, and InN: A review. *J. Vac. Sci. Technol. B* **10**, 1237–1266 (1992).

38. Eimerl, D., Davis, L., Velsko, S., Graham, E. K. & Zalkin, A. Optical, mechanical, and thermal properties of barium borate. *J. Appl. Phys.* **62**, 1968–1983 (1987).
39. Li, R., Wang, L., Wang, X., Wang, G. & Chen, C. Dispersion relations of refractive indices suitable for KBe₂BO₃F₂ crystal deep-ultraviolet applications. *Appl. Opt.* **55**, 10423 (2016).
40. Zernike, F. Refractive Indices of Ammonium Dihydrogen Phosphate and Potassium Dihydrogen Phosphate between 2000 Å and 1.5 μ. *JOSA* **54**, 1215–1220 (1964).
41. Sasaki, T., Mori, Y. & Yoshimura, M. Progress in the growth of a CsLiB₆O₁₀ crystal and its application to ultraviolet light generation. *Opt. Mater.* **23**, 343–351 (2003).
42. Marcuse, D. Coupling coefficients for imperfect asymmetric slab waveguides. *Bell Syst. Tech. J.* **52**, 63–82 (1973).
43. Marcuse, D. Coupled-mode theory for anisotropic optical waveguides. *Bell Syst. Tech. J.* **54**, 985–995 (1975).
44. Yariv, A. Coupled-mode theory for guided-wave optics. *IEEE J. Quantum Electron.* **9**, 919–933 (1973).
45. Stegeman, G. I. & Seaton, C. T. Nonlinear integrated optics. *J. Appl. Phys.* **58**, R57 (1985).
46. Tien, P. K. Light waves in thin films and integrated optics. *Appl. Opt.* **10**, 2395–2413 (1971).
47. Troha, T. *et al.* UV second harmonic generation in AlN waveguides with modal phase matching. *Opt. Mater. Express* **6**, 2014 (2016).

48. Armstrong, J. A., Bloembergen, N., Ducuing, J. & Pershan, P. S. Interactions between Light Waves in a Nonlinear Dielectric. *Phys. Rev.* **127**, 1918–1939 (1962).
49. Fejer, M. M., Magel, G. A., Jundt, D. H. & Byer, R. L. Quasi-phase-matched second harmonic generation: tuning and tolerances. *IEEE J. Quantum Electron.* **28**, 2631–2654 (1992).
50. Hum, D. S. & Fejer, M. M. Quasi-phases matching. *Comptes Rendus Phys.* **8**, 180–198 (2007).
51. Burton, W. K., Cabrera, N. & Frank, F. C. The Growth of Crystals and the Equilibrium Structure of their Surfaces. *Philos. Trans. R. Soc. Lond. Math. Phys. Eng. Sci.* **243**, 299–358 (1951).
52. Shitara, T. & Nishinaga, T. Surface Diffusion Length of Gallium during MBE Growth on the Various Misoriented GaAs(001) Substrates. *Jpn. J. Appl. Phys.* **28**, 1212–1216 (1989).
53. Kimoto, T. & Matsunami, H. Surface kinetics of adatoms in vapor phase epitaxial growth of SiC on 6H-SiC{0001} vicinal surfaces. *J. Appl. Phys.* **75**, 850 (1994).
54. Mita, S., Collazo, R., Rice, A., Dalmau, R. F. & Sitar, Z. Influence of gallium supersaturation on the properties of GaN grown by metalorganic chemical vapor deposition. *J. Appl. Phys.* **104**, 013521 (2008).
55. Bryan, I. *et al.* Surface kinetics in AlN growth: A universal model for the control of surface morphology in III-nitrides. *J. Cryst. Growth* **438**, 81–89 (2016).
56. Koukitu, A., Takahashi, N. & Seki, H. Thermodynamic Study on Metalorganic Vapor-Phase Epitaxial Growth of Group III Nitrides. *Jpn. J. Appl. Phys.* **36**, L1136–L1138 (1997).

57. Gaddy, B. E. Predictive Calculations of Defects in Thin-Film Heterostructures. (2013).
58. Reshchikov, M. A. & Morkoç, H. Luminescence properties of defects in GaN. *J. Appl. Phys.* **97**, 061301 (2005).
59. Alkauskas, A., McCluskey, M. D. & Van de Walle, C. G. Tutorial: Defects in semiconductors—Combining experiment and theory. *J. Appl. Phys.* **119**, 181101 (2016).
60. Heyd, J., Scuseria, G. E. & Ernzerhof, M. Hybrid functionals based on a screened Coulomb potential. *J. Chem. Phys.* **118**, 8207 (2003).
61. Kohn, W. & Sham, L. J. Self-Consistent Equations Including Exchange and Correlation Effects. *Phys. Rev.* **140**, A1133–A1138 (1965).
62. Hohenberg, P. & Kohn, W. Inhomogeneous Electron Gas. *Phys. Rev.* **136**, B864–B871 (1964).
63. Lyons, J. L., Janotti, A. & Van de Walle, C. G. Carbon impurities and the yellow luminescence in GaN. *Appl. Phys. Lett.* **97**, 152108 (2010).
64. Lyons, J. L. & Walle, C. G. V. de. Computationally predicted energies and properties of defects in GaN. *Npj Comput. Mater.* **3**, 12 (2017).
65. Condon, E. A Theory of Intensity Distribution in Band Systems. *Phys. Rev.* **28**, 1182–1201 (1926).
66. Franzen, S. The Franck-Condon Factor. Available at: http://www4.ncsu.edu/~franzen/public_html/CH433/workshop/fc/fc.html.
67. Hughes, A. E. Zero-phonon Transitions and Vibrational Structure. *J. Phys. Colloq.* **28**, C4–55 (1967).
68. Bagal, A. S. Fabrication of Subwavelength Periodic Nanostructures using Immersion Interference Lithography. (2012).

69. Yoshida, S., Misawa, S. & Itoh, A. Epitaxial growth of aluminum nitride films on sapphire by reactive evaporation. *Appl. Phys. Lett.* **26**, 461 (1975).
70. Yoshida, S. Improvements on the electrical and luminescent properties of reactive molecular beam epitaxially grown GaN films by using AlN-coated sapphire substrates. *Appl. Phys. Lett.* **42**, 427 (1983).
71. Amano, H., Sawaki, N., Akasaki, I. & Toyoda, Y. Metalorganic vapor phase epitaxial growth of a high quality GaN film using an AlN buffer layer. *Appl. Phys. Lett.* **48**, 353 (1986).
72. Akasaki, I., Amano, H., Koide, Y., Hiramatsu, K. & Sawaki, N. Effects of AlN buffer layer on crystallographic structure and on electrical and optical properties of GaN and Ga_{1-x}Al_xN ($0 < x \leq 0.4$) films grown on sapphire substrate by MOVPE. *J. Cryst. Growth* **98**, 209–219 (1989).
73. Sasaki, T. & Matsuoka, T. Substrate-polarity dependence of metal-organic vapor-phase epitaxy-grown GaN on SiC. *J. Appl. Phys.* **64**, 4531–4535 (1988).
74. Nakamura, S. & Mukai, T. High-Quality InGaN Films Grown on GaN Films. *Jpn. J. Appl. Phys.* **31**, L1457 (1992).
75. Daudin, B., Rouvière, J. L. & Arlery, M. Polarity determination of GaN films by ion channeling and convergent beam electron diffraction. *Appl. Phys. Lett.* **69**, 2480 (1996).
76. Hwang, C.-Y. *et al.* Effect of substrate pretreatment on growth of GaN on (0001) sapphire by low pressure metalorganic chemical vapor deposition. *J. Vac. Sci. Technol. A* **13**, 672–675 (1995).
77. Dimitrov, R. *et al.* Two-dimensional electron gases in Ga-face and N-face AlGa_xN/GaN heterostructures grown by plasma-induced molecular beam epitaxy and metalorganic chemical vapor deposition on sapphire. *J. Appl. Phys.* **87**, 3375 (2000).

78. Collazo, R., Mita, S., Aleksov, A., Schlessler, R. & Sitar, Z. Growth of Ga- and N- polar gallium nitride layers by metalorganic vapor phase epitaxy on sapphire wafers. *J. Cryst. Growth* **287**, 586–590 (2005).
79. Sumiya, M. & Fuke, S. Review of polarity determination and control of GaN. *MRS Internet J. Nitride Semicond. Res.* **9**, e1 (2004).
80. Mohn, S. *et al.* Polarity Control in Group-III Nitrides beyond Pragmatism. *Phys. Rev. Appl.* **5**, (2016).
81. Ramachandran, V. *et al.* Inversion of wurtzite GaN(0001) by exposure to magnesium. *Appl. Phys. Lett.* **75**, 808 (1999).
82. Wright, J., Moe, C., Sampath, A. V., Garrett, G. A. & Wraback, M. Fabrication of periodically poled AlN with sub-micron periods. *Phys. Status Solidi C* **8**, 2331–2333 (2011).
83. Pezzagna, S., Vennéguès, P., Grandjean, N., Wieck, A. D. & Massies, J. Submicron periodic poling and chemical patterning of GaN. *Appl. Phys. Lett.* **87**, 062106 (2005).
84. Mita, S. Polarity control in GaN epilayers grown by metalorganic chemical vapor deposition. (2008).
85. Liu, F. *et al.* Direct Observation of Inversion Domain Boundaries of GaN on c-Sapphire at Sub-ångstrom Resolution. *Adv. Mater.* **20**, 2162–2165 (2008).
86. Hussey, L. *et al.* Sapphire decomposition and inversion domains in N-polar aluminum nitride. *Appl. Phys. Lett.* **104**, 032104 (2014).
87. Guo, W. *et al.* Comparative study of etching high crystalline quality AlN and GaN. *J. Cryst. Growth* **366**, 20–25 (2013).
88. Guo, W. *et al.* KOH based selective wet chemical etching of AlN, Al_xGa_{1-x}N, and GaN crystals: A way towards substrate removal in deep ultraviolet-light emitting diode. *Appl. Phys. Lett.* **106**, 082110 (2015).

89. Li, D. *et al.* Selective etching of GaN polar surface in potassium hydroxide solution studied by x-ray photoelectron spectroscopy. *J. Appl. Phys.* **90**, 4219 (2001).
90. Zhuang, D. & Edgar, J. H. Wet etching of GaN, AlN, and SiC: a review. *Mater. Sci. Eng. R Rep.* **48**, 1–46 (2005).
91. Stutzmann, M. *et al.* Playing with Polarity. *Phys. Status Solidi B* **228**, 505–512 (2001).
92. Collazo, R., Mita, S., Rice, A., Dalmau, R. F. & Sitar, Z. Simultaneous growth of a GaN p/n lateral polarity junction by polar selective doping. *Appl. Phys. Lett.* **91**, 212103 (2007).
93. Kirste, R. *et al.* Polarity control and growth of lateral polarity structures in AlN. *Appl. Phys. Lett.* **102**, 181913 (2013).
94. Hussey, L. *et al.* Direct Observation of the Polarity Control Mechanism in Aluminum Nitride Grown on Sapphire by Aberration Corrected Scanning Transmission Electron Microscopy. *Microsc. Microanal.* **20**, 162–163 (2014).
95. Takeuchi, M. *et al.* Improvement of crystalline quality of N-polar AlN layers on c-plane sapphire by low-pressure flow-modulated MOCVD. *J. Cryst. Growth* **298**, 336–340 (2007).
96. Rigler, M. *et al.* Optical characterization of Al- and N-polar AlN waveguides for integrated optics. *Appl. Phys. Express* **8**, 042603 (2015).
97. Alden, D. *et al.* Fabrication and structural properties of AlN submicron periodic lateral polar structures and waveguides for UV-C applications. *Appl. Phys. Lett.* **108**, 261106 (2016).
98. Bagal, A. & Chang, C.-H. Fabrication of subwavelength periodic nanostructures using liquid immersion Lloyd's mirror interference lithography. *Opt. Lett.* **38**, 2531 (2013).

99. Walsh, M. E. Nanostructuring magnetic thin films using interference lithography. (Massachusetts Institute of Technology, 2000).
100. Marcuse, D. Radiation losses of dielectric waveguides in terms of the power spectrum of the wall distortion function. *Bell Syst. Tech. J.* **48**, 3233–3242 (1969).
101. Mita, S. *et al.* Impact of gallium supersaturation on the growth of N-polar GaN. *Phys. Status Solidi C* **8**, 2078–2080 (2011).
102. Keller, S. *et al.* Influence of the substrate misorientation on the properties of N-polar GaN films grown by metal organic chemical vapor deposition. *J. Appl. Phys.* **102**, 083546 (2007).
103. Brown, D. F. *et al.* Growth and characterization of N-polar GaN films on SiC by metal organic chemical vapor deposition. *J. Appl. Phys.* **104**, 024301 (2008).
104. Zauner, A. R. A. *et al.* Homo-epitaxial growth on the N-face of GaN single crystals: the influence of the misorientation on the surface morphology. *J. Cryst. Growth* **240**, 14–21 (2002).
105. Han, J. *et al.* OMVPE growth and gas-phase reactions of AlGa_N for UV emitters. *J. Cryst. Growth* **195**, 291–296 (1998).
106. Allerman, A. A. *et al.* Growth and design of deep-UV (240–290nm) light emitting diodes using AlGa_N alloys. *J. Cryst. Growth* **272**, 227–241 (2004).
107. Lundin, W. V. *et al.* High growth rate of AlN in a planetary MOVPE reactor. *Tech. Phys. Lett.* **36**, 1133–1135 (2010).
108. Northrup, J. E., Neugebauer, J. & Romano, L. T. Inversion domain and stacking mismatch boundaries in GaN. *Phys. Rev. Lett.* **77**, 103 (1996).
109. Hussey, L. K. Characterization and Extended Defect Control in III-Nitrides. (2014).

110. Hite, J. K., Twigg, M. E., Mastro, M. A., Eddy, C. R. & Kub, F. J. Initiating polarity inversion in GaN growth using an AlN interlayer. *Phys. Status Solidi A* **208**, 1504–1506 (2011).
111. Hite, J. K., Zoll, R., Mastro, M. A. & Eddy, C. R. Role of growth parameters in equalizing simultaneous growth of N- and Ga-polar GaN by MOCVD: Role of growth parameters in equalizing simultaneous growth of N- and Ga-polar GaN by MOCVD. *Phys. Status Solidi C* **11**, 458–461 (2014).
112. Brown, C. G. *et al.* Frequency conversion in free-standing periodically oriented gallium nitride. in (eds. Vodopyanov, K. L. & Schepler, K. L.) 97310E (2016). doi:10.1117/12.2213447
113. Hite, J. Progress in periodically oriented III-nitride materials. *J. Cryst. Growth* doi:10.1016/j.jcrysgro.2016.08.042
114. Hoffmann, M. P. Polarity control and doping in aluminum gallium nitride. (DTIC Document, 2013).
115. Hoffmann, M. P. *et al.* Growth and characterization of Al_xGa_{1-x}N lateral polarity structures: Growth and characterization of Al_xGa_{1-x}N lateral polarity structures. *Phys. Status Solidi A* **212**, 1039–1042 (2015).
116. Hoffmann, M. P. *et al.* Fabrication and characterization of lateral polar GaN structures for second harmonic generation. in (ed. Razeghi, M.) 86311T (2013). doi:10.1117/12.2008827
117. Carlone, C., Lakin, K. M. & Shanks, H. R. Optical phonons of aluminum nitride. *J. Appl. Phys.* **55**, 4010–4014 (1984).
118. Serpek, O. Process of producing aluminum nitrid. (1911).
119. Serpek, O. Process for the manufacture of aluminum nitrid. (1917).
120. Long, G. & Foster, L. M. Aluminum Nitride, a Refractory for Aluminum to 2000° C. *J. Am. Ceram. Soc.* **42**, 53–59 (1959).

121. Taylor, K. M. & Lenie, C. Some Properties of Aluminum Nitride. *J. Electrochem. Soc.* **107**, 308–314 (1960).
122. Pastrňák, J. & Roskovcova, L. Morphologie und Wachstumsmechanismus von AlN-Einkristallen. *Phys. Status Solidi B* **7**, 331–338 (1964).
123. Slack, G. A. & McNelly, T. F. Growth of high purity AlN crystals. *J. Cryst. Growth* **34**, 263–279 (1976).
124. Schlessner, R., Dalmau, R. & Sitar, Z. Seeded growth of AlN bulk single crystals by sublimation. *J. Cryst. Growth* **241**, 416–420 (2002).
125. Zhuang, D., Herro, Z. G., Schlessner, R. & Sitar, Z. Seeded growth of AlN single crystals by physical vapor transport. *J. Cryst. Growth* **287**, 372–375 (2006).
126. Herro, Z. G., Zhuang, D., Schlessner, R., Collazo, R. & Sitar, Z. Seeded growth of AlN on N- and Al-polar AlN seeds by physical vapor transport. *J. Cryst. Growth* **286**, 205–208 (2006).
127. Lu, P. *et al.* Seeded growth of AlN bulk crystals in m- and c-orientation. *J. Cryst. Growth* **312**, 58–63 (2009).
128. Hartmann, C. *et al.* Preparation of deep UV transparent AlN substrates with high structural perfection for optoelectronic devices. *CrystEngComm* **18**, 3488–3497 (2016).
129. Bryan, Z. *et al.* High internal quantum efficiency in AlGaN multiple quantum wells grown on bulk AlN substrates. *Appl. Phys. Lett.* **106**, 142107 (2015).
130. Pastrňák, J. & Roskovcova, L. Optical Absorption Edge of AlN Single Crystals. *Phys. Status Solidi B* **26**, 591–597 (1968).
131. Slack, G. A., Schowalter, L. J., Morelli, D. & Freitas Jr., J. A. Some effects of oxygen impurities on AlN and GaN. *J. Cryst. Growth* **246**, 287–298 (2002).

132. Strassburg, M. *et al.* The growth and optical properties of large, high-quality AlN single crystals. *J. Appl. Phys.* **96**, 5870–5876 (2004).
133. Bickermann, M., Epelbaum, B. M. & Winnacker, A. Characterization of bulk AlN with low oxygen content. *J. Cryst. Growth* **269**, 432–442 (2004).
134. Bickermann, M. *et al.* Faceting in AlN bulk crystal growth and its impact on optical properties of the crystals. *Phys. Status Solidi C* **9**, 449–452 (2012).
135. Collazo, R. *et al.* On the origin of the 265 nm absorption band in AlN bulk crystals. *Appl. Phys. Lett.* **100**, 191914 (2012).
136. Gaddy, B. E. *et al.* Vacancy compensation and related donor-acceptor pair recombination in bulk AlN. *Appl. Phys. Lett.* **103**, 161901 (2013).
137. Irmscher, K. *et al.* Identification of a tri-carbon defect and its relation to the ultraviolet absorption in aluminum nitride. *J. Appl. Phys.* **114**, 123505 (2013).
138. Schulz, T. *et al.* Ultraviolet luminescence in AlN. *Phys. Status Solidi B* **248**, 1513–1518 (2011).
139. Lu, P. *et al.* Different optical absorption edges in AlN bulk crystals grown in m- and c-orientations. *Appl. Phys. Lett.* **93**, 131922 (2008).
140. Walle, C. G. V. de & Neugebauer, J. First-principles calculations for defects and impurities: Applications to III-nitrides. *J. Appl. Phys.* **95**, 3851–3879 (2004).
141. Epelbaum, B. M., Bickermann, M. & Winnacker, A. Seeded PVT Growth of Aluminum Nitride on Silicon Carbide. *Mater. Sci. Forum* **433–436**, 983–986 (2003).
142. Alcock, C. B., Itkin, V. P. & Horrigan, M. K. Vapour Pressure Equations for the Metallic Elements: 298-2500K. *Can Met. Q* **23**, 309–313 (1984).

143. Bryan, Z. *et al.* Fermi level control of compensating point defects during metalorganic chemical vapor deposition growth of Si-doped AlGaN. *Appl. Phys. Lett.* **105**, 222101 (2014).
144. Reddy, P. *et al.* Point defect reduction in wide bandgap semiconductors by defect quasi Fermi level control. *J. Appl. Phys.* **120**, 185704 (2016).
145. Kaess, F. *et al.* The effect of illumination power density on carbon defect configuration in silicon doped GaN. *J. Appl. Phys.* **120**, 235705 (2016).
146. Varshni, Y. P. Temperature dependence of the energy gap in semiconductors. *Physica* **34**, 149–154 (1967).
147. Huxter, V. M. Optical and Material Properties of Colloidal Semiconductor Nanocrystals. (University of Toronto, 2009).
148. O’Leary, S. K. & Lim, P. K. On determining the optical gap associated with an amorphous semiconductor: A generalization of the Tauc model. *Solid State Commun.* **104**, 17–21 (1997).
149. Gaddy, B. E. *et al.* The role of the carbon-silicon complex in eliminating deep ultraviolet absorption in AlN. *Appl. Phys. Lett.* **104**, 202106 (2014).
150. Silvestri, L., Dunn, K., Prawer, S. & Ladouceur, F. Hybrid functional study of Si and O donors in wurtzite AlN. *Appl. Phys. Lett.* **99**, 122109 (2011).
151. Guo, Q. & Yoshida, A. Temperature Dependence of Band Gap Change in InN and AlN. *Jpn. J. Appl. Phys.* **33**, 2453 (1994).
152. Fujii, Y., Yoshida, S., Misawa, S., Maekawa, S. & Sakudo, T. Nonlinear optical susceptibilities of AlN film. *Appl. Phys. Lett.* **31**, 815 (1977).
153. Slack, G. A. The Intrinsic Thermal Conductivity of Aln. *JPHYSICHEMSOLIDS J Phys Chem Solids* **48**, 641 (1987).

154. Bahabad, A., Murnane, M. M. & Kapteyn, H. C. Quasi-phase-matching of momentum and energy in nonlinear optical processes. *Nat. Photonics* **4**, 570–575 (2010).
155. Yan, T. *et al.* Growth of MgO doped near stoichiometric LiNbO₃ single crystals by a hanging crucible Czochralski method using a ship lockage type powder feeding system assisted by numerical simulation. *CrystEngComm* **16**, 6593 (2014).
156. Mizuuchi, K., Morikawa, A., Sugita, T. & Yamamoto, K. Efficient Second-Harmonic Generation of 340-nm Light in a 1.4 μm Periodically Poled Bulk MgO: LiNbO₃. *Jpn. J. Appl. Phys.* **42**, L90 (2003).
157. Myers, L. E. *et al.* Quasi-phase-matched optical parametric oscillators in bulk periodically poled LiNbO₃. *JOSA B* **12**, 2102–2116 (1995).
158. Chen, Q. & Risk, W. P. Periodic poling of KTiOPO₄ using an applied electric field. *Electron. Lett.* **30**, 1516–1517 (1994).
159. Hu, X. P., Xu, P. & Zhu, S. N. Engineered quasi-phase-matching for laser techniques [Invited]. *Photonics Res.* **1**, 171 (2013).
160. *Ferroelectric Crystals for Photonic Applications.* **91**, (Springer Berlin Heidelberg, 2014).
161. Kitaeva, G. K. *et al.* Terahertz wave generation in periodically poled lithium niobate crystals fabricated using two alternative techniques. *Laser Phys. Lett.* **10**, 055404 (2013).
162. Saleh, M. F., Giuseppe, G. D., Saleh, B. E. A. & Teich, M. C. Photonic Circuits for Generating Modal, Spectral, and Polarization Entanglement. *IEEE Photonics J.* **2**, 736–752 (2010).

163. Ishizuki, H., Fujimura, M., Suhara, T. & Nishihara, H. LiNbO₃ waveguide quasi-phase-matched sum-frequency generation device for high-efficiency optical sampling. *Electron. Commun. Jpn. Part II Electron.* **84**, 29–36 (2001).
164. Sulser, F., Poberaj, G., Koechlin, M. & Günter, P. Photonic crystal structures in ion-sliced lithium niobate thin films. *Opt. Express* **17**, 20291 (2009).
165. Ebert, C. B. Quasi-Phasematched Waveguides for Infrared Nonlinear Optics Using GaAs/Ge/GaAs Heteroepitaxy. (1998).
166. Bloom, G. *et al.* Optical parametric amplification of a distributed-feedback quantum-cascade laser in orientation-patterned GaAs. *Opt. Lett.* **35**, 505 (2010).
167. Hildenbrand, A. *et al.* Compact efficient mid-infrared laser source: OP-GaAs OPO pumped by Ho³⁺:YAG laser. in (eds. Titterton, D. H. & Richardson, M. A.) 81870H (2011). doi:10.1117/12.898118
168. Kizilyalli, I. C., Edwards, A. P., Nie, H., Disney, D. & Bour, D. High Voltage Vertical GaN p-n Diodes With Avalanche Capability. *IEEE Trans. Electron Devices* **60**, 3067–3070 (2013).
169. Scott, M. J. *et al.* Merits of gallium nitride based power conversion. *Semicond. Sci. Technol.* **28**, 074013 (2013).

11 Acknowledgements

I would like to thank everyone who has helped and supported me during the course of my Ph.D. work. I give special thanks to the following people:

- I am very grateful to my advisor Professor Axel Hoffmann, for his guidance and support and for giving me the opportunity to be part of an international collaborative project.
- I am deeply thankful to my research advisor Professor Zlatko Sitar, also for his guidance and support, as well as his relentless effort to ensuring the high quality of my research.
- I am also eternally indebted to my research and thesis advisor Professor Ramón Collazo, for his continued motivation, inexhaustible patience and invaluable mentoring.
- I am sincerely thankful to Professor Marko Zgonik and Ph.D. candidate Tinkara Troha, for the collaborative work and many fruitful discussions.
- Special thanks to Professor Douglas Irving and Joshua Harris for their support and collaboration regarding density functional theory based calculations.
- Thanks to my research colleagues Alex Franke, Andrew Klump, Biplab Sarkar, Christian Nenstiel, Felix Kaess, Felix Nippert, Gordon Callsen, Hayden Breckenridge, Isaac Bryan, James Tweedie, Jankowski Nadja, Lindsay Hussey, Luis Hernandez, Marc Hoffmann, Milena Bobea, Pramod Reddy, Quiang Guo, Robert Rounds, Ronny Kirste, Sarah Schlichting, Seiji Mita, Shun Washiyama, Stefan Kalinowski, Thomas Kure, Wei Guo, Will Mecouch and Zachary Bryan.
- I am also thankful to Professor Jon-Paul Maria and his research group for allowing me to use their research facilities and for their support.
- I am grateful to Professor Chih-Hao Chang and Dr. Abhijeet Bagal, for their support and providing the laser interference lithography setup.

Also, I would like to acknowledge CONACYT-Mexico for their financial support as well as support from the NSF and ARO.

To my mother, this dissertation is dedicated to you, thank you for your love and support and for making this possible.